The Investigation of Alanine/EPR Dosimetry, Dose Enhancement caused by AuNPs and the Novel Synthesis of Bimetallic-Nanoparticles via Neutron Capture

A thesis submitted in fulfilment of the requirements for the degree of Doctor of Philosophy

Clare Louise Smith

M.Sc., La Trobe University, Australia

B.Sc. (Hons), La Trobe University, Australia

School of Health and Biomedical Sciences

College of Science, Engineering and Health

RMIT University

November, 2017

Declaration

I certify that except where due acknowledgement has been made, the work is that of the author alone; the work has not been submitted previously, in whole or in part, to qualify for any other academic award; the content of the thesis is the result of work which has been carried out since the official commencement date of the approved research program; any editorial work, paid or unpaid, carried out by a third party is acknowledged; and, ethics procedures and guidelines have been followed.

I acknowledge the support I have received for my research through the provision of an Australian Government Research Training Program Scholarship.

Clare L. Smith

29th of November 2017

Acknowledgements

I firstly and mostly want to thank my wonderful supervisor Assoc. Prof Moshi Geso; I cannot thank you enough for taking me on as a student and the kindness and support you have shown me. I have learnt so much from you, which I hope to take with me in my future working life. I also want to thank my co-supervisor Dr Stephen Best from The University of Melbourne; you have been an invaluable source of help, support and understanding and I am grateful to you. Also, I want to thank Sioe See Volaric for teaching me how to operate the EPR and being so willing to give up her time, also thank you to Dr Simon Drew, Rob Enis and Greg Ellis from The University of Melbourne.

I am also thankful to my fellow lab group members for their ongoing support and laughs, particularly; Frank Gagliardi, Andrew Sheng An Lim, Esho Youkana and Merfat Algethami. Also, to my office mates; Susan Syu Mi Sam, Uma Devi Do Jai Prakash Rai and Chris Lynch thanks for the help and support. I also want to thank the support staff from the numerous RMIT facilities I have used, particularly the Department of Medical Radiations and its staff, as well as; Robert Brown (Histology), Dr Simon Young (Pharmacy), Paul Morrison (Separation Science) and Dr Yilias Sabri (Applied Chemistry).

Also many thanks to the staff at other facilities who were so accommodating and allowed me to use their instruments and equipment, particularly; The Alfred Hospital: Dr Trevor Ackerly and Neil Brouwer, The Hyogo Ion Beam Medical Center: Kai Katahira, Yseu Tsunei, and Prof. Tominaga Takahiro, Australian Nuclear Science and Technology Organisation (ANSTO): Dr John Bennett and Attila Stopic, and the grant from the Australian Institute of Nuclear Science and Engineering (AINSE), and

finally, The Austin Hospital; Dr Henri Tochon Danguy, Dr John Sachinidis, Stan Poniger and Harris Panopoulos. I also wish to thank the wonderful contacts and friendships formed at the 18th Solid State Dosimetry Conference (SSD18) in Munich Germany, 2016, and in particular the incredible help and kindness of Dr Reiner Eßer from Dosimetrics, and Joe & Lisa Rotunda from Rotunda Scientific Technologies.

Finally, I want to thank my lovely daughters; Sasha Moo and Sammy Bear, for all their love and at times much needed distractions, and my mum for the help given. Lastly I want to thank my friends for their ongoing enthusiasm and friendship, particularly; Thomas, Martha, Samantha, Kerry, Margitta, Sam Snr (who I miss very much), Andrea, Ellen, Kate and her father Paul 'Cobra'. Also, the fantastic editing and words of wisdom by Dr Liz Ankers, and the inspiration from Dr Michelle Jones-Lennon to start this PhD. Lastly, I want to thank Anita for helping me during a difficult time and Maryana for the patience shown and invaluable insights gained.

Dedication

I dedicate this thesis to my dad, Alexander (Sasha), who passed away on the 11th of August 2016, I miss you very much. As well, to my children Sasha Louise and Samantha Michelle; you have been through so much and I do all this to improve our future lives together.

Format of this Thesis

This thesis is divided into seven chapters. The first chapter is the Introduction and provides an inclusive overview of relevant topics and themes within, and is based on recent literature. The next five chapters describe multiple projects which were completed, and each chapter is divided into several parts starting with an introduction, methods (including all the materials, experimental methodologies used and sources of potential experimental uncertainty), results and discussion and lastly a concluding section. The final chapter of this thesis examines the overall conclusions formed from this work and possible future directions to be examined.

Contents

List of Figures

List of Tables

Publications

1. **Smith, C.L**, Ackerly, T., Best, S., Gagliardi, F., Kie, K., Little AM, P., Mccorkell, G., Sale, C., Tsunei, Y., Tominaga, T.,Volaric, S. S., Geso, M. (2015). Determination of dose enhancement caused by gold-nanoparticles irradiated with proton, x-rays (kV and MV) and electron beams, using alanine/EPR dosimeters. *Radiation Measurements*, 82, 122 – 128.

2. **Smith, C.L**, Best, S.P., Gagliardi, F., Tominaga, T., Geso, M. (2017). The effects of gold nanoparticles concentrations and beam quality/LET on dose enhancement when irradiated with X-rays and protons using alanine/EPR dosimetry. *Radiation Measurements*, accepted 31st of January 2017, in press.

3. **Smith, C.L**, Ankers, E., Best, S.P., Gagliardi, F., Tominaga, T., Geso, M. (2017). Investigation of IRGANOX®1076 as a dosimeter for clinical X-ray, electron and proton beams and its EPR angular response. *Radiation Physics and Chemistry*, 141, 284-291.

4. Geso, M., Ackerly, T., Lim, S. A., Best, S. P., Gagliardi, F., **Smith, C.L**, (2017). Application of the 'Spiking' method to the measurement of low dose radiation (≤ 1 Gy) using alanine dosimeters. *Applied Radiation and Isotopes*, accepted.

Under review

5. **Smith, C.L**, Best, S.P., Gagliardi, F., Tominaga, T., Geso, M. (2017). The effects of gold-nanoparticle size on dose enhancement when irradiated with X-rays, electrons and protons using alanine/EPR dosimetry. *Radiation Measurements*.

Conference Presentations

1. **Smith, C.L**, Best, S.P, Tominaga, T., Geso, M. (2016). Determination of dose enhancement caused by gold-nanoparticles when irradiated with X-rays and protons using alanine/EPR dosimeters; *the 18th International Conference on Solid State Dosimetry: SSD18, Munich, Germany, 3rd-8th of July 2016.*

Prizes

1. Publication Award, 2nd place prize; f*or an essential contribution to an outstanding publication by a Higher Degrees by Research student*, RMIT University, May 2017.

2. Beautiful Science Award, 2nd place prize; f*or an outstanding contribution by a Higher Degrees by Research student for promoting scientific research*, RMIT University, August 2017.

General Abbreviations and Acronyms

a.u.	Arbitrary units
Au	Gold
AuHg	Gold/mercury
AuHgNPs	Gold/mercury-nanoparticles
AuNPs	Gold-nanoparticles
BiNP	Bismuth-nanoparticles
BiMetNPs	bimetallic-nanoparticles
CPS	Counts per second
DE	Dose enhancement
EPR	Electron Paramagnetic Resonance
FCC	Face-centred-cubic
FTIR	Fourier transform infrared spectroscopy
Hg	Mercury
HVL	Half value layer
ICP-MS	Inductively coupled plasma mass spectroscopy
IWSS	IRGANOX®1076 wax solid solutions
LET	Linear Energy Transfer
LINAC	Linear accelerator
MetNPs	Metal-nanoparticles or metallic-nanoparticles
OSL	Optically stimulated luminescence
P1	The central alanine EPR peak
P2 & P3	The second and third alanine EPR peaks, located either side of P1
PVP	Poly(vinylpyrrolidinone)
ROS	Reactive oxygen species
R1	The main alanine radical formed

R2 & R3	The second and third alanine radicals formed
SSD	Source to Surface Distance
TLD	Thermo Luminescent Dosimeters
w/w	weight per weight

Abstract

This thesis investigated five key areas, which are each presented as a chapter, with the major aims and findings summarized below:

1. The dose enhancement (DE) levels caused by secondary electron emissions from gold nanoparticles (AuNPs) were investigated by impregnating spherical AuNPs of varying sizes (1.9, 5 & 15 nm) and concentrations (3, 2 and 1 %) within the dosimeter alanine. The AuNP/alanine composites were irradiated alongside control pellets (alanine) with different quality beams (kV and MV X-rays, electrons and protons) and the yield of alanine radicals quantified by Electron Paramagnetic Resonance (EPR) spectroscopy. For X-rays (kV and MV) increasing AuNP concentration yielded increased DE, and was greatest for kV X-rays overall (55 % DE for 3 %, 5nm AuNP /alanine composites, which decreased to 15 % DE for the 1 %-composites). Similarly, the effects of AuNP size on DE levels was clearer for kV X-ray irradiations with a preference for the smaller 1.9 nm sized AuNPs. Whilst MV X-ray irradiations did show the same AuNP size preference, the effects of concentration were more noticeable on DE, which was consistent with the literature. Irradiations with charged particles; electrons (6 MeV) and protons (150 MeV) showed no such dependence on either AuNP concentration or size and consistently yielded DE levels of ≤ 9 % (electrons) and ≤ 5 % (protons). These results agree well with recent Monte Carlo simulations, (which report little to no secondary electron production) and support cell and animal studies for AuNPs irradiated with protons that suggest the higher DE seen (ca.15 to 20 %) is due to other processes, such as; the production of reactive oxygen species (ROS) generated from the aqueous media in cells.

Abstract

2. The suitability of IRGANOX®1076 as a near-tissue equivalent radiation dosimeter was investigated for various radiotherapy beam types; kV and MV X-rays, electrons and protons over clinically-relevant doses. Pellets consisting of solid solutions of IRGANOX®1076 in wax (IWSS) were manufactured, which yielded a single EPR peak after exposure to ionising radiations, and was attributed to the phenoxyl radical obtained by net loss of $H^{\bullet}$. Whilst, irradiation of solid IRGANOX®1076 produced a doublet signal, consistent with the formation of the phenol cation radical, obtained by electron loss. The IWSS pellets gave reliable dose measurements for exposures as low as 2 Gy, and a linear dose response for all types of radiations examined. Post- measurements for proton irradiations (up to 77 days) indicate good signal stability with minimal signal fading (between 1.6 to 3.8 %), and no significant change with the orientation of the sample. Overall, IWSS pellets are ideal for applications in radiotherapy dosimetry, and can easily be prepared in wax and moulded to different shapes.

3. Alanine is well known to have an EPR angular dependant response which alters its peak amplitudes. It is understood that water bound within alanine affects the EPR cavities resonance and promotes radical transformations causing signal variation. Means to overcome this include; averaging several measurements at different angles within the cavity, and using an internal EPR standard. This work examined an alternative method using alanine pellets manufactured with the binder (paraffin wax) as the bulk material (approximately 90 %) with alanine dispersed within (approximately 10 %). The sensitivity of the amplitude EPR signal when rotated within the cylindrical axis of the EPR cavity was investigated, with alanine-wax pellets showing a deviation range of; 1.14 to 2.06 % (3 days

post-irradiation), which was comparable to commercial alanine pellets; 0.95 to 1.91 %. After approximately 30 days post-irradiation, the wax-alanine pellets remained stable, without being stored in a controlled environment; 1.56 to 1.93 %, whilst the commercial pellets deviation range had increased; 2.04 to 3.18 % despite being kept in a controlled environment. This simple method offers an alternative means to overcome EPR signal variation, without having to store the wax-samples in a highly controlled environment.

4. Currently alanine dosimeters are limited in their potential use in radiotherapy, mainly by poor sensitivity at low radiation doses (< 5 Gy), which was addressed in this work by implementation of a new protocol called ‘spiking’. A set of alanine dosimeters were ‘spiked’ with a large dose of radiation, (approximately 30 Gy of 6 MV X-rays) then subjected to additional doses ranging between 0.5 and 10 Gy. The radical yield obtained following exposure to ionising radiation was measured by EPR spectroscopy and quantified using the central peak of the alanine radical species. After subtraction of the contribution from the "spike" dose, a linear correlation between both the dose and the area of the central EPR signal was obtained for doses of 0.5 Gy (regression value of 0.9890), and for the central peak’s amplitude (regression value of 0.9895). Overall, this method allowed quantification of doses as low as 0.5 Gy, and offers many advantages as a technique; it is easy to perform, requires no complex EPR signal analysis, and (by the addition of a large spike dose) is not susceptible to baseline distortions at low doses (<10 Gy), and may extend the current usage of alanine dosimeters in radiotherapy.

5. Finally, the novel formation of the bimetallic nanoparticle (BiMetNP); AuHgNP by neutron capture was investigated. Neutron bombardment of AuNPs was completed at ANSTO, with gamma spectrum analysis confirming the formation of the unstable ^{198}Au isotope. After a sufficient decay time, inductively coupled plasma mass spectroscopy (ICP-MS) positively identified the stable ^{198}Hg isotope, thus confirming the formation of the BiMetNP product. Analysis of the γ-decay of the unstable ^{198}Au isotope was perfumed and quantified over time (1 to 10 hours) using thermo luminescent dosimeters (TLD100s), OSL (optically stimulated luminescence) nanoDots® and Gafchromic films (EBT3 and RTQA2-1010), with good agreement between all techniques. These confirm that neutron bombardment of a mono-metallic-nanoparticle offers an alternative means to synthesize alloy-type BiMetNP products, which are not readily formed using current wet-chemistry methods (which favour a core and layer BiMetNP product). Furthermore, the γ- decay of the ^{198}Au isotope has potential as a theranostics agent, capable of emitting a localised radiation dose at a tumour site, whilst simultaneously allowing real time imaging.

Chapter 1: Background, theory and literature review

1.1 Overview

This chapter aims to explain the fundamentals of radiotherapy and how it results in cancer cell death. Recent literature on the use of metallic-nanoparticles (MetNPs) with external beam radiotherapy was examined, and the physics behind these interactions leading to enhanced cancer cell death was investigated. The interactions of matter with varying types of radiation were also reviewed.

Reports of DE caused by AuNPs was reviewed and discrepancies in the literature between cell and animal studies compared to computer modelling for AuNPs irradiated with protons examined. Advantages and limitations of current dosimeters used in radiotherapy were also investigated, with particular focus on the well-studied EPR dosimeter alanine, including its current limitations for use in clinical applications. Finally, the role of AuNPs and their therapeutic benefit in radiotherapy, and the potential advantages of BiMetNPs in this area are also studied.

1.2 Radiotherapy

It was estimated by the International Agency for Research on Cancer (IARC) that in 2012 there were 7.6 million deaths worldwide due to cancer [1]. In 2015 this had increased to 8.7 million deaths worldwide and an additional

17.5 million new cancer cases diagnoses [2]. Today radiotherapy is one of the most common forms of treatment available to cancer sufferers, with over 50% of people diagnosed undergoing radiotherapy at some point in their treatment [1].

1.2.1 How does radiotherapy work

Radiotherapy aims to target and destroy cancerous tumours within the body, with high precision, whilst minimizing radiation damage to the adjacent healthy tissues [3]. To achieve this more personalised modalities capable of accurately targeting the cancer have been sought, as well as, agents called radio-sensitizers, which can readily enter a cancer tumour and be retained, whilst simultaneously sensitizing the tumour to the incoming radiation. Such agents promote greater cell damage and death to the target cancerous cells, and minimise damage to the surrounding healthy tissue.

Radiotherapy is based on ionizing radiation, which is of sufficient energy to remove an electron from an atom at the target site, and generate an ion (i.e. causes ionisation). The ejected electron, plus the excess energy discharged by the ion as it returns to a ground energy state, both act to damage the surrounding target cells. The radiation dose delivered to the cells acts in two different ways; either *directly* damaging the cell's DNA (single or double strand breakage which is more lethal) or *indirectly* by forming radicals from the surrounding water, which also act to damage the cell's DNA [4, 5] (**Figure 1-1**). Therefore, cancer cell death is not instantaneous but rather can take several hours or days to occur [1].

The irradiation damage inflicted on a cancer cell results in the inability to divide and metastasize, ultimately causing cell death and tumour reduction [4]. Whilst the exact mechanism is not completely understood, three known processes are involved:

1. *Apoptosis*- the cells undergo programmed death rather than repair [6].
2. *Mitotic death*- the cells fail to segregate correctly, resulting in abnormal morphology and multiple nuclei. For solid tumours this is the most common means of cell death [1].
3. *Senescence*- the cells permanently lose the ability to proliferate, and apoptosis follows [1].

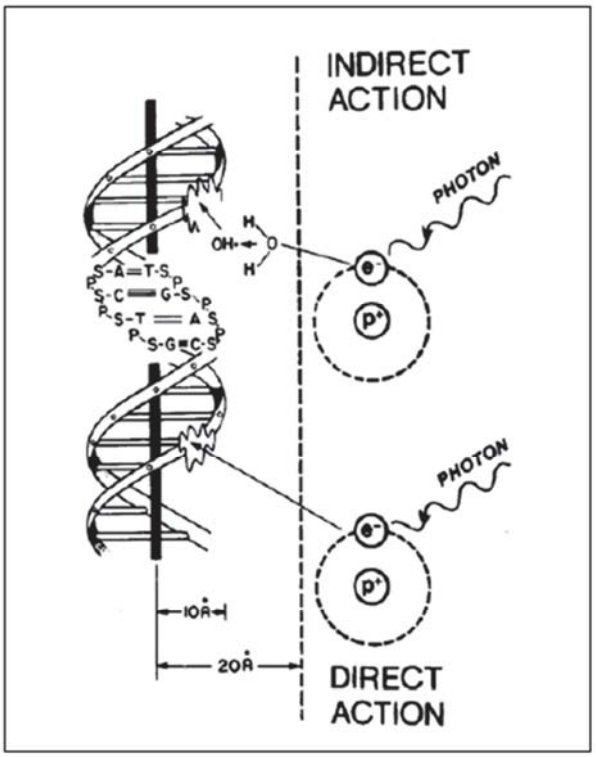

Figure 1-1. Radiation is either direct or indirect in how it damages cancer cell DNA. The incoming photon ejects an electron, which acts directly to damage cancer cells DNA or indirectly to form radicals that go on to damage the cancer cells DNA [7].

1.2.2 Photon radiotherapy

Radiotherapy is administered to a patient either *externally* using beams (electrons, photons etc.) or *internally* using a radioactive material implanted within the

tumour (brachytherapy), which as it decays, delivers a highly localised dose of radiation to the tumour [8].

External delivery utilizes two beam types; photons or particles. Photons (X-ray and gamma rays) are the energy quanta with no mass and low linear energy transfer (LET) [9]. Since the discovery of X-rays by Wilhelm Konrad Roentgen in 1895 [1, 10], their use to treat cancer has revolutionized medicine and provided hope to sufferers for over 100 years, thus making photon based radiotherapy the most common form of treatment used in the world today. X-rays are generated by a X-ray tube (with an energy range of 25-150 kV) [10] or electron linear accelerators (LINAC), which produces high energy X-rays and electron beams in the megavolt range (2-25 MV) [11]. The X-rays/ photons produced are delivered to the patient during treatment in accordance with a treatment plan, which is determined using the known interactions between photons and matter (the patient's tissue), and are described below. Other interaction processes, such coherent scattering, are negligible over the range of energies employed in this research and are not described.

1.2.2.1 How photons interact with matter

The three main processes of how photons interact with matter are; the photoelectric effect, Compton scattering and pair-production, and are all descried below. In all three processes energy is deposited by the incoming photon, and is dependent on; the energy of the incoming photon (beam energy), and the atomic number (Z) and electron density (σ) of the target material [4]. The electron that is then consequently ejected from an atom within the target material goes on to interact with another nearby atom, resulting in further ionisation and excitation events [12].

1.2.2.1.1 The photoelectric effect

The photoelectric effect occurs when the incident photon collides and transfers all of its energy to an inner shell electron. The energy gained by the electron is greater than the orbital binding energy of the electron shell it occupies, so the electron is ejected from the atom. The newly formed ion is both excited and chemically reactive, so to stabilize itself an outer shell electron is moved to the newly vacant inner shell position (**Figure 1-2**), and in doing so releases energy as an X-ray (called a characteristic X-ray as it is related to the energy difference between the electron shell levels that the electron moves between). This characteristic X-ray may then interact with a neighbouring outer shell electron, in a process referred to as a secondary photoelectric effect [4], which in turn causes the electron to be ejected and is known as an Auger electron (**Figure 1-2**).

Photoelectric interactions are dominant for matter of high atomic mass (Z) when interacting with photons of energies (E) < 100 keV, [12] and causes the greatest damage to cancer cells. The probability of the photoelectric effect occurring is therefore dependent on approximately: Z^3 / E^3 [12].

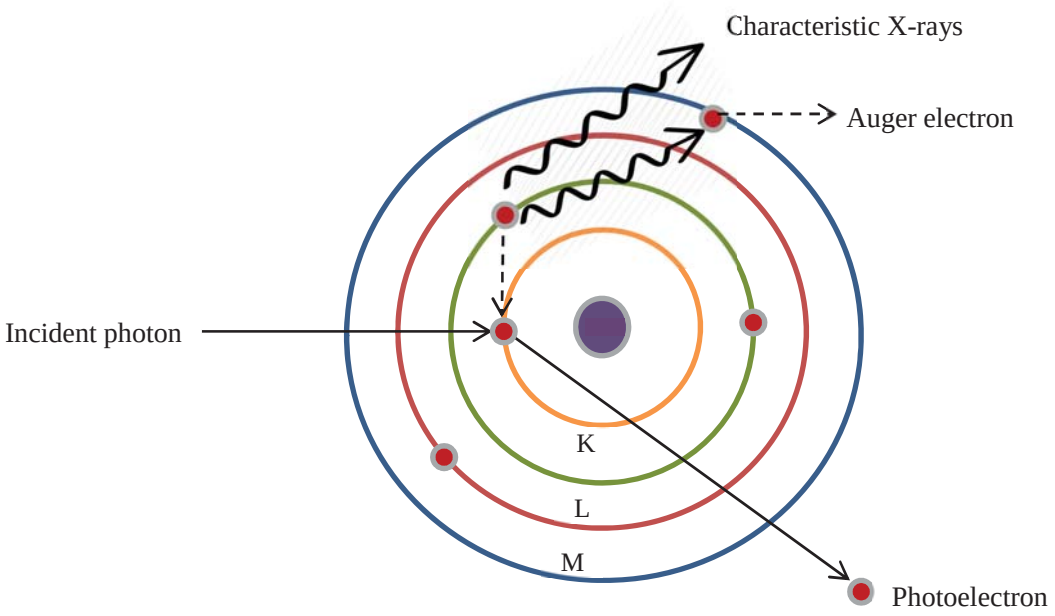

Figure 1- 2. A diagram of the photoelectric effect. An incident photon removes an inner shell electron, whose vacant space is filled by an outer shell electron. The subsequent characteristic X-ray is released causing the emission of a second outer shell electron.

1.2.2.1.2 Compton interactions

Compton interactions are dominant for photon energies between 100 keV to 20 MeV [8]. The incoming photon only interacts with an atom's outer shell electrons, and only part of its total energy is transferred to the electron. The outer shell electron is ejected, whilst the remaining energy is emitted as a scattered photon (**Figure 1-3**). The likelihood of Compton interactions occurring is dependent on a materials electron and physical density (as only low energy outer shell electrons are involved) and not its atomic number (Z).

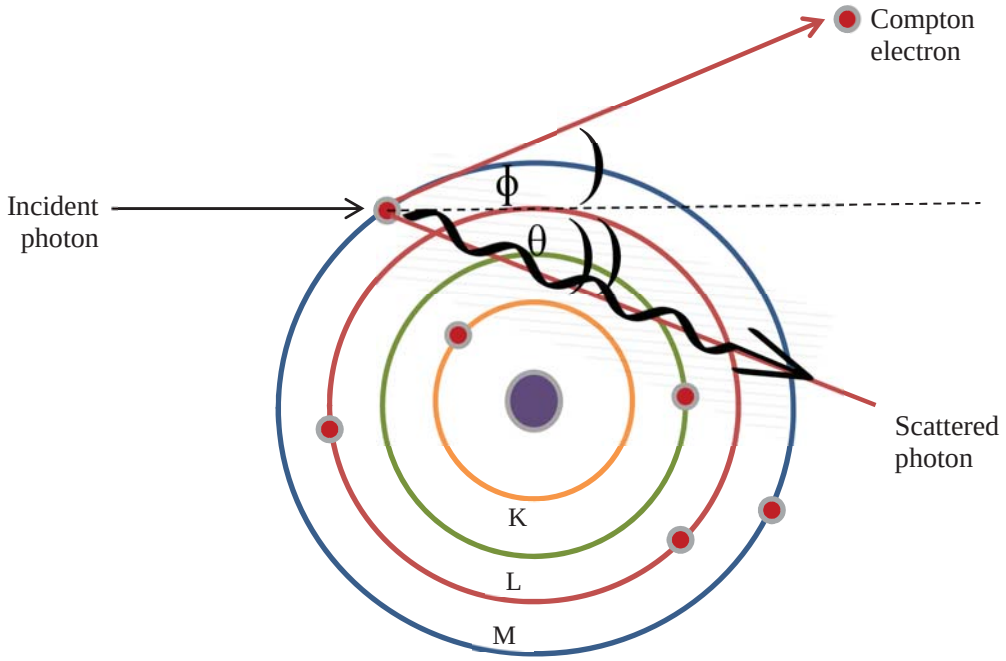

Figure 1-3. The Compton interaction showing the incoming photon interacting with an outer shell electron, and the subsequent scattered photon.

1.2.2.1.3 Pair-Production

Pair-production occurs when the incoming photon gets close to the atomic nuclei and interacts with its Coulomb field (or electromagnetic field); resulting in the formation of an electron (e-) and positron (e+) pair (**Figure 1-4**). The electron and positron interact with surrounding electrons and rapidly lose energy until the positron comes to rest and is annihilated, releasing two photons in opposite directions (which is the basis for Positron Emission Tomography (PET) imaging). Whilst, pair-production generally requires high energies > 1.02 MeV, high Z materials increase the likelihood of pair-production occurring at lower energies [8].

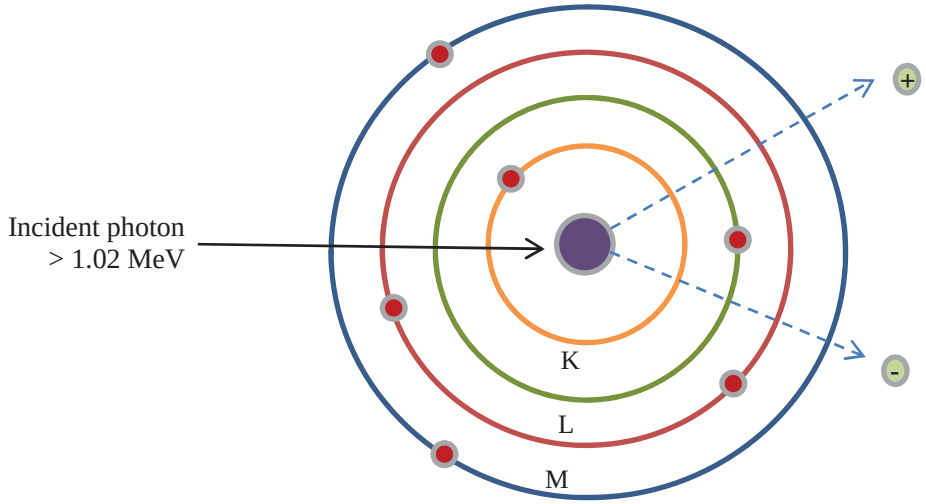

Figure 1-4. Pair-production occurs when the incident photon interacts with the nucleus, and results in the production of an electron and a positron pair.

In the three processes described the transfer of energy from the incoming photons causes emissions from the target material in the form of; photoelectrons, Auger electrons, characteristic X-rays, Compton electrons, scattered photons and positrons. In targeted radiotherapy it is these secondary emissions from photon-atom interactions that are utilized to kill cancer cells, particularly low-energy electrons, which deposit their energy as radiation dose within the surrounding medium, causing biological damage.

The amount of radiation that is absorbed or attenuated by a medium (tissue) is defined by the equation (**1-1**), which describes the attenuation of number of monoenergetic photons in a well collimated beam.

$$I(x) = I_o e^{-\mu x} \qquad (1\text{-}1)$$

Where:

I(x) = the intensity of the photons after passing through a material

Io = the initial intensity of the photons prior to passing through the material

μ = linear attenuation coefficient of the material/medium (cm^{-1})

x = the distance travelled by the photons (material thickness)

Attenuation occurs when the incoming photon intensity (I_o) is reduced (I) after passing through a material of a given thickness (x). Each material has a linear attenuation coefficient (μ), which is the probability of an incoming photon being scattered or absorbed by the atoms within one cubic centimetre (cm^3) of the material [12], and is therefore dependent on its density.

The linear attenuation coefficient is often divided by a material's density, to yield the mass attenuation coefficient (μ/ρ), which is dependent only on the materials atomic composition, and is indicative of the photons 'lost' when passing through a material [13]. It is this process which is used in radiotherapy to determine the amount of radiation dose (energy) absorbed by tissue during treatment, and what the likely biological effects are for a patient undergoing treatment [12].

1.2.3 Particle radiotherapy

Particle therapies are an important treatment modality and include; electrons, protons, neutrons and heavy ions such as carbon ions. Whilst electron beams, which are regularly used in the treatment of superficial lesions [14], are easily produced using LINACs, other forms of high-mass particle therapy are not as prevalent, with only 29 particle accelerators worldwide, compared to 7,500 LINACs listed in 2009 [10]. This is mainly due to the expensive set-up costs associated with construction and shielding, and large areas of land need to house the facility.

Despite this high-mass particles, particularly protons and heavy ions, are advantageous as they deposit more energy deeper within tissue [10], and have very different energy profiles compared to X-rays. Unlike photons, particles release minimal

energy upon entry into tissue, and instead deposit their energy completely at a point of depth called the “Bragg peak”, before exiting with no further energy release (**Figure 1-5**). This energy deposition profile is extremely useful in radiotherapy as damage to healthy tissue above and below the target site is reduced. Therefore, by selecting the particle’s energy, one can control the depth at which the energy is deposited, so that maximal damage is inflicted only at the tumour site.

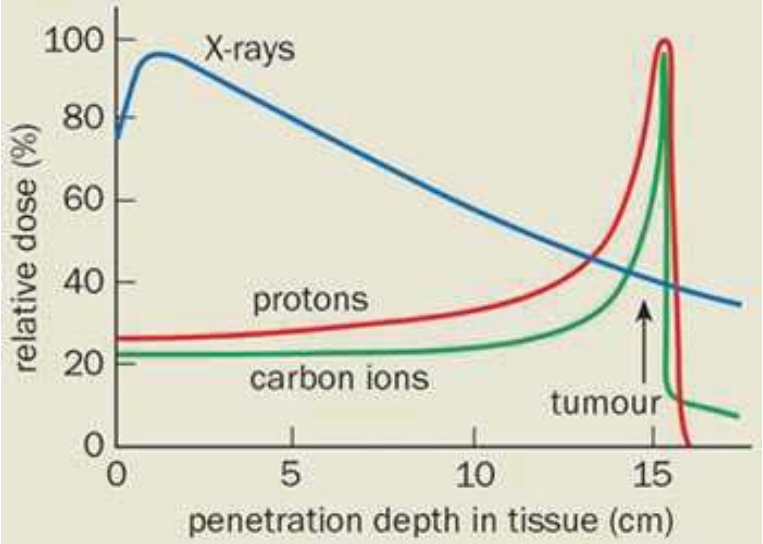

Figure 1-5. The energy deposition profiles of X-rays (blue), protons (red) and carbon ions (green), showing the dose deposition with increasing depth within tissue and the Bragg peak at the site of the tumour [15].

Unlike protons and ions, neutrons have no charge and are therefore not as predictable in their interactions with matter. Whilst, neutron beams are not commonly used in radiotherapy treatments they have shown promise with cancers of the head, neck and prostate [16-18], but are generally used as last line treatment, as the risks outweigh the potential benefit.

1.2.3.1 Neutron interactions with matter

When a collision between a neutron and atomic nuclei occurs one of three interactions result: scattering (elastic or inelastic), capture/absorption or fission [19] (**Figure 1-6**). For thermal neutrons with energies < 0.5 eV any of these three interactions can occur [19], and are described below.

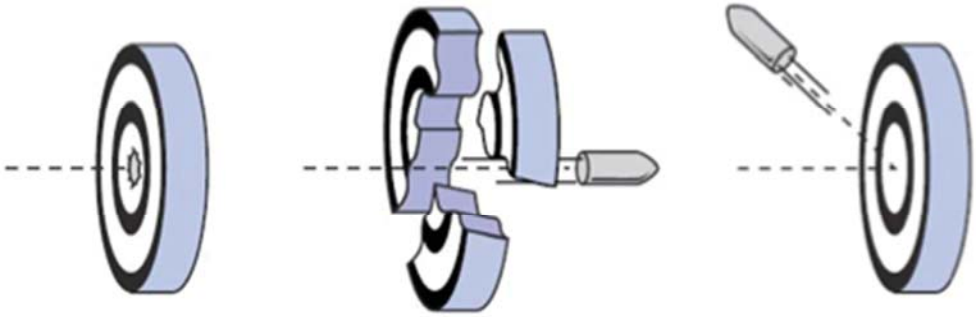

Figure 1-6. The three main interactions of neutrons: absorption, fission and scattering. The neutron is represented as a bullet interacting with a bullseye (matter) [19].

1.2.3.1.1 Neutron scattering

Elastic scattering

Also termed neutron moderation, the collision between the nucleus and matter alters the neutron's direction and energy, so that after multiple collisions the neutron has lost all its kinetic energy and stops. In this interaction the nucleus of the atoms involved do not become excited and remain in the ground state [20].

Inelastic Scattering

In this interaction the neutron loses part of its kinetic energy to the target nucleus, and if enough energy is transferred the nucleus can become excited, and emit secondary radiation (gamma radiation) as it returns to its ground state.

1.2.3.1.2 Neutron absorption/capture

In neutron capture the incoming neutron is absorbed into the target nucleus, to form the next higher isotope (Atomic mass +1). The nucleus is in an excited state and emits gamma rays, and even a proton or alpha particle to stabilize itself [20], and it is this process which is utilized in neutron capture therapy [17].

1.2.3.1.3 Neutron fission

Fission occurs when an incoming neutron collides with a large nucleus and splits it into smaller nuclei, releasing large amounts of energy. Typically the fission products are unequal in mass [20], with neutrons, photons and other products also being generated, and it is this process that can result in chain reactions (**Figure 1-7**).

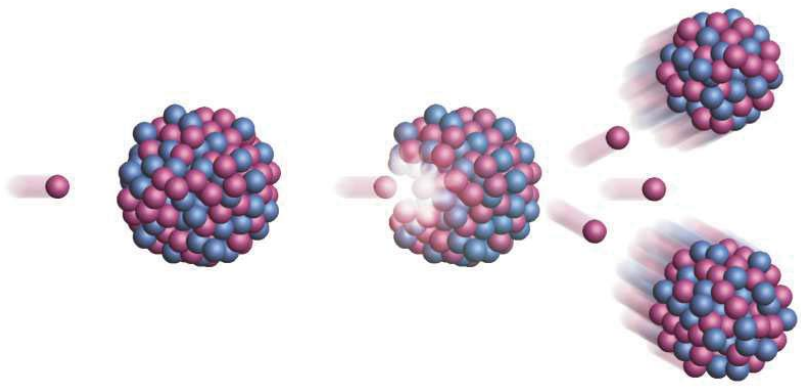

Figure 1-7. The fission process showing the incoming neutron colliding with a nucleus and forming smaller nuclei and two neutrons for further reaction [21].

1.2.3.2 Proton interactions with matter

Protons interact with the electrons and nucleus of atoms in matter via three main processes, as shown in **Figure 1-8**.

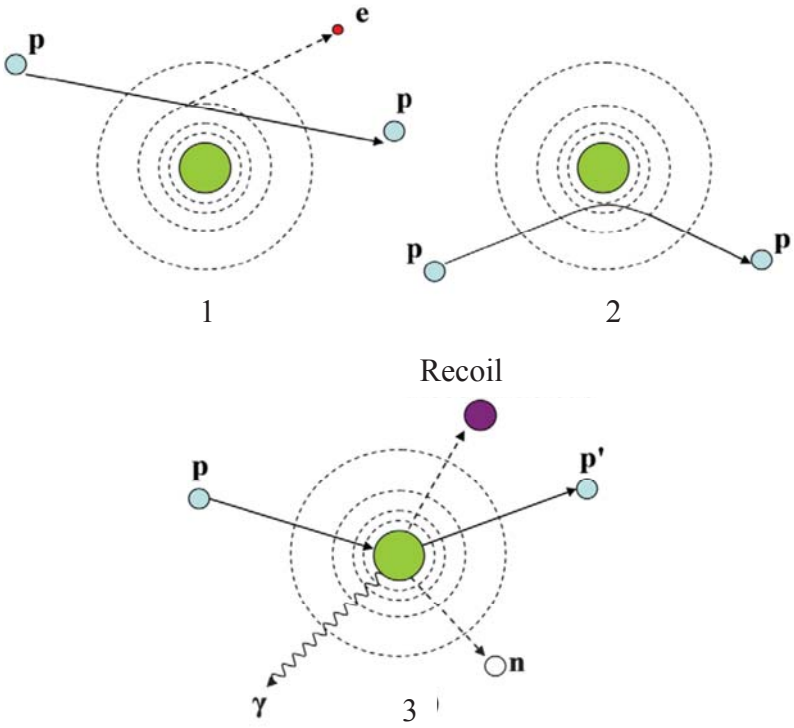

Figure 1-8. The three interaction of protons with atoms in matter (where *p* is a proton, *e* an electron, *n* a neutron and *p'* a proton from the nucleus): (1) Inelastic Coulombic interactions, where small energy losses occur (2) Elastic Coulomb interactions, where the proton is deflected from the nucleus by repulsive forces (3) Non-elastic nuclear interactions, where the incoming proton is absorbed into the nucleus and other nuclei particles are ejected (adapted from [22]).

The energy loss rate of a proton or heavy charged particle as it moves through a material is called the linear stopping power (S), and is defined as the quotient of dE and dx; where E is the mean energy loss and x is the distance traversed through a material/absorber. It should be noted that dx is reflective of only a small part of the total

length travelled by a particle, which deviates from a linear path due to scattering, particularly as energy decreases.

Often the rate of energy loss is expressed without reference to the mass density of the incident particle, so that the mass stopping power for a beam is more simply expressed as is shown in equation (**1-2**) [22].

$$\frac{S}{\rho} = \frac{dE}{\rho.dx} \qquad (1\text{-}2)$$

Where:

ρ = the mass density of the material/absorber.

However, the Bethe-Bloch equation is most commonly used to describe the average energy loss for a heavy charged particle (whose mass is greater than that of an electron) as it is absorbed by a material, and is shown in equation (**1-3**).

$$\frac{S}{\rho} = -\frac{dE}{\rho dx} = 4\pi N_A r_e^2 m_e c^2 \frac{Z}{A}\frac{z^2}{\beta^2}\left[\ln\frac{2m_e c^2\gamma^2\beta^2}{I} - \beta^2 - \frac{\delta}{2} - \frac{C}{Z}\right] \qquad (1\text{-}3)$$

Where:

N_A = Avogadro's number

r_e = the classical electron radius or the Thomson scattering length

m_e = the electron mass

z = the charge of the particle (for a proton z =1)

Z = the atomic number of the material/absorber

A = the atomic mass of the material/absorber

c = the speed of light

β = v/c where v is the velocity of the incoming particle

$\gamma = (1 - \beta^2)^{-\frac{1}{2}}$

I = a constant that is the mean excitation (ionization) potential of the material/absorber

δ = a density correction used to account for electron shielding by distant electrons, which reduces the energy loss

C = a correction factor that is only needed for low energy particles whose velocity is less than or similar to that of the orbital velocity of the bound electrons within a shell.

The interactions of protons in matter (**Figure 1-8**) are described in more detail below.

1.2.3.2.1 Inelastic Coulombic interactions

Protons have a much larger mass [23] and energy, relative to the electron's binding energy within an atom. Therefore, when a proton collides with an outer shell electron, energy is transferred and excitation and ionization of the atoms occurs (number 1 in **Figure 1-8**), and the electron can travel macroscopic distances if the energy transferred is sufficient [23]. Although, the collisions do not significantly alter the protons direction, many such collisions result in a total loss of energy, bringing the

proton to rest. The distance travelled by the proton in a medium during this process is referred to as its range [23].

1.2.3.2.2 Elastic Coulombic interactions

In matter, the proton's path is only significantly changed when it encounters the nucleus of the atom (number 2 in **Figure 1-8**). The repulsive Coulombic elastic interaction between the much larger nucleus and proton deflects it from its path and can completely alter its trajectory [22].

1.2.3.2.3 Non-elastic nuclear interactions

Non-elastic nuclear interactions occur less frequently and require the incoming proton to have sufficient energy to overcome the Coulomb force of the nucleus (number 3 in **Figure 1-8**). The incoming proton enters the nucleus and irreversibly changes the composition of the nucleus by emitting a neutron, proton, deuteron, triton or heavier ion [22].

1.3 Dosimeters in radiotherapy

As stated earlier, radiotherapy aims to deliver a highly tailored dose deposition to cancerous targets, whilst minimizing the damage to normal healthy surrounding tissues [3, 24]. As treatment plans increase in complexity, often involving multiple radiation fields that utilize image guided 4D-CT, PET and MRI, so too has the need to more accurately measure the radiation dose actually being given, to validate the treatment planning outcomes.

There are many different types of dosimeters currently available for use in radiotherapy centres [25], with each possessing its own set of advantages and

disadvantages that warrant and limit its use. Radiotherapy centres typically use three sets of dosimeters; ionisation chambers (parallel plate and Farmer type) for calibration and quality assurance, and TLDs and diodes for *in vivo* patient dosimetry.

1. 3.1 The 'ideal' dosimeter

The ideal dosimeter for use in clinical radiotherapy would possess the following qualities:

- small in size (allowing for small-field dosimetry use [26]),
- independent to the beam energy (so that no correction factors have to be applied),
- immune to changes in the angle of radiation delivery, and the dose rate of administration [26],
- malleable (so custom geometrical forms can be made),
- accurate at low doses (0.5 to 2 Gy) [27],
- tissue equivalent in composition (for more reliable dose estimation in humans) [25],
- have long term post-irradiation signal stability that is not destroyed during the read-out process,
- can be read onsite (where the patient is treated),
- is unaffected by temperature changes during irradiation [25],
- inexpensive (making it disposable), and
- easy to read and interpret [25].

Whilst many dosimeters are available, one that fulfils the majority of these requirements is still sought. In **Sections 1.3.1.1** to **1.3.1.5** some of the most commonly

used radiotherapy dosimeters are described and their advantages and disadvantages presented.

1.3.1.1 Thermo-luminescent dosimeters (TLDs)

TLDs usually consist of lithium fluoride doped with a combination of metal impurities; typically magnesium and titanium. When irradiated, electrons absorb energy and transition from the low-energy 'Valance band' to the higher-energy 'Conduction band' (**Figure 1-9**). However, when the electrons release their excess energy in an attempt to return to their original band they become trapped in an 'electron trap' formed by the metal impurities present [25]. During the read-out process, when the TLDs are heated, the electrons escape the trap and emit light as they return to the Valance band (**Figure 1-9**), which is directly related to the amount of radiation received.

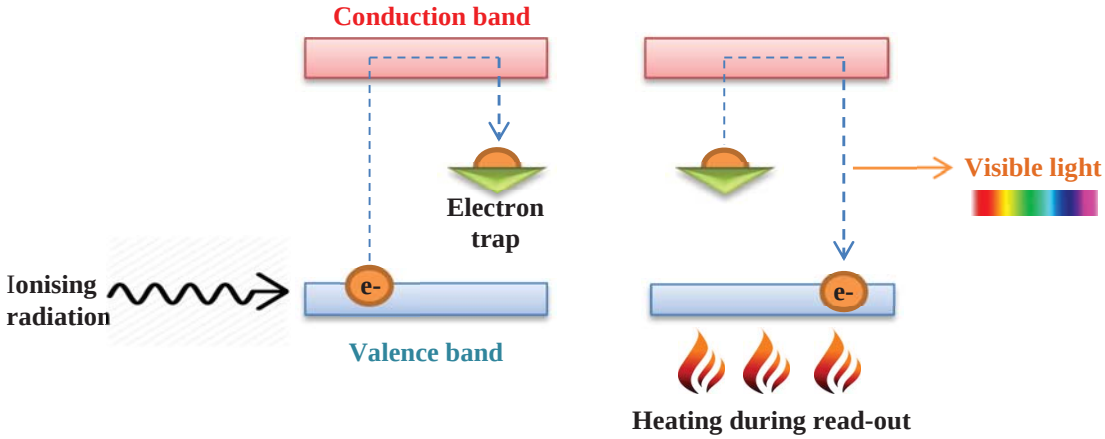

Figure 1-9. The process that occurs for electrons within a TLD; energy is absorbed and the electrons become trapped (after de-excitation from the Conduction band. The read-out process returns the electrons to the lowest-energy state by creating a visually detectable measurement indicative of the radiation dose received.

TLDs are favoured due to their small size (which can be as small as $1mm^3$), no cables are needed, reusable after annealing, are independent to the direction of radiation received and the dose rate used, making them popular for *in vivo* dosimetry [25, 28]. However, TLDs suffer from post- irradiation fading, delayed read-out (approximately one hour), non-tissue equivalence, higher sensitivity to low energy photons (which must be corrected for), require high temperature annealing before use, have poor reproducibility (±2%) [25, 26, 28] and UV/visible light exposure can elicit both an increase in energy absorption, as well as signal reduction within the dosimeter [26].

1.3.1.2 Diodes

Diodes are often employed in specialized dosimetry roles, such as the verification of modulated beams and *in vivo* dosimetry. Typically, the diodes used in radiotherapy are either a diamond or silicon [26] semi-conductor that consist of three different zones (**Figure 1-10**). The first zone is the ‘p-type’ zone, which is doped with group 13 elements (within the p-block of the periodic table), and includes the elements; boron and gallium. On the other side of the diode is the ‘n-type’ zone, which is doped with group 15 elements (within the n-block of the periodic table), and include; phosphorous and arsenic. The p-type and n-type areas are separated within the diode by an area called the ‘depletion zone’ (**Figure 1-10**) where under steady state conditions few free electrons exist within this region [25]. When irradiated, electrons are excited into the conduction band; however, those in the p-type and n-type areas have an extremely short lifetime and recombine or relax very quickly, so that only the electrons in the depletion areas contribute to the measured current. Therefore, the more radiation dose received, the greater the number of electrons produced, and the stronger the current detected [25, 28].

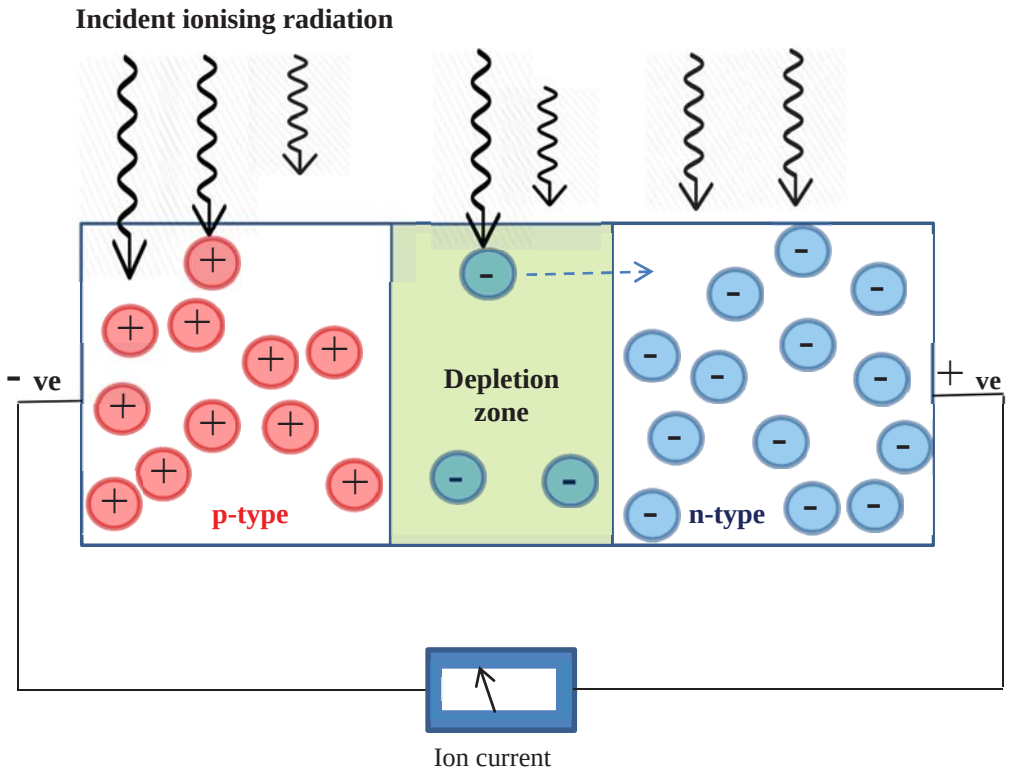

Figure 1-10. The irradiation of a diode produces electrons in the depletion zone, which cross to the n-type zone and generate a current.

Diodes are advantageous as they are highly sensitive, small in size, can be read-out instantly and have excellent reproducibility [25, 28]. However, like TLDS, diodes suffer from non-tissue equivalence, as well as, energy dependence, a narrow range of temperature usage (although this can be corrected for), need cables, pertubates the treatment beam [28] and requires ongoing recalibration due to radiation damage.

1.3.1.3 Fricke dosimeters and PRESAGE®

Radiotherapy has also widely employed chemical detectors, which utilize a reporter chemical to signal an interaction with ionizing radiation. Examples include; Fricke dosimeters and gels, which undergo changes in their optical density and magnetic properties when aqueous Fe^{2+} is converted to Fe^{3+}. Another example is PRESAGE®, which undergoes a visible colour change, from which the absorbance

difference can be linearly related to the amount of absorbed radiation dose received [29]. PRESAGE® contains a halogenated carbon species (usually chloroform or bromoform) that when irradiated cleaves the halogen-carbon bond to form a radical species, which then reacts with a reporter dye (usually leucomalachite green (LMG) [29] to produce an observable colour change. However, both these types of dosimeters are affected by UV light and temperature, which can alter the signal, producing large uncertainties in measurements.

1.3.1.4 Ionisation chambers

The most commonly used detector in radiotherapy centres worldwide is the ionisation chamber, and is employed as a calibration standard for determining the absorbed dose delivered by an external beam [25]. Typically, the chamber is open to air or filled with a noble gas; such as helium, neon, or argon [28], with a voltage applied across two electrodes; the anode (positive) and cathode (negative), to create an electric field [28] (**Figure 1-11**).

Often the electrode plates are positioned parallel to one another, which is a design feature of the commonly used 'parallel plate ionisation chamber'[28]. The other type often used is the cylindrical chamber designed by Farmer, also known as the 'thimble' due to the chamber shape, which ranges in volume size from 0.1 and 1 cm^3 [30]. Incoming ionising radiation (photons, electrons, charged particle etc.) enters the chamber and ionises the air or gas molecules within, producing an ion pair (typically a positive ion and an electron), which migrate to the oppositely charged electrode and produce a current or an electrical pulse depending on the design.

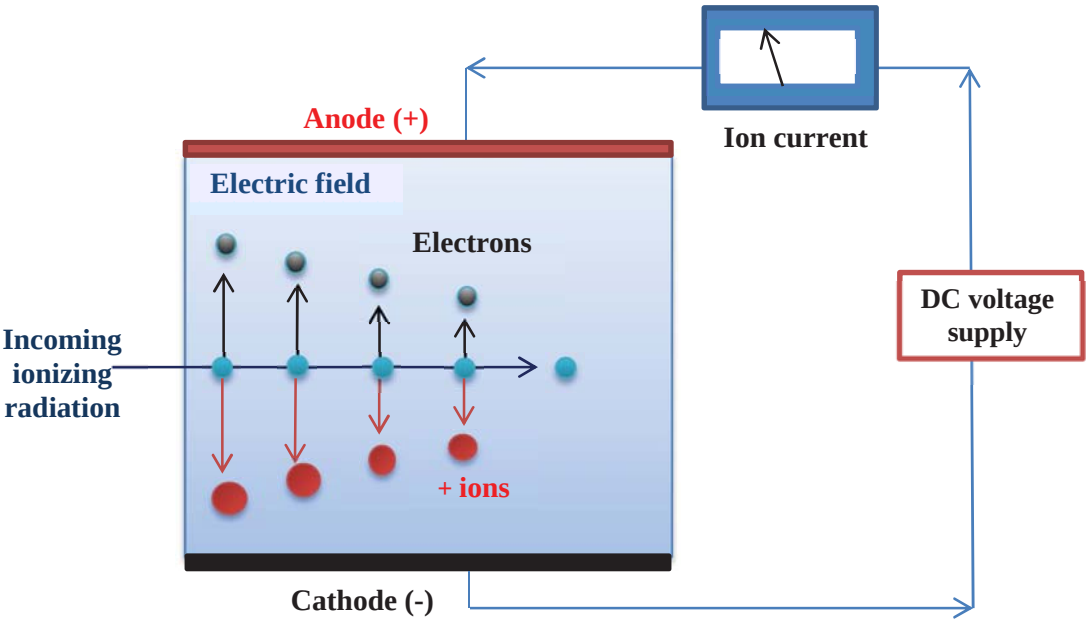

Figure 1-11. A schematic of the ionisation chamber showing the migration of the positive ions (red) to the negative cathode and the electrons (black) to the positive anode after an ionisation event within the chamber.

As the charge detected is related to the number of ion pairs formed, the dose deposited by the incoming ionising radiation can be determined according to the equation (**1-4**) [25]:

$$Q = \frac{P_{ion} e \, \rho \, v \, D}{W} \qquad (1\text{-}4)$$

Where:

Q = the charge collected

D = the mean dose deposited

v = the volume of air within the chamber

P_{ion} = the correction factor for ion recombination

e = the electron charge

ρ = the air density

W = the mean energy needed in air to produce an electron-ion pair

A correction factor for ion recombination (P_{ion}) is needed for instances when the ions formed do not migrate to the electrode plates fast enough and recombine. This occurs when the voltage applied to the chamber is too low or the dose rate is too high, such that the electric field is unable to collect all the ions formed, and underestimates the dose deposited. Similarly, if the voltage applied is too high; secondary ionisation events can occur, causing an overestimate of the energy deposited [25]. Correction factors for standard environmental conditions are also applied and include; temperature (at T_0 22 °C) and pressure (at P_0 101.33 kPa) but are not required for relative humidity over the range 20 to 80 % [31].

1.3.1.5 Radiochromic films

The use of radiochromic films in medical radiation dosimetry has increased greatly since their introduction in the early 1990s [25], with current commercial films having usable dose ranges from less than 1 Gy and up to many kGy [32]. Because of their high sensitivity radiochromic films are often employed in radiotherapy for two dimensional (2D) imaging of dose distribution and can provide high spatial resolution. Whilst film is sensitivity to visible light, energy dependent and non- tissue equivalence[25], this can reduced by storing exposed films in darkness and applying correction factors.

The films consist of an active layer; a poly-diacetylene based crystalline solid material, [25] positioned in-between two polyester layers. When exposed to ionising

radiation polymerisation of the crystalline solid material (active layer) occurs to produce a permanent, visible colour change, without the need for film development [25, 33]. The films are typically scanned in transmission mode, and the amount of light transmitted through the film is relatable to dose. However, as polymerisation is a slow process, the films must be left for a minimum of 6 hours and maximum of 24 hours before being scanned and quantified [33].

As stated earlier, each dosimeter type listed has advantages and disadvantages associated with its use in clinical radiotherapy. Another class of dosimeters are the EPR based dosimeters, of which alanine is probably the best known and studied, and its limits and advantages are examined below.

1.3.2 EPR dosimeters

In 1944 Soviet Russian scientist Evgeny Zaviosky first observed EPR in paramagnetic samples [34], allowing for the identification and quantification of free radical species present within a sample. EPR is based on the fact that every electron has a magnetic moment and spin state (m_s), which when present in a magnetic field will either align itself parallel (lower energy state $m_s = -1/2$) or anti-parallel (higher energy state ($m_s = +1/2$) with the field [35]. As a radical species has a single unpaired electron, it is able to move between the energy states when exposed to an increasing magnetic field and constant microwave energy and fixed frequency. Therefore, when the energy difference between the two energy states (parallel and anti-parallel) matches that of the applied microwave power (**Figure 1-12**), the unpaired electron is able to transition either by absorbing (lower to higher) or emitting (higher to lower) energy as a

photon. As more electrons are found in the lower energy state [35] an overall absorption of energy occurs, which generates the EPR spectrum.

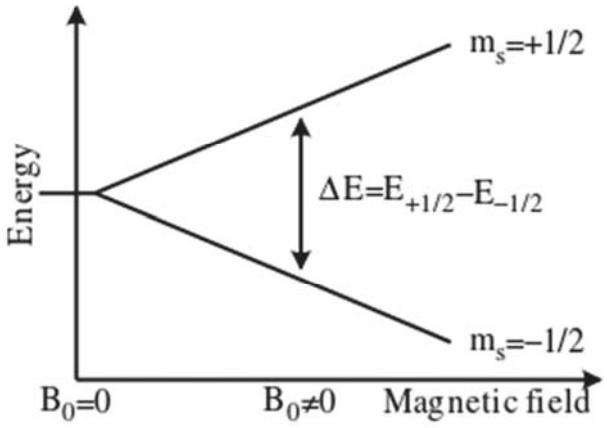

Figure 1-12. The change in energy states between parallel and non-parallel alignment electron spin occur when an increasing magnetic field is applied at a constant microwave power and frequency [35].

Today EPR based detectors (**Figure 1-13**) are used for both industrial and clinical radiation applications, and rely on a chemically reactive species forming a stable radical when irradiated, which is directly related to the radiation dose received. It is also very important that the radical species does not undergo further reactions post-irradiation.

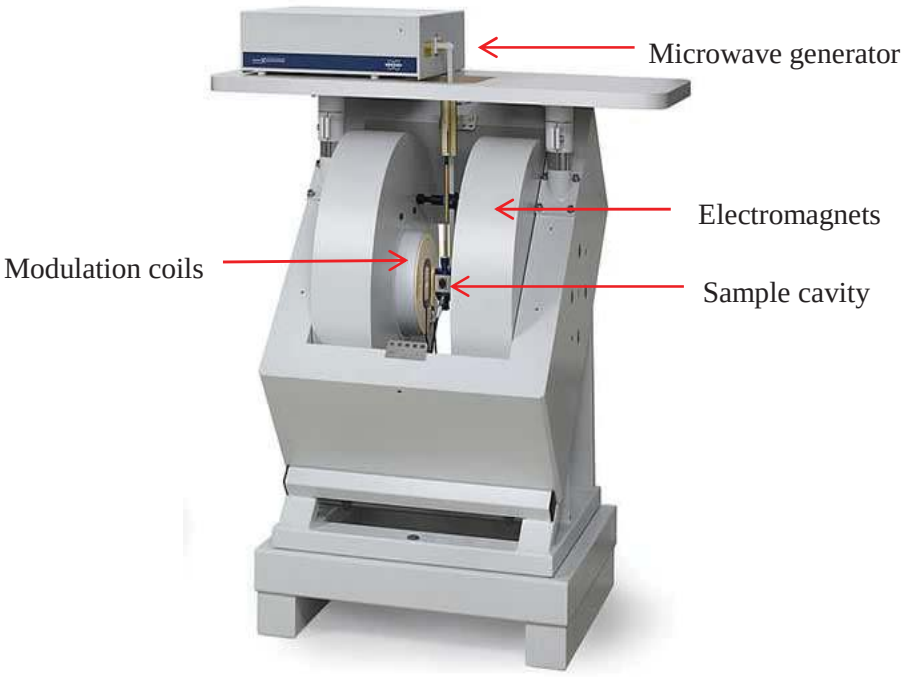

Figure 1-13. A Bruker EPR spectrometer indicating the main features shown.

1.3.2.1 How an EPR spectrum is formed

A material can only be considered useful for EPR dosimetry if after exposure to ionising radiation a large amount of stable unpaired electron radical species are formed, which do not regenerate or form other species over time. Such a radical species will produce a detectable EPR signal, and the amount or concentration of which is directly related to the absorbed dose received, which allows for quantification.

Each radical species formed has its own unique EPR spectrum, which is defined by the following characteristics; shape, line width and resonance field (**Figure 1-14**).

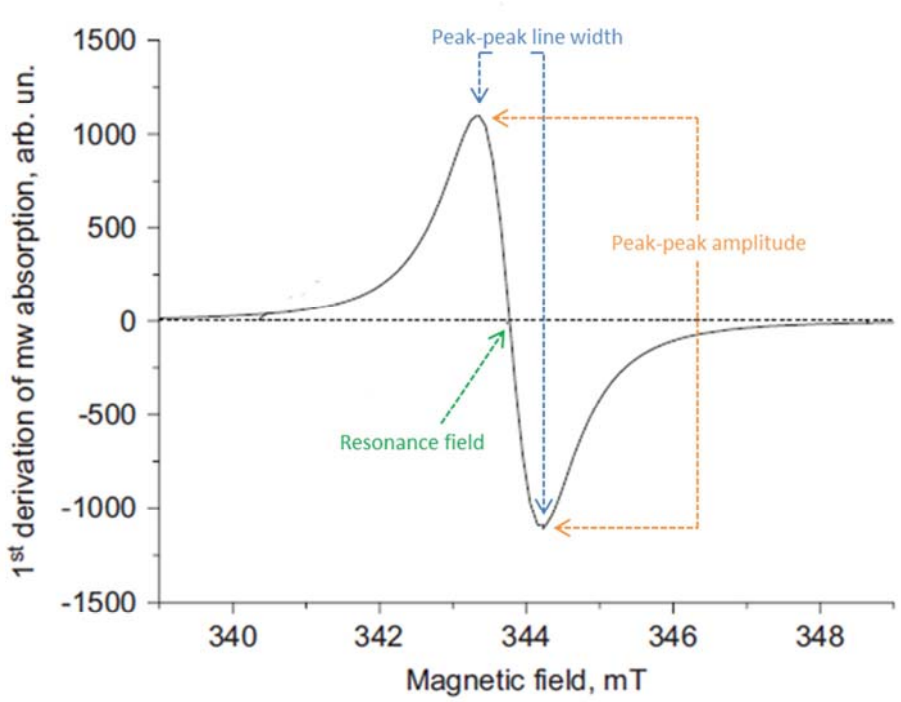

Figure 1-14. The main characteristics of an EPR spectrum used to quantify the radical species (adapted from [36]).

Five types of EPR spectrometers are used routinely worldwide (**Table 1-1**). An increase in sensitivity comes with an increase in frequency, resulting in a smaller EPR resonance cavity, and consequently smaller useable sample size. Furthermore, increased sensitivity also increases the cavities sensitivity to water present within a sample, due to microwave absorption, which adversely affects the resonance and spectrum produced [37]. The X-band is the most commonly used EPR spectrometer worldwide [36] as it has a good balance between sensitivity and allowable sample size. Whilst it does not have the sensitivity of the W and Q bands the effects of water content within the sample are not as large, and it is more sensitive than the lower frequency bands; L and S.

Table 1-1 The frequency (GHz) and corresponding resonance magnetic fields (mT) for various EPR spectrometers in use [36].

Microwave band	Frequency (GHz)	Resonance magnetic field (mT)
L	1.1	39.2
S	3.0	107
X	9.75	350
Q	34.0	1200
W	94.0	3400

1.3.2.2 Alanine/EPR dosimeters

Historically alanine dosimeters have been used for high dose (kGy scale) food irradiation and medical equipment sterilisation. More recently alanine has been successfully used in radiotherapy [38-43] to doses of approximately 5 Gy, and extensively reviewed for this application [25, 44]. Alanine dosimeters are an attractive option for clinical radiotherapy as they have many of the 'ideal' dosimeter properties: tissue equivalency, good stability post-irradiation (when stored correctly), as EPR is non-destructive they can be repeatedly scanned without degradation, are independent of the energy of radiation used [41], dose rate, angle of irradiation, and are commercially available and relatively inexpensive.

Alanine dosimeters also show promise for use with high LET radiation in radiotherapy, such as protons and heavy ions [42, 45], which is a high growth area in radiotherapy. Onori *et* al. [45] reported good linearity, reliability, and sensitivity down to 5 Gy for a 62 MeV proton beam (within the therapeutic range) for alanine dosimeters. Additionally, Michalec *et al.* [42] more recently documented the full dosimetry characteristics of alanine for 60 MeV proton beams.

1.3.2.2.1. The alanine EPR spectrum

When alanine is irradiated three radical species are formed; denoted as R1, R2 and R3 (**Figure 1-15**).

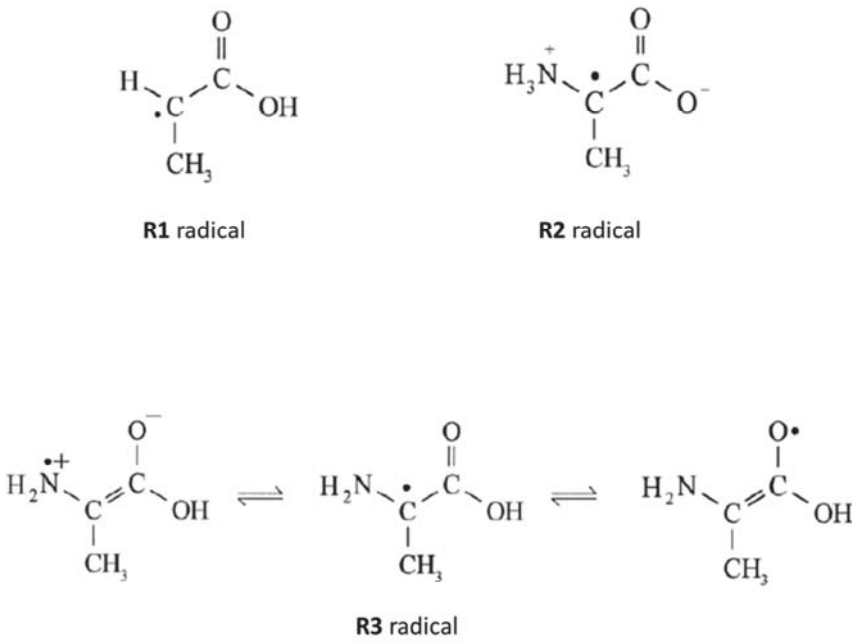

Figure 1-15. The three alanine radicals R1, R2 and R3 formed following irradiation of alanine; R1 is the main stable radical species formed [46].

The resultant alanine EPR spectrum consists of five peaks in a 1:4:6:4:1 ratio [47] (**Figure 1-16**). The large central peak is due to the unpaired electron on the central carbon, formed by deamination, which is the R1 radical [46] (**Figure 1-15**), whilst the remaining peaks are due to hyperfine interactions between the R1 radical and the surrounding four hydrogens, according to the structure CH_3-C·H-COO [41]. Measurements of the central peak's amplitude, are directly related to the amount of radiation received [48].

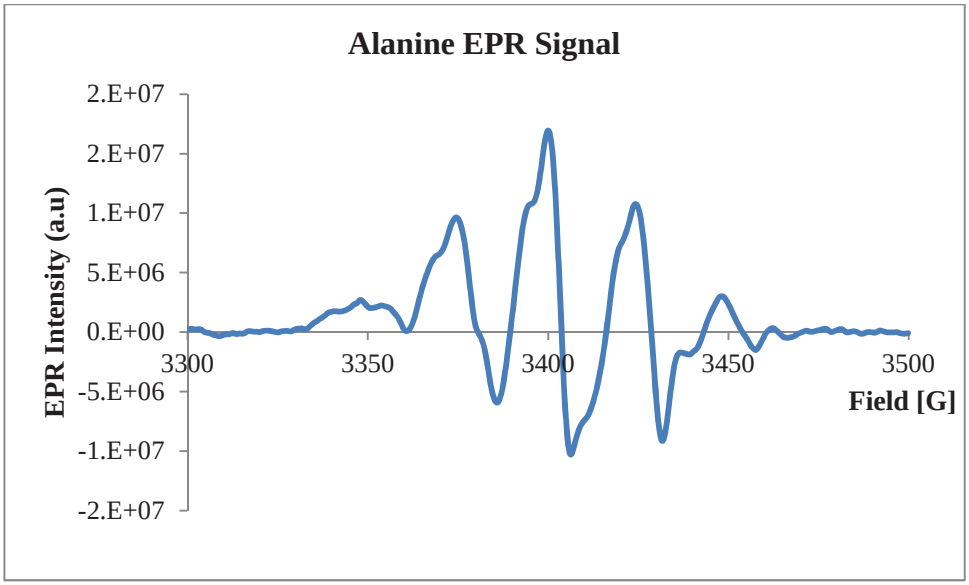

Figure 1-16. The EPR signal for alanine, showing the large central peak, from which amplitude measurements are made.

Heydari *et al*. [46] showed that at room temperature R1 contributes approximately 55% of the EPR spectrum, R2 approximately 35% and R3 the remaining 10% [46] (**Figure 1-15**). Whilst, increasing the temperature was shown to change this composition and the EPR spectrum formed. Work by Dolo and Feaugas [49] also showed that water diffusion in and out of alanine, plus interactions between the three radicals formed all act to affect the resultant spectrum and most importantly, the amplitude of the central peak (**Figure 1-16**).

1.3.2.2.2 Limits of alanine dosimeters

Currently, alanine dosimeters are limited by poor sensitivity at doses below 5 Gy [26, 50], and much effort has been made to remedy this. Simply increasing the mass of alanine is not preferable [48], as this increases the dosimeter size, which limits its use in radiosurgery and intensity-modulated radiation therapy, where narrow photon beams are used [26, 39]. The inclusion of additives such as; metal-nanoparticles (MetNPs)

[39, 51], gadolinium [50] and potassium iodide [51] to increase the amount of secondary electrons generated (thus increasing the amplitude of the resultant EPR spectra) is also limited by the energy of radiation used and therefore its usefulness. As materials with high atomic numbers have increased physical density this increases the probability of photoelectric interactions (and the production of Auger electrons) for low energies (kV), whilst for higher energy X-rays (MV) and charged particles the Compton Effect dominates. As well, the addition of foreign materials alters the alanine composition and hence tissue equivalence, making it non-comparable to human tissue [41].

An alternative approach to improving the sensitivity of alanine dosimeters is to concentrate on the protocols used for measurement of the EPR spectrum and quantifying the signal due to the radical species. Haskell *et al*. [52] and Hayes *et al*. [48] have successfully measured approximately 100 mGy doses using commercial alanine dosimeters using a complex multi-step EPR procedure that requires several days to complete. Later work by Nagy *et al*. [53] reduced the procedure to a single day with an overall uncertainty of 1.5 to 4.0 % (1 standard deviation) for doses between 1 to 5 Gy, however, this adaptation requires modification of the EPR spectrometer. Higher sensitivity can be obtained by the use of EPR spectrometers with a higher microwave frequency where Chen *et al*. [54] demonstrated measurement of 5 Gy doses for miniature alanine pellets (1.5 mm diameter x 2.5 mm length) containing approximately 2 mg DL-alanine using a K band (24 GHz) spectrometer. Later Chen *et al*. [55] manufactured L-alanine/2-methylalanine blended dosimeters (approximately 2.4 to 3.2 mg) and measured doses as low as 0.5 Gy [47]. While this approach is attractive, there is a significant increase in cost and maintenance of the EPR spectrometer in moving

from conventional X-band (9.5 GHz) to K-band and the use of higher frequency microwave sources is currently not practicable in clinical applications.

1.3.2.2.3 Alanine dosimetry in the future?

For alanine to become a realistic alternative to current dosimeters used in radiotherapy (ionisation chambers, TLDs, diodes), it needs to gain sensitivity for low-dose measurements (approximately 0.2 to 10 Gy), and be read using the more commonly available X-band EPR spectrometer.

1.4 Nanoparticles in radiotherapy

The ability to synthesise materials on the nanometre scale has greatly changed the direction of many areas of research and development in recent times (**Figure 1-17**). The unique properties of materials when present in the nanoscale, such as electrical conductivity, magnetic properties and optical changes has led to increased research in fields such as; material technologies, biological applications, and electronics [56].

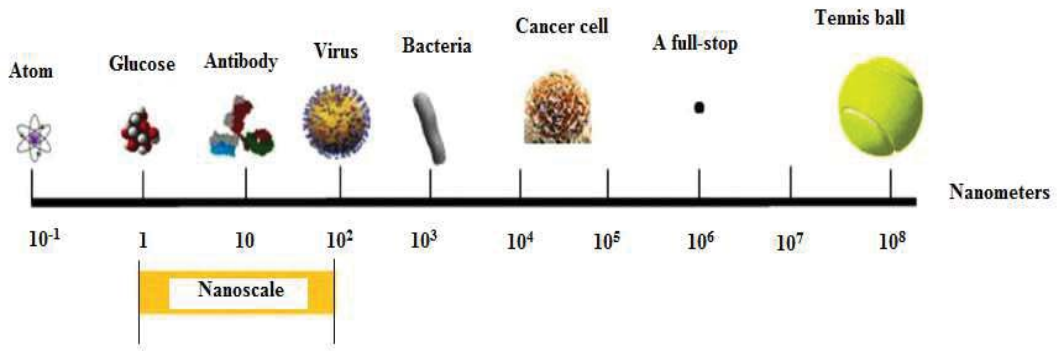

Figure 1-17. The nanometre scale showing size comparisons relative to other items (adapted from [57])

Today the investigation of potential applications of MetNPs as imaging and therapeutic agents in radiotherapy is ever growing and well investigated [58-61]. Nanoparticles often possess unique properties, which are not present in the bulk material. Given that they have a larger surface-to-volume ratio, which increases with decreasing particle size [62], more surface atoms can partake in a given interaction. This differs to the bulk material as the majority of its atoms are locked within the inner-central framework and unable to participate.

1.4.1 Gold-nanoparticles (AuNPs)

The interactions of AuNPs have been well studied in medical-radiation applications [24, 39, 63-67] mainly with photons, and are of interest as they possess several properties that make them attractive:

- High atomic number (Z=79), which increases the probability of photoelectric interactions occurring (the main process by which cancer tumours are damaged).
- A naturally high affinity and retention within the leaky microvasculature system of tumour cells [68] due to strong binding affinities for thiol (-SH) and amine groups ($-NH_2$) [61, 69, 70]. As tumour blood vessels have poorly aligned endothelial cells, the AuNPs can readily enter and are retained due to poor lymphatic drainage [71], making them a useful target for external beam radiotherapy [71, 72] (**Figure 1-18**).
- AuNPs are highly biocompatible and typically less toxic [73] than their chemical counterparts used in cancer treatment [58].

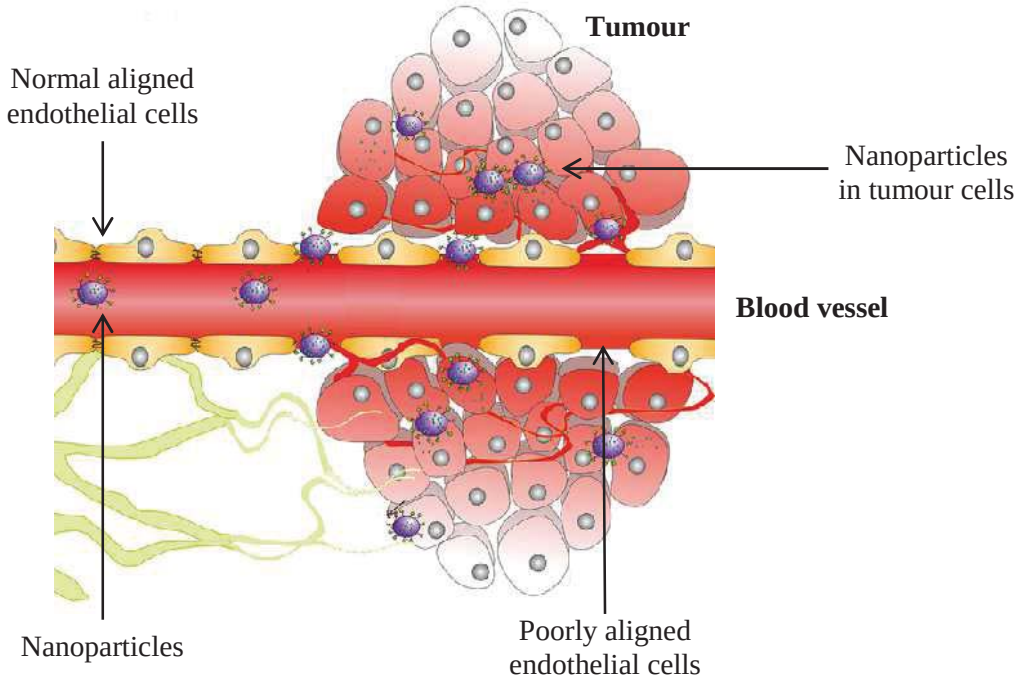

Figure 1-18. A depiction of the entry of nanoparticles into the leaky microvascular system of tumours and retention within the tumour cells (adapted from [74]).

The use of gold and AuNPs as radiosensitizers was first identified by Hainfeld et al. [4], during *in vivo* computed tomography (CT) studies, which showed at energies between 10 to 100 keV gold absorbed approximately 100 times more X-rays than soft tissue. Therefore, it was realized that if gold was present at the tumour site, one could significantly increase the localised dose received by the tumour without any adverse effects to the healthy surrounding tissue. Similarly, Monte Carlo simulations suggest that when AuNPs are uniformly distributed in a tumour they can increase the production of secondary electrons (that damage cells) using a 50 kV X-ray by a factor of 2000 when compared to an equivalent volume of water [24, 75].

However, the DE levels caused by AuNPs when irradiated with ions and protons are still under investigation. Differences in the reported benefit between cell and animal studies [24, 76, 77] and computer simulations [59, 78] suggests that the processes

occurring are not completely understood, and the actual benefits of proton and ion radiotherapy are not clear [79]. Whilst photon ionization is homogeneous and the interactions with nanoparticles are highly probable this is not the case for particle beams, as the likelihood of interactions occurring are reduced, and therefore, the production of Auger electrons [79].

Kim *et al* [80] reported approximately 20 % DE for 14 nm AuNPs in *in vivo* when irradiated with 40 MeV protons, and suggested that the increase is due to a cascade effect of Auger electrons being released, and the generation of ROS as shown in **Figure 1-19**.

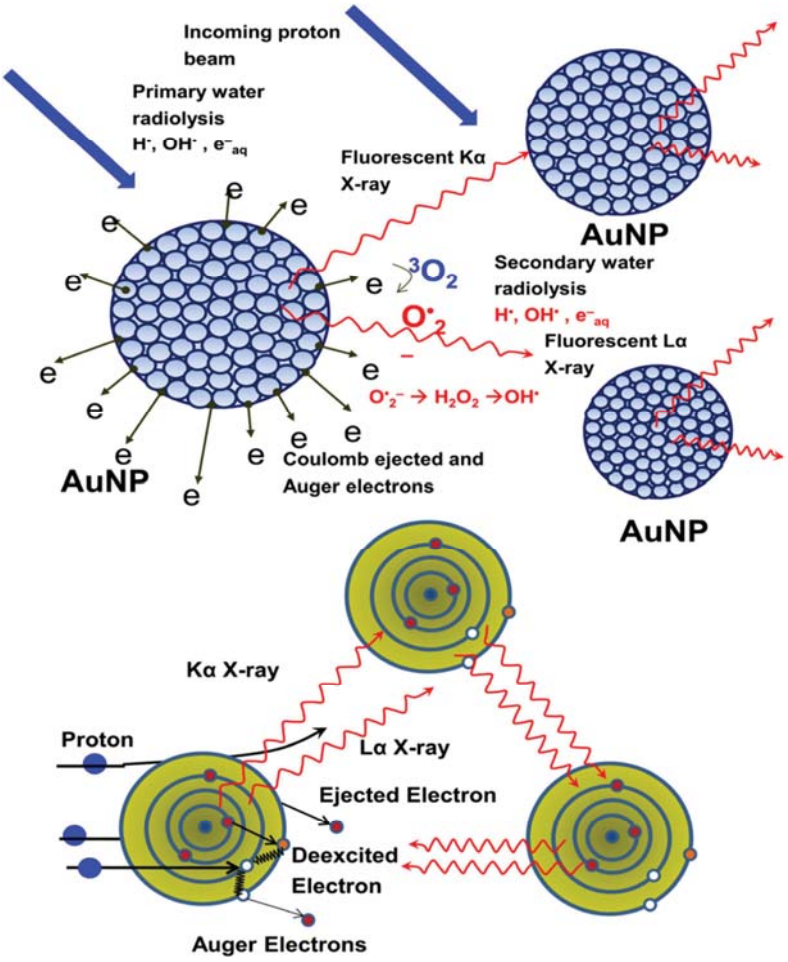

Figure 1-19. The first diagram shows the proposed mechanism for proton-irradiated AuNPs generating ROS. Protons interact with AuNPs and produce Auger electrons, which generate water radicals in the aqueous media. The lower diagram depicts how gold atoms eject electrons and emit X-rays after proton irradiation, which may cause other gold atoms in close proximity to release more secondary electrons [80].

Whilst Monte Carlo simulations by Walzlein *et al.* [79] found for proton energies of 2, 80 and 300 MeV that the radial dose contributions were low (enhancement factor of two), occurred within nanometre distances from the MetNP, and could only be partially attributed to Auger electron production. Similarly, Jeynes *et al.* [81] used simulations and cell studies to compare the production of secondary electron emissions by AuNPs (50 nm diameter) when irradiated with protons ranging in energy from 1 to 250 MeV and kV X-rays (maximum of 250 kV). Whilst enhancement was

seen for kV X-rays, AuNPs only produced modest amounts of secondary electrons when irradiated with protons.

Based on these reports the DE by AuNPs irradiated with protons is of interest, and warrants further investigations to accurately assess the relative contribution of a radical based mechanism for the enhanced efficacy of combined AuNP proton beam irradiation.

1.4.2 Bimetallic-nanoparticles (BiMetNPs)

The study of BiMetNPs in many fields has increased in recent times due to their unique physiochemical properties, interactions and composition [73, 82, 83], which is often greater than the properties of the individual MetNPs they consist of [73, 84]. For this reason BiMetNPs are of interest for use in radiotherapy as they could increase the dose deposition to a target, and have greater uptake and retention properties. Current wet-chemistry methods to synthesize BiMetNPs are limited by the type of BiMetNPs produced; which either consist of two metals present in a NP as an alloy or one-metal present at the NP core with a second-metal layered on top. The latter method is favoured as it is easier to separate the BiMetNP product from the reaction mixture. Overall, the main wet-chemistry methods used to produce BiMetNPs are:

- A one-pot reduction of two different metal salts with a reducing agent, typically sodium borohydride [73, 85], followed by the addition of a protective capping agent like PVP.
- The layered addition of a secondary metal by deposition onto a MetNP core [86].
- The generation of metal ions using high-energy lasers or electron beams, which are then added to a solution of soluble MetNPs [82, 83, 87].

However, these methods are limited by the following issues:

- Time consuming- requiring long preparation and reaction times.
- Require large amounts of reducing agents and solvents - which have an economic and environmental impact.
- Often produce metal salt by-products- making separation of the products difficult [88].

Due to these limitations alternative methods for BiMetNP production have been sought, which ideally favour BiMetNPs of an alloy composition rather than the layered composition. As well, a method that does not use harmful solvents or reducing agents (which form salts and by-products) is preferred.

1.5 Thesis objectives

The objectives of this thesis are to provide greater insight into key areas of radiotherapy research that is both novel and innovative. The five main areas investigated are divided into chapters with the objectives of each summarised below:

1.5.1 Chapter 2- Dose enhancement due to AuNP size, concentration and beam quality

This chapter aimed to quantify and fully investigate the levels of radiation DE caused by the presence of AuNPs using alanine as a phantom and dosimeter. As DE depends on various factors related to the AuNP, such as; size, concentration, beam energy etc. it was decided to systematically investigate each parameter. AuNPs are advantageous as they have been well studied in the literature. Recent discrepancies between the levels of DE attributed to AuNPs when irradiated with protons as reported

by Monte Carlo simulated algorithms- which are fully physics based- are in stark contrast to high DE reported for *in vitro* and *in vivo* studies. Therefore, it was this discrepancy that was investigated and an area of focus for this chapter.

By incorporating AuNPs within an alanine dosimeter, such that the alanine acts as a reporter for the generation of extra secondary electrons due to the presence of the AuNPs, a direct comparison to alanine (without AuNPs present), when irradiated under the same conditions, would allow for differences in DE to be quantified. Specifically this method allowed the following objectives to be investigated:

- The effects of beam quality/ LET (as used within clinical radiotherapy) on the generation of secondary electrons when irradiating AuNPs over clinically relevant doses (2 to 20 Gy).
- The effects of AuNP concentration on the amount of DE observed when irradiating with different radiotherapy beam types over clinically relevant doses.
- The effects of different sized AuNPs (manly smaller sizes which are not well studied) on levels of DE, again when irradiating with different radiotherapy beam types over clinically relevant doses.

1.5.2 Chapter 3- Examination of the novel dosimeter IRGANOX®1076

The novel dosimeter IRGANOX®1076 has shown potential for use as a radiotherapy dosimeter due to its simple EPR spectrum, good long term post-irradiation signal stability, near tissue equivalence, low toxicity and low cost. Therefore, this work examined the following objectives to assess its suitability as a radiotherapy dosimeter:

- The response of IRGANOX®1076 to clinical beams; including kV and MV X-rays, protons and electrons over clinical doses (2 to 20 Gy).
- The stability of the IRGANOX®1076 radical and resultant EPR signal produced over time.
- The deviation in EPR angular response of the signal produced when rotated around the central axis of the EPR cavity, and hence its orientation dependence. As IRGANOX®1076 forms only a single radical species and is hydrophobic; it is less likely to be affected by water content and radical transformations as alanine.
- Comparisons of the IRGANOX®1076 EPR signal with alanine samples irradiated under the same conditions and clinical doses.

1.5.3 Chapter 4- A comparison of the EPR angular response of alanine and IRGANOX®1076

Means to reduce the EPR angular response of alanine when rotated within the EPR cavity are to be investigated. As alanine is highly hygroscopic, exposure to air moisture is thought to both promote post-irradiation radical transformations, and affect the samples water content, which alters the EPR cavity resonance. Together these effects change the EPR spectrum and the amplitude of the central peak, and reduce measurement reliability. Therefore, by encasing alanine within wax, such that the wax acts as a barrier between alanine and the environment, water absorption is limited, and may reduce the EPR angular response. This chapter investigated the following objectives:

- The orientation dependence (angular response) of alanine-wax pellets, commercial alanine pellets and alanine powder samples when rotated around the central axis of the EPR cavity.
- Compare the EPR angular response of the alanine-wax samples to that of the novel dosimeter IRGANOX®1076 (also encased in wax).
- The stability of all samples (alanine-wax pellets, commercial alanine pellets, alanine powder and IRGANOX®1076-wax pellets) over time.f
- Determination of suitable storage conditions for the wax pellet samples to maintain signal reproducibility.

1.5.4 Chapter 5- Investigation of the novel method 'spiking' to determine low doses (<2 Gy) using alanine dosimeters

A novel method to improve alanine's usage as a clinical dosimeter in radiotherapy centres was evaluated. Alanine has been used extensively in industries requiring high dose radiation monitoring (kilo-Grey scale) such as medical equipment and food sterilization. However, more recently attempts to use alanine as a routine low-dose dosimeter in clinical environments or as a secondary standard have been examined, mainly because of its unique properties; such as near tissue equivalence and low-cost. Currently, its application was limited by the distortion of the EPR signal produced at doses below 5 Gy, preventing an accurate measurement of the central peak's (P1) amplitude. To overcome this issue the following objectives were examined:

- Assessment of the novel method 'spiking'; whereby a large spike dose is given to a set of alanine dosimeters prior to a smaller dose (ranging from 0.5 Gy to 10 Gy) for determining low doses of radiation as used in a clinical environment.

- Quantification of the EPR signals produced following each set of irradiations, such that suitable EPR conditions are determined to allow for detectable differences in the alanine radical species produced.
- Establishment of a reliable spiking protocol that does not require complex EPR post-analysis to be conducted.

1.5.5 Chapter 6- The formation of bimetallic-nanoparticles by neutron capture

Finally, this chapter investigated the novel synthesis of BiMetNPs by neutron bombardment, and the formation of an alloy-type product. AuNPs underwent long and short neutron exposures and the following objectives were investigated:

- Determination of the ^{198}Au atoms formation following neutron bombardment using gamma spectrum analysis to confirm neutron capture had occurred.
- Identification of the mercury isotope (^{198}Hg) using ICP-MS after sufficient decay times to confirm the formation of the BiMetNP product.
- Detection of the gamma-decay process of the unstable ^{198}Au isotope to ^{198}Hg using different detectors available, to confirm its potential usage as an imaging agent.

Chapter 2: Dose enhancement due to AuNP size, concentration and beam quality

The majority of the contents of this chapter has been published in two publications. Refer to Appendices i and ii for permission to reproduce published materials.

2.1 Introduction

The chief aim of this research was to measure the effects of spherical AuNPs of different concentrations and sizes on the delivered dose by various radiations with emphasis on protons. In this study AuNPs/alanine composites were prepared based on previous work by Guidella and Baffa [47] which gave a qualitative estimate of the DE of alanine resulting from the inclusion of MetNPs when exposed to low energy X-rays. In addition to the more limited energy range of this study, the experimental conditions did not meet the requirements needed to allow quantification of the dose, and are addressed in this work.

The DE levels caused by the AuNPs are estimated by comparison of the EPR spectroscopy signal's amplitude for alanine, to alanine impregnated with AuNPs and radiated with the same exposure "dose", and the experimental conditions satisfy full scatter conditions.

2.1.1 Alanine dosimetry

Alanine dosimeters and their use as dosimeters are discussed in **Section 1.3.2.2**, including properties that make them an attractive option for clinical radiotherapy, and current limitations at low dose ranges. Given that alanine dosimeters have also been tested for high LET radiations, such as protons and heavy ions [42, 45], alanine is a suitable dosimeter for the investigations proposed, showing good linearity, reliability, and sensitivity down to 5 Gy for a 62 MeV proton beam [45].

2.1.2 AuNP DE size and concentration: kV and MV X-rays

The mechanisms responsible for DE when irradiating AuNPs with kV and MV energy range X-rays are well known [47, 77] and presented in **Section 1.2.2.1**. In brief; low energy X-rays (kV range) when interacting with gold, which has a high atomic number (Z =79), favour the photoelectric effect, resulting in increased production of secondary electrons; photoelectrons (high energy) and Auger electrons (low energy) [89]. The emitted electrons deposit energy, which either directly damages DNA; via single or double stranded breakages [4] or indirectly by generating aqueous radicals (ROS), which also damage DNA and cause cell death [81, 90, 91]. At higher energies (6 to 10 MV range) DE for AuNPs decreases [4, 56, 77, 92] as Compton interactions dominant, and are not dependent on the atomic number.

Whilst, this process is well studied for both *in vitro and in vivo* using kV and MV energy ranges, conflicting results for the role of AuNP size and concentration are evident due to differing cell lines, tumour permeability (how easily the AuNPs can enter), retention factors (how long the AuNPs are retained within the tumour cells) (**Section 1.4.1**), AuNP capping agents and the irradiation beam energy used [93-97]. Likewise,

numerous Monte Carlo simulations have also investigated DE levels due to AuNP concentration for kV energies.

However, four recent studies have focused on both AuNP concentration and size, when irradiated with kV and/or MV X-ray beams [89, 92, 98-100]. The findings for kV energy X-ray irradiations show that DE increases with increasing AuNP concentration, and decreasing AuNP size, whilst for MV energy X-rays; DE increases with increasing AuNP concentration, however, AuNP size is not as important and the effects are less than that for concentration. Lechtman et al. [99] examined AuNPs of 1.9, 5, 30 and 100 nm sizes, which were irradiated with various brachytherapy seeds, 300 kV and 6 MV X-rays. As expected 6 MV X-rays showed the lowest DE, but for lower energy photons the smallest AuNP (1.9 nm) yielded the highest DE levels.

Similarly, Hossain and Su [101] used 50, 110 and 300 kV X-rays to irradiate AuNPs (also bismuth and platinum-nanoparticles) ranging in size from 2 to 400 nm, and found that DE levels increased with decreasing MetNP size or increasing concentration (DE for 7 mg/g of BiNP was 1.3 when irradiated with a 50 kVp source, which increased to 9.99 for 350 mg/g concentrations). Similarly, Mesbahi et al. [92] reported in 2013 comparable findings for kV energy irradiations of AuNPs (30, 50 and 100 nm). AuNPs (30 nm, 7 mg/g) irradiated with a 70 keV source yielded DE of 1.5, which increased to 2.3 for 18 mg/g AuNP concentrations. However, for MV X-rays, whilst a small increase in DE was evident for increasing AuNP concentrations, no such relationship was found for AuNP size (DE was 1.01 for 30 nm AuNPs irradiated with 6 MV X-rays, and remained unchanged for 50 nm and 100 nm AuNPs) [92]. The same results were seen by Hwang et al. [98] for MV X-rays (4, 6, 10 and 15 MV) used to irradiate AuNPs gadolinium and iodine nanoparticles, ranging from 25, 50, 75, 100 and 125 nm in size at concentrations of 7, 18 and 30 mg/ g (of water), with an increase in

nanoparticle size affording only a modest increase in DE (DE for 6 MV X-ray irradiations were 1.017 for 25 nm AuNPs, and increased to 1.029 for 125 nm AuNPs), whilst increasing MetNP concentrations had a much greater effect (DE was 1.017 for 7 mg/g of 25 nm AuNPs irradiated with 6 MV X-rays, and increased to 1.032 for 30 mg/g) [98].

2.1.3 AuNP DE size and concentration: charged particles (electrons and protons)

The DE that occurs when irradiating AuNPs (and other high Z elements in metallic-nanoparticles) with charged particles, such as electron and proton beams, is not as well understood as for photons [79]. Limited studies are reported for electron irradiations, but Rahman et al. [24] reported approximately 4 % DE for 1.9 nm AuNPs measured using cells, which is similar to *in vivo* measurements by Chang *et al* [102] who reported 5 to 10% DE in tumour bearing mice containing AuNPs, irradiated with electrons.

However, significant DE for proton irradiations of AuNPs has been reported for cell/animal studies; Kim *et al* [80] measured a ca. 20% DE for 14 nm AuNPs with 40 MeV proton beams in *in vivo* studies, which was attributed to an increase in the levels of ROS generated by the interaction of the AuNPs with the added protons. Earlier work by Polf *et al* [103] yielded similar DE levels (ca. 15 to 20 %) for *in vitro* studies using AuNPs irradiated with 160 MeV protons. This is in direct contrast to recent Monte Carlo simulations reported by Jeynes *et al* [81] and Walzlein *et al* [79] which reported insignificant amounts of secondary electrons being emitted and subsequently little to no DE.

Recent works have focused on the biological effects within cells as the source of this difference in DE levels between cell/animal studies to computer simulations, and in particular on the production of ROS in the presence of metallic-nanoparticles [104-106]. Notably, Lee *et al* [91] analysed the DNA fragments of tumour cells after irradiation with protons, and from the cleavage patterns produced identified ROS as the key mediator for inducing cell death for proton irradiations. Further work [90] showed an increase in ROS production when AuNPs were present in cells and irradiated with kV X-rays, and was also observed by Kim *et al* [80] who reported a 12 to 36 % increase in ROS when irradiating cells containing AuNPs with protons. More recently, Sicard-Roselli *et al* [107] observed a similar result and concluded that the AuNPs played a catalytic role in the formation of ROS, which required a more inclusive protocol in radiotherapy to better model the DNA damage and cell death that occurred.

Therefore, the aim of this research was to further examine the levels of DE due to AuNPs by using alanine to measure the production of secondary electrons when varying AuNP concentration (3, 2 and 1 %), size (1.9, 5 and 15 nm) and beam quality. The information gained from this work will further the current understanding of the mechanisms involved in DE, and in particular for charged particles (protons) which are less understood [81]. To do this; AuNP/alanine composites were manufactured and placed as a uniform layer within a wax pellet, and irradiated simultaneously with control wax pellets containing only alanine. By direct comparison with the control pellets of the EPR signal of the alanine radical formed (due to deamination of the alanine molecule) the levels of DE for all AuNP concentrations was determined and attributed to the formation of secondary electrons formed due to the presence of AuNPs.

2.2 Methods

2.2.1 Preparation of AuNP/alanine composites

All chemicals used if this work were of analytical grade, and used without further purification. L-Alanine (≥ 98 %) was purchased from Sigma Aldrich, and all references to alanine within this work pertain to L-Alanine. The AuNPs used within were of three sizes, as shown and purchased from Nanoprobes as capped nanoparticles:

- 1-mercapto-(triethylene Gycol) methyl ether functionalized AuNPs (5nm)
- AuroVist™ 15 nm AuNPs
- AuroVist™ 1.9 nm AuNPs

2.2.1.1 5 nm AuNP/alanine composites (3, 2 and 1 % AuNP content)

Composites of 5 nm- AuNP/alanine were produced by dissolving 80 mg (mass of Au) of 5 nm 1-mercapto-(triethylene gycol) methyl ether functionalized AuNPs in 4 mL of Milli Q water in a small beaker. The mixture was sonicated to disperse the crystals uniformly yielding a dark purple solution, and added at room temperature to a stirred solution of L-alanine in Milli Q water. Composites were prepared as follows; 3 %: 4 mL of the purple solution added to 2.587 g of alanine, 2 %: 2 mL of the purple solution added to 1.960 g of alanine, 1 %: 1 mL of the purple solution added to 1.980 g alanine. The resulting solutions were stirred for approximately 5 minutes, then placed in an oven overnight at approximately 60 to 65 °C to remove all water and yield the dried L alanine/AuNP composite (**Figure 2-1**) as a purple/grey solid (3 %: 2.693 g, 2 %: 2.043 g, 1 %: 2.059 g).

Figure 2-1. The dried purple/grey solid; L-alanine/AuNP (5 nm, 1 %) composite.

2.2.1.2 15 nm AuNP/alanine composites (3, 2 and 1 % AuNP content)

Composites of 15 nm- AuNP/alanine were produced by adding 40 mg (mass of Au content) AuroVist™ 15 nm AuNPs in 0.2 mL phosphate buffered saline solution (pH 7.4) to Milli Q water (3.8 mL). The solution was filtered through a 0.22 mm hydrophilic polysulphonic membrane syringe bacterial filter (supplied by Nanoprobes) and the dark red/purple filtrate was collected (4 mL). The solution was added at room temperature to a stirred solution of L-alanine in Milli Q water. Composites were prepared as follows; 3 %: 3 mL of the red/purple solution was added to 0.970 g of alanine, 2 %: 4 mL of the red/purple solution added to 1.960 g of alanine, 1 %: 1 mL of the red/purple solution added to 0.990 g alanine. The resulting solutions were stirred for approximately 5 minutes, then placed in an oven overnight at approximately 60 to 65 °C to remove all water and yield the dried L alanine/AuNP composite (**Figure 2-2**) as a purple solid (3 %: 0.968g, 2 %: 1.899 g, 1 %: 0.990 g).

Figure 2-2. The dried purple solid; L-alanine/AuNP (15 nm, 3 %) composite.

2.2.1.3 1.9 nm AuNP/alanine composites (3, 2 and 1 % AuNP content)

Composites of 1.9 nm- AuNP/alanine were produced by dissolving 40 mg (mass of Au) of AuroVist™ 1.9 nm AuNPs in 4 mL of Milli Q water in a small beaker. The mixture was sonicated to disperse the crystals uniformly yielding a dark brown solution, and added at room temperature to a stirred solution of L-alanine in Milli Q water. Composites were prepared as follows; 3 %: 3 mL of the purple solution added to 0.970 g of alanine, 2 %: 2 mL of the purple solution added to 0.980 g of alanine, 1 %: 1 mL of the purple solution added to 0.990 g alanine. The resulting solutions were stirred for approximately 5 minutes, then placed in an oven overnight at approximately 60 to 65 °C to remove all water and yield the dried L alanine/AuNP composite (**Figure 2-3**) as a purple/grey solid (3 %: 0.926 g, 2 %: 0.956 g, 1 %: 0.971 g).

Figure 2-3. The dried grey/purple solid; L-alanine/AuNP (1.9 nm, 2 %) composite.

2.2.2 TEM of alanine/AuNP composites

Nanoparticle morphology, size and distribution was examined using the JEOL 1010 transmission electron microscope with Gatan Orius SC600 CCD Camera, by dissolving the solid in a small amount of isopropanol and drying a drop of the colloidal suspension on a strong carbon grid (GSCu 200C-50) or mesh copper holey carbon grid.

The nanoparticles were spherical and well dispersed, with an average size of 2.9 ± 1.1 nm (1.9 nm AuNPs), 8.2 ± 1.7 nm (5 nm AuNPs) and 18.6 ± 1.2 nm (15 nm AuNPs).

A typical TEM scan of the AuNP/alanine composite samples is shown in **Figure 2-4** for 5 nm AuNPs, and **Figure 2-5** for 1.9 nm AuNPs and **Figure 2-6** for 15 nm AuNPs.

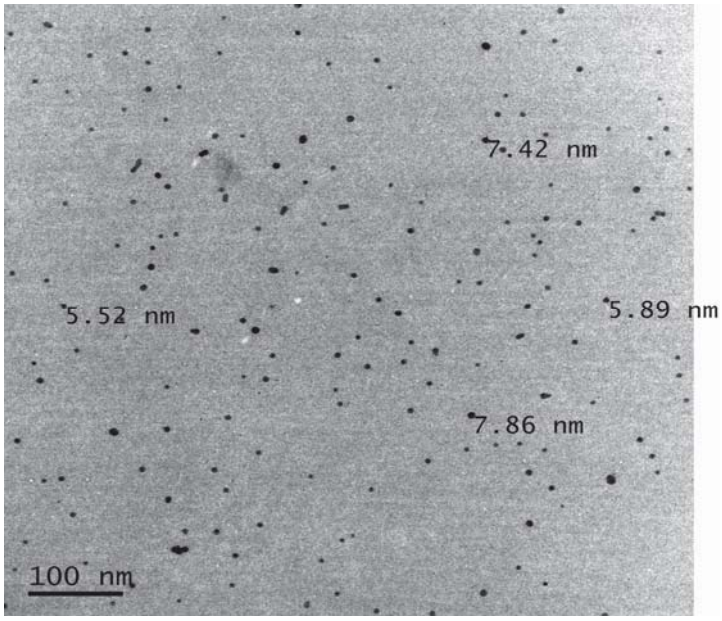

Figure 2-4. TEM scan of alanine with AuNPs (5 nm) dispersed (black circles) on strong carbon grid.

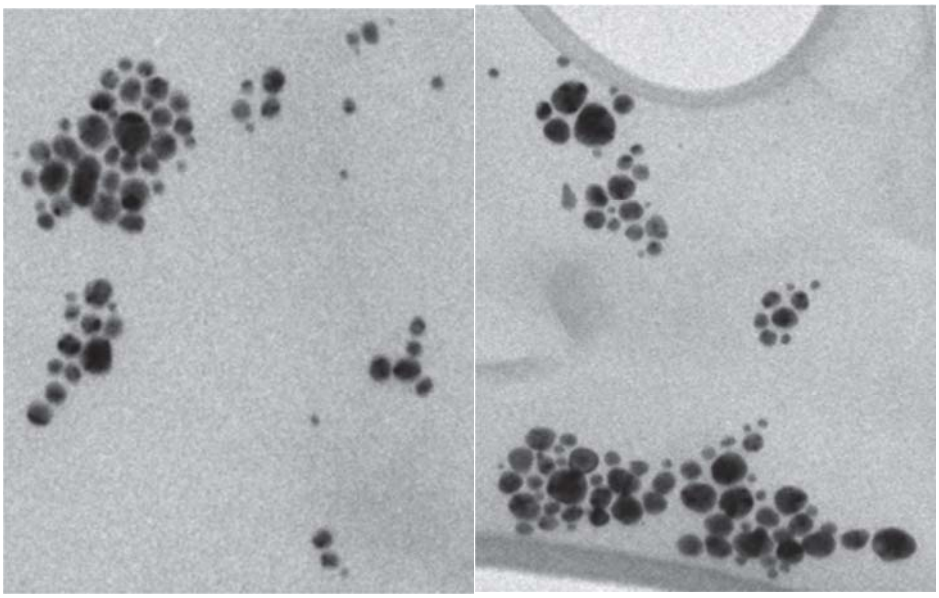

Figure 2-5. TEM scan of alanine with AuNPs (15 nm) dispersed (black circles) on holey carbon grid.

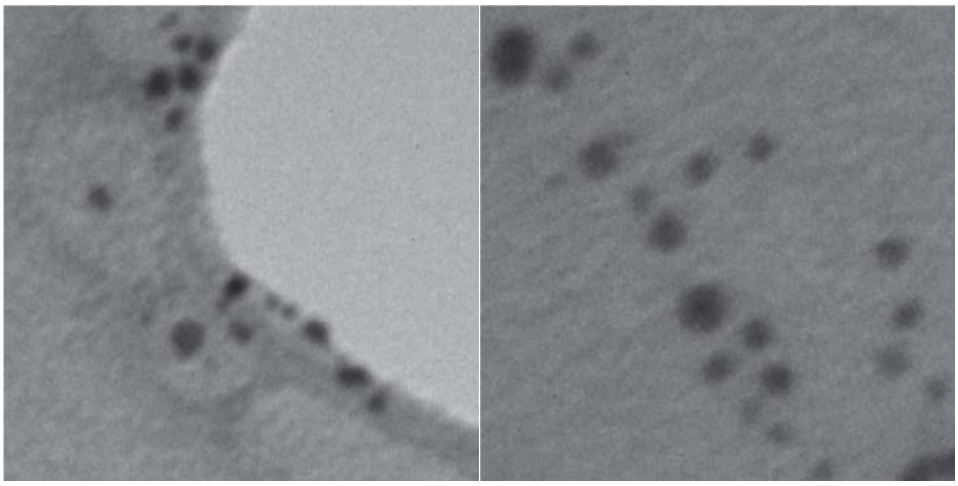

Figure 2-6. TEM scan of alanine with AuNPs (1.9 nm) on holey carbon grid.

2.2.3 FTIR of alanine/AuNP composites

Fourier transfer infrared (FTIR) spectrum was recorded using a Bruker Tensor 27 spectrometer using a KBr pellet, in the region between 4000 and 40 cm^{-1}, and spectra obtained is shown in **Figure 2-7**.

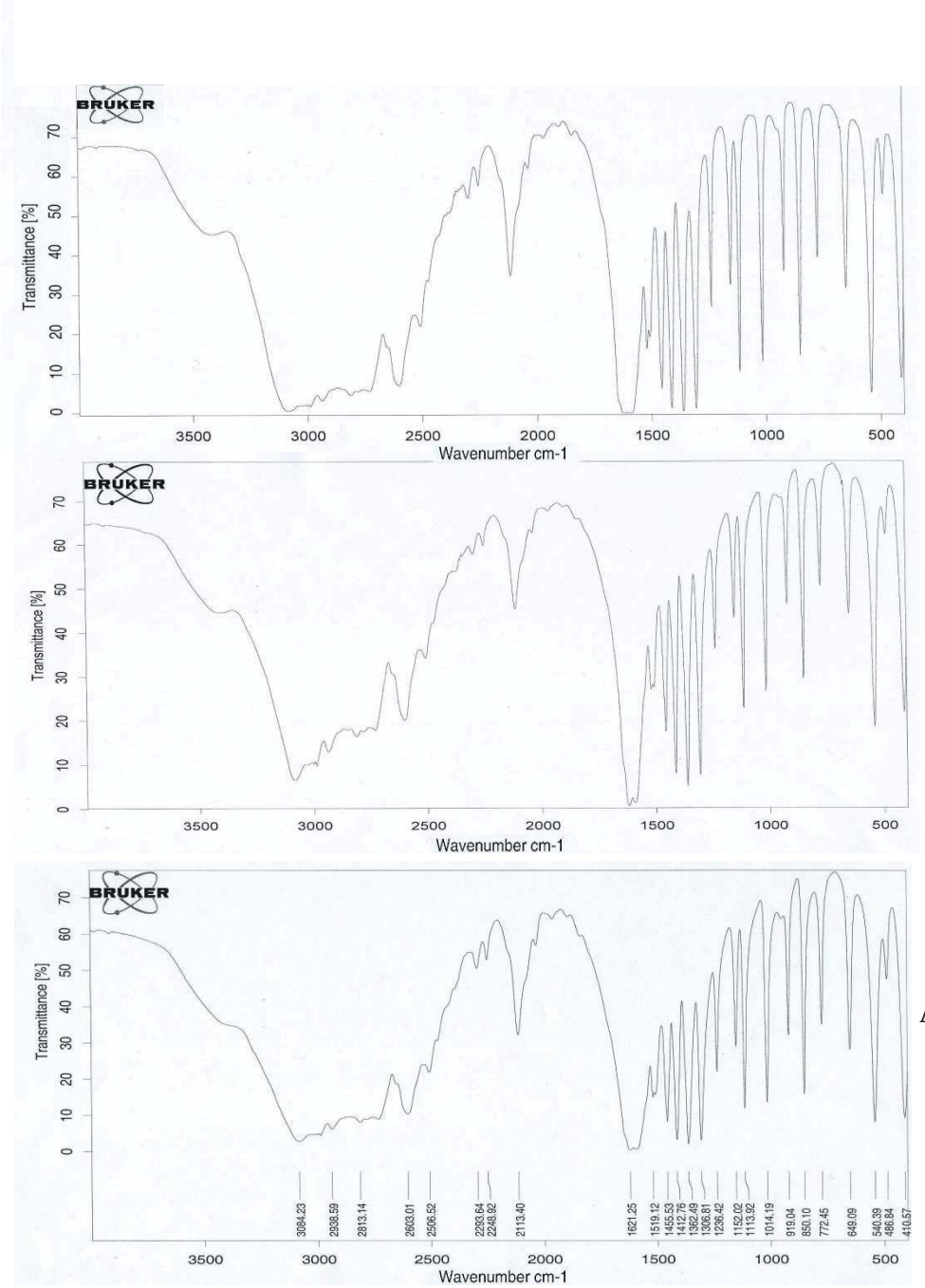

Figure 2-7. The FTIR spectrum for 1.9, 5 and 15 nm Au/alanine composites with the major bands present in all three spectra.

The major bands evident in all three AuNP sizes are in agreement with those reported in the literature (**Table 2-1**) [38] and include the band at 2113 cm^{-1} due to NH_3^+ bending, the band at 1621 cm^{-1} due to NH_3^+asymmetric stretching, the bands at 1413

and 1307 cm^{-1} due to symmetric stretching of the COO^- group, and lastly the band at 1362 cm^{-1} due to CH_2 wagging and CH_3 asymmetric stretching.

Table 2-1. A summary of the major bands in the FTIR spectrum recorded for the Au/alanine composites containing AuNPs of 1.9, 5 and 15 nm (adapted from [38]).

Wavenumber (cm-1)	Assignment
540	COO− rock
649	COO− scissoring
772	O−C−O bending
850	C−C−N symmetric stretching
919	C−C−N symmetric stretching
1014	C−N symmetric stretching
1113	COO− symmetric stretching
1152	COO− symmetric stretching; NH3 + rock
1236	COO− symmetric stretching
1307	COO− symmetric stretching
1362	CH_2 wagging; CH_3 asymmetric stretching
1413	COO− symmetric stretching
1456	CH symmetric stretching
1519	NH_3+ symmetric stretching
1621	NH_3+ asymmetric stretching
2113	NH_3 + bending
2603	CH asymmetric stretching
3084	NH_3 + symmetric stretching

2.2.4 Preparation of AuNP/alanine and alanine-wax pellets

Paraffin wax was obtained from Leica Biosystems as Paraplast Tissue Embedding Medium. All work within this section was completed in the RMIT Bundoora Histology teaching laboratories using the Leica® embedding stations to dispense the molten wax into the moulds, this allowed for the rate of flow of the

warmed liquid wax to be controlled and for uniform and consistent wax pellets to be produced.

A set of silica moulds were manufactured with multiple rectangular inserts cut out, each measuring 10 x 5 x 5 mm (**Figure 2-8**). The silica moulds were warmed so that the molten paraffin wax did not harden upon contact, which ensured the pellets were of good construction and prevented sheering as the wax was added in two stages.

Figure 2-8. The silica moulds used to fabricate the wax pellets (left) and the moulds being filled with molten wax to form the top layer (right).

Approximately two drops of molten paraffin wax was added to the bottom of the warmed mould then a uniform layer of either AuNP/alanine composite (30 mg) or L-Alanine (30 mg) was added. The powder was placed on top of the molten wax, and an additional 3 to 4 drops of molten wax was then added over the solid powder to fill the mould. The mould was then cooled and the wax pellet removed, excess wax was trimmed to yield uniform wax pellets (measuring 10 x 5 x 5 mm) of L-Alanine/AuNP (dark in colour) or L-Alanine (white). Only pellets with an even distribution of solid through the wax at approximately 2 mm depth were used (**Figure 2-9**).

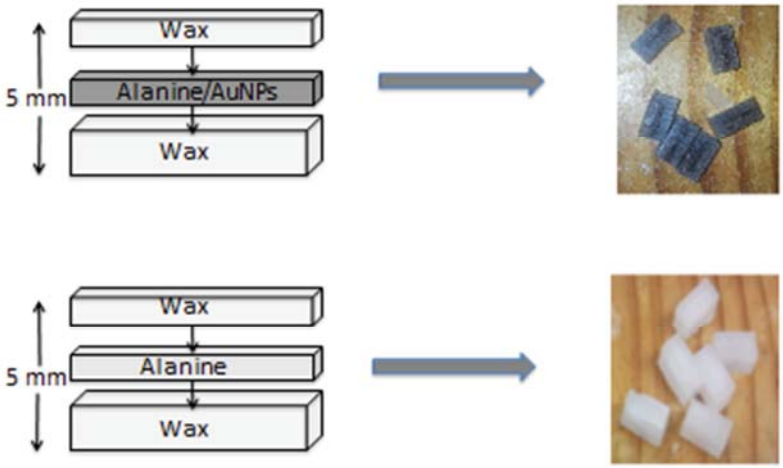

Figure 2-9. Production of wax pellets with alanine crystals of two formats; with AuNPs (upper) and without (lower).

2.2.5 Irradiation conditions of AuNP/alanine composites and control alanine-wax pellets

All x-ray (kV and MV) and electron irradiations were completed at the William Buckland Radiotherapy Centre, Alfred Hospital, Melbourne, Australia, and proton irradiations were completed at the Hyogo Ion Beam facility in Japan.

Nominal doses of 2, 5, 10, 15 and 20 Gy were given, and administered as accumulative doses. This was done by initially irradiating all samples with a 2 Gy dose, from which the first set of samples were removed (total dose of 2 Gy received). A second dose of 3 Gy was then administered to the remaining samples, and a second set removed (total dose of 5 Gy received). A third irradiation of 5 Gy dose was given to the remaining samples, and a third set removed (total dose of 10 Gy received). The process was continued until all samples had been irradiated with the correct total dose, and is summarized in **Table 2-2**.

Table 2-2. Showing the accumulative dose method used to irradiate samples, so that all receive 2, 5, 10, 15 and 20 Gy dose, for this work three independent samples were used per nominal dose received.

Pellet #	Dose given (Gy)	Accumulative dose received (Gy)
1	2	2
2	3	5
3	5	10
4	5	15
5	5	20

Prior to irradiation, all wax pellets were placed within a silica holder of the same dimensions such that there were no air gaps between the pellets (**Figure 2-10**). 'Dummy' wax pellets were fabricated which were colourful and designed to be easily distinguished from the 'real' wax pellet samples. The dummy pellets were used to fill any gaps within the moulds, and maintain full scatter conditions when irradiating. After receiving the required dose, wax pellet samples were removed and replaced with 'dummy' wax pellets, again to prevent any air gaps being present during irradiation.

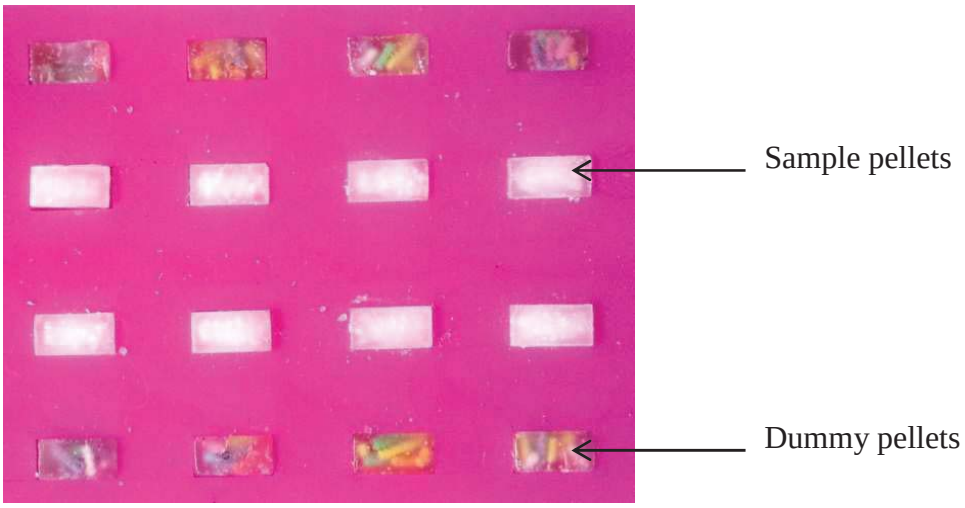

Figure 2-10. Showing the wax pellet samples positioned in the moulds prior to irradiation, with the colourful dummy pellets.

The wax composites were placed on top of the back-scatter medium and irradiated using different types of radiations. Conditions for each irradiation setup are shown in **Table 2-3** and **Figure 2-11**. For all irradiations (X-rays and charged particles) the alanine-wax pellets were then scanned by EPR and the peak intensity was plotted against their depth in the phantom.

Table 2-3. Irradiation conditions used for the different types of radiations measured.

Radiation	Unit	Energy	Back Scatter Medium	Build-Up Cap	SSD	Field Size
kV X-rays	PENTAK HF150T Therapx series 3 Unit	80 kV	2 cm solid-water and 10 cm acrylic	Not used	25cm	10cm circular cone Half-value layer (HVL) HVL of 2.2 mm Al
MV X-rays	Varian 21iX LINAC	6 MV	15 cm solid-water	5cm	95cm	10 x 10cm^2
Electrons	Varian 21iX LINAC	6 MeV	15 cm solid-water	13mm	95cm	10 x 10cm^2
Protons	Hyogo Ion Beam Centre	150 MeV SOBP 5cm	15 cm solid-water	Not used	95 cm	20 x 20cm^2

a. kV X-rays

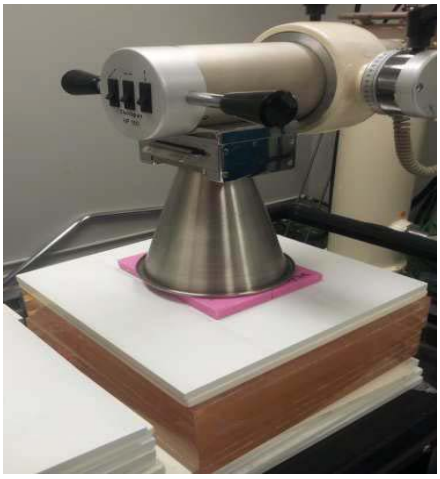

b. MV X-rays

c. Electrons

d. Protons

Figure 2-11 a-d. The set-up and irradiation of the AuNP/alanine-wax pellets for all beam types used; (a) kV X-rays, (b) MV X-rays, (c) electrons and (d) protons.

2.2.6 Spread out proton beam (SOPB) depth-dose-curve using alanine

Alanine-wax pellets were prepared as for the L-Alanine-wax pellets (**Section 2.2.4**), so that each pellet measured 10 x 5 x 5 mm and contained 30 mg of alanine uniformly embedded within paraffin wax. In a solid-water block, a pre-cut channel (depth 5 mm and width 5 mm) was filled with the alanine-wax pellets so that there was no gaps in-between each pellet. The solid-water block and pellets were positioned

vertically with supports on either side (**Figure 2-12**) and irradiated with a 150 MeV proton beam to a nominal dose of 8 Gy.

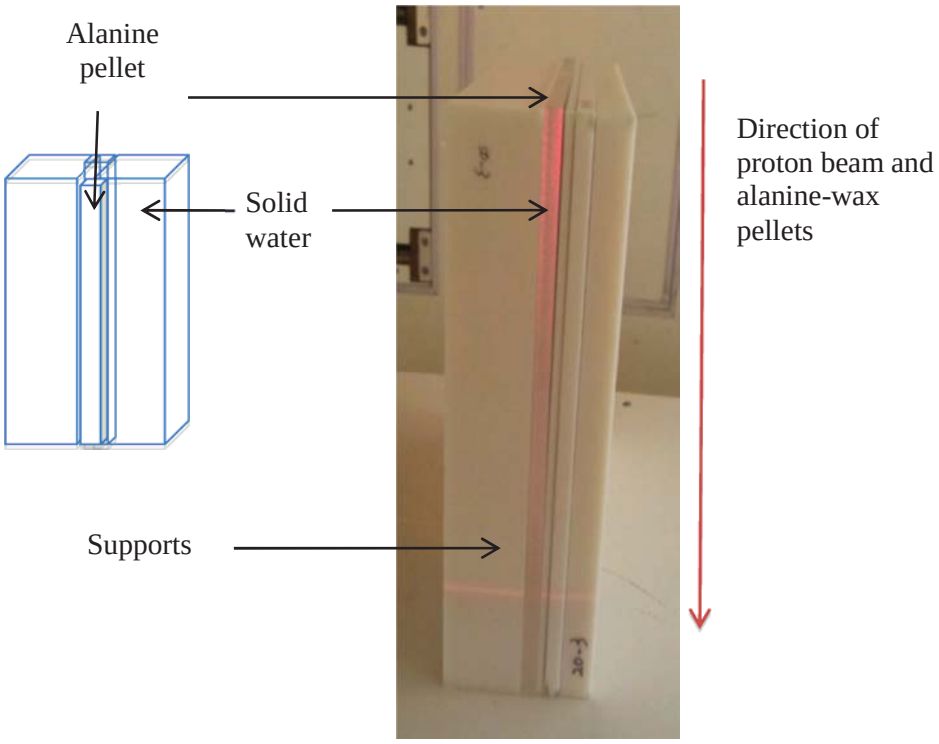

Figure 2-12. The solid-water slab with channel containing alanine pellets was placed between supports (for full scatter conditions) and irradiated with protons (direction of beam and pellet orientation is shown).

The relation of dose and monitor count (Gy/count) was determined by an ionization chamber (Semiflex chamber Type-31013 volume 0.03 cm^2) at the centre of Spread-Out Bragg Peak (SOBP) in a water phantom under the same conditions as the irradiated samples. The required physical dose (Gy) is delivered by the multiple beam pulse method.

2.2.7 EPR spectroscopy conditions and uncertainties

The EPR spectra of all the irradiated samples were recorded on a BRUKER Elexsys 9.5 GHz. After irradiation all samples were stored in controlled conditions as stated previously for a minimum of 24 hours before EPR analysis, unless stated here.

All wax pellet samples were placed vertically in a quartz tube (internal diameter = 7 mm), and positioned in the centre of the cylindrical cavity. An o-ring was fitted to the outside of the tube to ensure the pellet was consistently positioned in the centre of the cylindrical cavity (**Figure 2-13**). The spectrometer settings for all measurements were: number of scans, 5; centre field, 3400 G; microwave power, 0.5024 mW; sweep time, 10.50 s; sweep width 150 G; modulation amplitude, 4.0 G; time constant, 10.24 ms; modulation frequency, 100 kHz; receiver gain, 75 dB.

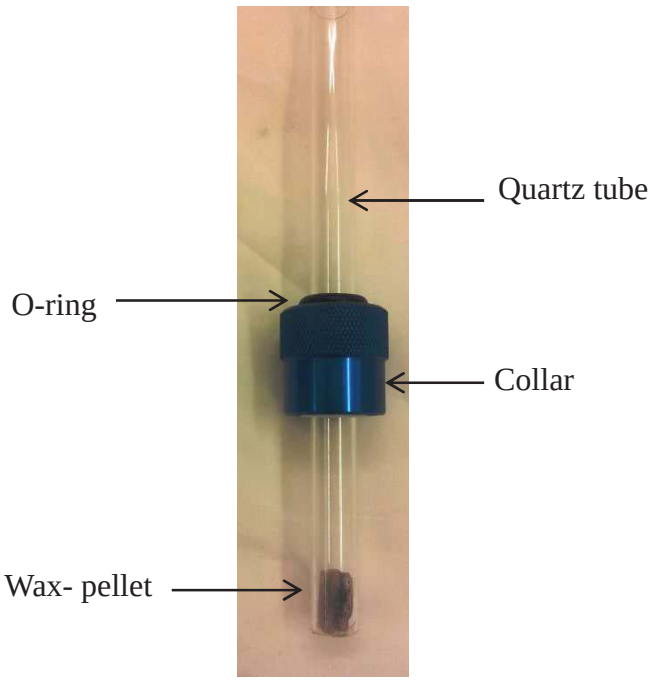

Figure 2-13. The wax pellet sample within the quartz tube and O-ring used to maintain the position within the EPR cavity.

The response of the pellets to the nominal doses delivered by X-ray sources, electron and the proton beams is quantified by the concentration of the R1 alanine radical generated (**Figure 1-15**). The uncertainty in the determination of the EPR signal amplitude depends on the signal intensity, and is estimated to be between 1.5 % and 4 % for alanine dosimetry [53], this being consistent with repeated measurements from the same sample. The errors associated with the data presented in this chapter represent the average of at least three independent samples.

2.2.8 Irradiation standards and uncertainty

The kV unit is calibrated with ionisation chambers calibrated at Australian Radiation Protection and Nuclear Safety Agency **(**ARPANSA), using the IPEMB protocol. The MV X-rays and MeV electron irradiations were performed on clinically used medical LINACs, calibrated to 1cGy/monitor unit (MU) in accordance with international protocols TRS398. The dose/ MU was calibrated with an ionisation chamber that has been calibrated at (ARPANSA), which is a secondary standards laboratory. The uncertainty for kV X-rays is less than 3 % and less than 2 % for MV X-rays and MeV electron doses*.

For proton beams; prior to irradiation of the samples, the ionization chamber setting with a water equivalent phantom was irradiated to determine the prescribed dose and dose rate at the monoenergetic Bragg peak and also at the centre of the spread-out Bragg peak (SOBP). Both the monoenergetic and 3 cm spread-out depth dose in water were then measured by the ionization chamber for reference. The uncertainty of the given dose is 2 %. The proton range is 14 cm, with a LET of 1.07 keV/micron.

** From private communications with Dr Trevor Ackerly, chief physicist at the William Buckland Radiotherapy Centre, Alfred Hospital, Australia.*

2.3 Results

The results for varying AuNPs concentrations (1, 2 and 3 % w/w) and sizes (1.9, 5 and 15 nm) are presented below and are divided into four sections based on the irradiation type used; kV X-rays (**Section 2.3.1**), MV X-rays (**Section 2.3.2**), electrons (**Section 2.3.3**) and protons (**Section 2.3.4**). The DE values are also presented, and a final comparison between the AuNP size effects in **Section 2.3.5**. Levels of DE were determined as the difference in signal amplitude to that of the control (containing no AuNPs) at the same nominal dose, for instance, a 55 % variation between the amplitude of the alanine control signal to that of the AuNP/alanine composite at a given dose, indicates a 55 % DE caused by the generation of secondary electrons.

Two separate irradiations were completed for X-rays (kV and MV) and electrons examining AuNP/alanine composites containing 1, 2 and 3 % AuNPs (w/w) of 1.9, 5 and 15 nm sizes, as this size range is not well represented in the literature (**Section 2.1.2**). Whilst only one set of measurements were completed for proton irradiations as this work was carried out in Japan with limited funding and beam time available.

2.3.1 X-rays: kV ranges

The DE for AuNPs of all sizes and concentrations irradiated with kV X-rays is clearly evident in the results below. Comparisons between the control alanine EPR

signal and the AuNP/alanine composites shows a large response, with the smallest AuNP size used (1.9 nm) yielding the largest DE levels.

2.3.1.1 1.9 nm AuNPs

The EPR response of the 1.9 nm AuNP/alanine composites (3 to 1 % v/w) and control L-alanine are shown in **Figure 2-14 a & b**. All irradiated samples gave linear responses with regression values ranging between 0.995 to 0.997 (**Figure 2-14 a**) and 0.995 to 0.999 (**Figure 2-14 b**).

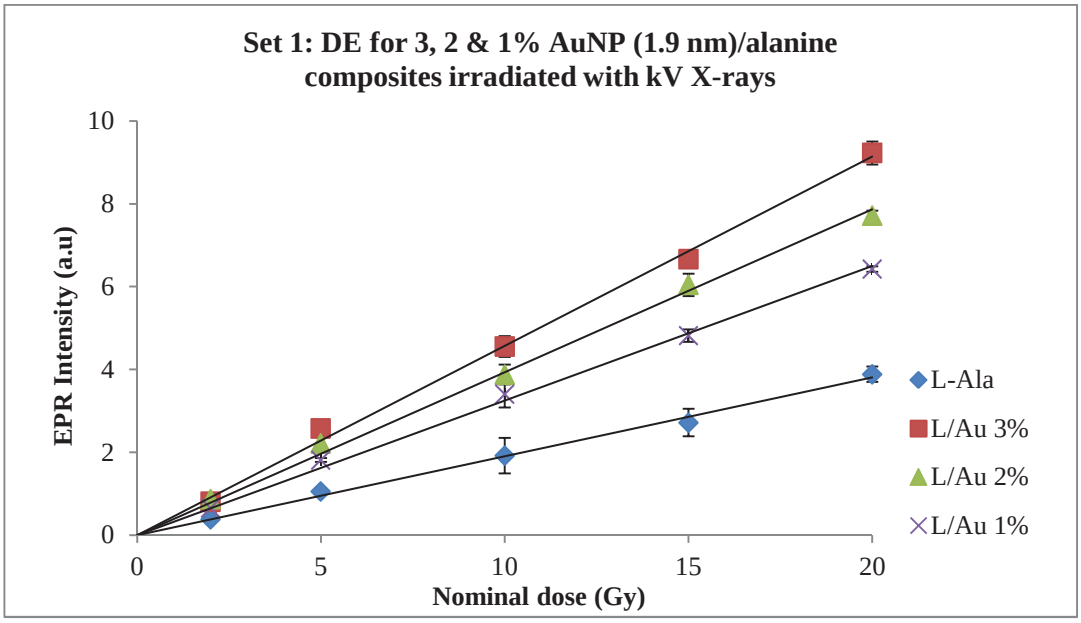

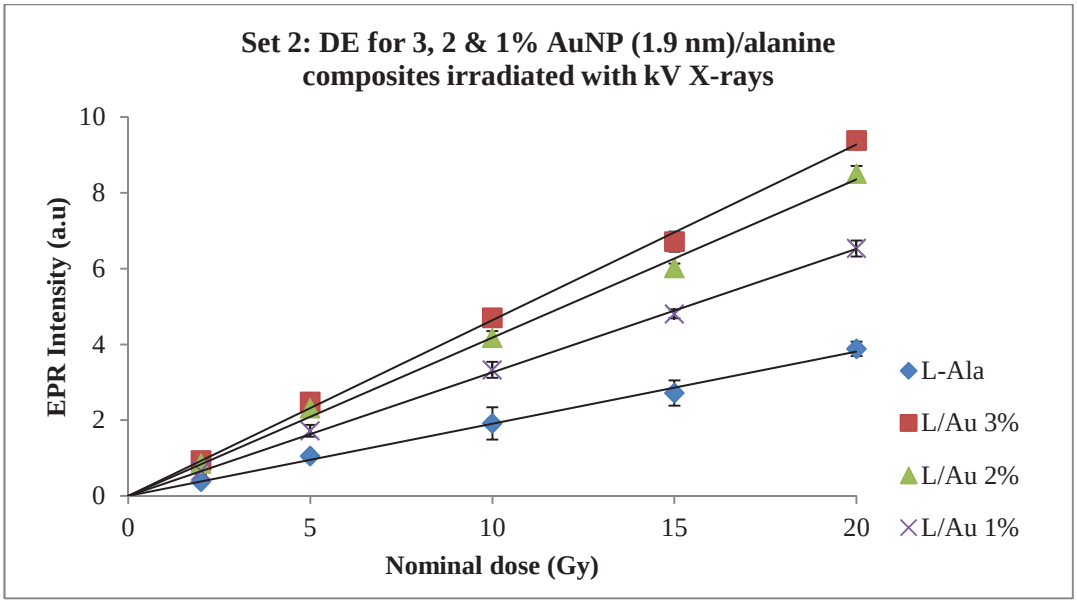

Figure 2-14 a & b. The EPR signal amplitude obtained from alanine and alanine/ AuNP (1.9 nm) composites; 3 to 1 % w/w after exposure to various doses of 80 kV X-rays, sample set 1 (a) and 2 (b).

The level of DE presented in **Table 2- 4 a & b** shows a range of 113 to 147 % for 3% AuNP composites over the doses investigated, 99 to 129 % for the 2 % composites and 63 to 77 % for the 1 % composites.

Table 2-4 a & b. The levels of DE (%) determined for the first (a) and second (b) set of AuNP (1.9 nm)/alanine pellets (3 to 1 %) irradiated with kV X-rays.

Dose (Gy)	Alanine	3% Au	DE %	2% Au	DE %	1% Au	DE %
2	0.38	0.81	113	0.87	129	0.65	71
5	1.05	2.57	145	2.21	110	1.81	72
10	1.92	4.55	138	3.87	102	3.40	77
15	2.72	6.66	145	6.04	122	4.82	77
20	3.88	9.23	138	7.71	99	6.42	65

Dose (Gy)	Alanine	3% Au	DE %	2% Au	DE %	1% Au	DE %
2	0.38	0.94	147	0.85	125	0.66	75
5	1.05	2.48	136	2.31	120	1.72	63
10	1.92	4.70	145	4.17	117	3.33	74
15	2.72	6.71	147	6.01	121	4.80	77
20	3.88	9.38	142	8.50	119	6.53	68

2.3.1.2 5 nm AuNPs

The EPR response of the 5 nm AuNP/alanine composites (3 to 1 % v/w) and control L-alanine are shown in **Figure 2-15 a & b**. Both sets of 3 to 1 % AuNP/alanine composites irradiated with kV X-rays gave linear responses with high regression values ranging between 0.981 to 0.990 (**Figure 2-15 a**) and 0.992 to 0.997 (**Figure 2-15 b**).

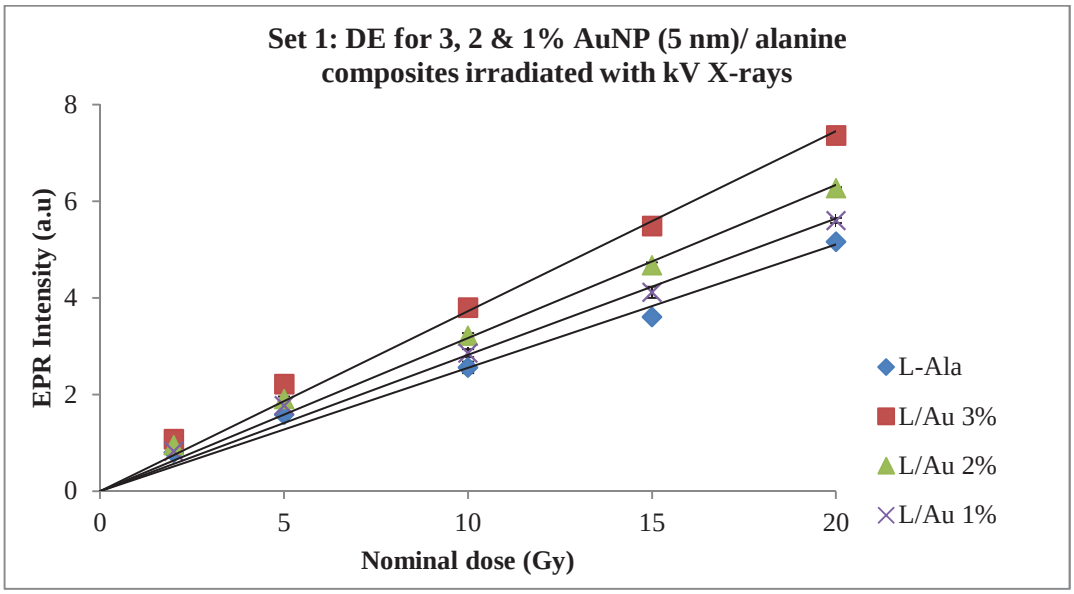

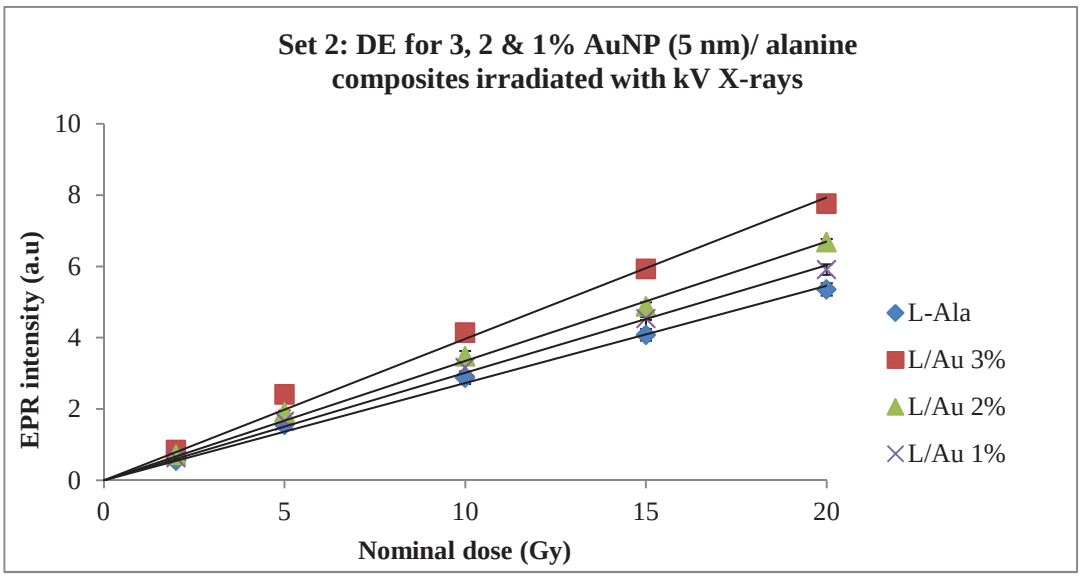

Figure 2-15 a & b. The EPR signal amplitude obtained from alanine and alanine/ AuNP (5 nm) composites; 3-1 % w/w after exposure to various doses of 80 kV X-rays, sample set 1 (a) and 2 (b).

DE levels obtained (**Table 2-5 a & b**) show a 35 to 55 % enhancement for 3% AuNP composites over the dose range investigated, which decreased to 19 to 29 % for the 2 % composites and to 4 to 15 % for the 1 % composites.

Table 2-5 a & b. The levels of DE (%) determined for the first (a) and second (b) set of AuNP (5 nm)/alanine pellets (3 to 1 %) irradiated with kV X-rays.

Dose (Gy)	Alanine	3% Au	DE %	2% Au	DE %	1% Au	DE %
2	0.79	1.073	35	0.95	19	0.82	4
5	1.58	2.212	40	1.91	20	1.77	12
10	2.56	3.798	48	3.21	25	2.86	12
15	3.61	5.486	52	4.67	29	4.11	14
20	5.16	7.363	43	6.27	21	5.60	9

Dose (Gy)	Alanine	3% Au	DE %	2% Au	DE %	1% Au	DE %
2	0.55	0.85	53	0.71	29	0.64	15
5	1.56	2.41	55	1.90	22	1.66	7
10	2.88	4.14	44	3.48	21	3.16	10
15	4.08	5.93	45	4.88	20	4.54	11
20	5.35	7.76	45	6.68	25	5.91	10

2.3.1.3 15 nm AuNPs

The EPR response of the 15 nm AuNP/alanine composites (3 to 1 % v/w) and control L-alanine are shown in **Figure 2-16 a & b**. Both sets of 3 to 1 % AuNP/alanine composites irradiated produced linear responses and regression values ranging between 0.990 to 0.994 (**Figure 2-16 a**) and 0.993 to 0.996 (**Figure 2-16 b**).

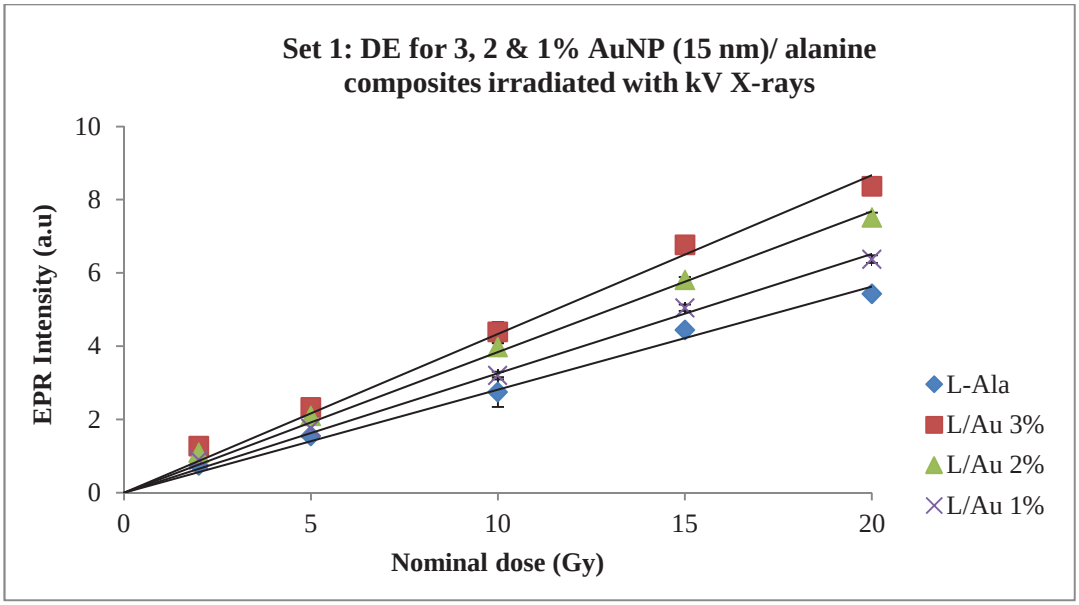

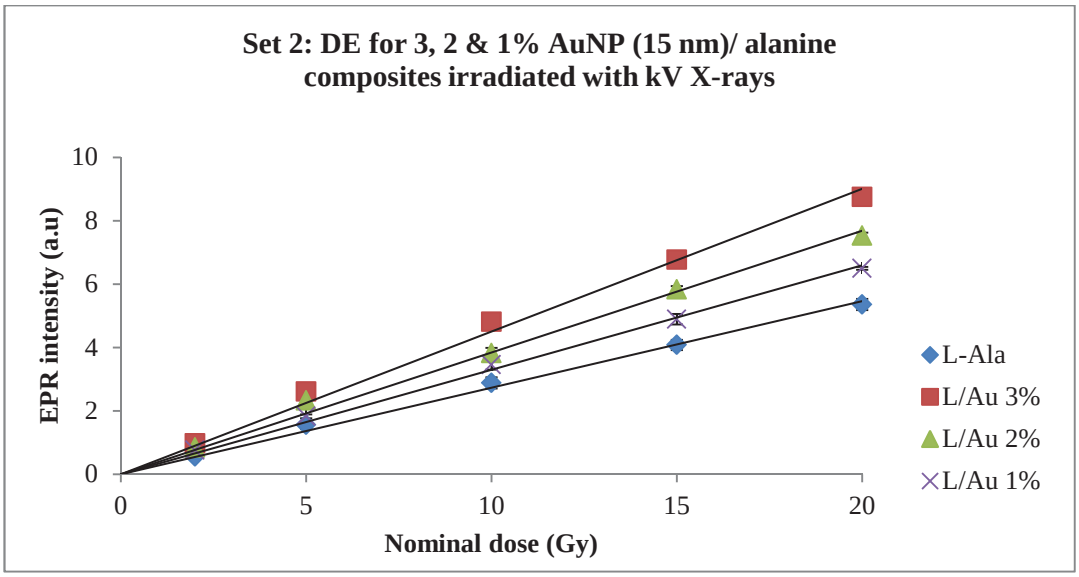

Figure 2-16 a & b. The EPR signal amplitude obtained from alanine and alanine/ AuNP (15 nm) composites; 3 to 1 % w/w after exposure to various doses of 80 kV X-rays, sample set 1 (a) and 2 (b).

Table 2-6 a & b show a DE of 50 to 75 % for 3 % AuNP composites, which decreased to 31 to 52 % for the 2 % composites and 14 to 37 % for the 1 % composites.

Table 2-6 a & b. The levels of DE (%) determined for the first (a) and second (b) set of AuNP (15 nm)/alanine pellets (3 to 1 %) irradiated with kV X-rays.

Dose (Gy)	Alanine	3% Au	DE %	2% Au	DE %	1% Au	DE %
2	0.74	1.27	71	1.09	47	0.89	20
5	1.55	2.32	50	2.09	35	1.76	14
10	2.75	4.39	60	3.97	44	3.20	16
15	4.45	6.77	52	5.81	31	5.05	14
20	5.43	8.37	54	7.51	38	6.38	17

Dose (Gy)	Alanine	3% Au	DE %	2% Au	DE %	1% Au	DE %
2	0.55	0.971	75	0.84	52	0.76	37
5	1.56	2.610	68	2.33	50	1.83	18
10	2.88	4.808	67	3.82	33	3.45	20
15	4.08	6.772	66	5.83	43	4.89	20
20	5.35	8.751	63	7.53	41	6.50	21

2.3.2 X-rays: MV ranges

Overall irradiations with 6 MV X-rays for all the AuNP sizes and concentrations investigated gave lower DE levels compared with the kV X-ray irradiations. Whilst the effects of increasing concentration are evident and yielded higher DE levels (**Section 2.3.1**), as for the kV X-ray irradiations, this was not so clear for AuNP size. However, the smaller sized 1.9 nm AuNPs did give slightly higher DE values, followed by the 15 nm AuNPs, and the 5 nm AuNPs.

2.3.2.1 1.9 nm AuNPs

Figure 2-17 a & b show a linear response for all concentrations investigated with regression values ranging between 0.940 to 0.979 (**Figure 2-17 a**) and 0.976 to 0.983 (**Figure 2-17 b**).

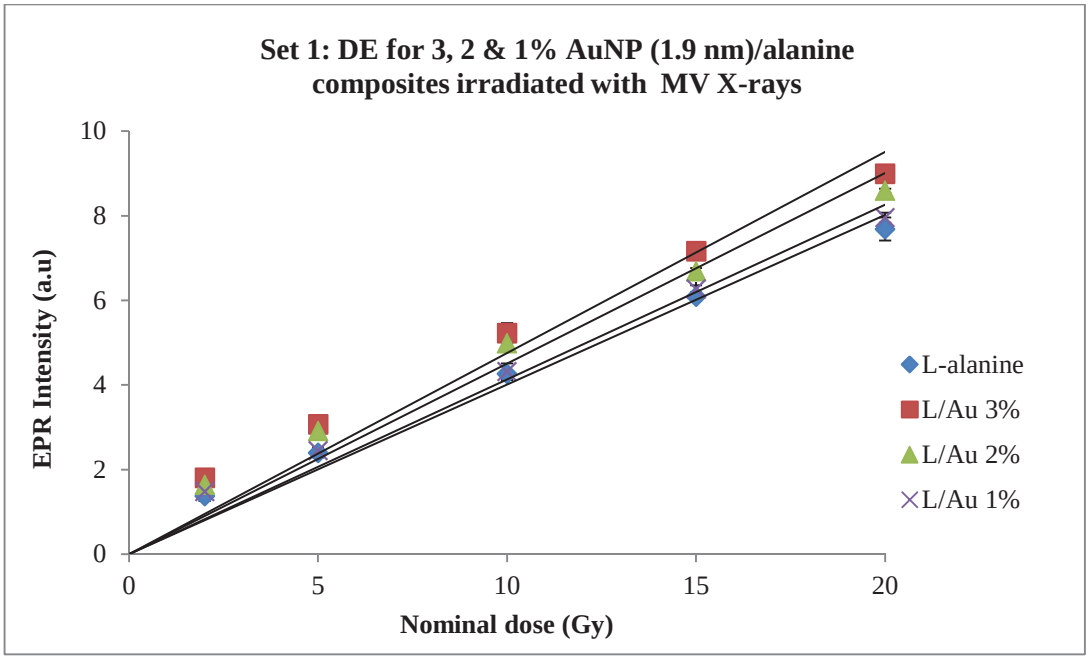

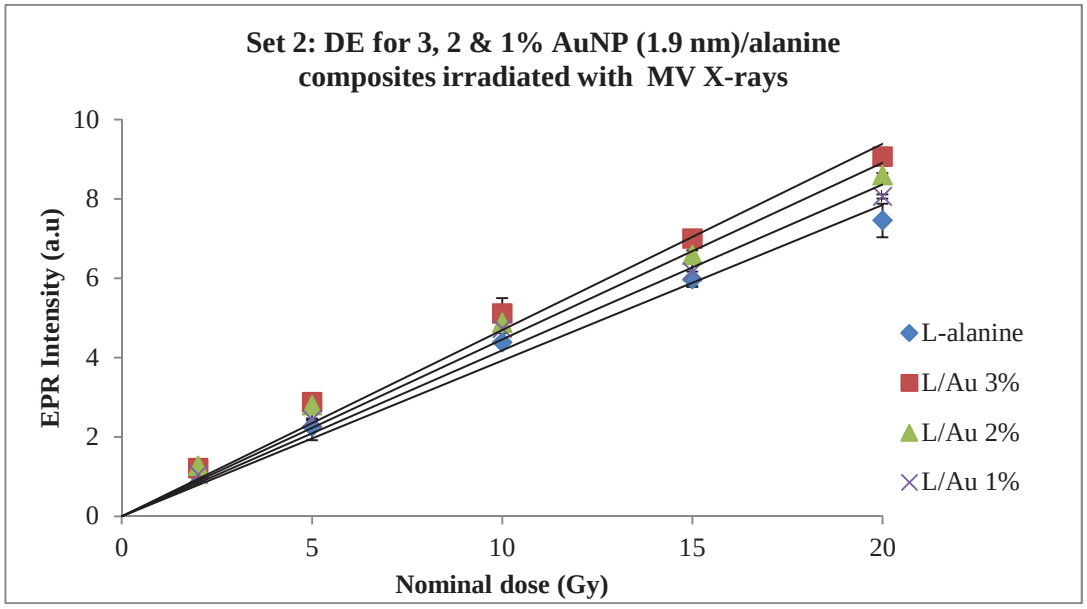

Figure 2-17 a & b. The EPR signal amplitude obtained from alanine and alanine/ AuNP (1.9 nm) composites; 3 to 1 % w/w after exposure to various doses of 6 MV X-rays, sample set 1 (a) and 2 (b).

DE values ranged from 16 to 31 % for 3 % AuNP composites across all doses investigated (**Table 2-7 a & b**), and 10 to 24 % DE for 2 % AuNP composites, which decreased to 1 to 8 % for the 1 % composites.

Table 2-7 a & b. The levels of DE (%) determined for the first (a) and second (b) set of AuNP (1.9 nm)/alanine pellets (3 to 1 %) irradiated with 6 MV X-rays.

Dose (Gy)	Alanine	3% Au	DE %	2% Au	DE %	1% Au	DE %
2	1.37	1.956	31	1.64	19	1.48	7
5	2.39	3.070	28	2.91	22	2.32	2
10	4.26	5.228	23	4.98	17	4.31	1
15	6.09	7.161	18	6.68	10	6.27	3
20	7.69	8.993	17	8.59	12	7.96	3

Dose (Gy)	Alanine	3% Au	DE %	2% Au	DE %	1% Au	DE %
2	1.03	1.22	19	1.34	24	1.21	3
5	2.25	2.88	28	2.79	24	2.44	8
10	4.39	5.11	16	4.88	11	4.73	8
15	5.97	7.00	17	6.59	10	6.16	3
20	7.45	9.06	22	8.59	15	8.06	8

2.3.2.2 5 nm AuNPs

All AuNP concentration (1 to 3 %) gave a linear response (**Figure 2-18 a & b**) with regression values ranging between 0.992 to 0.996 (**Figure 2-18 a**) and 0.977 to 0.981 (**Figure 2-18 b**).

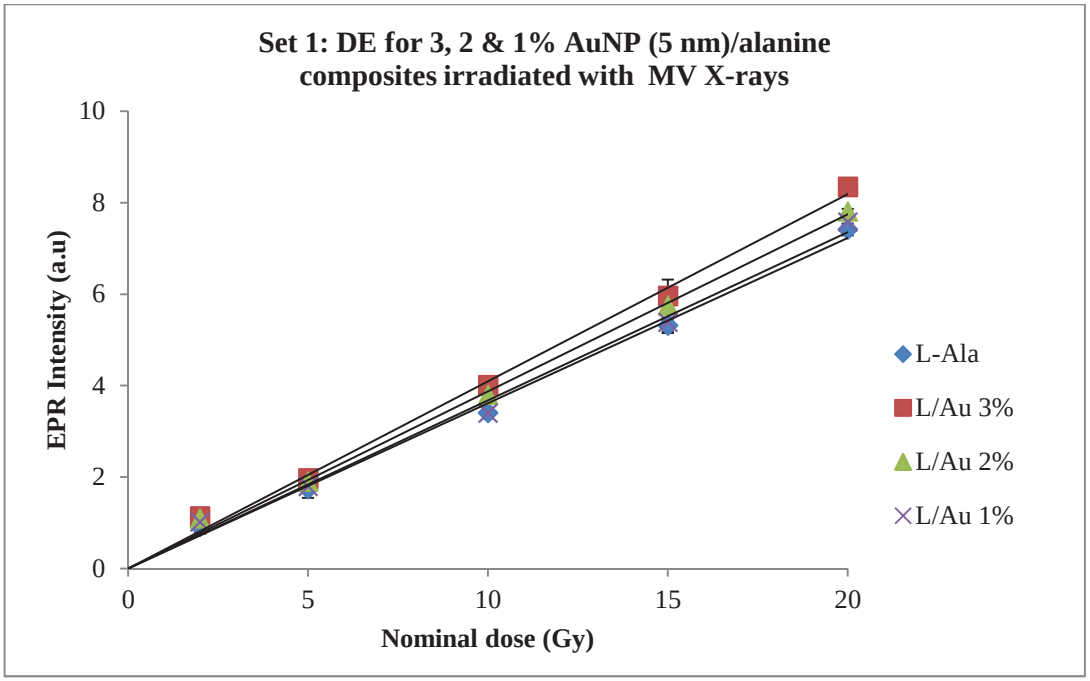

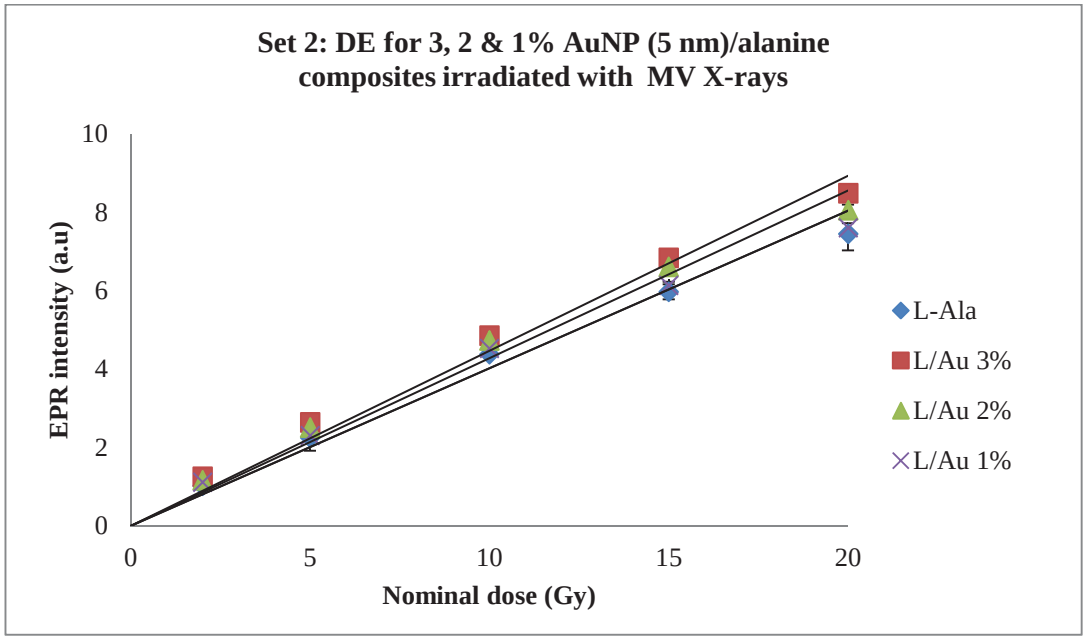

Figure 2-18 a & b. The EPR signal amplitude obtained from alanine and alanine/ AuNP (5 nm) composites; 3 to 1 % w/w after exposure to various doses of 6 MV X-rays, sample set 1 (a) and 2 (b).

Over the doses investigated the 3 % AuNP composites gave a DE range of 11 to 24 % (**Table 2-8 a & b**), 5 to 17 % DE for the 2 % AuNP composites, and 0 to 11 % for the 1 % composites.

Table 2-8 a & b. The levels of DE (%) determined for the first (a) and second (b) set of AuNP (5 nm)/alanine pellets (3 to 1 %) irradiated with 6 MV X-rays.

Dose (Gy)	Alanine	3% Au	DE %	2% Au	DE %	1% Au	DE %
2	0.92	1.14	24	1.10	19	1.02	11
5	1.74	1.97	14	1.90	10	1.80	3
10	3.40	4.01	18	3.79	12	3.40	0
15	5.32	5.96	12	5.75	8	5.38	1
20	7.41	8.35	13	7.81	5	7.58	2

Dose (Gy)	Alanine	3% Au	DE %	2% Au	DE %	1% Au	DE %
2	1.03	1.26	22	1.32	14	1.32	9
5	2.25	2.64	17	2.51	12	2.31	3
10	4.39	4.86	11	4.74	8	4.53	3
15	5.97	6.84	14	6.62	11	6.14	3
20	7.45	8.50	14	8.06	8	7.61	2

2.3.2.3 15 nm AuNPs

Figure 2-19 a & b shows a linear response for all concentrations investigated with regression values ranging between 0.988 to 0.994 (**Figure 2-19 a**) and 0.988 to 0.993 (**Figure 2-19 b**).

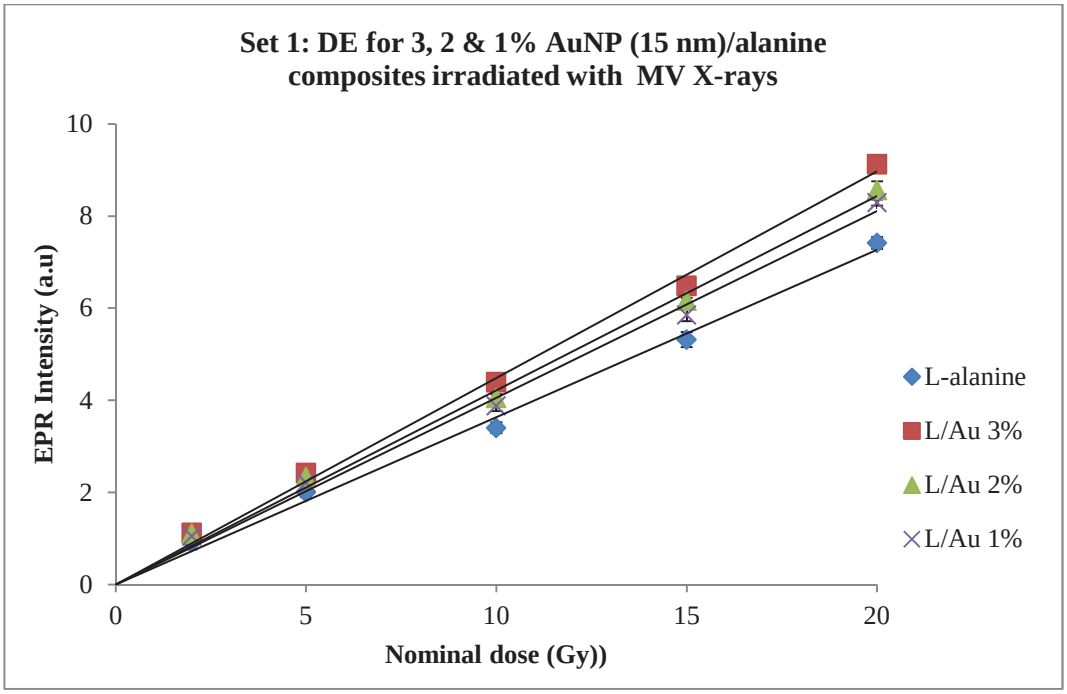

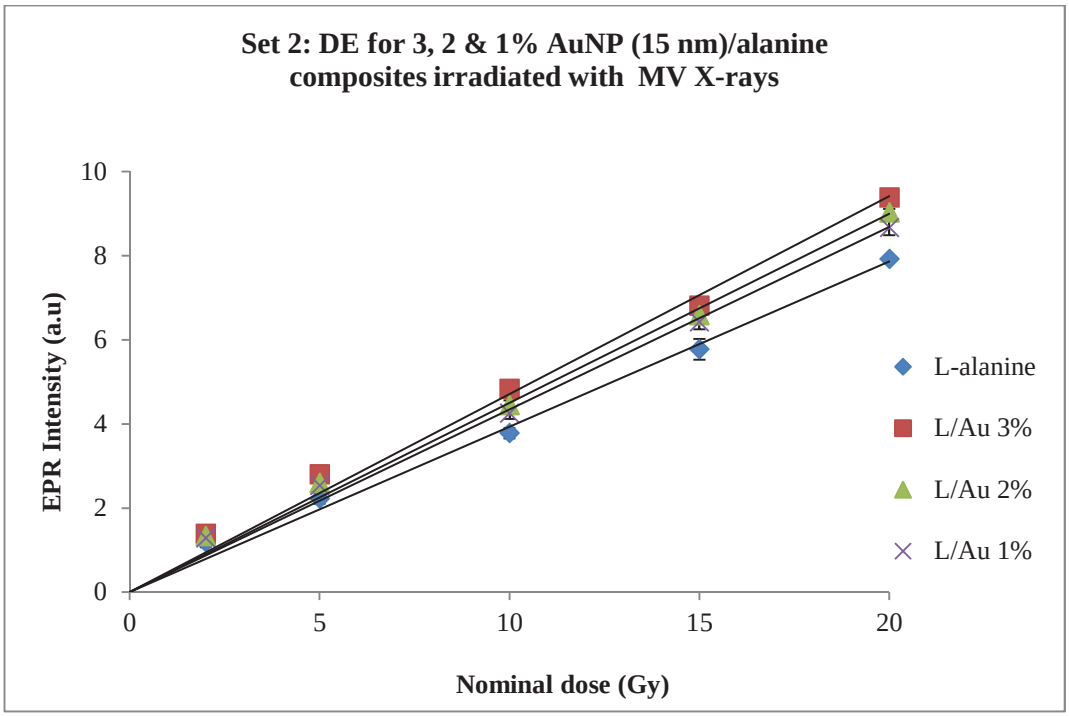

Figure 2-19 a & b. The EPR signal amplitude obtained from alanine and alanine/ AuNP (15 nm) composites; 3 to 1 % w/w after exposure to various doses of 6 MV X-rays, sample set 1 (a) and 2 (b).

DE levels ranged from 17 to 29 % for the 3 % AuNP composites across all doses investigated (**Table 2-9 a & b**), and 14 to 20 % DE for the 2 % AuNP composites, which decreased to 9 to 14 % for the 1 % composites.

Table 2-9 a & b. The levels of DE (%) determined for the first (a) and second (b) set of AuNP (15nm)/alanine pellets (3 to 1 %) irradiated with 6 MV X-rays.

Dose (Gy)	Alanine	3% Au	DE %	2% Au	DE %	1% Au	DE %
2	0.92	1.217	22	1.20	20	1.28	14
5	2.00	2.423	21	2.33	16	2.22	11
10	3.40	4.393	29	4.04	19	3.88	14
15	5.32	6.483	22	6.16	16	5.86	10
20	7.41	9.127	23	8.57	16	8.29	12

Dose (Gy)	Alanine	3% Au	DE %	2% Au	DE %	1% Au	DE %
2	1.18	1.38	17	1.26	12	1.22	9
5	2.22	2.80	26	2.59	17	2.54	14
10	3.78	4.83	28	4.44	18	4.26	13
15	5.78	6.81	18	6.58	14	6.42	11
20	7.92	9.38	18	9.02	14	8.67	9

2.3.3 Electrons

DE was low for all AuNP sizes and concentrations examined (≤ 9 %) when irradiated with a 6 MeV electron beam.

2.3.3.1 1.9 nm AuNPs

Figure 2-20 a & b shows a linear response for all concentrations investigated with regression values ranging between 0.987 to 0.989 (**Figure 2-20a**) and 0.993 to 0.995 (**Figure 2-20 b**).

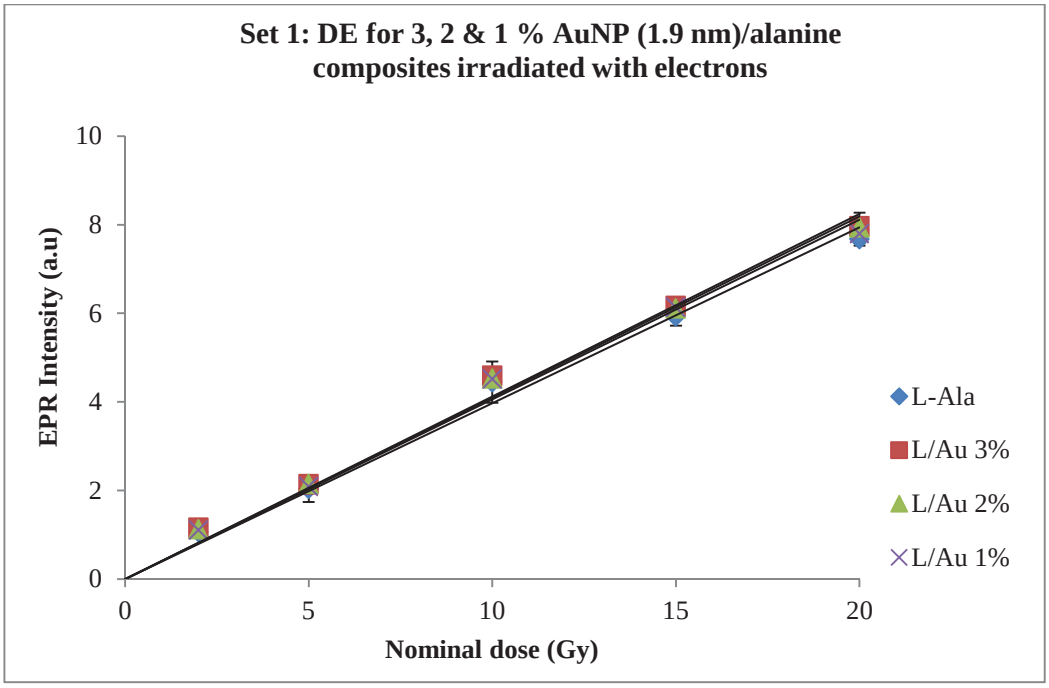

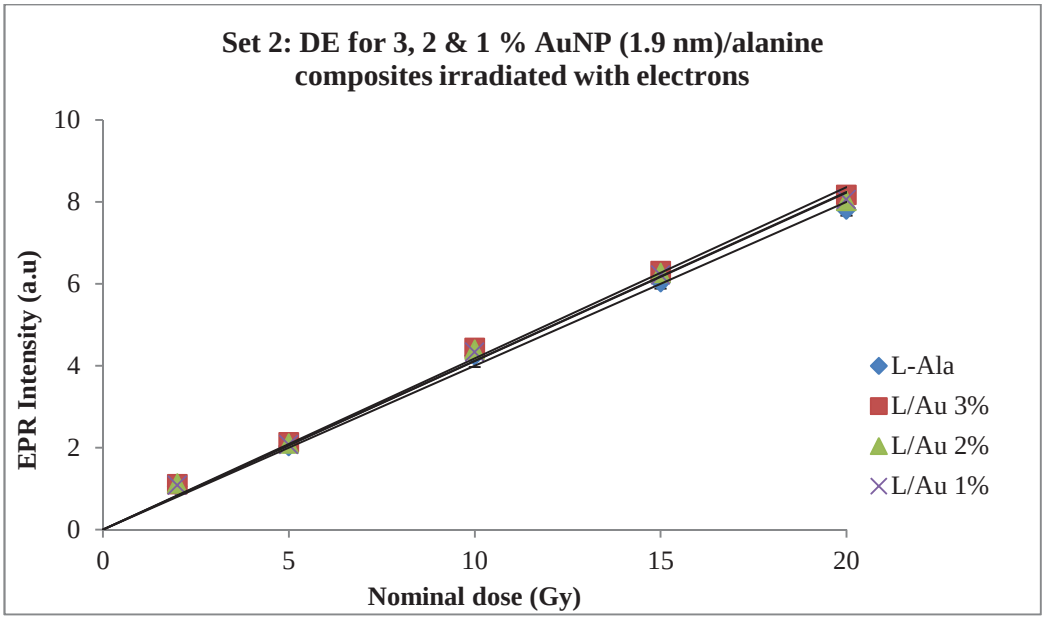

Figure 2-20 a & b. The EPR signal amplitude obtained from alanine and alanine/ AuNP (1.9 nm) composites; 3 to 1 % w/w exposed to various doses of 6 MeV electrons, sample set 1 (a) and 2 (b).

The DE values observed over the doses investigated ranged from 3 to 9 % for 3 % AuNP composites, 2 to 6 % DE for the 2 % AuNP composites, and 2 to 4 % for the 1 % composites (**Table 2-10 a & b**).

Table 2-10 a & b. The levels of DE (%) determined for the first (a) and second (b) set of AuNP (1.9 nm)/alanine pellets (3 to 1 %) irradiated with 6 MeV electrons.

Dose (Gy)	Alanine	3% Au	DE %	2% Au	DE %	1% Au	DE %
2	1.07	1.160	9	1.12	5	1.11	4
5	2.04	2.137	5	2.15	5	2.09	2
10	4.44	4.589	3	4.53	2	4.52	2
15	5.93	6.168	4	6.11	3	6.04	2
20	7.68	7.962	4	7.94	3	7.80	2

Dose (Gy)	Alanine	3% Au	DE %	2% Au	DE %	1% Au	DE %
2	1.05	1.11	5	1.12	6	1.09	3
5	2.04	2.13	4	2.10	3	2.08	2
10	4.24	4.44	5	4.39	3	4.33	2
15	6.04	6.31	4	6.26	4	6.22	3
20	7.81	8.17	5	8.02	3	8.06	3

2.3.3.2 5 nm AuNPs

There was minimal variation in the dose (≤ 8 %) as measured by the control alanine and the AuNP/alanine samples when irradiated with a 6 MeV electron beam for both sets of experiments **Figure 2-21 a & b**. Regression values ranged between 0.986 to 0.991 (**Figure 2-21 a**) and 0.992 to 0.993 (**Figure 2-21 b**).

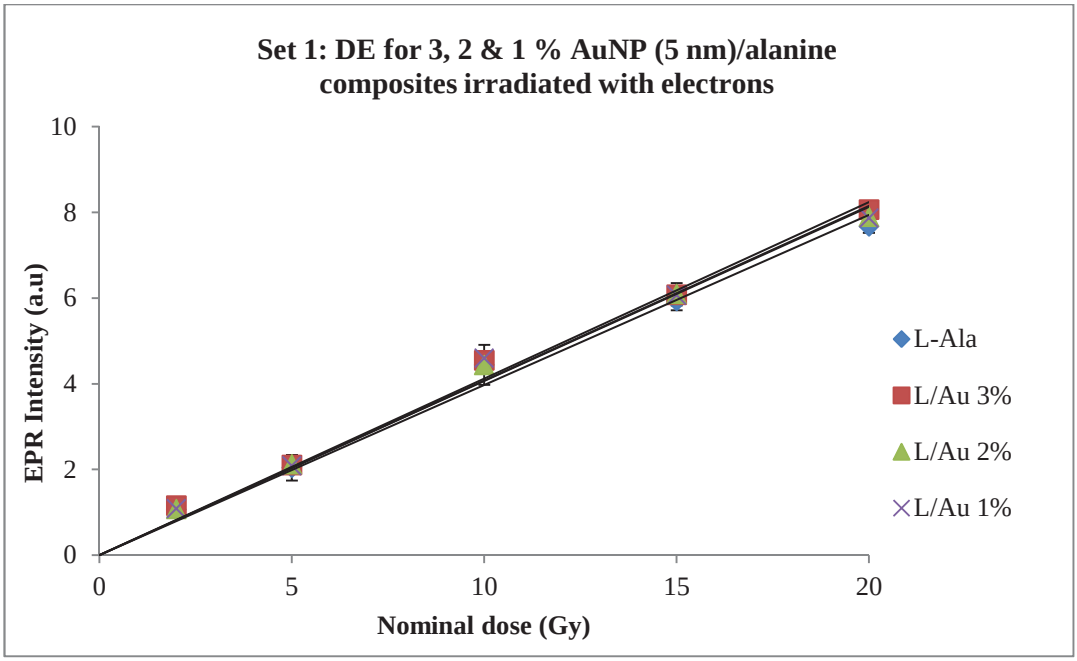

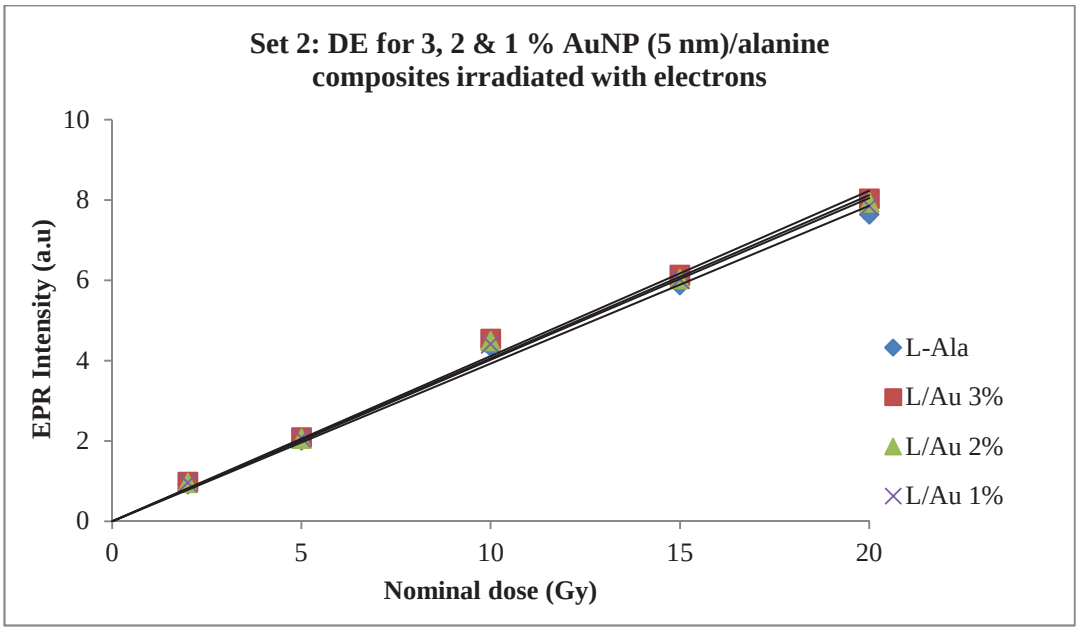

Figure 2-21 a & b. The EPR signal amplitude obtained from alanine and alanine/ AuNP (5 nm) composites; 3 to 1 % w/w exposed to various doses of 6 MeV electrons, sample set 1 (a) and 2 (b).

Table 2-11 a & b shows the DE values, which ranged from 2 to 8 % for 3 % AuNP composites, 0 to 4 % and 1 to 4 % DE for 2 % and 1 % composites respectively.

Tables 2-11 a & b. The levels of DE (%) determined for the first (a) and second (b) set of AuNP (5nm)/alanine pellets (3 to 1 %) irradiated with electrons.

Dose (Gy)	Alanine	3% Au	DE %	2% Au	DE %	1% Au	DE %
2	1.07	1.15	8	1.08	1	1.09	2
5	2.04	2.10	3	2.12	4	2.09	2
10	4.44	4.55	2	4.44	0	4.60	3
15	5.93	6.08	3	6.09	3	6.07	2
20	7.68	8.06	5	7.89	3	7.87	3

Dose (Gy)	Alanine	3% Au	DE %	2% Au	DE %	1% Au	DE %
2	0.92	0.98	7	0.95	3	0.96	4
5	2.01	2.08	4	2.05	2	2.07	3
10	4.35	4.54	4	4.48	3	4.41	1
15	5.88	6.13	4	6.03	3	6.02	2
20	7.64	8.03	5	7.93	4	7.85	3

2.3.3.3 15 nm AuNPs

Figure 2-2a & b shows a linear response for all concentrations investigated with regression values ranging between 0.987 to 0.991 (**Figure 2-22a**) and 0.982 to 0.985 (**Figure 2-22 b**).

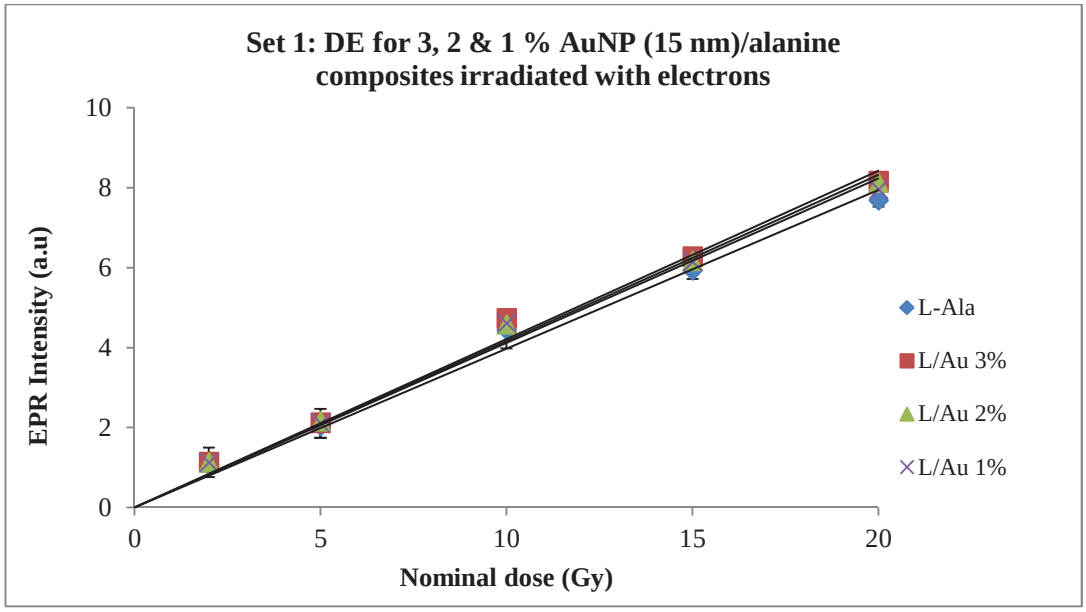

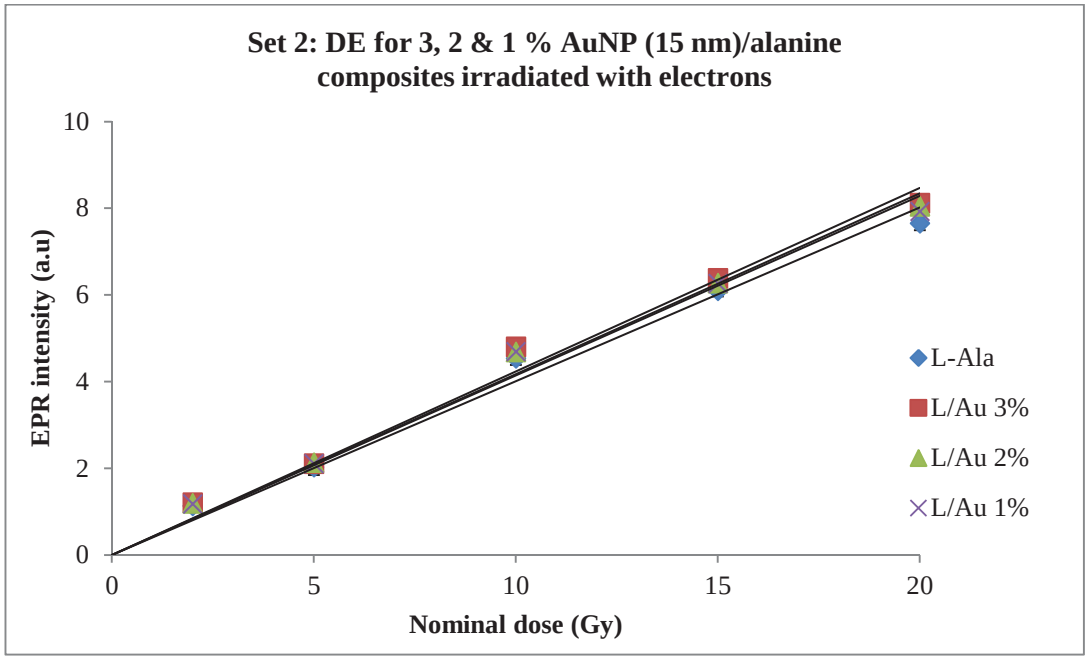

Figure 2-22 a & b. The EPR signal amplitude obtained from alanine and alanine/ AuNP (15 nm) composites; 3 to 1 % w/w exposed to various doses of 6 MeV electrons, sample set 1 (a) and 2 (b).

DE values ranged from 4 to 7 % for 3 % AuNP composites across all doses investigated (**Table 2-12a & b**), and 3 to 6 % DE for both the 2 % and 1 % AuNP composites.

Table 2-12 a & b. The levels of DE (%) determined for the first (a) and second (b) set of AuNP (15 nm)/alanine pellets (3 to 1 %) irradiated with 6 MeV electrons.

Dose (Gy)	Alanine	3% Au	DE %	2% Au	DE %	1% Au	DE %
2	1.07	1.13	6	1.12	5	1.13	6
5	2.04	2.12	4	2.15	5	2.11	3
10	4.44	4.73	6	4.58	3	4.61	4
15	5.93	6.28	6	6.16	4	6.14	4
20	7.68	8.16	6	8.12	6	7.96	4

Dose (Gy)	Alanine	3% Au	DE %	2% Au	DE %	1% Au	DE %
2	1.13	1.21	7	1.19	5	1.18	4
5	2.02	2.11	4	2.13	5	2.10	4
10	4.54	4.80	6	4.68	3	4.69	3
15	6.09	6.39	5	6.27	3	6.26	3
20	7.65	8.12	6	8.04	5	7.93	4

2.3.4 Protons

Lastly, the response of the alanine/AuNP composites was examined for proton beam irradiations, as this was a large focus of this work, given the discrepancies in past studies using computer simulations and animal/cell models (**Section 2.1.3**).

The suitability of the alanine-wax dosimeters to characterise the proton beam is illustrated by longitudinal measurements of a stack of alanine-wax pellets (**Figure 2-23**). The path length through each pellet is 1 cm, this providing the spatial resolution for measurement of the depth dependence of the delivered dose. The Bragg peak is marked by the sharp drop in the alanine radical yield (**Figure 2-23**). This approach to determination of the depth-dose curve is simple and has a spatial resolution limited by the minimum size of the alanine composites needed to give a well-defined EPR signal.

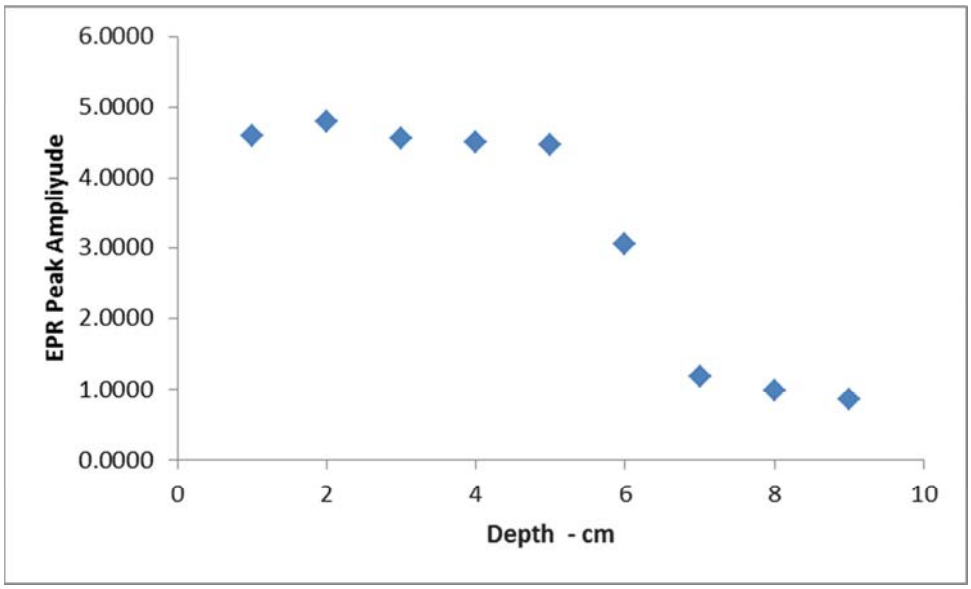

Figure 2-23. EPR signal amplitude (divided by 100,000) against depth, representing the spread Bragg peak of 150 MeV proton beam.

To confirm the validity of the result for the higher energy proton beam used in this study the linearity of the response for the alanine-wax composite materials used with the ion-chamber calibrated dose was examined for exposures well above the usual clinical dose (20 Gy) for the 150 MeV proton beam (**Figure 2-24**).

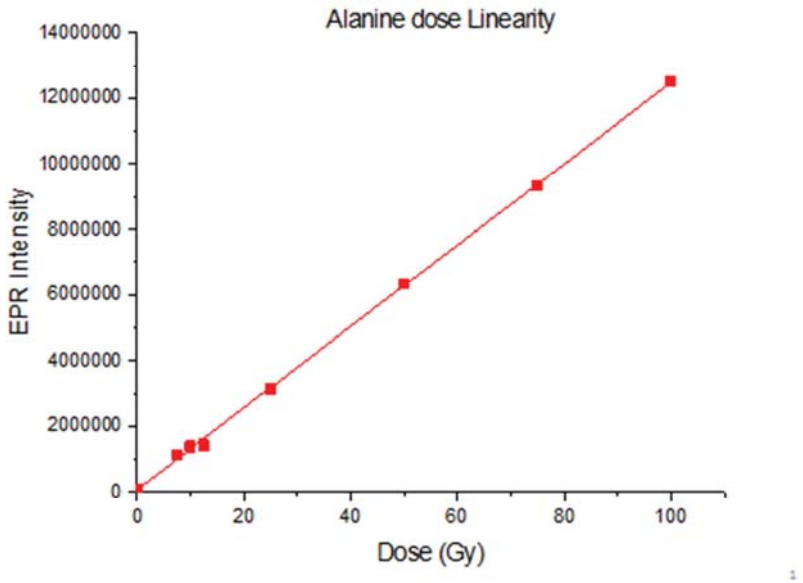

Figure 2-24. The linearity of alanine dose response over a wide range of proton doses.

All AuNP/alanine composites irradiated with protons (150 MeV, SOBP) showed no dependence on the AuNP size or concentration and consistently yielded DE levels of ≤ 5 %.

2.3.4.1 1.9 nm AuNPs

Alanine composites containing 1.9 nm AuNPs irradiated with 150 MeV protons (SOBP) gave linear responses with regression values ranging from 0.977 to 0.982 (**Figure 2-25**).

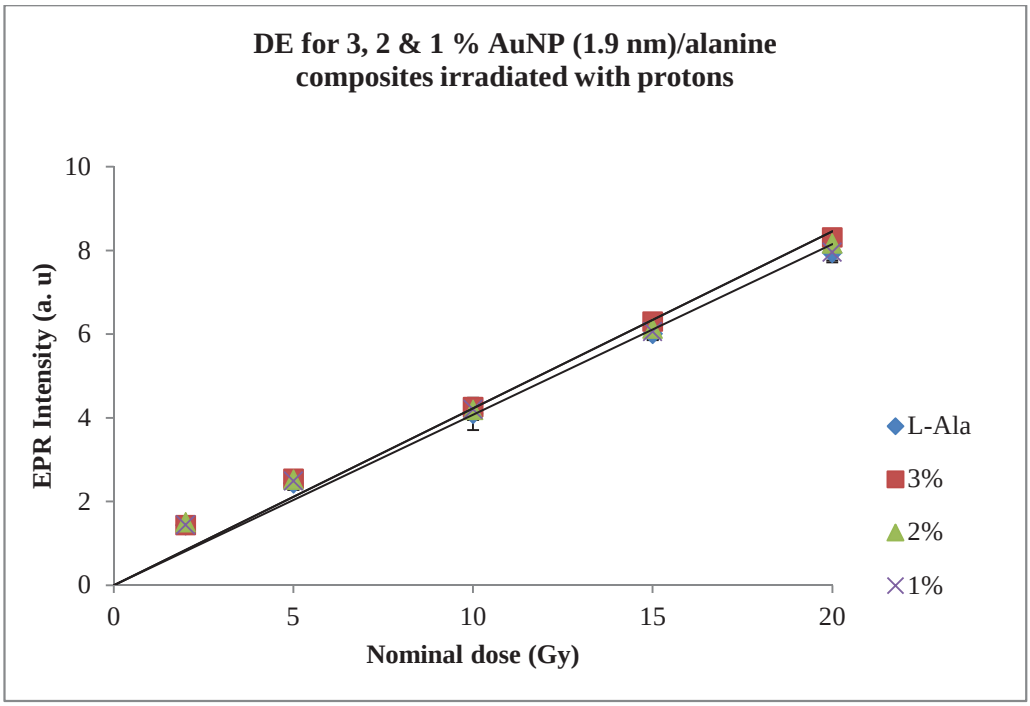

Figure 2-25. EPR signals of alanine-wax pellets with and without AuNPs (1.9 nm) showing the levels of DE following exposure to 150 MeV proton beam.

Radiation DE levels of ≤ 5% was observed for all composites (3, 2 and 1 %) and are presented in **Table 2-13**.

Table 2-13. The levels of DE (%) determined for AuNP (1.9 nm)/alanine pellets (3 to 1 %) irradiated with 150 MeV protons.

Dose (Gy)	Alanine	3% Au	DE %	2% Au	DE %	1% Au	DE %
2	1.432	1.484	4	1.499	5	1.505	5
5	2.435	2.537	4	2.519	3	2.484	2
10	4.092	4.250	4	4.187	2	4.201	3
15	6.005	6.296	5	6.130	2	6.156	3
20	7.941	8.309	5	8.159	3	8.023	1

2.3.4.2 5 nm AuNPs

Alanine composites containing 5nm AuNPs irradiated with 150 MeV protons (SOBP) gave linear responses with regression values ranging from 0.978 to 0.984 (**Figure 2-26**).

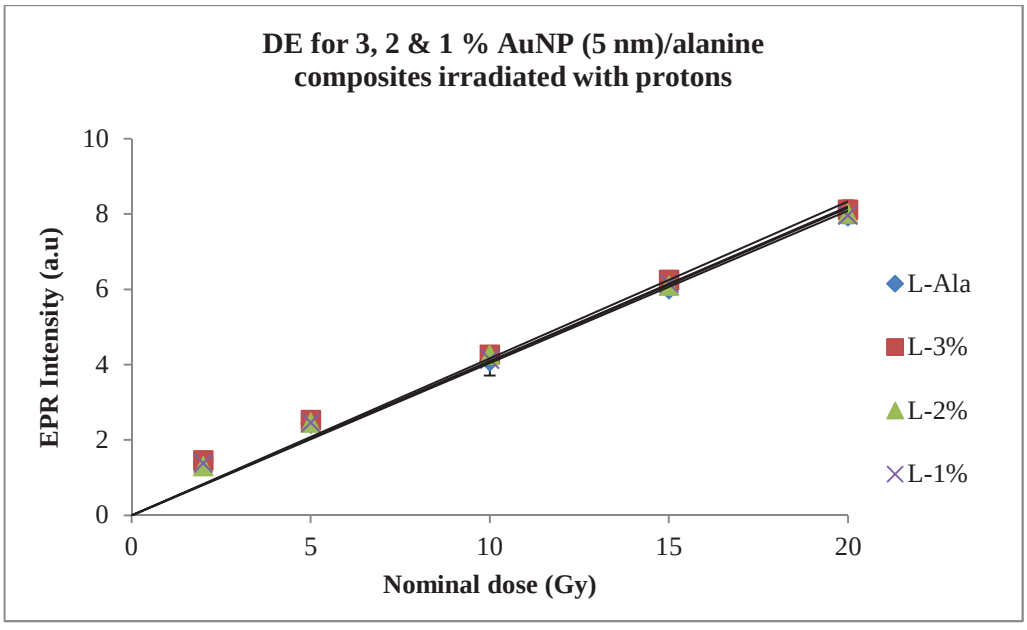

Figure 2-26. EPR signals of alanine-wax pellets with and without 5 nm AuNPs showing DE following exposure to a 150 MeV proton beam.

DE levels of ≤ 4 % was observed for all composites (3, 2 and 1 %) and are shown in **Table 2-14**.

Table 2-14. The levels of DE (%) determined for AuNP (5 nm)/alanine pellets (3 to 1 %) irradiated with 150 MeV protons.

Dose (Gy)	Alanine	3% Au	DE %	2% Au	DE %	1% Au	DE %
2	1.43	1.46	2	1.30	-9	1.38	-4
5	2.44	2.53	4	2.46	1	2.46	1
10	4.09	4.26	4	4.26	4	4.14	1
15	6.01	6.25	4	6.10	2	6.15	2
20	7.94	8.11	2	8.01	1	7.96	0

2.3.4.3 15 nm AuNPs

Alanine composites containing 15nm AuNPs irradiated with 150 MeV protons (SOBP) gave linear responses with regression values ranging from 0.982 to 0.983 (**Figure 2-27**).

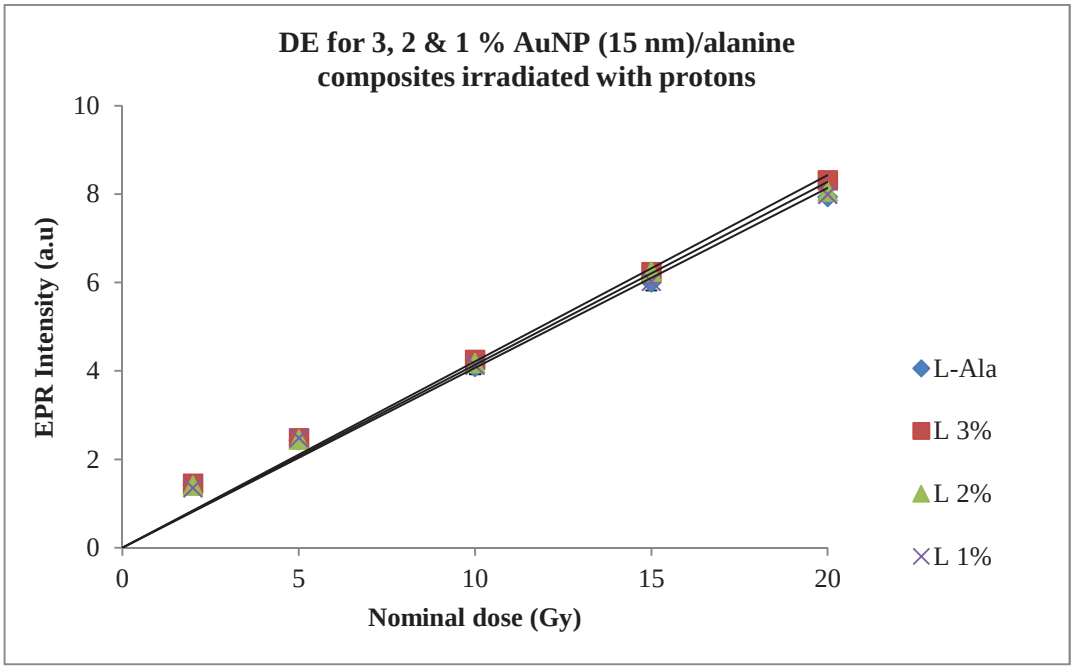

Figure 2-27. EPR signals of alanine-wax pellets with and without 15 nm AuNPs showing DE following exposure to a 150 MeV proton beam.

For all composites (3, 2 and 1 %) investigated, DE levels of ≤ 5 % was observed (**Table 2-15**).

Table 2-15. The levels of DE (%) determined for AuNP (15 nm)/alanine pellets (3 to 1 %) irradiated with 150 MeV protons.

Dose (Gy)	Alanine	3% Au	DE %	2% Au	DE %	1% Au	DE %
2	1.43	1.45	1	1.41	-2	1.36	2
5	2.44	2.48	2	2.45	1	2.49	2
10	4.09	4.26	4	4.18	2	4.13	1
15	6.01	6.24	4	6.25	4	6.02	2
20	7.94	8.32	5	8.06	2	8.00	3

2.3.5. Summary of the results based on AuNP size, concentration and beam quality

The DE achieved for the different beam types used to irradiate the AuNP/alanine composites containing different AuNP sizes and concentrations are summarized in **Table 2-16**.

Table 2-16. The levels of DE (%) determined for all AuNP /alanine composites examined when irradiated with different beam types.

		DE (%)			
AuNP size	**AuNP %**	**kV X-rays**	**MV X-rays**	**Electrons**	**Protons**
1.9 nm	**3**	130 ± 17	23.5 ± 7.5	6 ± 3	4.5 ± 0.5
	2	114 ± 15	17 ± 7	4.5 ± 1.4	3.5 ± 1.5
	1	70 ± 17	4.5 ± 3.5	3 ± 1	3 ± 2
5 nm	**3**	45 ± 10	17.5 ± 6.5	5 ± 3	3 ± 1
	2	14.5 ± 4.5	11 ± 6	2 ± 2	-2.5 ± 6.5
	1	9.5 ± 5.5	5.5 ± 5.5	2.5 ± 1.5	-1 ± 3
15 nm	**3**	62.5 ± 12.5	23 ± 6	5.5 ± 1.5	3 ± 2
	2	41.5 ± 10.5	17 ± 3	4.5 ± 1.5	1 ± 3
	1	25.5 ± 11.5	11.5 ± 2.5	4.5 ± 1.5	2 ± 1

The effects of AuNP concentration on DE are evident for both kV and MV X-ray irradiations; however the effects of AuNP size are clearer for the kV results

compared to the MV results, showing a preference for the 1.9 nm particles, followed by 15 nm and lastly the 5 nm AuNPs (**Figure 2-28**). Neither electron nor proton irradiations showed a DE dependence on the AuNP concentration or size.

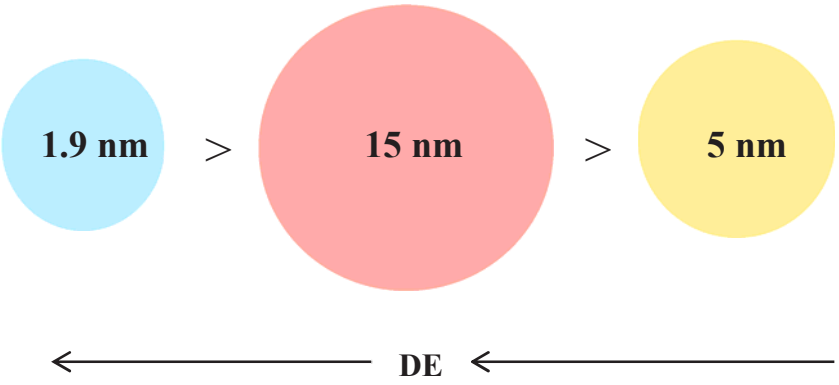

Figure 2-28. The influence of AuNP size and levels of DE as measured for kV X-rays.

2.4 Discussion

The effects of AuNP size and concentration upon the levels of DE achieved when irradiated with different quality beams are discussed below, with the results for kV and MV X-ray irradiations presented first, followed by irradiations with electrons and protons. The results are also compared with other recent studies reported, and the results, particularly for proton irradiations, are important because of the discrepancies in DE levels achieved when irradiating AuNPs in cell and animal models compared with computer simulations.

2.4.1 X-rays: kV and MV ranges

2.4.1.1 AuNP concentration

The higher DE values achieved for the kV X-rays compared to MV X-ray irradiations for the same sized AuNPs and concentrations is consistent with literature

reports for energies below 100 keV, and the increased DE due to the dominance of the photoelectric effect [24, 41]. Whilst for MV energy ranges (6 to 10 MV) the photoelectric effect is replaced by the Compton effect as the dominant interaction.

These results (both kV and MV X-rays) show a linear increase in DE when increasing AuNP doping levels (**Sections 2.3.1** and **2.3.2**), with 3% AuNP/alanine composites producing the largest DE for all sizes examined, followed by 2 % AuNP/alanine, and 1 % AuNP/alanine composites yielding the lowest DE levels, which is in agreement with simulations for both kV and MV X-ray irradiations of AuNPs [92, 98, 99].

2.4.1.2 AuNP size

For kV X-ray irradiations DE was greatest for the 1.9 nm AuNPs; 113 to 147 % (3 % composites) (**Table 2-4 a & b**), followed by the 15 nm AuNPs: 50 to 75 % (3 % composites) (**Table 2-6 a & b**), and lastly the 5 nm AuNPs: 35 to 55 % (3 % composites), which consistently gave the lowest levels of DE for all concentrations examined (**Table 2-5 a & b**). These results agree with the computer simulations by Lechtman *et al* [99] and Hossain and Su [101], which reported higher DE levels for smaller sized AuNPs when irradiated with kV energy X-rays, and is known to occur because of the larger surface-to-volume ratio of smaller sized nanoparticles [62].

However, it is not clear why the 15 nm AuNPs gave a higher DE response than the 5 nm, and could be due to the AuNPs polymeric capping reabsorbing the ejected electrons, and causing a decrease in the DE levels measured. Further analysis is needed to determine the possibility of this occurring, and larger sized AuNPs to conclude this part of the study.

The dependence on AuNP size and DE levels was not as evident for MV X-ray irradiations (**Tables 2-7 to 2-9**), although a similar size preference as seen for the kV X-ray results was evident; with 1.9 nm AuNPs yielding a 16 to 31 % increase (3 % composites) (**Table 2-7 a & b**), closely followed by 15 nm; 17 to 29 % (3 % composites) (**Table 2-9 a & b**) and lastly 5 nm; 11 to 24 % (3 % composites) (**Table 2-8 a & b**). These results agree with MV X-ray irradiation simulations by Mesbahi *et al* [92] who reported a clear relationship between increasing AuNP concentration and increasing DE, but not so for the different AuNP sizes investigated. Similarly, Hwang *et al* [98] found that decreasing MetNP size afforded only a modest increase in DE levels when irradiating with MV X-ray, whilst increasing MetNP concentrations yielded a much greater DE response. The influence of AuNP size for both kV and MV X-rays is summarized in **Figure 2-28**.

2.4.2 Electrons and protons

2.4.2.1 AuNP concentration and size

AuNP size and concentration showed no clear effect on DE levels measured when irradiated with electrons or protons **Sections 2.3.3** and **2.3.4**. The levels of DE for electrons was ≤ 9 % (for all AuNP sizes and concentrations investigated, **Tables 2-10** to **2-12**), and is in agreement with documented results for the same beams as measured using cells in culture study (about 4 %) [24], and is further supported by *in vivo* measurements by Chang *et al* [102] who reported 5 to 10 % DE in tumour bearing mice containing AuNPs, when irradiated with electrons. The small increase in radical generation for the AuNP/alanine composites is most likely due to the increase in the physical density in the case of Alanine/AuNP, leading to an increase in the probability

of collision and Bremsstrahlung electron interactions, and an increase in the number of free radicals generated.

Significant radiation DE (ca. 20 %) of 45 MeV proton beams caused by 14 nm AuNPs was reported in *in vivo* studies by Kim *et al* [80]. The high level of DE relative to the difference in cross section is surprising and may be associated with secondary processes such as the release of Auger electrons. Since the dose response of the alanine dosimeter relates to the yield of radical species, the DE of alanine/AuNP in wax pellets provides a direct means of assessing the relative contribution of a radical based mechanism for the enhanced efficacy of combined AuNP proton beam irradiation. The small DE (ca. 5 %, **Tables 2-13** to **2-15**) is larger than the difference in density of the AuNP doped and undoped alanine-wax pellets and is consistent with the increase in radical yield for a given proton beam dose being linked to the absorption cross-section of the dosimeter with only a small enhancement due to secondary processes associated with the AuNPs. The results obtained align very well with the Monte Carlo simulation data recently reported by Jeynes *et al* [81] and Walzlein *et al* [79] simulated the proton beam DE at various distances away from the AuNP core and showed almost no DE is predicted at distance further than ca. 1 mm from the AuNP.

Furthermore, the results suggest that the large DE for mouse tumours reported by Kim *et al* [80] is not due to enhanced radical generation, and when taking into account the differences between the two studies; beam quality, AuNP size, and concentration, the difference in DE may be partially attributed to the generation of ROS in aqueous media, which alanine is unable to detect. Misawa and Takahashi [90] reported the yield of ROS is significantly enhanced by the presence of AuNPs and identified the production of hydroxyl radicals (OH^{-}) and superoxide anion (O^{-2}) as well as other free radicals. Recent work by Davidson and Guo [108] used highly water-

soluble (approximately 100 nm diameter), and irradiated with kV X-rays, after accounting for the average physical enhancements due to other sources, such as; nanoscale physical enhancement, chemical enhancement, and anti-enhancement, the largest enhancement was obtained for AuNPs present in water, with a 4.5-fold increase in DE due to the generation of ROS. As well, a recent study by Yao *et al* [109] showed that AuNPs also act, via strong binding to the target DNA, to chemically increase the radiosensitivity of the surrounding biomolecules.

These results highlight the importance of biological and chemical effects that increase the radiosensitization of cells; such as ROS in animal and cell studies [104-106]. Furthermore, this suggests a greater need for understanding of the DE processes occurring within cells, and their potential inclusion in future radiotherapy models [107].

2.5 Conclusions

The amount of radiation DE caused by different concentrations and sizes of AuNPs irradiated with varying quality beams; X-ray (kV and MV) electrons and protons, was investigated using AuNP/alanine composites in wax. The response of the alanine dosimeters reflects the radical yield following irradiation and in all experiments this mirrors the differences in absorption cross section, with some modification associated with secondary processes.

Low energy (80 kV) X-rays yielded the highest DE values and was linearly dependent on the AuNP concentration (3, 2 and 1 %). The higher AuNP content resulted in higher DE, which agrees with literature results along with an increased photoelectric cross section. The smallest sized AuNPs (1.9 nm) gave the highest DE overall, which also agrees with recent Monte Carlo simulations. For MV X-ray

irradiations DE was not as large as for kV X-rays, and is consistent with the literature and the dominance of Compton interactions at this energy range. Whilst a dependence on AuNP concentration was observed it was small in comparison to kV X-ray irradiations and the effect of AuNP size was only slightly evident. These results are in agreement with recent Monte Carlo computer simulations and the effects seen for AuNPs interacting with kV and MV X-rays.

The results for electron irradiations agree well with published cell studies using electron beams, as well as with proton simulation data. No such dependence on AuNP concentration or size was observed for both electron or proton irradiations and DE levels were ≤ 9 % and ≤ 5 % respectively. These results suggest that the much larger than expected DE resulting from proton irradiation of AuNP loaded tumours does not result from an increase in the yield of radical species. The increased efficacy is more likely due to the presence of AuNPs in biological systems catalysing other chemical processes (such as ROS), which occur when irradiated with high LET beams, and would account for the greater radiosensitization observed in cell/animal studies. Therefore, for high-energy proton beams the recent Monte Carlo simulations provide a good estimate of the enhanced radical yield following addition of AuNPs to alanine.

In conclusion, alanine dispersed in wax can be used as a phantom and dosimeter for dose distribution measurements delivered by all radiation types used in radiotherapy including protons. This work was able to show for the first time radiation DE using alanine impregnated with AuNPs for proton beams. This study is extended further in the next chapter of the thesis, by the examination of a new material as a possible radiotherapy dosimeter, and investigates its responses to different quality beams, particularly protons.

Chapter 3: Examination of the novel dosimeter IRGANOX®1076

The majority of contents from this chapter has been published. Refer to Appendices iii for permission to reproduce published materials.

3.1 Introduction

As the primary aim of radiotherapy is to deposit a highly tailored dose to cancerous targets, whilst minimizing damage to healthy surrounding tissues [3, 24], it is vital to reliably measure the radiation dose delivered using tissue equivalent dosimeters. Tissue equivalent dosimeters are preferred, as non-tissue equivalent dosimeters require approximations and hence have associated errors. As stated in **Section 1.3** the most commonly used dosimeters in radiotherapy are ionisation chambers, TLDs and diodes, which are not tissue equivalent. More recently, EPR dosimeters, and in particular alanine, have been investigated as an alternative for radiotherapy dosimetry. Reasons for the interest in alanine are discussed in **Section 1.3.2.2**, and include the fact that it is a tissue-equivalent dosimeter. However, alanine is currently limited by its poor sensitivity at low doses (< 5 Gy) [38, 39, 50] [40], as are commonly used in radiotherapy applications. Recent attempts to extend the usable range of alanine to approximately 1 Gy have been discussed in **Section 1.3.2.2**, as well as practical limitations of the methods trialled.

Further issues with alanine dosimeters include the complicated EPR spectrum due to a mixture of radicals with a dependence of the intensity of the central EPR signal on the rotational orientation of the sample in the cavity. The extent of this variation was determined by Dolo and Garcia [110] and shown to range between 9 to 40 % for commercially available powders, and 2 to 10 % for commercial pellets. As alanine is highly hygroscopic [111], the variation in band profile has been attributed to differing water content of the alanine sample [49], which may be due to relaxation effects or changes to the radical composition post-irradiation, however, these effects are not fully understood [110]. The angular dependence of the EPR spectrum of alanine does not preclude use of the material for dosimetric applications provided that the reported signal is the average of measurements obtained for a range of angles [48, 53, 112, 113].

Despite the many desirable features of alanine as a radiotherapy dosimeter [25], issues related to the hygroscopic nature of the material and attendant complications with signal measurement provide significant barriers to its more widespread use. These problems can be avoided by selection of a material with a composition similar to alanine (hence keeping its advantages) but being hydrophobic and giving a single stable radical when irradiated, i.e. reducing its limitations. For applications in radiotherapy the properties a dosimeter should ideally possess are discussed in **Section 1.3.1** but briefly include; small in size, malleable (so custom geometrical forms could be made so that full scatter conditions are maintained when in contact with non-planar surfaces), sensitive to low doses (1 to 2 Gy), tissue equivalent (for more reliable dose estimation), stable post-irradiation, inexpensive (making it disposable), and easy to read/interpret [25]. The experiments reported herein demonstrate that IRGANOX®1076 has the characteristics of a more adequate radiotherapy dosimeter.

3.1.1 IRGANOX®1076

IRGANOX®1076 (**Figure 3-1**) is a 1, 3, 5 trisubstituted phenol compound, which when irradiated gives a radical stabilised by the aromatic ring. The bulky alkyl groups at the reactive ortho and para sites (**Figure 3-2**) prevent further reactions [114] thus making the radical highly stable. The radical may result from simple ionisation with formation of a phenol radical cation characterised by a doublet EPR signal, due to electron coupling with the phenol proton, or may result from loss of a hydrogen atom giving a phenoxyl radical characterised by a singlet in the EPR. The EPR spectrum of solid solutions of IRGANOX®1076 in wax, post irradiation consists of a single peak, which is easy to measure and quantify, and is consistent with the phenoxyl radical [115-118] (**Figure 3-3**).

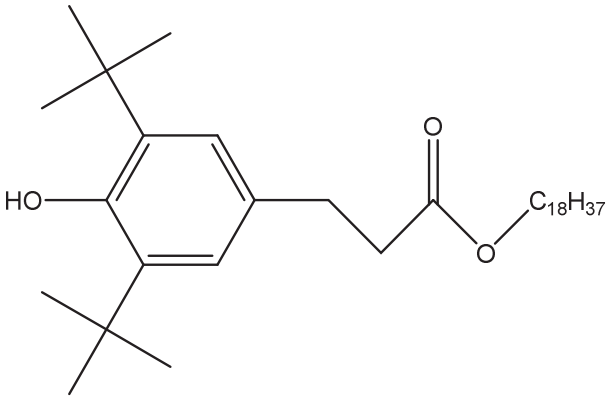

Figure 3-1. Chemical structure of IRGANOX®1076, showing sterical hindrance at the ortho and para positions.

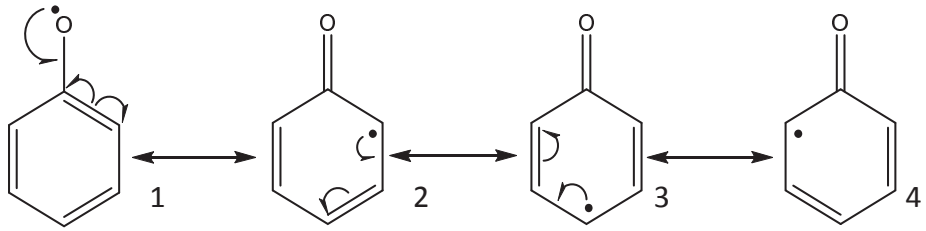

Figure 3-2. The resonance structures of the phenoxy radical, showing increased reactivity at the ortho (structures 2 and 4) and para (structure 3) positions.

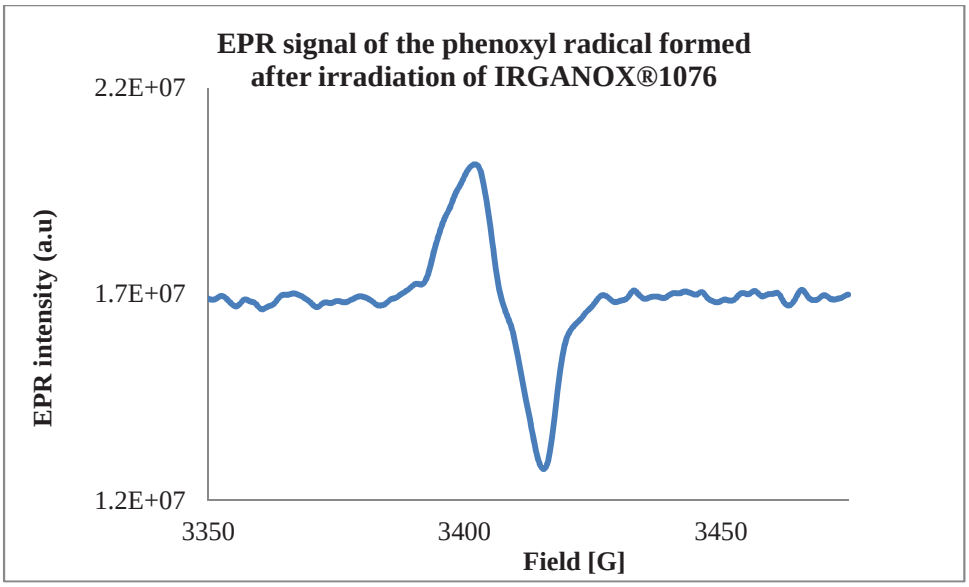

Figure 3-3. The typical EPR signal for IRGANOX®1076 phenoxyl radical.

IRGANOX®1076 is inexpensive, readily available, approved by the US Food and Drug Administration (FDA) [119] and has a mass energy absorption coefficient value that is comparable to water and tissue [120], which are all desirable properties for radiotherapy based dosimeters. Initial work by Marrale *et al.* [120] of suspensions of IRGANOX®1076 in wax binder irradiated with ^{60}Co photons found good linearity over a dose range of 12 to 60 Gy, and signal stability of up to 30 days post-irradiation. Interestingly the EPR spectrum reported in these studies has the form of a doublet, indicating a phenol radical cation. Later Marrale *et al.* [27] extended this to studying the signal enhancement for IRGANOX®1076 containing 5 % (w/w) gadolinium oxide

(Gd_2O_3) when irradiated with neutrons and gamma photons. For neutrons signal enhancement was increased approximately ten times but no such increase was observed for gamma photons.

These results suggest a broader applicability of IRGANOX®1076 as a potential dosimeter for other routinely used radiotherapy beams, in particular protons, which are gaining popularity in clinical use. Wax pellets containing a higher WAX:IRGANOX®1076 ratio (70:30) were manufacture, which improved the malleability of the material, and as well, this composition yielded a solid solution – that is, the IRGANOX®1076 dissolves in warmed wax, which on cooling, gives solid containing wax-solvated solute molecules.

The response of the IRGANOX®1076 wax solid state (IWSS) pellets to different nominal doses of 2, 5, 10, 15 and 20 Gy using X-rays (kV and MV) and charged particles (protons and electrons) was examined, and EPR reproducibility and orientation dependence assessed. Finally the EPR signal response for alanine-wax pellets containing the same mass (w/w) of dosimeter material (30 mg) were compared for the same nominal doses (2 to 20 Gy) and irradiation beams.

3.2 Methods

3.2.1 Preparation of IRGANOX®1076 wax solid state (IWSS) pellets

IRGANOX®1076, Octadecyl 3-(3,5-di-tert-butyl-4-hydroxyphenyl)propionate, (≥99 %) was purchased from Sigma Aldrich and used without further purification. Paraffin wax was obtained from Leica Biosystems as Paraplast Tissue Embedding Medium (mp: 56 to 57 °C).

Rectangular moulds constructed of silica measuring 10 x 5 x 5 mm were warmed and approximately two drops of molten paraffin wax was added to the bottom of the mould. IRGANOX®1076 (30 mg) was added to the molten wax and allowed to dissolve, forming the upwards face as illustrated in **Figure 3-4**. An additional 3 to 4 drops of molten wax was then added over the solid to fill the mould.

The mould was then cooled and the wax pellet removed, excess wax was trimmed to yield uniform wax pellets (measuring 10 x 5 x 5 mm) with a homogenous layer of wax and IRGANOX®1076 of approximately 2 to 3 mm depth.

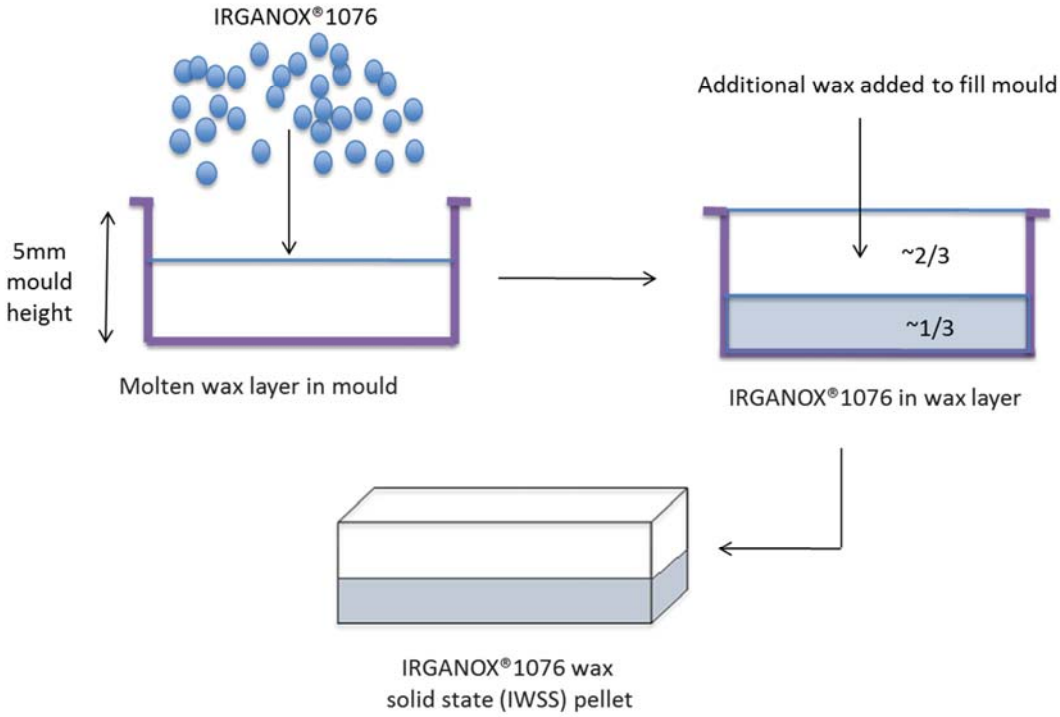

Figure 3-4. The formation of the IRGANOX®1076 (approximately 30 %) wax solid state (IWSS) pellet.

3.2.2 Sample irradiation

IWSS pellets were placed within a silica holder of the same dimensions, such that there were no air gaps between the pellet and mould (**Figure 2-9**). The pellet

surface containing the homogenous mixture of wax and IRGANOX®1076 was placed upwards within the mould for irradiation as shown in **Figure 3-5**. For MV X-rays the dose delivered was to the surface of the silica holder containing the wax pellets, which was positioned at a depth beyond the point of maximum dose where the LINAC (Varian Novalis) was calibrated to 1 cGy/monitor unit (MU). For proton irradiation the samples were positioned within the centre of the spread out Bragg peak (SOBP). After receiving the required dose, the IWSS pellets were removed and replaced with 'dummy' wax pellets.

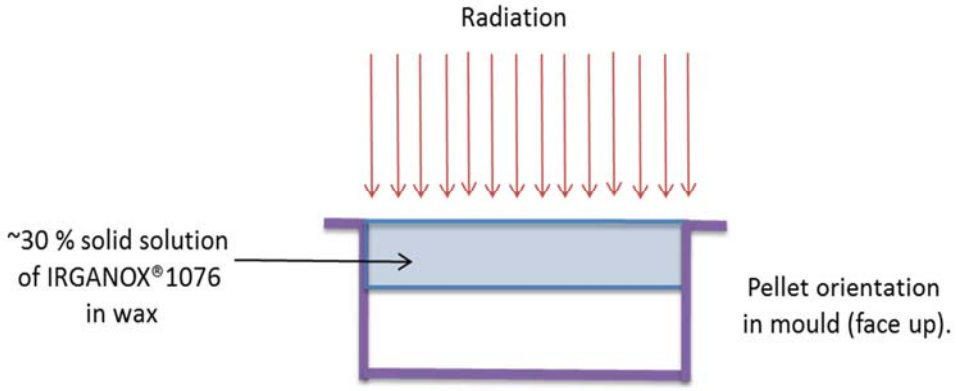

Figure 3-5. Showing the orientation of the IWSS pellet when irradiated.

3.2.3 Irradiation conditions, standards and uncertainty

The standards and uncertainties for all beam types used in this investigation have been described previously in **Section 2.2.8**. The X-ray (kV and MV), electron and proton irradiations were conducted as described in **Section 2.2.5**. The IWSS pellets were placed on top of the back-scatter medium and irradiated using different types of radiations (**Table 3-1**).

For dose response measurements, all samples received nominal doses of 2, 5, 10, 15 and 20 Gy, and is detailed in **Table 2-2**. For angular response measurements, all samples received 30 Gy (6 MV X-rays).

Table 3-1. The types of radiations to which IWSS pellets were exposed, and the conditions used.

Radiation	Generator	Energy	Back Scatter Medium	Build-Up Cap	SSD	Field Size
kV X-rays	PENTAK HF150T Therapx series 3 Unit	80 kV	2 cm solid-water and 10 cm acrylic	Not used	25 cm	10 cm circular cone HVL of 2.2 mm Al
MV X-rays	Varian 21iX LINAC Varian True Beam LINAC	6 MV 10 MV 18 MV	15 cm solid-water	5 cm	95 cm	10 × 10 cm^2
Electrons	Varian 21iX LINAC	6 MeV	15 cm solid-water	13 mm	95 cm	10 × 10 cm^2
Protons	Hyogo Ion Beam Centre	150 MeV, SOBP 5cm	15 cm solid-water	1 cm (to place it at centre of SOBP)	95 cm	20 × 20 cm^2

3.2.4 EPR scanning conditions

The EPR spectra of the irradiated samples were obtained using the conditions described in **Section 2.2.7**, and five repeat scans recorded. The standard spectrometer settings for all measurements were: 340 mT centre field, 2.00 mW microwave power, 10.28 s sweep time, 2.0 mT sweep width, 0.4 mT modulation amplitude, 10.24 ms time constant, 100 kHz modulation frequency and 75 dB receiver gain.

3.2.5 EPR angular response

All angular response measurements were conducted using the standard settings but with a longer sweep time (21.05 s) and time constant (82 ms). A goniometer was used to determine the angle of measurement and the sample manually rotated to the new position.

3.2.6 Sample storage

After irradiation, all samples were stored in a sealed container and the temperature and humidity was monitored using a digital thermal/hygrometer gauge. The temperature was maintained at, or below 24 °C and the relative humidity remained below 50 %.

3.2.7 EPR measurements

The response of IWSS pellets to the nominal doses delivered by X-ray sources, electron and the proton beams is quantified by the concentration of phenoxyl radicals generated (**Figures 3-2** and **3-3**). The uncertainty in the determination of the EPR signal amplitude depends on the signal intensity, which is estimated to be between 1.5 % and 4 % for alanine dosimetry [53], this being consistent with repeated measurements from the same sample. The errors associated with the data presented in this chapter represent the average of at least three independent samples.

3.3 Results

3.3.1 Phase dependence of the EPR signal of IRGANOX®1076 following irradiation

The EPR signal produced by the radical species formed after irradiation of the IWSS pellets and solid IRGANOX®1076 is shown in **Figure 3-6 a &c**. Irradiation of the IWSS pellets (IRGANOX®1076 in solution) results in loss of the hydrogen radical (H·) and an EPR singlet, whilst for the crystalline matrix; loss of an electron produces the phenol cation and an EPR doublet. Partial dissolution in wax (10 %) gives a mixture of the singlet and doublet EPR signals (**Figure 3-6 b**). The singlet peak's amplitude (peak to peak) was used for all EPR measurements within this study, and was greater than the amplitude for the doublet signal (irradiated under same conditions; energy, dose, weight of sample), providing better quantification and signal to noise (S/N) ratio compared to the doublet.

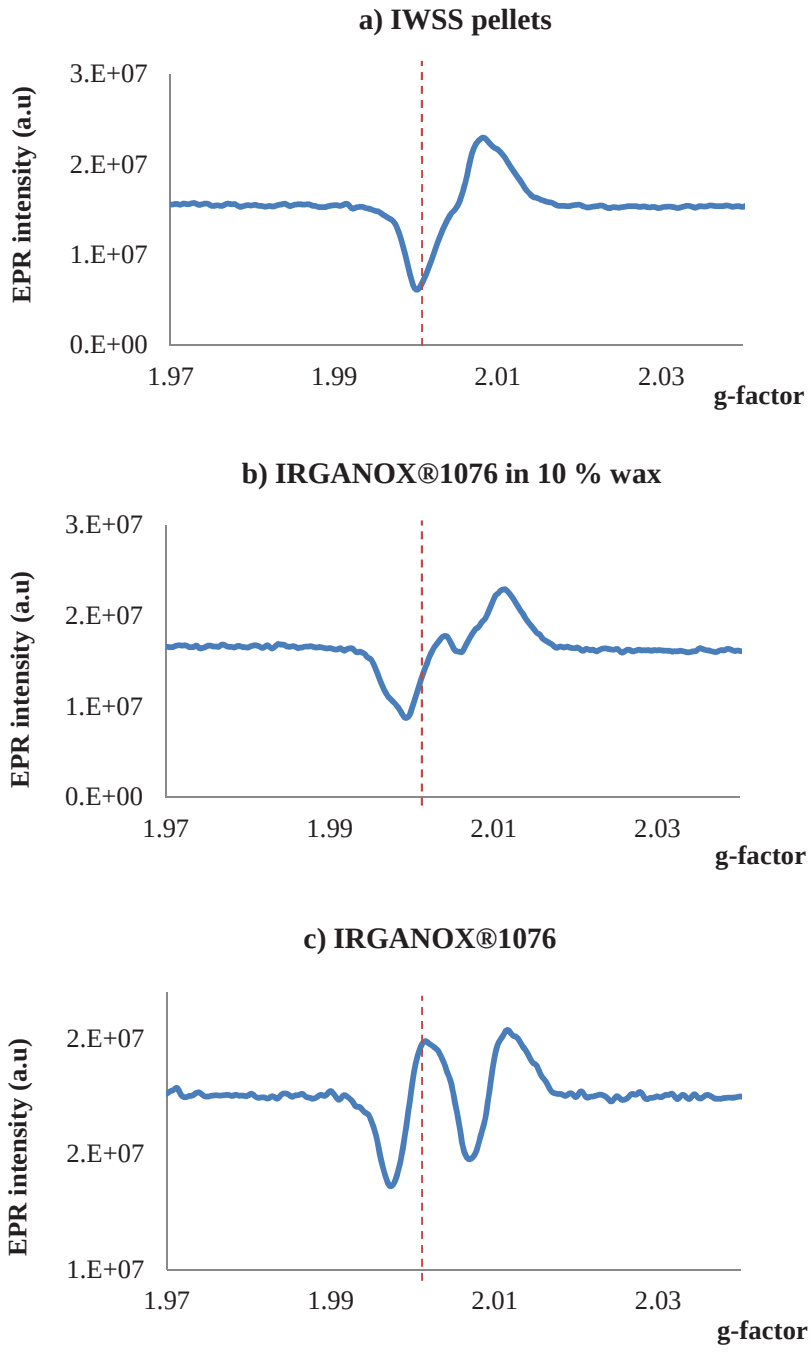

Figure 3-6. The EPR signal for the phenoxyl radical formed after irradiation of IWSS pellets (a) and when present in approximately 10 % wax (b), and lastly the doublet signal formed after irradiation of solid IRGANOX®1076 (c) (Note: different irradiation & EPR conditions were used to generate c).

3.3.2 Linear response and LET dependence

The response of IWSS pellets to different radiation beams, for the nominal doses delivered (after ion chamber calibration), is shown in **Table 3-2** and **Figure 3-7**. The error bars on the plot correspond to the standard deviation between three independent measurements at each nominal dose, and were fitted with a linear function with intercept set at origin. The nominal dose values (x-axis) used was determined by calibrated ionisation chamber measurements.

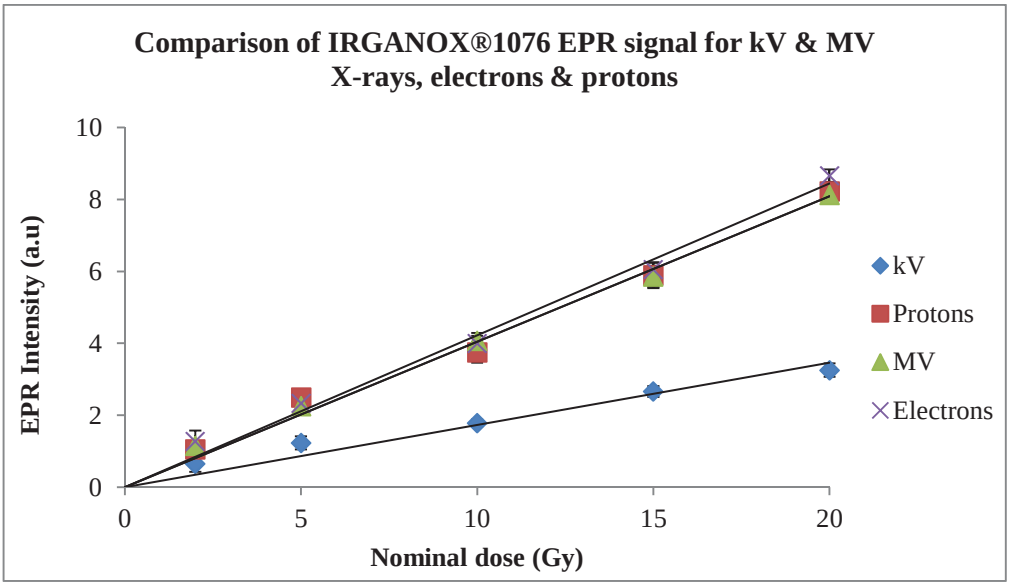

Figure 3-7. Overlay of the radiation types measured (kV & 6 MV X-rays, electrons and protons), showing the energy independence of IRGANOX® 1076 as IWSS pellets (each dose measured represents the average of at least 3 independent samples).

Table 3-2. The average EPR signal amplitude for IWSS pellets (each average represents at least three separate wax pellets measured) after irradiation with different quality beams and doses.

Dose (Gy)	kV ($\bar{x}$)	σ	Protons ($\bar{x}$)	σ	MV ($\bar{x}$)	σ	Electrons ($\bar{x}$)	σ
2	0.54	0.24	1.06	0.12	1.15	0.01	1.27	0.30
5	1.07	0.15	2.50	0.14	2.25	0.24	2.33	0.28
10	1.79	0.10	3.75	0.29	4.07	0.23	4.00	0.22
15	2.66	0.15	5.89	0.36	5.86	0.29	6.05	0.19
20	3.32	0.21	8.23	0.18	8.13	0.13	8.66	0.17

The relative response of the IWSS pellets (**Figure 3-7**) shows that the linearity of the response of the dosimeter for radiation doses from 2 to 20 Gy with correlation coefficients ranging from 0.979 to 0.993. The results show the samples are independent of the radiation type but that the sensitivity of the dosimeter is less for kV X-rays than for the MV X-rays, electrons and protons. Consequently, the same calibration can be used for the different forms of LET radiation.

3.3.3 Dependence of the EPR signal response over the MV X-ray energy range

The energy independence for MV X-rays was further examined by irradiating IWSS pellets with 6, 10 and 18 MV X-rays. **Table 3-3** shows the average and standard deviation values for the EPR signal measured for three to five pellets irradiated at each nominal dose, and the averages are plotted in **Figure 3-8** with a standard deviation (range of 0.009 to 0.512) corresponding to the error bars. As for the LET response, IWSS pellets show an independent response to different MV energies.

Table 3-3. The average EPR signal amplitude for IWSS pellets (each average represents between three to five separate wax pellets measured) after irradiation with different MV energy beams and doses.

	6 MV		10 MV		18 MV	
Dose (Gy)	$(\bar{x})$	**σ**	$(\bar{x})$	**σ**	$(\bar{x})$	**σ**
2	1.15	0.01	0.95	0.07	1.09	0.06
5	2.25	0.24	2.16	0.49	2.14	0.21
10	4.07	0.23	4.37	0.51	4.60	0.22
15	5.86	0.29	5.96	0.34	6.09	0.24
20	8.13	0.13	8.22	0.23	8.29	0.09

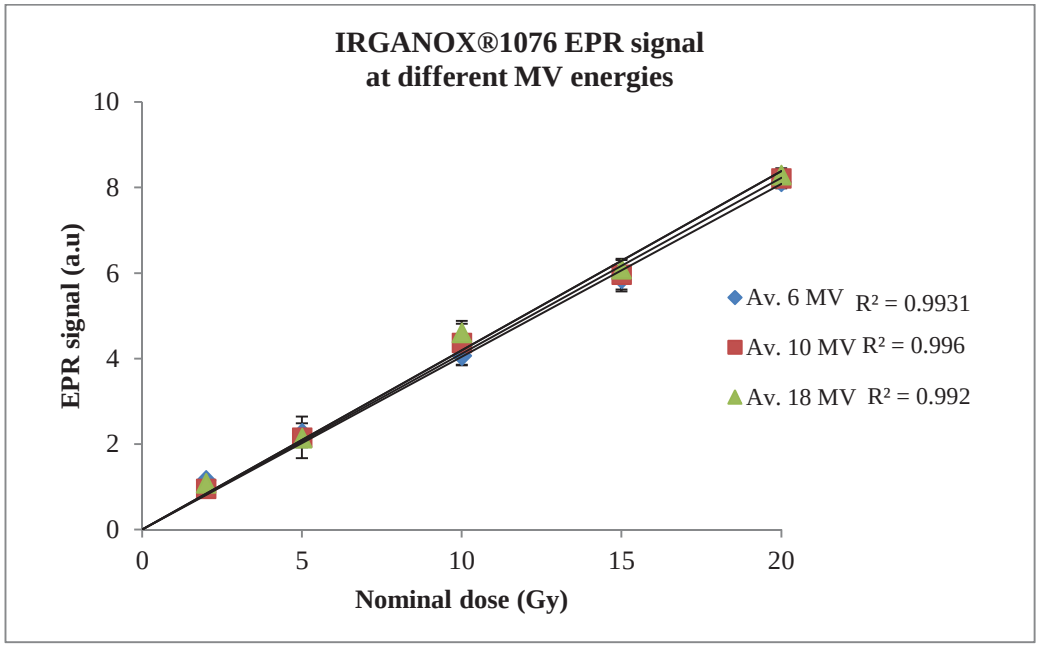

Figure 3-8. Comparison of the average EPR signal for amplitude measured for IWSS pellets after irradiation with different energy MV X-rays (6, 10 and 18 MV), at the same nominal doses (which represents the average of at least 3 independent samples).

3.3.4 Stability of EPR signal post-irradiation

The stability of the IRGANOX®1076 EPR signal post-irradiation with protons was monitored by repeated measurements of a set of samples over an extended period; 4 to 466 days (**Figure 3-9**, **Table 3-4**). In all cases up until 77 days the change in the

signal intensity was less than the measured uncertainty (**Table 3-5**). While the difference in signal is less than the error of the individual measurements the observation that in all cases there was a reduction in signal with time may suggest some fading of the signal; however this is clearly a minor effect.

Table 3-4. The average EPR signal amplitude for IWSS pellets (each average represents three separate wax pellets measured) after irradiation with protons at different nominal doses, and the signal stability over time.

	Time (days)							
Dose (Gy)	**4 ($\bar{x}$)**	**σ**	**5 ($\bar{x}$)**	**σ**	**10 ($\bar{x}$)**	**σ**	**26 ($\bar{x}$)**	**σ**
2	1.06	0.12	1.12	0.22	1.07	0.27	1.15	0.29
5	2.50	0.14	2.51	0.20	2.74	0.34	2.48	0.25
10	3.64	0.39	3.55	0.40	3.50	0.49	3.35	0.47
15	5.89	0.36	5.89	0.25	5.92	0.35	5.96	0.23
20	8.19	0.23	8.14	0.16	8.07	0.15	8.07	0.17

Continued beneath

	Time (days)					
Dose (Gy)	**40 ($\bar{x}$)**	**σ**	**77 ($\bar{x}$)**	**σ**	**466 ($\bar{x}$)**	**σ**
2	1.22	0.25	1.03	0.25	1.24	0.16
5	2.19	0.19	2.46	0.41	2.20	0.46
10	3.36	0.44	3.51	0.23	3.13	0.22
15	5.75	0.24	5.76	0.10	5.23	0.09
20	8.06	0.19	8.05	0.41	7.30	0.23

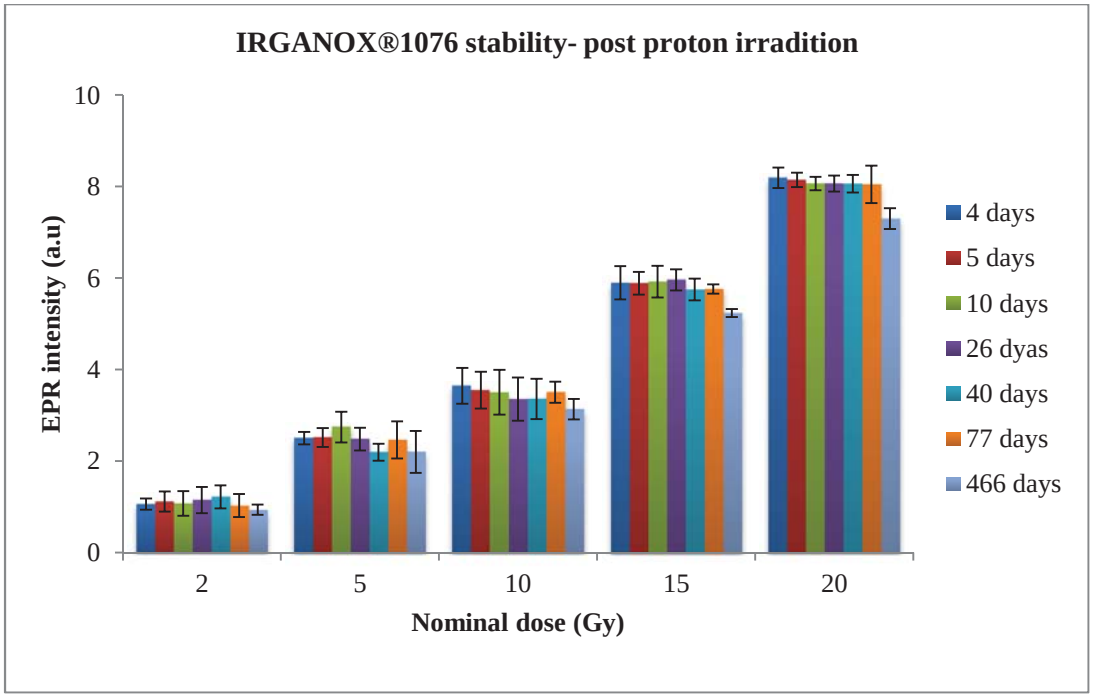

Figure 3-9. Stability of IRGANOX®1076 EPR signal measured over 466 days post-irradiation with 150 MeV protons (each measurement represents the average of at least 3 independent samples).

Table 3-5. Comparison of EPR signal intensity at 4 and 77 days post-irradiation.

Dose (Gy)	EPR signal 4 days ($\bar{x}$)	EPR signal 77 days ($\bar{x}$)	Percentage (%) Difference
2	1.06	1.03	-2.9
5	2.50	2.46	-1.6
10	3.64	3.51	-3.8
15	5.89	5.76	-2.3
20	8.19	8.05	-1.8

Clearly, after 466 days changes in the signal intensity are noticeable (**Table 3-6**), with fading >10 %, which is larger than the errors associated with each individual measurements.

Table 3-6. Comparison of EPR signal intensity at 4 and 466 days post-irradiation.

Dose (Gy)	EPR signal 4 days ($\bar{x}$)	EPR signal 466 days ($\bar{x}$)	Percentage (%) Difference
2	1.06	0.94	-11.5
5	2.50	2.20	-12.0
10	3.64	3.13	-14.0
15	5.89	5.23	-11.2
20	8.19	7.23	-10.9

3.3.5 EPR cavity angular response

The sensitivity of the amplitude EPR signal to a rotation about the cylindrical axis of the sample in the EPR cavity was investigated using a set of five IWSS pellets irradiated with a 30 Gy dose of 6 MV X-rays. Measurements were completed three days post irradiation, and included spectra recorded at 45° increments covering the range 0 to 360°. These experiments showed only minor variations (< 2 %) in signal intensity to a rotation of the sample in the microwave cavity of the EPR (**Figure 3-10**). The variations in signal amplitude were cyclical and of a low magnitude, and are most likely due to a small eucentricity of the rotation axis (slight deviations), which cause a relative change in the position of the sample in the microwave cavity. An alternate explanation, that the signal intensity is due to instability of the spectrometer, can be dismissed based on the reproducibility of the EPR intensity for samples rotated by 360° (**Table 3-7**). These observations are consistent with the homogeneous character of a solid solution and the formation of a single dominant radical following irradiation and contrasts with the more complex, sample-dependent, orientation-dependent EPR spectra obtained from L-alanine [110].

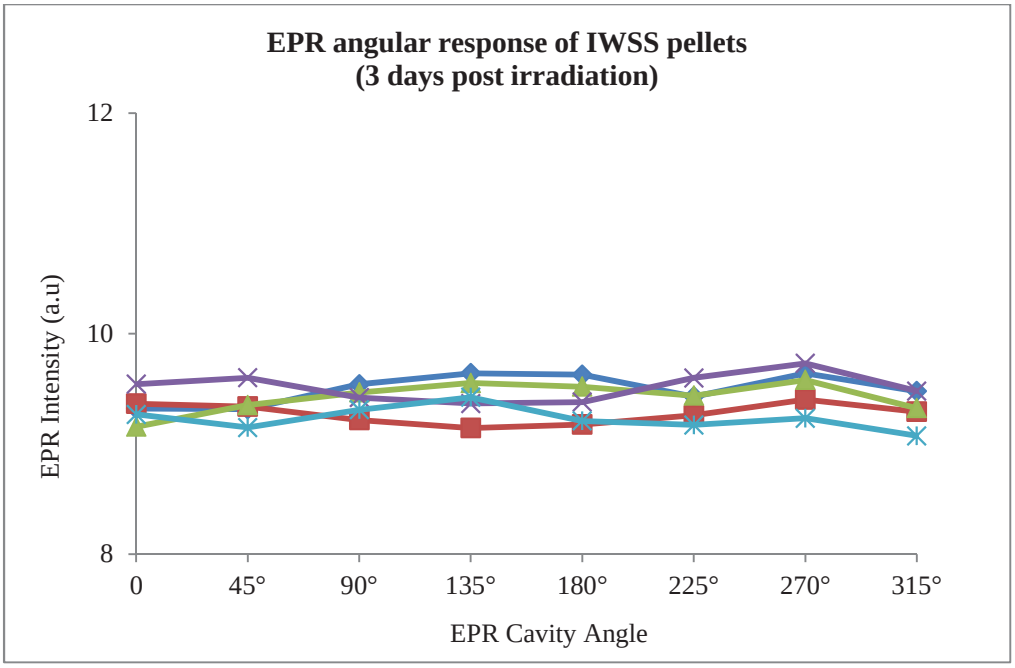

Figure 3-10. The angular response of IWSS pellets as rotated within the EPR cavity.

Table 3-7. Comparison of the IWSS pellets EPR signal intensity at the starting angle (0°) and after one-full rotation was completed (360°).

	IWSS pellets EPR signal at start (0°) and end (360°) of EPR cavity rotation			
Pellet #	**0°**	**360°**	**Difference (%)**	**Drift (%)**
1	9.32	9.32	100.04	-0.04
2	9.37	9.33	99.63	0.37
3	9.16	9.17	100.20	-0.20
4	9.54	9.51	99.63	0.37
5	9.27	9.24	99.73	0.27

As expected for a homogenous sample there was no significant variation of the measured signal.

3.3.6 Comparison with alanine

A comparison with the amplitude of the EPR signal produced when irradiating wax pellets containing the same weight of alanine, which were manufactured and

described in **Section 2.2.4**, were made. The results for kV and MV irradiations are shown in **Table 3-8**, and the EPR signal intensity for three samples per dose plotted in **Figures 3-11** and **3-12**. For irradiation with electrons and protons the results are shown in **Table 3-9**, and plotted in **Figures 3-13** and **3-14**.

Table 3-8. Comparison of the EPR signal intensity for IWSS and alanine-wax pellets irradiated with kV and MV X-rays.

	kV X-rays				MV X-rays			
Dose (Gy)	**Alanine**	**σ**	**IRG**	**σ**	**Alanine**	**σ**	**IRG**	**σ**
2	0.79	0.07	0.54	0.24	1.18	0.12	1.15	0.01
5	1.58	0.05	1.07	0.15	2.22	0.12	2.25	0.24
10	2.56	0.12	1.79	0.10	3.78	0.12	4.07	0.23
15	3.61	0.07	2.66	0.15	5.78	0.25	5.86	0.29
20	5.16	0.08	3.32	0.21	7.92	0.01	8.13	0.13

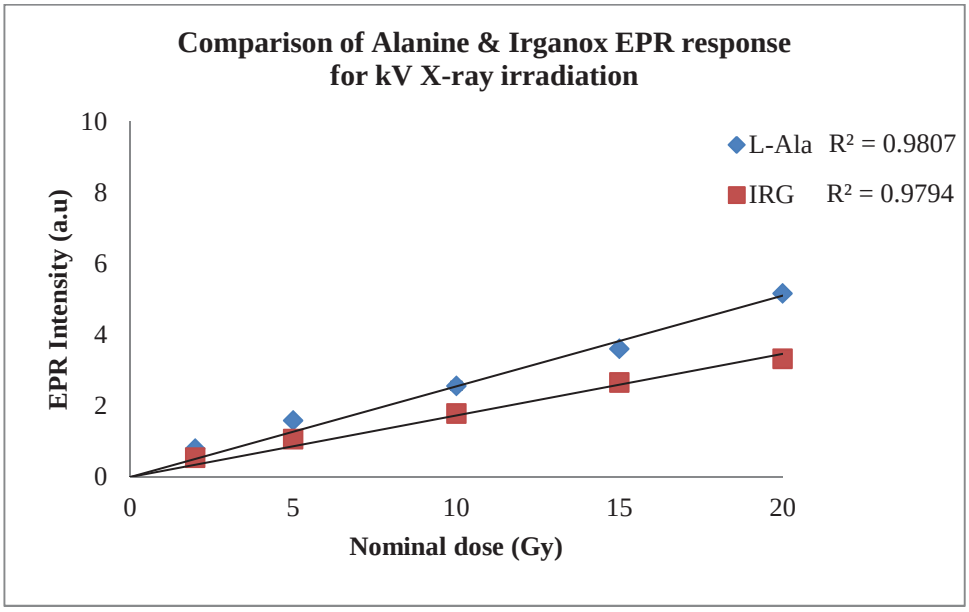

Figure 3-11. The EPR response of IWSS and alanine-wax pellet samples irradiated with kV X-rays (where each dose measured represents the average of at least 3 independent samples).

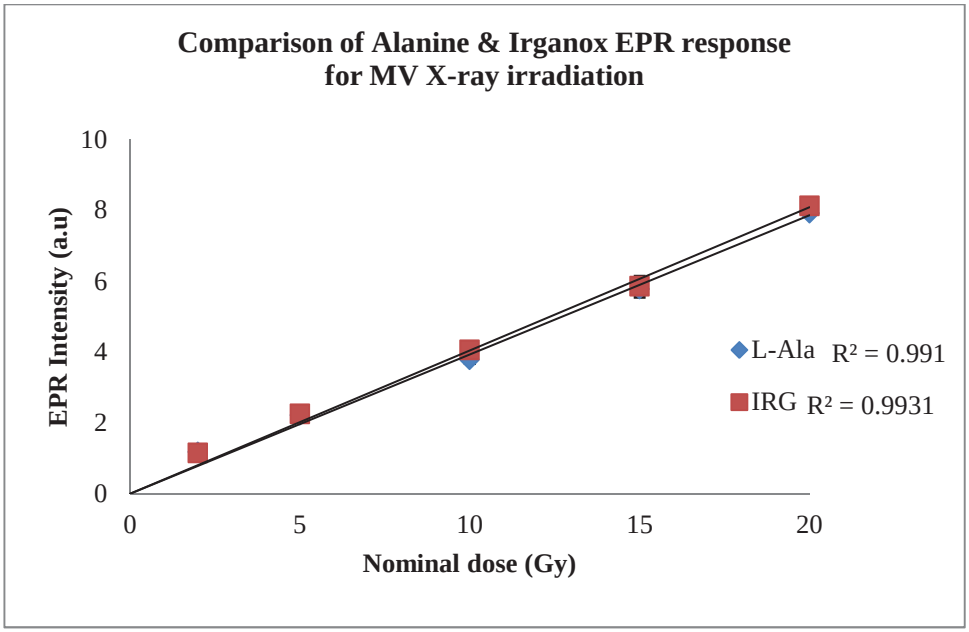

Figure 3-12. The EPR response of IWSS and alanine-wax pellet samples irradiated with MV X-rays (where each dose measured represents the average of at least 3 independent samples).

Table 3-9. Comparison of the EPR signal intensity for IWSS and alanine-wax pellets irradiated with electrons and protons.

	Electrons				Protons			
Dose (Gy)	**Alanine**	**σ**	**IRG**	**σ**	**Alanine**	**σ**	**IRG**	**σ**
2	1.13	0.11	1.27	0.30	1.43	0.08	1.06	0.12
5	2.02	0.18	2.33	0.28	2.44	0.16	2.50	0.14
10	4.54	0.16	4.00	0.22	4.09	0.38	3.75	0.29
15	6.09	0.12	6.05	0.19	6.01	0.10	5.89	0.36
20	7.65	0.16	8.66	0.17	7.94	0.19	8.223	0.18

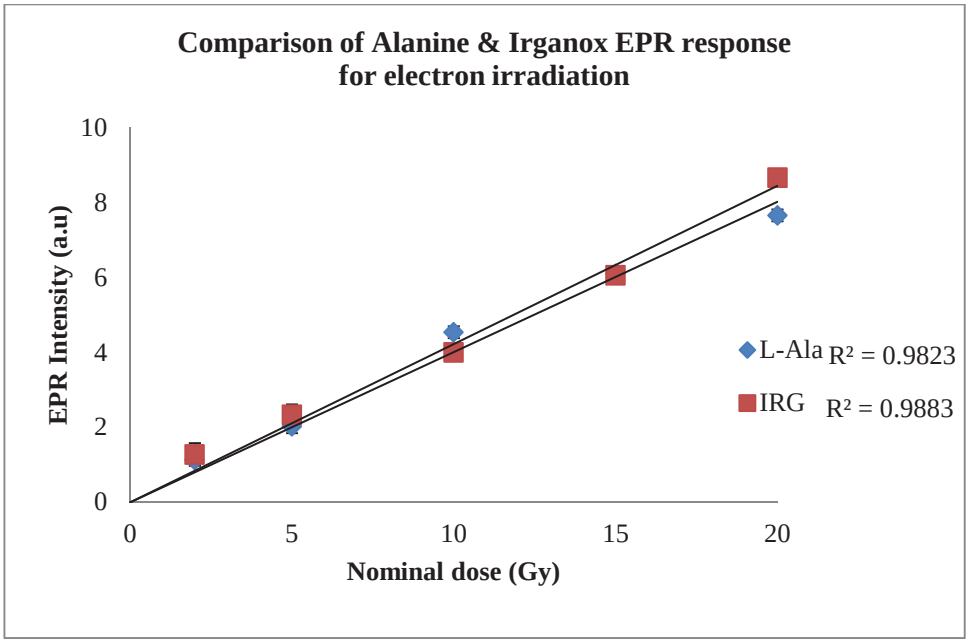

Figure 3-13. The EPR response of IWSS and alanine-wax pellet samples irradiated with electrons (where each dose measured represents the average of at least 3 independent samples).

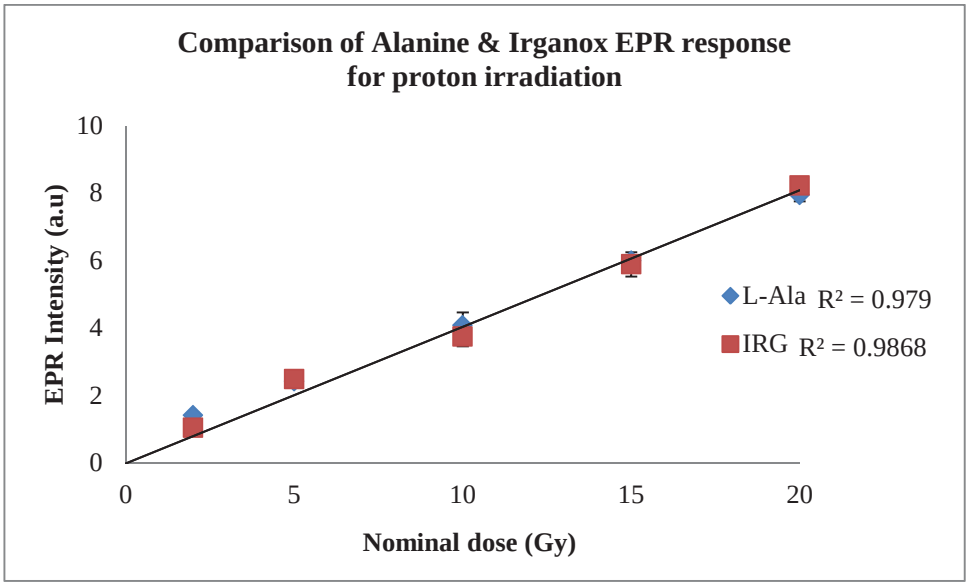

Figure 3-14. The EPR response of IWSS and alanine-wax pellet samples irradiated with protons (where each dose measured represents the average of at least 3 independent samples).

Irradiations with MV X-rays, electrons and protons show a similar EPR signal response between the IWSS pellets and the alanine-wax pellets. Whilst the IWSS pellets do yield slightly higher R^2 values; there are little differences in the results **Figures 3-12** to **3-14**. However, for kV X-ray irradiation (**Figure 3-11**) the IWSS pellets show a lower response compared to the alanine-wax pellets.

3.4 Discussion

The results for the novel dosimeter of IRGANOX® 1076 are discussed below, and focus on the two different radical species formed when irradiating IRGANOX® 1076 as a crystalline solid and when present as a solid solution in wax. The linear response of the material to different LET beams, the good EPR signal stability post-irradiation, and how it compares with alanine are also reviewed

3.4.1 Examination of the IRGANOX®1076 radical obtained following irradiation

The observed difference in EPR signal produced after irradiation of IRGANOX®1076 for crystalline samples and for solid solutions in wax points to distinctly different products for the photoionised molecule depending on the local environment of the absorbing molecule. The difference is particularly surprising given the long-chain para substituents on the phenol ring of IRGANOX® 1076. The observation of a doublet EPR signal for irradiated crystalline IRGANOX®1076 indicates strong coupling with a single proton and this can only be explained in terms of a predominant resonance structure corresponding to the oxygen (O) protonated form of structure 1 in **Figure 3-2**. This corresponds to simple photoionisation of the neutral

molecule. Clearly, the radical corresponding to structure 1 of **Figure 3-2** would give a single resonance and this would be formed by net loss of H˙ from the parent molecule. This may also be achieved by one-electron oxidation of the phenoxy anion [116, 121] or, as observed in this study, for solid solutions of IRGANOX®1076 in wax. In earlier work Marrale and co-workers [120] reported the EPR spectrum of "un-irradiated" and suspensions of crystalline IRGANOX®1076 in wax (90:10) and in both cases observed a doubled signal consistent with **Figure 3-6c**.

The sample of IRGANOX®1076 used in these studies did not give an observable EPR signal prior to irradiation. It is our contention that the sample of IRGANOX®1076 used by Marrale had previously been exposed to radiation, most likely in the course of customs or security checks. This observation highlights the long lifetime of the radical formed from irradiation of IRGANOX®1076. It also follows that suspensions of IRGANOX®1076 in wax will actually comprise a mixture of crystalline and dissolved sample and this will give a composite singlet:doublet signal according to the composition of the sample. We have conducted measurements of samples containing intermediate ratios of IRGANOX®1076 and wax and the resultant signal is a mixture of overlapping singlet and doublet band profiles. Under these circumstances the reproducibility of the dosimeter is greatest if the sample is in a single form. If wax is the medium for supporting the IRGANOX®1076 then a single form is only achieved by the use of solid solutions, as employed in this study. It is also noted that there is a small increase in signal to noise ($\sqrt{2}$) when estimating the EPR signal using the peak height of the singlet as opposed to the doublet.

3.4.2 Linear response and LET independence

The linear response of IRGANOX®1076 to dose is shown in **Figure 3-7**. The dose range extends up to 20 Gy with correlation coefficients ranging from 0.979 to 0.993. The EPR signal obtained for IRGANOX®1076 dosimeters following irradiation with different energy MV X-rays, electrons and protons (**Figures 3- 7** and **3-8**) was found to be independent of radiation type and LET as it displays the same signal amplitude for all three forms of radiation i.e. the same signal is observed for high LET protons as for low LET MV X-rays and electrons for the same dose. Our MV X-ray results agree well with those reported by [120], and extend the possible uses of IRGANOX®1076 to now include kV X-rays, electrons and protons.

For irradiation with 80 kV X-rays IRGANOX®1076 shows a reduced linear response to dose (**Figure 3-7**) when compared to that of MV X-rays, electrons and protons. The same reduction in sensitivity to dose when irradiated with lower energy photons is also observed with alanine dosimeters [41, 51, 122]. At energies below 100 keV a reduction in EPR signal of approximately 40 % (compared to ^{60}Co gamma irradiation) occurs [41]. For this reason alanine is not used in diagnostic radiology where low energy (20 to 60 keV) photons are typically used. Further investigation of the response by IRGANOX®1076 to low energy photons is needed to establish its application range.

In summary, with the current EPR measurement protocols IWSS pellets can be successfully used to quantify doses of approximately 2 Gy and higher. Further optimization of the EPR protocol used to measure the spectra may well extend this limit to 1 Gy, which would further extend the application of IRGANOX®1076 clinical radiotherapy contexts.

3.4.3 EPR stability post-irradiation

Since a key focus of this research is to assess the applicability of IRGANOX®1076 dosimeters to proton dosimetry it is important to consider the stability of the EPR signal after proton irradiation (**Figure 3-9**). The pellets were stored within the laboratory at standard conditions in a darkened environment, whilst humidity was not controlled; hygrometer measurements suggest that the relative humidity did not exceed 50 %.

The IWSS pellets were repeatedly measured post-irradiation starting from 4 days post to 466 days. The measurements show good reproducibility of the signal up until 77 days (**Table 3-4**), and signal fading over this period ranged from 1.6 % (5 Gy) to 3.8 % (10 Gy), (**Table 3-5**) this being comparable to experimental uncertainties. After 466 days changes in the signal fading was noticeable and ranged from 10.9 to 14.0 %, (**Table 3-6**). Overall, these measurements suggest that the IWSS pellets have high levels of stability when stored within a standard laboratory conditions for up to three months, however signal fading after more than one year is observable.

3.4.4 Comparison to alanine

Irradiations with MV X-rays, electrons and protons show a similar EPR signal response between the IWSS pellets and the alanine-wax pellets. Whilst the IWSS pellets do yield slightly higher R^2 values; there is little difference in the results **Figures 3-12** to **3-14**. However, for kV X-ray irradiation (**Figure 3-11**) a lowered response for the IWSS pellets compared to the alanine-wax pellets is observed. Whilst the alanine-wax pellets have a slightly higher R^2 value; 0.981 compared to the IWSS pellets; 0.979,

the reasons for this reduced signal intensity are not known and further measurements are needed. As stated earlier (**Section 3.4.2**) changes in alanine's dosimetric response for kV X-rays is well known, however, not readily explained in the literature. As IRGANOX®1076 shows the same decrease in radical yield for kV X-ray irradiations a similar response is occurring, and the differences between the kV results for alanine and IRGANOX®1076 may be reflective of another process, such as the bond-dissociation energy differences needed to form the dosimeter's radical species (-O-H for IRGANOX®1076 compared to -C-H for alanine). However, currently there is no such information regarding this in the literature, and further investigation is warranted.

3.5 Conclusions

IWSS pellets were found to have sufficient sensitivity to allow dose quantification over the range 2 Gy to 20 Gy for all radiation beams investigated (kV & MV X-rays, electron and protons) further; the signal is energy and LET independent for MV X-rays, electrons and protons. The phenoxyl radical formed is highly stable with little change in the EPR signal after >2 months post irradiation by protons; however signal fading was evident after approximately 15 months. Comparisons between the EPR signal intensity with alanine are comparable, whilst the shortcomings associated with the use of alanine in dosimeters (sensitivity at low dose, reproducibility of EPR spectra, multiple radical species, hydrophilicity, angular dependence of the EPR spectra) are either substantially (sensitivity at low dose) or completely eliminated by the use of IRGANOX®1076. The hydrophobic character of the material gives greater control over the composition and reproducibility of the dosimeters and helps avoid the

complexity of product distribution evident for alanine. The results demonstrated that wax is an ideal supporting medium provided that the IRGANOX®1076 is completely dissolved in the wax. Under these circumstances a single singlet is observed in the EPR which, unlike alanine, has an intensity independent on the orientation of the sample. Quantification of the EPR signal is relatively straightforward and this leads to an extension of the useful dose range to 2 Gy.

Based on these findings, it suggests that IRGANOX®1076 is superior to conventionally used dosimeters, particularly for high LET beams. The advantages of IRGANOX®1076 are; it's simple and easy to interpret EPR spectrum, tissue equivalence, low toxicity, low cost and ready availability and high wax solubility, allowing a dosimeter of any shape and size to be made, which is useful for in vivo dosimetry. Finally, it is believed that by further optimization of EPR settings its dose range may be extend to better than 1 Gy.

Chapter 4: A comparison of the EPR angular response of alanine and IRGANOX®1076

4.1 Introduction

Whilst alanine dosimeters have clear advantages for clinical radiotherapy; tissue equivalence, good stability post-irradiation, can be reused for accumulative dose studies, etc. (see **Section 1.3.2.2** for more details) they suffer from EPR angular response changes, which alters the amplitude of the central alanine peak when the sample is rotated within the EPR cavity (**Section 3.1**). Known as 'angular response' (and not to be confused with the angular response that occurs during irradiation) it must be taken into consideration when performing EPR measurements with alanine. Generally, to overcome this problem the sample is rotated and several measurements at various angles within the cavity are averaged to yield the reported signal [48, 53, 112, 113].

The contributing effects of the angular response have been extensively explored by Dolo et al. [49, 110, 123]. Dolo and Garcia [110] found by rotating alanine commercial pellets and powders in 10° increments 37 times (whereby the first and last measurements at 0° and 360° are the same position and was used to verify the stability of the EPR during the measurement process) and measuring the central peak's amplitude a roughly sinusoidal curve was obtained. The variation between measurements performed was greatest for powder and pellet samples containing large grain sizes and poor compacting with maximal deviation values ranging from 9 to 40% [110]. Whilst, highly compressed commercial alanine pellets with smaller grain sizes showed variations of 2 to10 % in signal amplitude [110]. They concluded that the averaging of several measurements at different angles did not adequately reflect the large variations seen in the results.

As alanine is highly hygroscopic [111] the differing water content within alanine was identified by Dolo and Feaugas [49] as likely causes for the angular response and variation in band profile observed. The water within the sample acted to alter the EPR signal produced in two ways; firstly, by affecting the resonance within the EPR cavity, and secondly, by changing the radical composition formed. This was in agreement with previous work by Abu and Otten [111] which had shown that water within alanine was either *free bound* and affects the quality (Q) factor of the EPR cavity by absorbing the microwave signal (which lowers the output peak signal) or *physically bound* which causes variations in the quantities of each radical formed.

Later work by Garcia and Dolo [110] concluded that radicals formed at the surface of alanine grains were unstable and readily underwent rearrangement and transformations, which altered the amplitude of the central EPR peak. This supported their earlier findings [123], showing how key features of the alanine spectrum changed

over time (4 to 16 days post-irradiation). Water diffusion, due to air moisture, was thought to be largely responsible for the changes occurring, therefore Dolo and Feaugas [49] suggested the use of a hydrophobic binder to protect alanine from environmental water and reduce its angular response.

A typical commercial alanine pellet contains approximately 4 to 15 % binder (Gamma-Service: 4 %, Harwell: 9 %, NPL: 9 %, FWT: 4 % and AWMesstechnik: 15 %), which offers little protection of the alanine from environmental water during the irradiation and read-out processes. However, commercial pellets use small grain sizes and high compacting, which does help to reduce water diffusion occurring [110]. Therefore, this chapter examines the use of a binder; paraffin wax, as the bulk constituent within the pellet (approximately 90 %) with alanine dispersed within (approximately 10 %). The paraffin wax should act to protect the alanine from environmental water and diffusion, thus helping to maintain chemical cohesion i.e. radical stability and limit relaxation effects within the cavity post-irradiation.

If successful this method will resolve the issue of angular response and help to reduce measurement uncertainty. However, if the angular variation is still observed, then this might well be more indicative of the inherent instability of the three alanine radicals formed. The angular response of the pellets was measured at 3 and 30 days post-irradiation at various angles within the EPR cavity. The protection offered by the wax was assessed and compared with the following samples:

i. Commercial alanine pellets (Synergyhealth containing 4 % binder),
ii. Alanine powder (fine grain) contained within gelatine capsules,
iii. IRGANOX®1076 powder (approximately 10 %) dispersed within paraffin wax (approximately 90 %).

IRGANOX®1076 is a novel dosimeter (**Figure 3-1**), and was chosen for examination in this work as it is both hydrophobic, forms only a single stable radical species when present as a solute in wax (IWSS) and exposed to ionising radiation. The EPR singlet formed is both easy to quantify and stable (**Figure 3-3**). The angular response of IRGANOX®1076 is of interest as a comparative means to evaluate alanine's response, and may highlight some of the issues inherent within alanine; mainly that it is hygroscopic and forms three radical species.

4.2 Methods

4.2.1 Preparation of alanine powder in capsules

L-Alanine (≥ 98 %) purchased from Sigma Aldrich was ground into a fine powder using a mortar and pestle, 60 mg of the powder was added to a cylindrical gelatine capsule (size 5, 1.0 x 0.5 cm), as commonly used for pharmaceutical purposes (**Figure 4-1**). The capsules were stored in vacuum sealed containers with silica beads to remove air moisture (humidity ≤ 40 % and temperature ≤ 25°C).

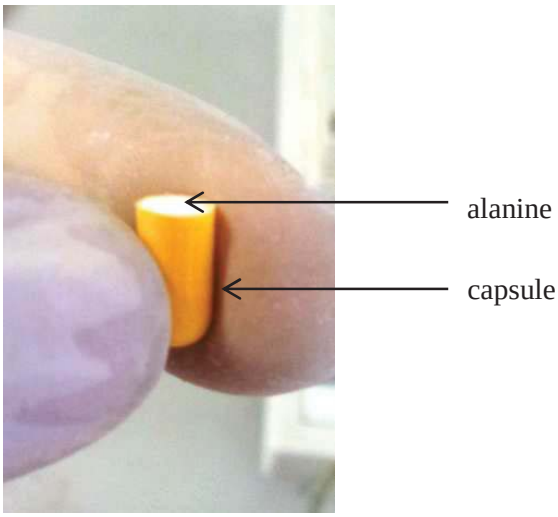

Figure 4-1. Alanine (60 mg) was added to a capsule (showing the lower half) prior to irradiation.

4.2.2 Preparation of alanine-wax pellets and IWSS pellets

The preparation of alanine-wax pellets is described in **Section 2.2.4**, and the IWSS pellets in **Section 3.2.1**.

4.2.3 Irradiation of samples

All irradiations were completed at the William Buckland Radiotherapy Centre, Alfred Hospital, Melbourne, Australia, using a Novalis Classic LINAC with 6 MV X-rays, with the standards and uncertainties described previously in **Section 2.2.8**. All samples were placed on top of 15 cm solid-water as the back-scatter medium, with a 5 cm solid water build-up, field size of 10 x10 cm^2 and source surface distance (SSD) of 95 cm and received a nominal dose of 30 Gy.

4.2.3.1 Synergyhealth alanine pellet irradiation setup

Five pellets were placed within a Perspex sheet (3 mm thickness) containing nine fabricated cavities of the same dimensions, such that there were no air gaps between the pellets (**Figure 4-2**). The remaining four cavities were filled with 'dummy' pellets, which were marked for easy identification and to prevent any air gaps being present during irradiation (**Figure 4-3**).

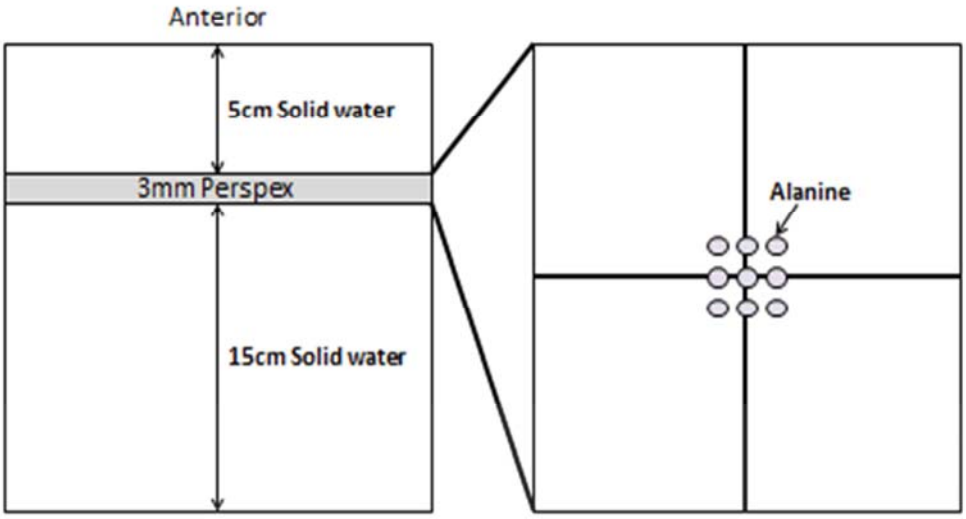

Figure 4-2. The irradiation setup used for Synergyhealth alanine pellets, showing the customized Perspex sheet and position of the alanine pellets within.

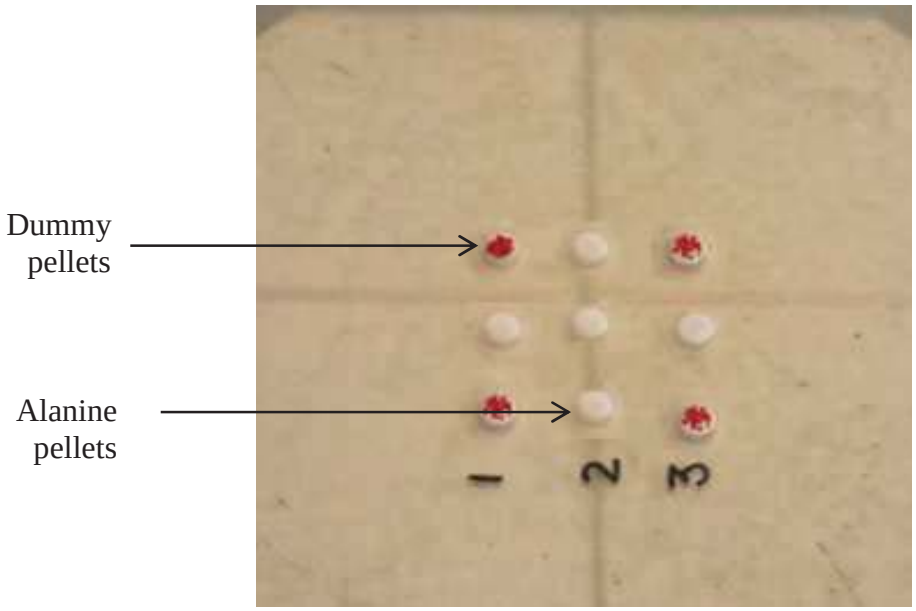

Figure 4-3. The placement of alanine pellets within a customized Perspex sheet, showing the marked 'dummy' pellets (coloured red) used to prevent air gaps being present during irradiation.

4.2.3.2 Capsule and wax pellet irradiation setup

Five samples each of alanine in wax pellets, alanine in capsules and IWSS pellets were placed within a silica holder with cut-out cavities of the same dimensions, such that there were no air gaps between the sample and mould. The wax pellet surface with the alanine or IRGANOX® 1076 was placed upwards for irradiation (**Figure 3.5**), and the remaining cavities were filled with 'dummy' pellets, which were marked for easy identification (**Figure 4-4**).

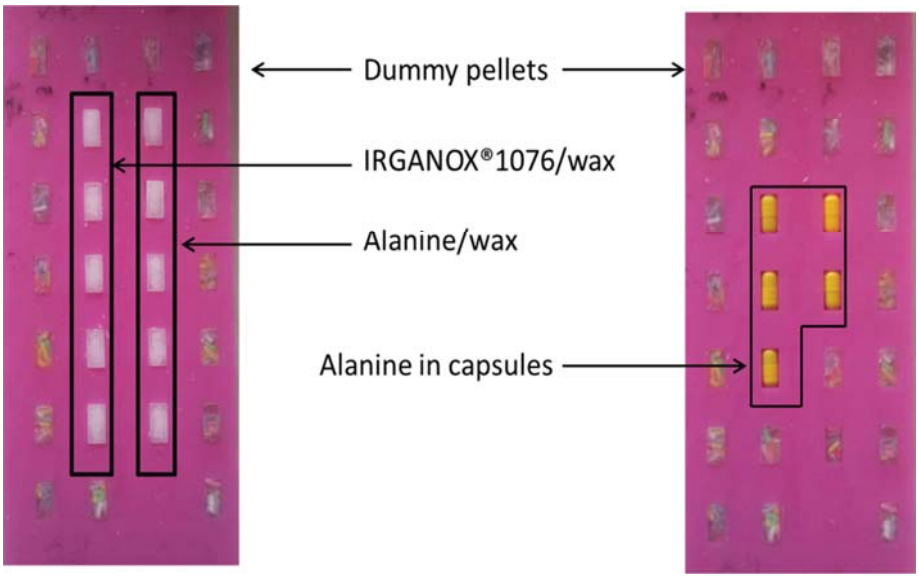

Figure 4-4. The setup for irradiation of alanine and IWSS pellets and capsules containing alanine powder (60 mg).

After irradiation all samples were stored in the same conditions as described earlier (commercial alanine pellets and alanine powders in capsules in controlled conditions, alanine-wax pellets and IWSS pellets at room temperature without humidity control) for approximately 72 hours before EPR analysis.

4.2.4 EPR conditions to determine angular response

The EPR spectra of the irradiated samples were obtained using the conditions described in **Section 2.2.7**. All wax pellet samples were placed vertically in a quartz tube (open ended, internal diameter; 7 mm), whilst the commercial alanine pellets were placed flat in the quartz tube. The capsules containing alanine powder were placed vertically in an EPR cold-finger liquid nitrogen quartz dewar flask, (Wilmad, 50 mL reservoir, internal diameter; 5.4 mm, outer diameter; 10 mm) to prevent capsule movement (**Figure 4-5**). A goniometer was used to determine the angle of measurement and the sample manually rotated to the new position.

Spectrometer settings were: number of scans, 5; centre field, 3400 G; microwave power, 2 mW; sweep time, 21.05 s; sweep width 200 G; modulation amplitude, 4.0 G; time constant, 82 ms; modulation frequency, 100 kHz; receiver gain, 75 dB.

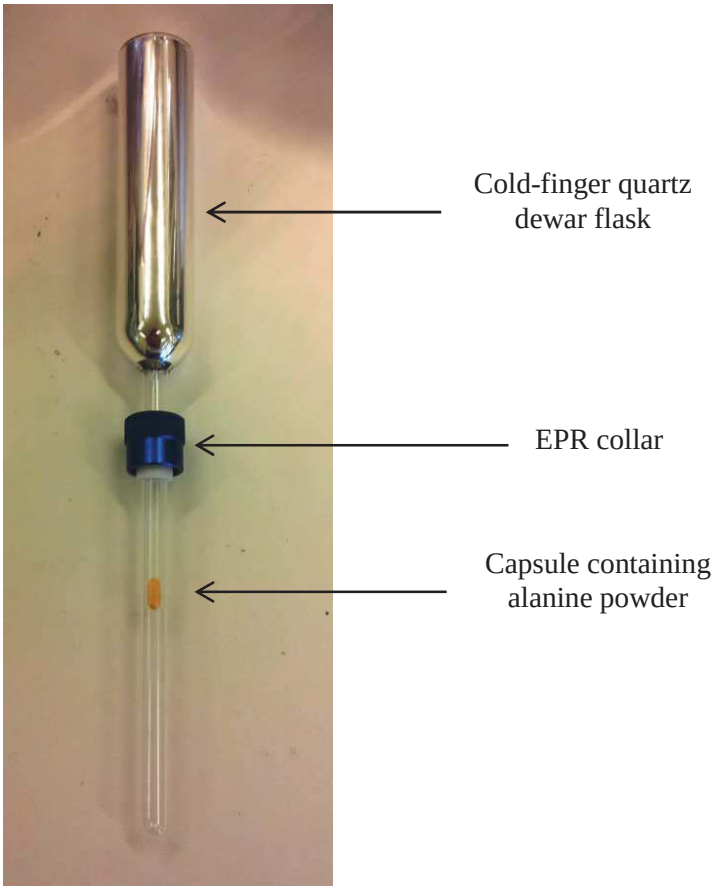

Figure 4-5. The cold-finger liquid nitrogen Dewar flask with the gelatine capsule containing alanine powder in position.

4.2.5 EPR stability and measurements

To maintain the simplicity of this study no post processing (manipulation of the spectra) of the EPR signal was performed. The angular variation was determined by measuring the amplitude of the central alanine peak (**Figure 1-16**) or single

IRGANOX®1076 peak (**Figure 3-3**) at 0° (position was chosen at random) (**Figure 4-6**).

Each pellet or capsule was rotated in 45° increments within the cavity, which gave eight measurements per sample (45°, 90°, 135°, 180°, 225°, 270°, 315° and 360°), so that the first angle (0°) was remeasured after one full rotation (360°) (**Figure 4-6**). The difference between the two values (0° and 360°) was used to determine the spectrometer drift as ≤ 0.90 % over the course of the measurement process, meaning that peak amplitude changes above 0.90 % are due to angular response only.

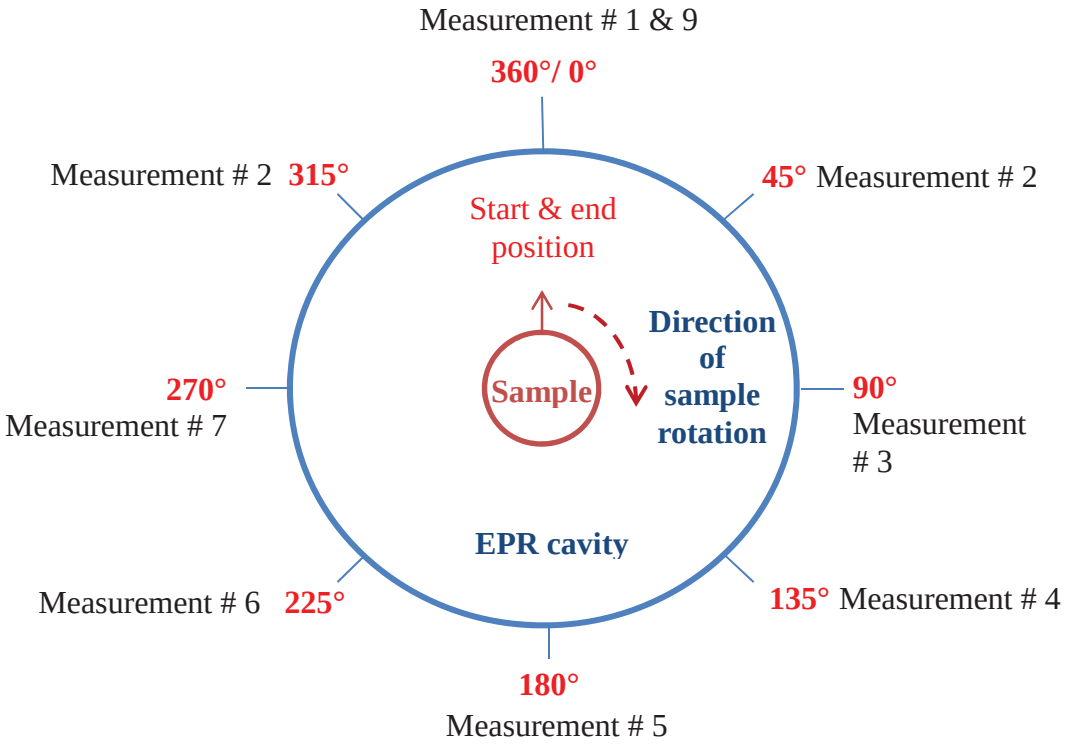

Figure 4-6. The position of the sample angles measured for each sample as it was rotated within the EPR cavity.

Measurements were completed at 3 and 30 days post-irradiation, which allowed for a long-term assessment of the wax pellet samples stability to be made. The resultant EPR peak height at 0° was normalized so that deviations at other angles (due to angular

response) were evident and comparable between the different sample types investigated. Within this work a deviation range is reported for a sample set containing five pellets or capsules, and represents the minimum and maximum deviation values obtained. Overall, four sample sets were examined; alanine in wax, IWSS pellets, commercially available alanine pellets (Synergyhealth) and gelatine capsules containing alanine powder.

4.2.6 Irradiation standards and uncertainty

The standards and uncertainties for the MV X-ray beam used in this investigation have been described previously in **Section 2.2.8**. The errors associated with the data presented in this paper represent the average of at least five samples measured.

4.3 Results

The angular response for all five sample types investigated; measured at 3 and 30 days post-irradiation with a nominal dose of 30 Gy (6MV X-rays) are shown in **Table 4-1** and **Figures 4-7** to **4-11**.

Table 4-1. The maximal deviation ranges determined for all samples investigated at 3 and 30 days post-irradiation.

Components	Form	Dosimeter (mg)	% dosimeter in pellet	Deviation range (3 days post) %	Deviation range (30 days post)
Alanine-wax	pellet	30	~10 %	1.14-2.06	1.56-1.93
IWSS	pellet	30	~10 %	0.99-1.50	0.82-1.58
Alanine: Synergy health	Commercial pellet	~55	~96 %	0.95-1.91	2.04-3.18
Alanine powder	capsule	60	N/A	3.55-4.37	3.23-5.43

4.3.1 The EPR angular response for alanine powder in capsules at 3 and 30 days post irradiation

Measurements of the alanine central peak's amplitude were collected at 45° increments within the EPR cavity, for 3 and 30 days post-irradiation. For each sample the measurement at 0° was selected as the normal, and assigned the value; 1.00, and used to normalise all raw measurements determined at other angles (**Tables 4-2** and **4-4**). Therefore, the angular response is the deviation from the normalised value (at 0°) for each angle investigated within the EPR cavity and was used to plot **Figure 4-7**, which shows the variation in response for alanine powder (Sigma Aldrich) in gelatine capsules at 3 and 30 days post-irradiation as it is rotated. The maximal deviation for all five samples at 3 days post-irradiation ranged between 3.55 to 4.37 % (samples 2 and 4, **Table 4-2**) and was similar at 30 days post-irradiation; 3.23 to 5.43 % (samples 3 and 5, **Table 4-3**).

Spectrometer drift was monitored by comparison of the EPR signal amplitude at the starting position (0°) and after one full rotation within the EPR cavity (360°) for each sample (**Table 4-4**), with consistent values and low variation; 0.31 to 0.82 % (3 days post-irradiation) and 0.31 to 0.85 % (30 days post-irradiation) obtained.

Table 4-2. The measured EPR signal amplitude and normalised values for five samples (1 to 5) at different angles within the EPR cavity, (note 0° and 360° are the same position within the cavity). The maximal deviation range is 3.55 (sample 2) to 4.37 % (sample 4).

	Sigma Aldrich alanine powder samples (3 days post)									
Angle	**1**	**1 norm**	**2**	**2 norm**	**3**	**3 norm**	**4**	**4 norm**	**5**	**5 norm**
0°	9.82	1.00	8.91	1.00	8.29	1.00	9.70	1.00	9.29	1.00
45°	10.00	1.02	9.29	1.04	8.63	1.04	9.53	0.98	8.63	0.93
90°	10.20	1.04	8.36	0.94	9.12	1.10	10.61	1.09	8.88	0.96
135°	9.70	0.99	8.87	1.00	8.51	1.03	10.43	1.08	9.03	0.97
180°	9.67	0.98	8.75	0.98	8.40	1.01	9.64	0.99	9.33	1.00
225°	10.65	1.08	8.97	1.01	9.17	1.11	9.67	1.00	9.55	1.03
270°	9.97	1.02	8.38	0.94	8.75	1.06	10.30	1.06	9.02	0.97
315°	9.18	0.93	8.63	0.97	9.05	1.09	10.40	1.07	9.85	1.06
360° (check)	9.75	0.99	8.86	0.99	8.28	1.00	9.78	1.01	9.26	1.00
($\bar{x}$)	9.90	1.01	8.77	0.98	8.74	1.05	10.04	1.03	9.20	0.99
σ	0.43	0.04	0.31	0.03	0.34	0.04	0.44	0.05	0.39	0.04
Max. dev. %	**4.34**	**4.34**	**3.55**	**3.55**	**3.89**	**3.89**	**4.37**	**4.37**	**4.23**	**4.22**

Table 4-3. The measured EPR signal amplitude and normalised values for five samples (1 to 5) at different angles within the EPR cavity. The maximal deviation range is 3.23 (sample 3) to 5.43 % (sample 5).

	Sigma Aldrich alanine powder samples (30 days post)									
Angle	**1**	**1 norm**	**2**	**2 norm**	**3**	**3 norm**	**4**	**4 norm**	**5**	**5 norm**
0°	9.57	1.00	8.95	1.00	9.45	1.00	9.40	1.00	9.16	1.00
45°	10.15	1.06	9.09	1.02	9.18	0.97	8.86	0.94	9.69	1.06
90°	9.47	0.99	9.26	1.03	9.40	0.99	8.80	0.94	10.46	1.14
135°	8.94	0.93	8.66	0.97	9.89	1.05	9.66	1.03	9.72	1.06
180°	8.96	0.94	9.36	1.05	9.08	0.96	9.57	1.02	8.84	0.97
225°	9.82	1.03	9.21	1.03	9.95	1.05	9.00	0.96	9.09	0.99
270°	9.36	0.98	9.71	1.08	9.62	1.02	8.77	0.93	9.69	1.06
315°	9.08	0.95	8.62	0.96	9.54	1.01	9.63	1.02	9.91	1.08
360° (check)	9.54	1.00	9.02	1.01	9.37	0.99	9.48	1.01	9.21	1.01
$(\bar{x})$	9.42	0.98	9.11	1.02	9.51	1.01	9.21	0.98	9.57	1.04
σ	0.43	0.04	0.36	0.04	0.31	0.03	0.39	0.04	0.52	0.06
Max. dev. %	**4.54**	**4.54**	**3.99**	**3.99**	**3.23**	**3.23**	**4.25**	**4.25**	**5.43**	**5.43**

Table 4-4. The drift in the EPR signal at 3 and 30 days post after measurement of all angles (0°/ 360° is the same point within the cavity) for L-alanine powder in capsules.

	3 Days				30 Days			
Pellet #	**0°**	**360°**	**Difference (%)**	**Drift (%)**	**0°**	**360°**	**Difference (%)**	**Drift (%)**
1	9.82	9.75	99.31	0.69	9.57	9.54	99.69	0.31
2	8.91	8.86	99.42	0.58	8.95	9.02	100.78	-0.78
3	8.29	8.28	99.88	0.12	9.45	9.37	99.15	0.85
4	9.70	9.78	100.82	-0.82	9.40	9.48	100.85	-0.85
5	9.29	9.26	99.64	0.36	9.16	9.21	100.55	-0.55

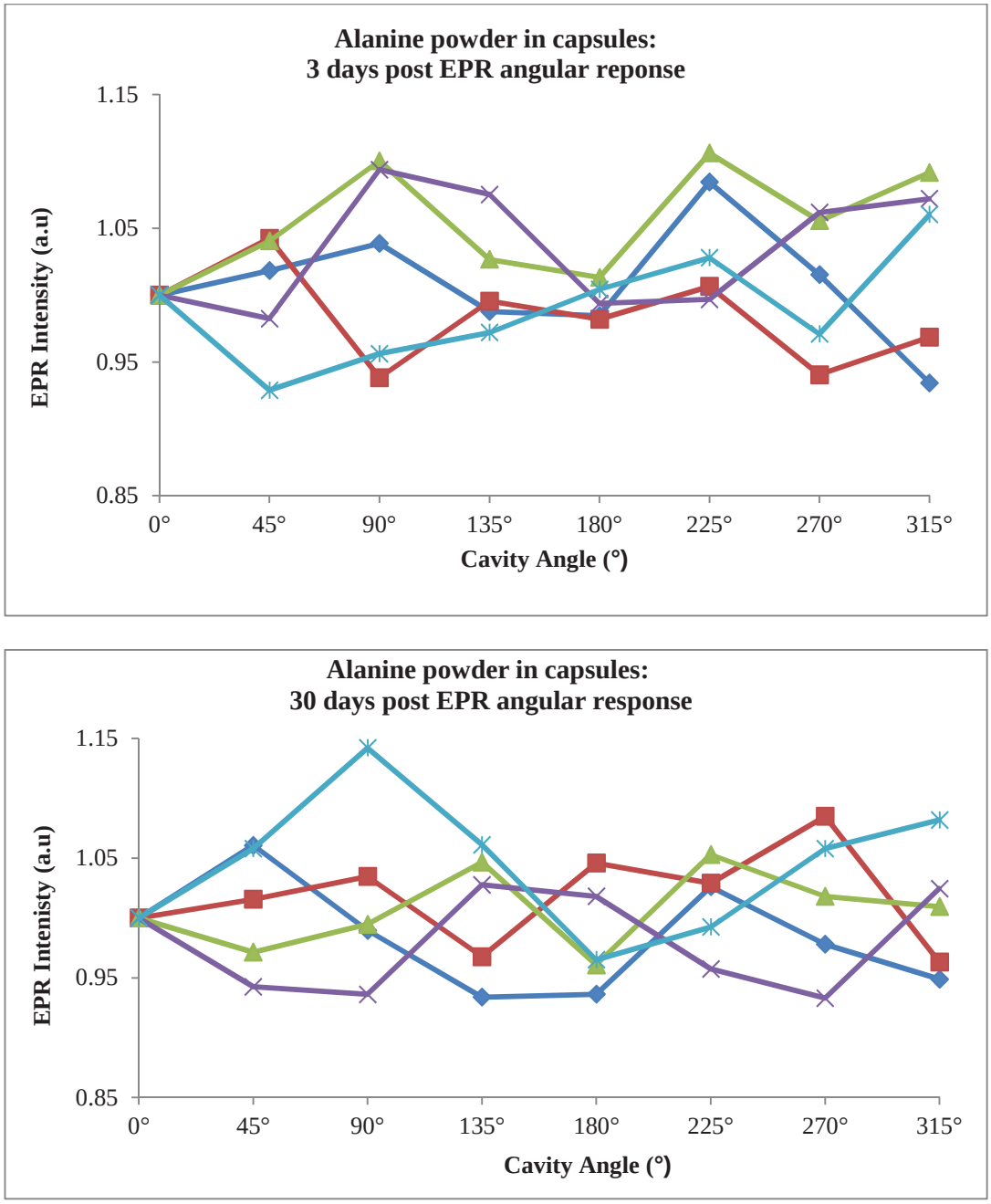

Figure 4-7. The large variation of the EPR signal produced for Sigma Aldrich alanine powder within capsules when rotated within the EPR cavity at 3 days (upper) and 30 days (lower) post-irradiation.

4.3.2 The EPR angular response for commercial alanine pellets (Synergyhealth) at 3 and 30 days post irradiation

The angular response for the Synergyhealth commercially produced alanine pellets at 3 and 30 days post-irradiation was determined for one full roation of the EPR

cavity. Raw measurements were collected at 45° increments and normalized (**Tables 4-5** and **4-6**) and plotted in **Figure 4-8**. The maximal deviation for all five samples, ranged between 0.95 to 1.91 % at 3 days post-irradiation (samples 4 and 5, **Table 4-5**), and increased to 2.04 to 3.18 % at 30 days post-irradiation (samples 1 and 4, **Table 4-6**). Spectrometer drift was low for both sets of measurements; 0.26 to 0.57 % (3 days post-irradiation) and 0.09 to 0.89 % (30 days post-irradiation) (**Table 4-7**).

Table 4-5. The measured and normalised EPR signal amplitude for five Synergyhealth alanine pellets (1 to 5) at different angles within the EPR cavity, (note 0° and 360° are the same position within the cavity). The maximal deviation range is 0.95 (sample 4) to 1.91 % (sample 5).

	Synergyhealth alanine pellets (3 days post)									
Angle	**1**	**1 norm**	**2**	**2 norm**	**3**	**3 norm**	**4**	**4 norm**	**5**	**5 norm**
0°	19.74	1.00	19.16	1.00	19.07	1.00	20.07	1.00	19.51	1.00
45°	19.28	0.98	19.18	1.00	19.28	1.01	19.56	0.97	19.67	1.01
90°	19.33	0.98	18.96	0.99	19.31	1.01	19.95	0.99	19.77	1.01
135°	19.81	1.00	19.33	1.01	18.76	0.98	19.65	0.98	19.71	1.01
180°	19.73	1.00	19.44	1.01	18.36	0.96	19.94	0.99	19.75	1.01
225°	19.58	0.99	19.44	1.01	18.65	0.98	19.67	0.98	19.90	1.02
270°	19.74	1.00	18.92	0.99	19.00	1.00	19.92	0.99	19.40	0.99
315°	19.61	0.99	19.21	1.00	19.16	1.00	19.65	0.98	18.71	0.96
360° (check)	19.68	1.00	19.27	1.01	19.15	1.00	19.99	1.00	19.46	1.00
($\bar{x}$)	19.60	**0.99**	19.21	**1.00**	18.95	**0.99**	19.80	**0.99**	19.55	**1.00**
σ	0.20	**0.01**	0.20	**0.01**	0.33	**0.02**	0.19	**0.01**	0.37	**0.02**
Max. dev. %	**1.01**	**1.01**	**1.02**	**1.02**	**1.75**	**1.75**	**0.95**	**0.95**	**1.91**	**1.91**

Table 4-6. The measured and normalised EPR signal amplitude for five Synergyhealth alanine pellets (1 to 5) at different angles within the EPR cavity. The maximal deviation range is 2.04 (sample 1) to 3.18 % (sample 4).

	Synergyhealth alanine pellets (30 days post)									
Angle	**1**	**1 norm**	**2**	**2 norm**	**3**	**3 norm**	**4**	**4 norm**	**5**	**5 norm**
0°	22.98	1.00	22.35	1.00	23.20	1.00	23.00	1.00	23.65	1.00
45°	22.74	0.99	21.97	0.98	23.03	0.99	22.90	1.00	23.62	1.00
90°	23.13	1.01	22.74	1.02	22.58	0.97	22.30	0.97	23.16	0.98
135°	23.64	1.03	22.40	1.00	22.01	0.95	22.37	0.97	23.71	1.00
180°	22.95	1.00	22.35	1.00	21.74	0.94	22.23	0.97	23.21	0.98
225°	22.43	0.98	21.10	0.94	22.96	0.99	21.63	0.94	22.15	0.94
270°	22.11	0.96	21.22	0.95	23.06	0.99	20.80	0.90	22.76	0.96
315°	23.13	1.01	22.83	1.02	23.05	0.99	22.02	0.96	22.53	0.95
360° (check)	22.82	0.99	22.15	0.99	23.22	1.00	23.11	1.00	23.44	0.99
$(\bar{x})$	22.89	**1.00**	22.12	**0.99**	22.70	**0.98**	22.16	**0.96**	23.10	**0.98**
σ	0.47	**0.02**	0.65	**0.03**	0.55	**0.02**	0.70	**0.03**	0.57	**0.02**
Max. dev. %	**2.04**	**2.04**	**2.93**	**2.93**	**2.41**	**2.41**	**3.18**	**3.18**	**2.48**	**2.48**

Table 4-7. The drift in the EPR signal at 3 and 30 days post after measurement of all angles (0°/ 360° is the same point within the cavity) for Synergyhealth alanine pellets.

	3 days				30 days			
Pellet #	**0°**	**360°**	**Difference (%)**	**Drift (%)**	**0°**	**360°**	**Difference (%)**	**Drift (%)**
1	19.74	19.68	99.70	0.30	22.98	22.82	99.30	0.70
2	19.16	19.27	100.57	-0.57	22.35	22.15	99.11	0.89
3	19.07	19.15	100.42	-0.42	23.2	23.22	100.09	-0.09
4	20.07	19.99	99.60	0.40	23	23.11	100.48	-0.48
5	19.51	19.46	99.74	0.26	23.65	23.44	99.11	0.89

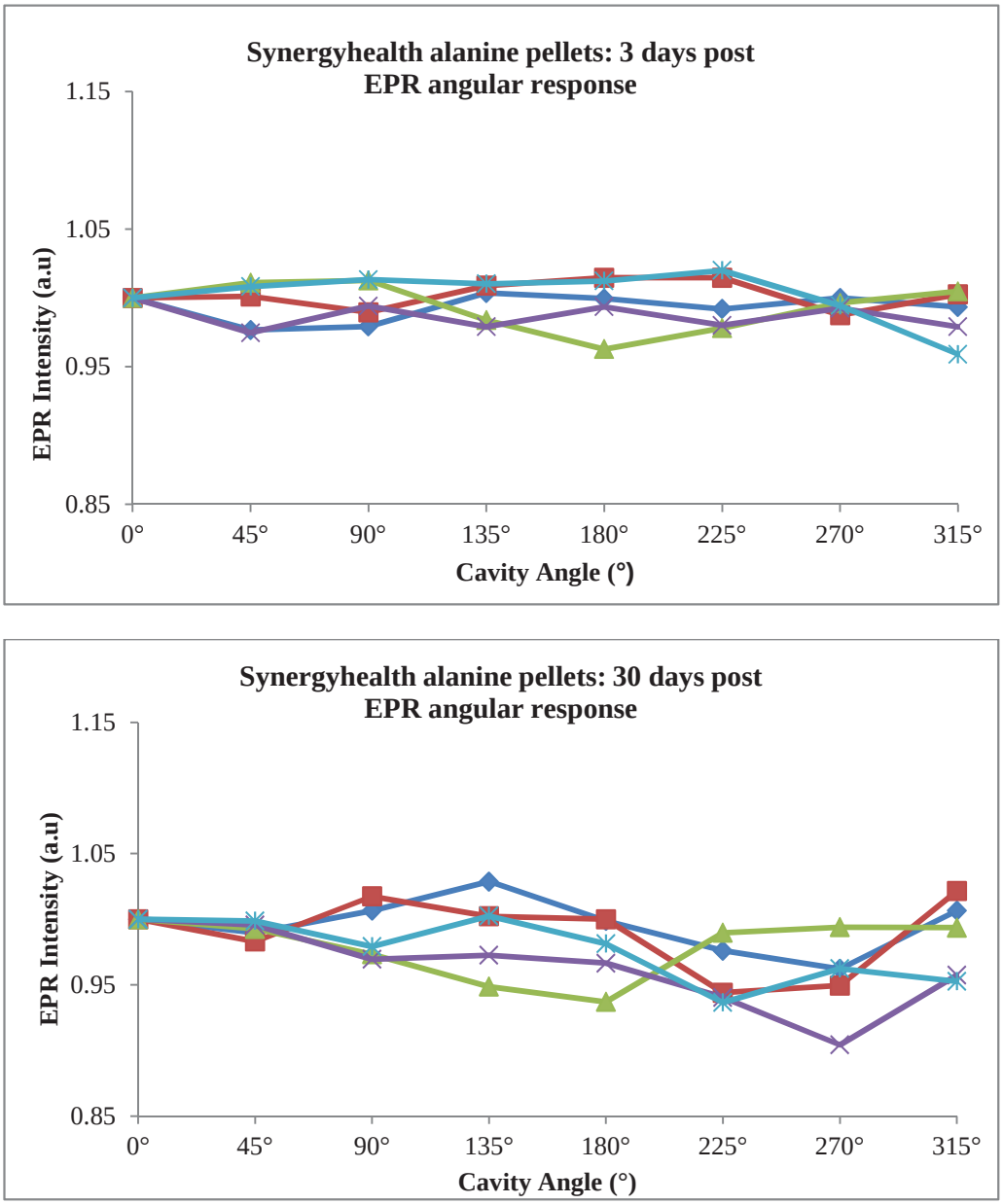

Figure 4-8. The angular variation for commercial alanine pellets manufactured by Synergyhealth as rotated within the EPR cavity at 3 days (upper) and 30 days (lower) post-irradiation.

4.3.3 The EPR angular response for alanine-wax pellets at 3 and 30 days post irradiation

The angular response for samples of alanine powder dispersed in wax when rotated in 45° increments within the EPR cavity was determined at 3 and 30 days post-

irradiation. The maximal deviation for each angle was determined (**Tables 4-8** and **4-9**) and plotted in **Figure 4-9** to show the deviation from the normal (1.00), which ranged between 1.14 to 2.06 % (samples 4 and 3, **Table 4-8**) at 3 days post-irradiation, and remained stable at 30 days post-irradiation; 1.56 to 1.93 % (samples 4 and 3, **Table 4-9**). Spectrometer drift was low and gave consistent results for both sets of measurements; 0.00 to 0.75 % (3 days post-irradiation) and 0.20 to 0.90 % (30 days post-irradiation) (**Table 4-10**).

Table 4-8. The measured and normalised EPR signal amplitude for five alanine- wax pellets (1 to 5) at different angles within the EPR cavity, (note 0° and 360° are the same position within the cavity). The maximal deviation range is 1.14 (sample 4) to 2.06 % (sample 3).

	Alanine-wax pellets (3 days post)									
Angle	**1**	**1 norm**	**2**	**2 norm**	**3**	**3 norm**	**4**	**4 norm**	**5**	**5 norm**
0°	10.50	1.00	10.50	1.00	11.00	1.00	10.70	1.00	10.66	1.00
45°	10.50	1.00	10.70	1.02	10.70	0.97	11.00	1.03	10.70	1.00
90°	10.15	0.97	10.50	1.00	10.34	0.94	10.90	1.02	10.56	0.99
135°	10.57	1.01	10.60	1.01	10.60	0.96	11.10	1.04	10.50	0.98
180°	10.20	0.97	10.50	1.00	10.80	0.98	10.90	1.02	10.55	0.99
225°	10.22	0.97	10.80	1.03	10.45	0.95	10.80	1.01	10.88	1.02
270°	10.20	0.97	10.80	1.03	10.41	0.95	11.00	1.03	10.98	1.03
315°	10.62	1.01	10.86	1.03	10.65	0.97	10.90	1.02	10.76	1.01
360° (check)	10.55	1.00	10.55	1.00	11.00	1.00	10.62	0.99	10.71	1.00
($\bar{x}$)	10.37	0.99	10.66	1.02	10.62	0.97	10.91	1.02	10.70	1.00
σ	0.19	0.02	0.15	0.01	0.22	0.02	0.12	0.01	0.17	0.02
Max. dev. %	**1.87**	**1.87**	**1.42**	**1.42**	**2.06**	**2.06**	**1.14**	**1.14**	**1.57**	**1.57**

Table 4-9. The measured and normalised EPR signal amplitude for five alanine-wax pellets (1 to 5) at different angles within the EPR cavity. The maximal deviation range is 1.56 (sample 4) to 1.93 % (sample 3).

Alanine-wax pellets (30 days post)										
Angle	**1**	**1 norm**	**2**	**2 norm**	**3**	**3 norm**	**4**	**4 norm**	**5**	**5 norm**
0°	9.40	1.00	9.78	1.00	10.00	1.00	9.67	1	9.54	1
45°	9.53	1.01	9.49	0.97	9.89	0.99	9.57	0.99	9.66	1.01
90°	9.65	1.03	9.35	0.96	9.57	0.96	9.64	1.00	9.81	1.03
135°	9.83	1.05	9.72	0.99	9.94	0.99	10.00	1.03	9.95	1.04
180°	9.67	1.03	9.81	1.00	10.02	1.00	9.71	1.00	10.00	1.05
225°	9.82	1.04	9.67	0.99	9.55	0.96	9.66	1.00	9.84	1.03
270°	9.80	1.04	9.50	0.97	9.66	0.97	9.65	1.00	9.69	1.02
315°	9.59	1.02	9.53	0.97	9.78	0.98	9.93	1.03	9.61	1.01
360° (check)	9.44	1.00	9.80	1.00	9.91	0.99	9.62	0.99	9.52	1.00
$(\bar{x})$	9.66	1.03	9.61	0.98	9.80	0.98	9.73	1.01	9.76	1.02
σ	0.15	0.02	0.16	0.02	0.19	0.02	0.15	0.02	0.16	0.02
Max. dev. %	**1.58**	**1.58**	**1.69**	**1.69**	**1.93**	**1.93**	**1.56**	**1.56**	**1.68**	**1.68**

Table 4-10. The drift in the EPR signal at 3 and 30 days post after measurement of all angles (0°/ 360° is the same point within the cavity) for alanine-wax pellets.

	3 days				**30 days**			
Pellet #	**0°**	**360°**	**Difference (%)**	**Drift (%)**	**0°**	**360°**	**Difference (%)**	**Drift (%)**
1	10.50	10.55	100.48	-0.48	9.40	9.44	100.46	-0.46
2	10.50	10.55	100.48	-0.48	9.78	9.80	100.20	-0.20
3	11.00	11.00	100.00	0.00	10.00	9.91	99.10	0.90
4	10.70	10.62	99.25	0.75	9.67	9.62	99.48	0.52
5	10.66	10.71	100.47	-0.47	9.54	9.52	99.79	0.21

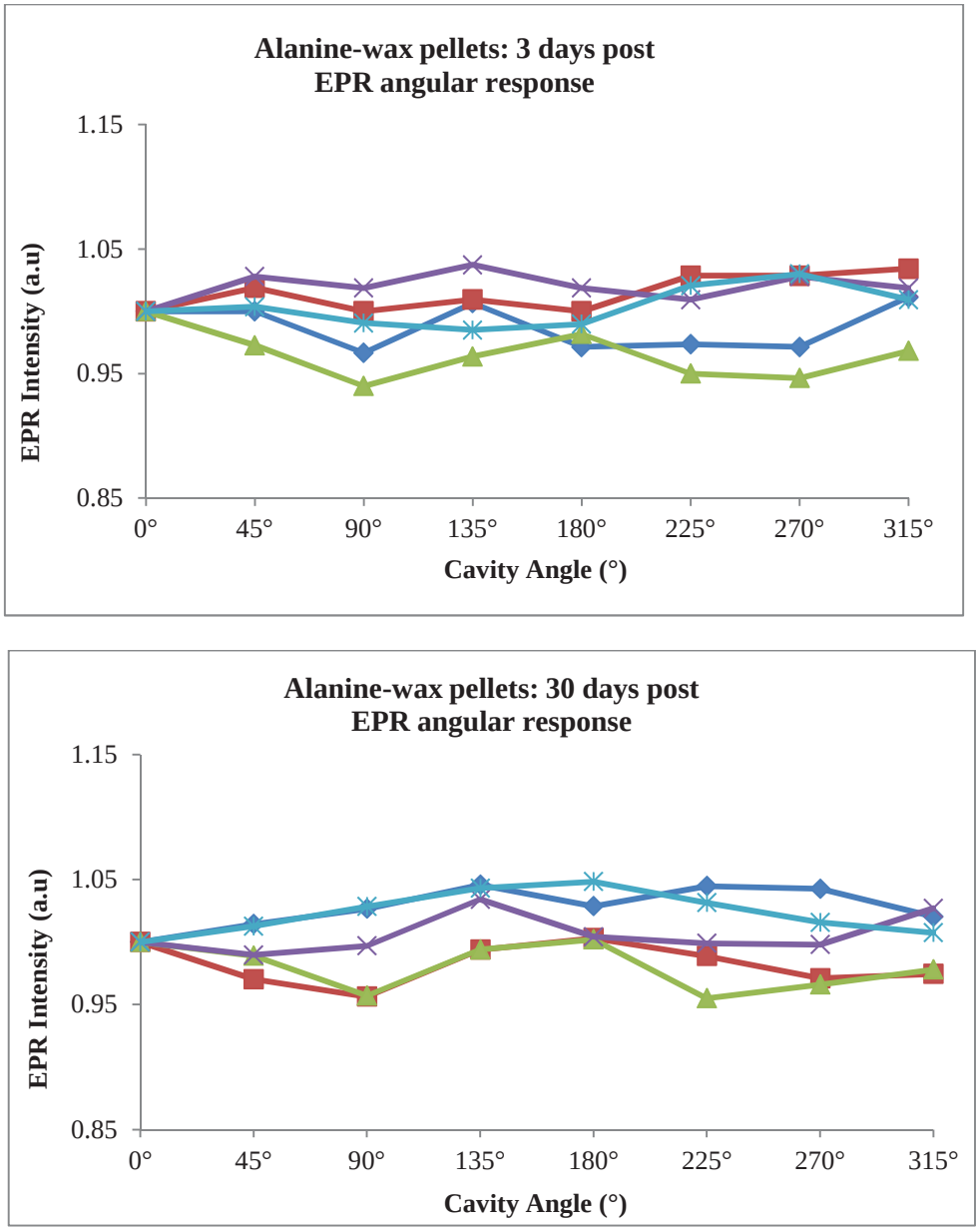

Figure 4-9. The EPR amplitude changes for samples containing alanine encased in wax when rotated within the EPR cavity at 3 days (upper) and 30 days (lower) post-irradiation.

4.3.4 The EPR angular response for alanine-wax pellets at 3 days post irradiation manufactured > 8 months prior to irradiation

The angular response for alanine powder dispersed in wax was determined for pellets made more than eight months prior to irradiation, and not stored under

controlled conditions (temperature and humidity was not monitored). Raw measurements were collected at 45° increments within the EPR cavity, and normalized (**Table 4-11**). The angular response for all angles investigated at 3 days post-irradiation is shown in **Figure 4-10**. The maximal deviation for each angle was determined and plotted to show the deviation from the normal (1.00), which ranged between 5.60 to 8.60 % at 3 days post-irradiation.

Table 4-11. The measured and normalised EPR signal amplitude for five alanine-wax pellets (1 to 5) at different angles within the EPR cavity, (note 0° and 360° are the same position within the cavity). The maximal deviation range is 5.60 (sample 1) to 8.60 % (sample 5).

	Alanine-wax pellets (> 8 months)									
Angle	**1**	**1 norm**	**2**	**2 norm**	**3**	**3 norm**	**4**	**4 norm**	**5**	**5 norm**
0°	10.92	1.00	8.77	1.00	9.98	1.00	11.60	1.00	11.10	1.00
45°	9.54	0.87	9.29	1.06	10.30	1.03	11.40	0.98	10.40	0.94
90°	10.40	0.95	9.85	1.12	8.61	0.86	9.60	0.83	8.97	0.81
135°	11.20	1.03	8.55	0.97	8.84	0.89	10.40	0.90	11.10	1.00
180°	11.14	1.02	8.47	0.97	9.92	0.99	11.30	0.97	11.80	1.06
225°	9.92	0.91	9.62	1.10	10.08	1.01	11.00	0.95	10.90	0.98
270°	10.69	0.98	9.35	1.07	8.93	0.89	9.64	0.83	9.63	0.87
315°	10.87	1.00	8.73	1.00	8.72	0.87	9.84	0.85	11.00	0.99
360° (check)	10.58	0.97	8.54	0.98	9.71	1.11	11.00	0.95	11.00	0.99
$(\bar{x})$	10.59	0.97	9.08	1.04	9.42	0.94	10.60	0.91	10.61	0.96
σ	0.59	0.05	0.52	0.06	0.71	0.07	0.83	0.07	0.91	0.08
Max. Dev. %	**5.60**	**5.60**	**5.70**	**5.70**	**7.50**	**7.50**	**7.84**	**7.84**	**8.60**	**8.60**

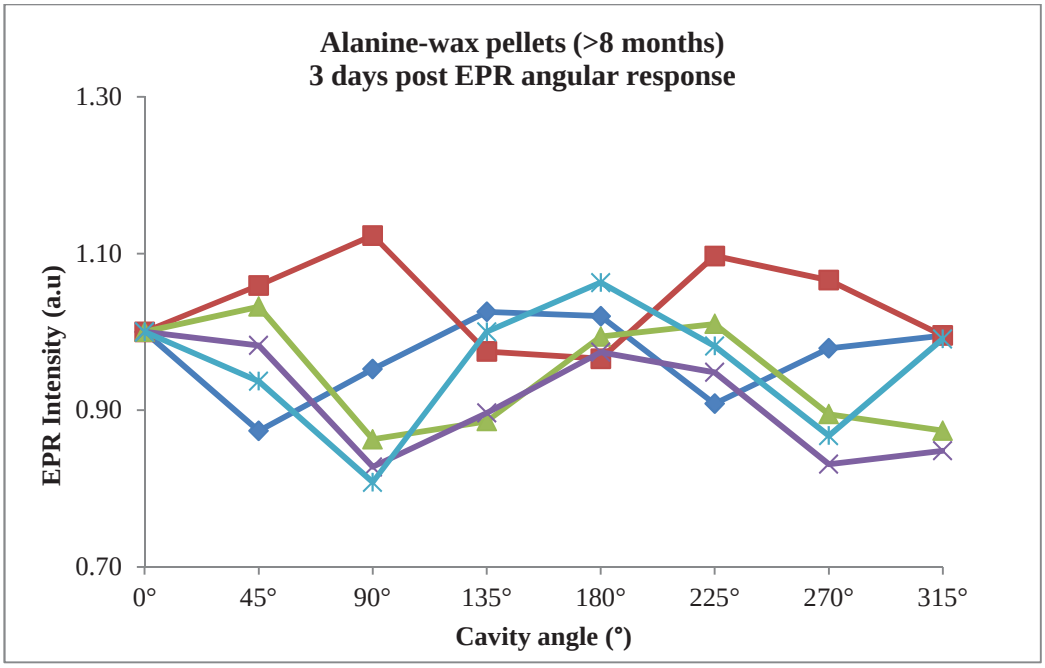

Figure 4-10. The EPR angular response for old alanine-wax pellets as rotated within the EPR cavity at 3 days post irradiation.

4.3.5 The EPR angular response for IWSS pellets at 3 and 30 days post irradiation

The angular response for IWSS pellets was determined by collecting raw measurements at 45° increments within the EPR cavity, measurements were normalized at 3 and 30 days post-irradiation (**Tables 4-12** and **4-13**) and are shown in **Figure 4-11**. The maximal deviation for each angle was determined as ranging between 0.99 to 1.50 % (samples 2 and 3, **Table 4-12**) at 3 days post-irradiation, which remained stable at 30 days post-irradiation; 0.82 to 1.58 % (samples 3 and 2, **Table 4-13**). Spectrometer drift was also low for both sets of results; 0.04 to 0.37 % (3 days post-irradiation) and 0.12 to 0.71 % (30 days post-irradiation) (**Table 4-14**).

Table 4-12. The measured and normalised EPR signal amplitude for five IWSS pellets (1 to 5) at different angles within the EPR cavity, (note 0° and 360° are the same position within the cavity). The maximal deviation range is 0.99 (sample 2) to 1.50 % (sample 3).

	IWSS pellets (3 days post)									
Angle	**1**	**1 norm**	**2**	**2 norm**	**3**	**3 norm**	**4**	**4 norm**	**5**	**5 norm**
0°	9.32	1.00	9.37	1.00	9.16	1.00	9.54	1.00	9.27	1.00
45°	9.32	1.00	9.34	1.00	9.35	1.02	9.60	1.01	9.15	0.99
90°	9.54	1.02	9.22	0.98	9.47	1.03	9.42	0.99	9.31	1.00
135°	9.64	1.03	9.14	0.98	9.55	1.04	9.37	0.98	9.42	1.02
180°	9.63	1.03	9.18	0.98	9.52	1.04	9.38	0.98	9.21	0.99
225°	9.43	1.01	9.26	0.99	9.44	1.03	9.60	1.01	9.17	0.99
270°	9.64	1.03	9.40	1.00	9.58	1.05	9.73	1.02	9.23	1.00
315°	9.48	1.02	9.29	0.99	9.32	1.02	9.48	0.99	9.07	0.98
360° (check)	9.32	1.00	9.33	1.00	9.17	1.00	9.51	1.00	9.24	1.00
$(\bar{x})$	9.50	1.02	9.27	0.99	9.42	1.03	9.51	1.00	9.23	1.00
σ	0.14	0.01	0.09	0.01	0.14	0.02	0.13	0.01	0.11	0.01
Max. dev. %	**1.43**	**1.43**	**0.99**	**0.99**	**1.50**	**1.50**	**1.33**	**1.33**	**1.16**	**1.16**

Table 4-13. The measured and normalised EPR signal amplitude for five IWSS pellets (1 to 5) at different angles within the EPR cavity. The maximal deviation range is 0.82 (sample 3) to 1.58 % (sample 2).

	IWSS pellets (30 days post)									
Angle	**1**	**1 norm**	**2**	**2 norm**	**3**	**3 norm**	**4**	**4 norm**	**5**	**5 norm**
0°	8.69	1.00	8.44	1.00	8.31	1.00	8.50	1.00	8.30	1.00
45°	8.42	0.97	8.58	1.02	8.29	1.00	8.49	1.00	8.20	0.99
90°	8.54	0.98	8.60	1.02	8.26	0.99	8.65	1.02	8.29	1.00
135°	8.76	1.01	8.62	1.02	8.21	0.99	8.61	1.01	8.37	1.01
180°	8.72	1.00	8.69	1.03	8.17	0.98	8.42	0.99	8.55	1.03
225°	8.68	1.00	8.76	1.04	8.16	0.98	8.39	0.99	8.39	1.01
270°	8.76	1.01	8.55	1.01	8.12	0.98	8.56	1.01	8.32	1.00
315°	8.77	1.01	8.33	0.99	8.19	0.99	8.41	0.99	8.52	1.03
360° (check)	8.72	1.00	8.50	1.01	8.26	0.99	8.51	1.00	8.35	1.01
$(\bar{x})$	8.67	1.00	8.57	1.02	8.21	0.99	8.50	1.00	8.37	1.01
σ	0.12	**0.01**	0.14	**0.02**	0.07	**0.01**	0.10	**0.01**	0.12	**0.01**
Max. dev. %	**1.44**	**1.44**	**1.58**	**1.58**	**0.82**	**0.82**	**1.13**	**1.13**	**1.41**	**1.41**

Table 4-14. The drift in the EPR signal (3 days post) for each IWSS pellet measured at the start (0°) and end (360°).

	3 Days				30 Days			
Pellet #	**0°**	**360°**	**Difference (%)**	**Drift (%)**	**0°**	**360°**	**Difference (%)**	**Drift (%)**
1	9.32	9.32	100.04	-0.04	8.69	8.72	100.35	-0.35
2	9.37	9.33	99.63	0.37	8.44	8.50	100.71	-0.71
3	9.16	9.17	100.20	-0.20	8.31	8.26	99.40	0.60
4	9.54	9.51	99.63	0.37	8.5	8.51	100.12	-0.12
5	9.27	9.24	99.73	0.27	8.3	8.35	100.60	-0.60

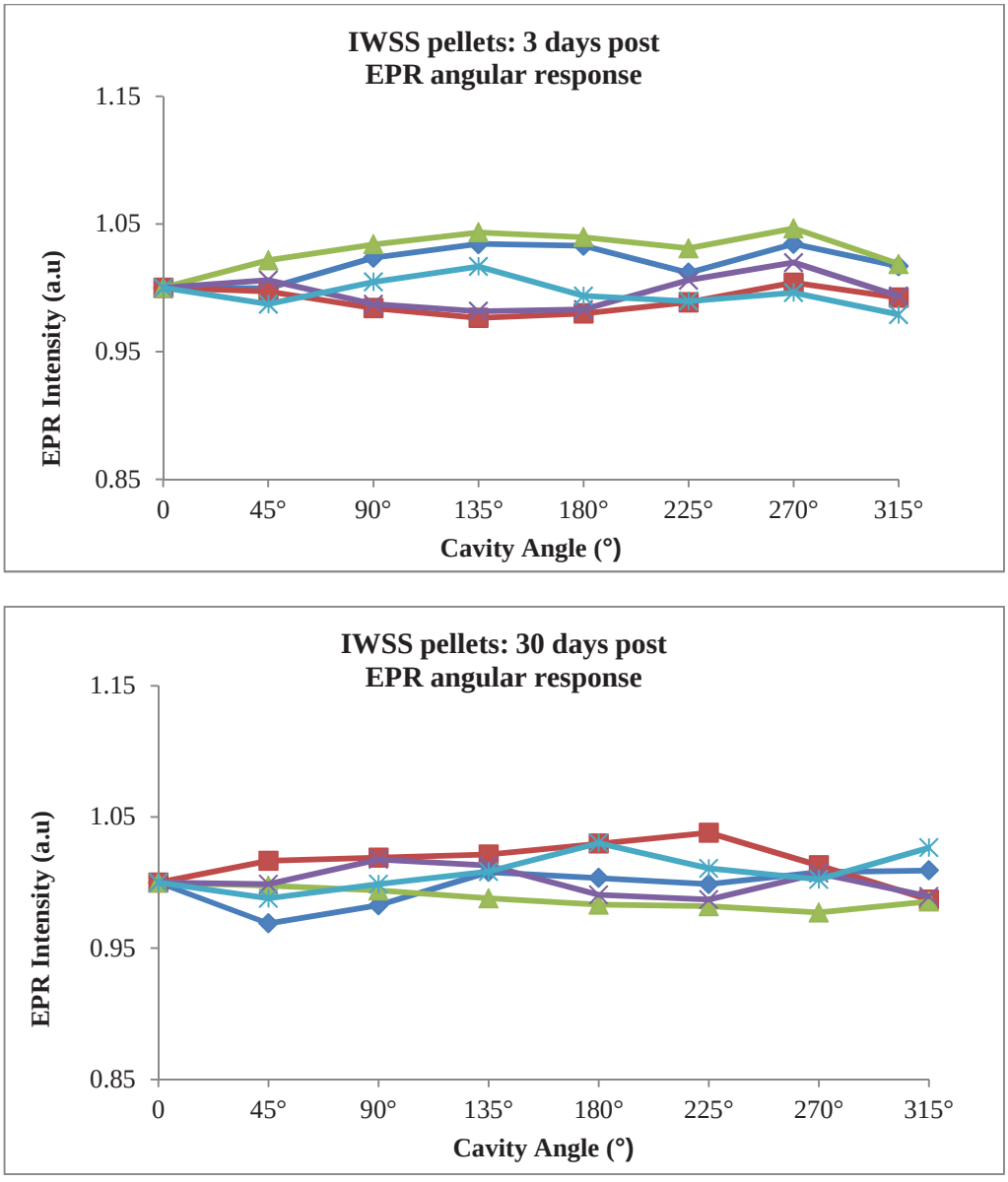

Figure 4-11. The variation in peak height for five samples of IRGANOX®1076 when rotated within the EPR cavity at 3 days (upper) and 30 days (lower) post-irradiation.

4.4 Discussion

The angular response of commercial alanine pellets and alanine powders was previously examined by Dolo et. al [49, 110, 123]. Water diffusion was identified as causing changes to alanine water content, which promoted radical transformations and resonance issues within the EPR cavity. Together, these effects altered the spectrum

profile and an angular dependence was observed [110, 123]. To minimize this effect, the average of multiple measurements at different angles within the EPR cavity is routinely used for alanine.

An alternative method was investigated, whereby alanine pellets were manufactured consisting of alanine powder present as the minor component (approximately 10 %) encased within a protective bulk material (approximately 90 %) to limit possible water diffusion. Paraffin wax was chosen as a suitable bulk material as it is hydrophobic, commonly used as a binder in commercially manufactured alanine pellets (typically ≤ 10 %), and does not affect the EPR signal produced.

To assess the protective ability of the wax pellets measurements at 3 and 30 days post-irradiation were completed, and compared to other alanine samples and the novel dosimeter IRGANOX®1076 also encased within wax. The protective ability provided by the wax was further tested post-irradiation as the samples were stored in darkened sealed containers without humidity and temperature being controlled (however it did not exceed 25 °C and 55 % RH respectively). Whilst, the commercial alanine pellets and capsules containing powder were stored in controlled conditions and monitored so that humidity was less than 40 % and temperature did not exceed 24 °C.

4.4.1 Comparison of alanine powders and commercial pellets to previous literature reports

The deviation range for alanine powder supplied by Sigma Aldrich (**Figure 4-7**) was 3.55 to 4.37 % (3 days post) and 3.23 to 5.43 % (30 days post), which is less than the 7 to 25 % ranges (at 2 weeks post-irradiation) reported by Dolo and Garcia [110] for their Merck and Fluka coarse grain samples. Grounding of the Sigma Aldrich powder prior to use may explain the reduced angular response, as low compacting of the

powder allows for easier water diffusion through the sample [111], resulting in higher angular responses. However, the deviation range is much larger than the approximately 1 % maximal deviation reported for the Merck fine grain powders [110], thus confirming the importance of smaller particle sizes. Placement of the powder within the gelatine capsules could account for the good signal stability observed after 30 days post-irradiation, as the casing would act to protect the alanine within from external water contamination.

Whilst the deviation range of the Synergyhealth pellets 0.95 to 1.91 % (at 3 days post) (**Figure 4-8**) was much less than the powder in capsule samples as expected, it was comparable (although slightly higher) with the approximately 1 % maximal deviation for the Gamma-Service and Bruker commercial alanine pellets investigated by Dolo and Garcia [110]. The pellets consist of approximately 4 % binder (wax), so low angular responses are likely to be due to small grain size and high compacting. However, as the alanine is the major component, no protection is provided by the wax binder to limit ongoing water interactions, and is evident at 30 days post-irradiation (**Figure 4-8**) as the deviation range had increased to 2.04 to 3.18 %, despite being stored in controlled conditions. This result suggests that water contamination is occurring and affecting the EPR cavities resonance and alanine's radical composition.

4.4.2 The angular response for alanine in wax pellets (3 and 30 days post-irradiation)

The angular responses for the alanine powder dispersed in wax samples are shown in **Figure 4-9**. At 3 days post-irradiation the deviation range was 1.14 to 2.06 % which is slightly higher than the Synergyhealth pellets; 0.95 to 1.91 %. Yet after 30 days the samples show good signal stability, and are relatively unchanged; 1.56 to1.93

% despite the samples not being stored in controlled conditions (for temperature and humidity), as opposed to the Synergyhealth pellets, whose deviation range nearly doubled to 2.04 to 3.18 % after 30 days post-irradiation. These results strongly suggest that the encasement of alanine within wax acts to protect it from environmental water and increases signal stability over time, thus lowering the observable angular response.

4.4.3 The effects of time and water diffusion on angular response for alanine in wax pellets

Alanine pellets manufactured more than 8 months prior to irradiation that had not been stored under controlled conditions (temperature and humidity was not monitored) were irradiated and the angular response determined at 3 days post-irradiation (**Figure 4-10**). The deviation was 5.60 to 8.60 %, which is approximately four-times higher than the alanine-wax samples irradiated just after manufacture; 1.14 to 2.06 % (**Figure 4-9**). These results show that water diffusion through the wax encasing has occurred over the time frame between manufacture and irradiation, and subsequently affected the EPR signals angular dependence.

4.4.4 The angular response for IWSS pellets (3 and 30 days post-irradiation)

A final comparison with IRGANOX®1076 powder dispersed in wax was also made (**Figure 4-11**), as IRGANOX®1076 is hydrophobic and forms only the phenoxyl radical species when solubilised in wax, it was thought that these factors and the additional protection offered by the wax surrounding to environmental water would yield a lowered angular response. The deviation range at 3 and 30 days post-irradiation was; 0.99 to 1.50 % and 0.82 to 1.58 % respectively, which was less than the alanine in

wax samples (1.14 to 2.06 % at 3 days post, 1.56 to 1.93 % at 30 days post), however, they were not statistically significant ($p > 0.05$). Further investigations and analysis are needed to indicate if the hydrophobic nature of IRGANOX®1076 and that it only forms a single radical species are advantageous in lowering the EPR angular dependence. Like the alanine in wax samples, the IWSS pellets were largely unchanged at 30 days post-irradiation, and provide further evidence that the wax when present as a bulk component acts to protect the sample within from external influences.

4.5 Conclusion

Dispersing alanine powder within wax, such that the wax is the bulk component, physically protects the alanine from external water and reduces its EPR angular response. At 3 days post-irradiation deviation ranges were low and comparable to the commercially manufactured alanine pellets (where alanine is the bulk component). However, at 30 days post-irradiation the protection provided by the wax was more clear, with the angular deviation ranges remaining largely unchanged, which was in sharp contrast to the commercial pellets, whose deviation ranges had nearly doubled, despite being stored in controlled conditions. Examination of alanine-wax pellets manufactured more than eight months prior to use showed a high angular dependence at 3 days post-irradiation, suggesting water contamination had occurred and the importance of using the samples within a reasonable time frame after manufacture or otherwise storing the samples in a controlled environment where humidity and temperature are actively monitored.

Overall, the IWSS pellets had the lowest angular responses; however this was not statistically significant. Further studies to determine if this was due to its

hydrophobic structure and that it only forms a single radical species when irradiated are needed.

Finally, pellets manufactured in this work would be useful in studies where irradiation and read-out are performed over multiple days, such as accumulative dose measurements in radiotherapy. The highly stable EPR signal obtained (at 30 days post-irradiation) and the pellets reduced sensitivity to environmental water would be of great benefit. Furthermore, the wax pellet can be moulded into any shape, allowing for highly customized patient dosimeters to be made.

Chapter 5: Investigation of the novel method ‘spiking’ to determine low doses (< 2 Gy) using alanine dosimeters

The majority of contents from this chapter has recently been accepted for publication.

5.1 Introduction

Developments in the application of radiotherapy such as utilisation of alternate beam types (MV and kV X-rays, electrons, protons, carbon ions) and treatment plans (image guided 4D-CT, PET and MRI) rely on the availability of convenient and reliable dosimeters that are sensitive in the dose ranges used for clinical practice. There remains the need to develop dosimeters able to quantify low radiation doses (≤ 2 Gy) and which also have the ‘ideal dosimeter properties as described in **Section 1.3.1**.

Previous investigations have shown that while dosimeters based on alanine are well placed to satisfy these demands for high dose regimes (**Section 1.3.2.2**), they do not have the sensitivity to give reliable measurements for doses of less than 5 Gy. In this chapter a protocol for preparation and use of alanine dosimeters that extends their useful range down to about 0.5 Gy i.e. extending their low dose dynamic range

approximately ten times is presented. This greatly expands the application of dosimeters of this sort to clinical application.

5.1.1 Current dosimeters in radiotherapy

As discussed in **Section 1.3**, the dosimeters that dominate current practise in radiotherapy are; ionisation chambers (**Section 1.3.1.4**) which give uniform responses over a range of energies, making them useful in calibration, quality assurance and dose measurement [124] and solid-state dosimeters such as; TLDs and diodes- for patient *in vivo* dosimetry measurements, and are both discussed in detail in **Sections 1.3.1.1** and **1.3.1.2**.

In radiotherapy applications TLDs are favoured due to their small sizes (dimensions of 1 mm^3), independence to dose direction and dose rate. However, they suffer from post-irradiation fading and non-tissue equivalence [25]. Whilst diodes are advantageous as they are highly sensitive, physically small, and allow real time read outs [25], and for these reasons are often employed in highly specialized dosimetry roles, such as modulated beam verification. However, unlike TLDs, they are energy and angular dependent, easily damaged by radiation, require recalibrated before use, and have a restricted operational temperature range [25]. Finally, both TLDs and diodes suffer from non-tissue equivalence, which further complicates their application in radiotherapy. This leaves a need for alternative dosimeters with tissue equivalence and properties that overcome the limitations stated above, making alanine a potentially suitable candidate.

5.1.2 Alanine dosimetry in radiotherapy

Exposure of alanine to radiation leads to the generation of several long-lived radical species that can be quantified by EPR spectroscopy. The spectrum of irradiated alanine consists of five peaks in a 1:4:6:4:1 ratio [47] (**Figure 5-**1). Traditionally the amplitude of the central feature [47] is measured and correlated with dose and is considered more reliable than the double integration of the peak [125].

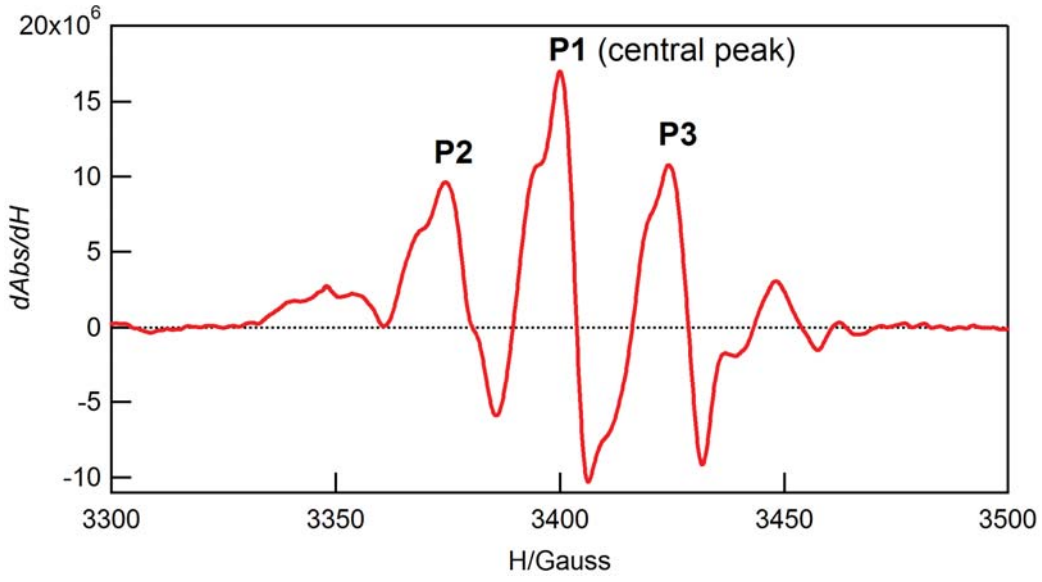

Figure 5-1. Typical EPR spectrum of the commercial alanine pellet subjected to ca. 30 Gy (6MV X-rays). The positive peaks in the differential are designated as shown in the figure.

However, the use of alanine dosimeters in radiotherapy is currently limited by their poor sensitivity at doses below 5 Gy [26, 50]. More seriously, baseline distortion even for doses between 5 and 10 Gy can impact on the measurement of the central peaks' amplitude [126]. Strategies to overcome this have been implemented, with a focus on increasing the sensitivity of alanine dosimeters physically, as well as the EPR

protocols utilized in their measurement, and are discussed in **Section 1.3.2.2** along with their limitations.

This chapter introduces a new and innovative technique which renders alanine dosimeters to be sensitive to 2 Gy and below, and is described below.

5.1.3 Standard addition or ‘spiking’

Standard addition or ‘spiking’ is an analytical chemistry technique used to enhance the measurement of weak signals by techniques such as atomic absorption spectroscopy (AAS) and gas chromatography (GS). The method involves the addition ‘spike’ of an analyte with a known large concentration [Y] to an ‘unknown’ analyte of low concentration [X] that is unable to be detected reliably by the analytical technique, and is shown in equation (**5-1**). The “spike” increases the unknown’s concentration or signal into a range which can be reliably measured by the instrument to give a combined signal [Y+X], [127]. Subtraction of the spike signal [Y] leaves the remainder to be attributed to the unknown [X]. It is this very method that is examined in this chapter; whereby using alanine dosimeters a low dose of radiation will become ‘visible’ to the EPR spectrometer by the addition of a larger ‘spike’ dose of radiation, thus overcoming the EPR instruments low sensitivity which currently prevents alanine’s usage in low dose (≤5 Gy) radiotherapy measurements.

$$\textit{Unknown [X] signal} = \textit{Unknown} + \textit{Spike [X+Y] signal} - \textit{Spike [Y] signal} \quad (5\text{-}1)$$

Another method, which is similar to spiking, is the additive dose method used in retrospective dosimetry (archaeological dating and radiation accidents) [128-131]. Here a sample of tooth or bone is measured using EPR [132] then irradiated with a series of

known large doses, to produce a dose response curve, which is back-extrapolated to determine the original unknown dose received. The additive method has been used in radiotherapy by Trompier et al. [133] to determine the over-exposure dose received by breast cancer patients at a centre in Poland, in this case measurements were conducted using a section of rib bone from the affected patients. While similar in strategy, this work differs to the additive dose method in that a single large dose is given to an alanine dosimeter prior to exposure to a smaller known dose, and the measured dose is obtained without calculation of a dose response curve. Currently, there are no precedents for the proposed technique for low dose radiation determination in radiotherapy, and the results presented in this chapter show that spiking does allow low doses down to 0.5 Gy to be determined by measuring either the height or single integration of the central peak in the EPR spectrum for alanine.

5.2 Methods

5.2.1 Alanine pellets

Commercial alanine pellets were purchased from Synergyhealth in Germany; each pellet contains 96 % L-alanine and 4 % binder, measuring 4.80 ± 0.1 mm in diameter and 3.00 ± 0.3 mm in height, with a recommended dose range from 10 Gy to 150 kGy. All alanine pellets were stored at room temperature, in vacuum sealed containers with silica beads to remove air moisture. Temperature and humidity was monitored using a digital thermal/hygrometer gauge and did not exceed 25°C and 40 % RH respectively.

5.2.2 Irradiation of alanine pellets

Sample irradiation was completed at the William Buckland Radiotherapy Centre, Alfred Hospital, Melbourne, Australia, using a Novalis Classic LINAC with 6MV X-rays.

During irradiation alanine pellets were housed within a Perspex sheet (3 mm thickness) with cavities of the same dimensions as the alanine dosimeters, such that there were no air gaps between the pellet and Perspex surrounds (**Figure 5-2**). During irradiation all cavities were filled with blank pellets so as to maintain a homogeneous medium.

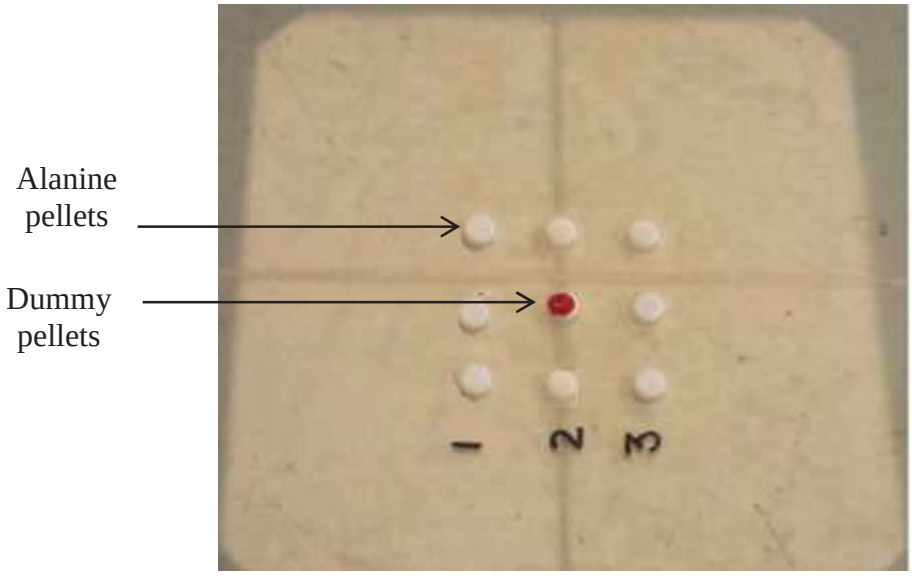

Figure 5-2. The replacement of alanine pellets with a blank pellet (coloured red) to maintain a homogeneous medium during irradiation.

The Perspex sheet was placed on top of 15 cm solid-water as the back-scatter medium, with a 5 cm solid water build-up, field size of 10 x10 cm^2 and SSD of 95 cm (**Figure 5-3**).

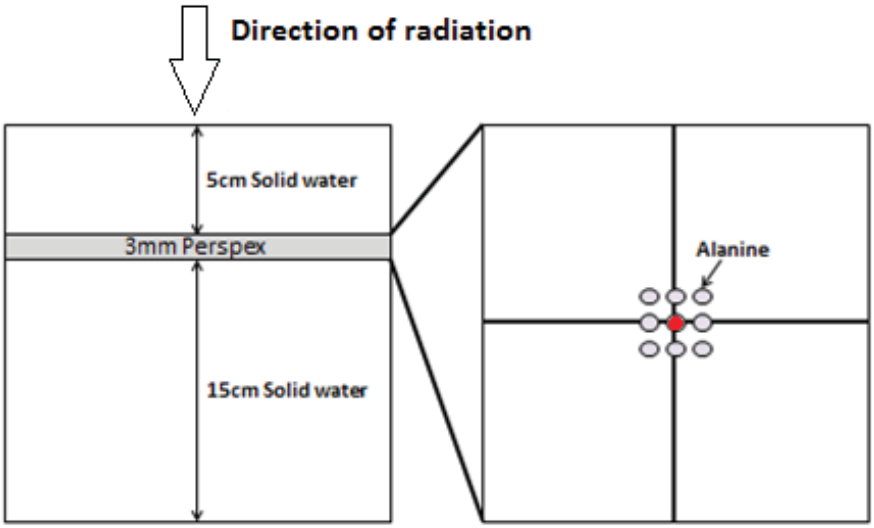

Figure 5-3. The setup used for irradiation of alanine pellets, showing the customized Perspex sheet.

After receiving the required dose, the pellets were removed and stored in a darkened container under controlled conditions as stated previously.

Initially pellets were irradiated with two doses administered as follows:

i. An initial spike dose of 20 Gy was delivered, after which the EPR signal was recorded (24 hours post irradiation). A calibration pellet was removed from each sample set of 6 pellets and used to account for signal changes over time.
ii. A second low dose of 0.5, 1.0 or 2.0 Gy was given to the remaining five pellets in the set and the EPR spectrum was re-recorded for all pellets (24 hours post irradiation).

A similar strategy was employed for a set of twenty four alanine dosimeters which were irradiated with a dose of 30 Gy. Six of these dosimeters were not subject to further irradiation and the remaining pellets received doses ranging from 0.5 to 10 Gy.

Triplicate measurements were conducted for each dose and are summarized in **Table 5-1**.

Table 5-1. Radiation doses given to all alanine pellets, showing the initial spike (30 Gy) and second low dose (0.5 to 10.0 Gy).

Number of pellets	1st Dose (Gy)	Number of pellets	2nd Dose (Gy)	Total dose (Gy)
4	30	3	0.5	**30.5**
4	30	3	1.0	**31.0**
4	30	3	1.5	**31.5**
4	30	3	2.0	**32.0**
4	30	3	5.0	**35.0**
4	30	3	10.0	**40.0**

The calibration pellet (which only received the initial spike of 20 Gy or 30 Gy) was remeasured and this value was used to extract the spike values of the other pellets from the set.

5.2.3 EPR signal analysis

All pellets were placed vertically in a quartz tube (internal diameter of 7 mm), fitted with an o-ring to ensure the pellet was consistently positioned in the centre of the cylindrical cavity. Initial results using a 20 Gy spike were ran with a total of three accumulative scans, but this was increased to ten accumulative scans for the second set of measurements conducted (Table 1). Data collection settings were as follows; centre field, 3400 G; microwave power, 2 mW; sweep time, 21.0 s; sweep width 200 G; modulation amplitude, 4.0 G; time constant, 81.92 ms; modulation frequency, 100 kHz; receiver gain, 75 dB.

The amplitude of the central peak and P2 and P3 peaks was measured using peak to peak analysis [126], and the single integration of the peaks performed using the Bruker Elexsys program, and the integration area used for analysis is shown in **Figure 5-4**.

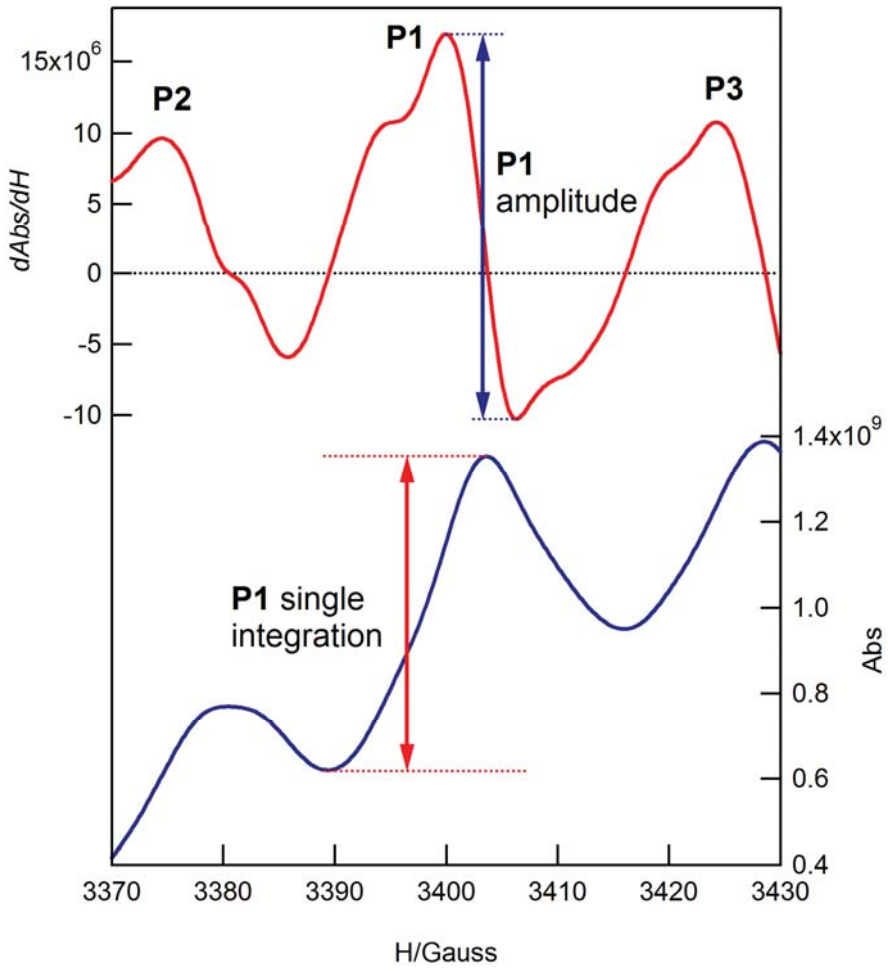

Figure 5-4. The alanine EPR spectrum showing the amplitude and single integration areas as used for the analysis of the P1 peaks.

The calibration pellet for each sample set accounts for any changes in the EPR signal over time. Pellet irradiation and EPR measurement was completed within one week.

Previous work (**Section 4.3.2**) had shown that the angular response for Synergyhealth pellets to be low (ranging between 0.95 to 1.91 % at 3 days post-

irradiation), meaning it is stable over the time course of this work. The addition of a calibration pellet with each sample set was incorporated to account for any changes in the spectrometer over time. All irradiations and measurements were completed within one week.

5.2.4 Measurement limitation

The data presented in this chapter is based on the measurements of the EPR signal amplitude, which is related to the alanine radical yield following exposure to set nominal doses delivered by X-ray sources. The nominal dose is based on measurements using a “parallel plate” ionisation chamber, with a 3 % uncertainty (**Section 2.2.8**). The data presented is an average of at least three measurements from independent samples, where the error bars represent the standard deviation between measurements.

5.3 Results

5.3.1 EPR measurements of the central alanine peak (P1)

5.3.1.1 20 Gy dose spike

Initially, 18 dosimeters received a spike of 20 Gy dose and were divided into three sets each containing six pellets. One pellet from each set was kept as a reference, and the remaining five pellets irradiated with a specified dose (0.5, 1, 2 Gy), where the stochastic uncertainty is estimated by the standard deviation for the five pellets subjected to the additional dose. The EPR signal for the calibration pellet was used as background to adjust the EPR measurement (spike plus smaller dose) of the other five pellets (**Tables 5-2** and **5-3**), which was then averaged. **Table 5-4** summarizes the

average EPR signal for both amplitude and single integration of the central peak (P1), and are plotted in **Figure 5-5**.

Table 5-2. EPR measurements for the P1 peak amplitude, with the calibration pellet 'a' which only received the 20 Gy spike.

Amplitude for P1 (central peak)				
Pellet #	**Spike (20 Gy)**	**2nd dose (Gy)**	**Spike + 2nd dose**	**-Spike**
1a	1.531	**2Gy**	1.821	0.290
b	1.502		1.969	0.177
c	1.505		2.021	0.226
d	1.515		2.006	0.201
e	1.497		1.973	0.186
f	1.488		1.954	0.176
2a	1.672	**1Gy**	1.958	0.286
b	1.667		2.025	0.067
c	1.628		1.997	0.056
d	1.665		1.919	0.005
e	1.620		2.020	0.130
f	1.609		2.048	0.142
3a	1.902	**0.5Gy**	2.324	0.422
b	1.921		2.420	0.077
c	1.880		2.390	0.088
d	1.845		2.282	0.015
e	1.950		2.388	0.016
f	1.904		2.398	0.072

Table 5-3. EPR measurements for the single integration of the P1 peak, the calibration pellets 'a' are highlighted.

Single integ. of P1 (central peak)				
Pellet #	**Spike (20 Gy)**	**2nd dose (Gy)**	**Spike + 2nd dose**	**-Spike**
1a	1.5654	**2 Gy**	1.8502	0.2848
b	1.5425		2.0769	0.2496
c	1.5504		2.0798	0.2446
d	1.5503		1.8631	0.0280
e	1.5218		2.0144	0.2078
f	1.5708		2.0544	0.1988
2a	1.7290	**1 Gy**	2.0202	0.2912
b	1.7279		2.0809	0.0618
c	1.6876		2.0481	0.0693
d	1.6505		2.0256	0.0839
e	1.6366		2.0822	0.1544
f	1.6429		2.1146	0.1805
3a	1.9452	**0.5 Gy**	2.4034	0.4582
b	1.9811		2.4808	0.0415
c	1.9354		2.4636	0.0700
d	1.8744		2.3302	-0.0024
e	1.9056		2.4645	0.1007
f	1.9440		2.4679	0.0657

Table 5-4. The averages and standard deviations of the EPR signals for each sample set (n=5) using the peak amplitude and single integration of the P1 peak. All pellets were subjected to a spike dose of 20 Gy.

		Amplitude P1		**Single integ. P1**	
Set	**2nd dose (Gy) -spike**	**$\langle I_{sample}-I_{reference}\rangle$**	**σ ($I_{sample}-I_{reference}$)**	**$\langle I_{sample}-I_{reference}\rangle$**	**σ ($I_{sample}-I_{reference}$)**
1	2.0	0.193	0.019	0.224	0.020
2	1.0	0.090	0.038	0.110	0.048
3	0.5	0.054	0.032	0.055	0.034

Whilst the relative error of the 2.0 Gy doses are comparatively small (**Figure 5-5**), good regression values (0.9935 and 0.9997 respectively) are obtained for both methods of quantifying the EPR signal, the relative errors for 1.0 and 0.5 Gy doses (both amplitude and integration measurements) are large, undermining the use of the approach for quantification of doses below ca. 1.5 Gy. The limit of detection was determined by calculating the EPR signal value (y) [134], using the equation below (**5-2**):

$$y = mean \text{ (for the lowest dose measured: I sample- I reference)} + n \text{ (number of pellets measured in the set)} \times [standard\ deviation\ of\ the\ lowest\ dose] \quad (5\text{-}2)$$

Using the equation for the fitted regression line the limit of detection was determined as; 2.23 Gy for the amplitude method and 2.01 Gy for the single integration method.

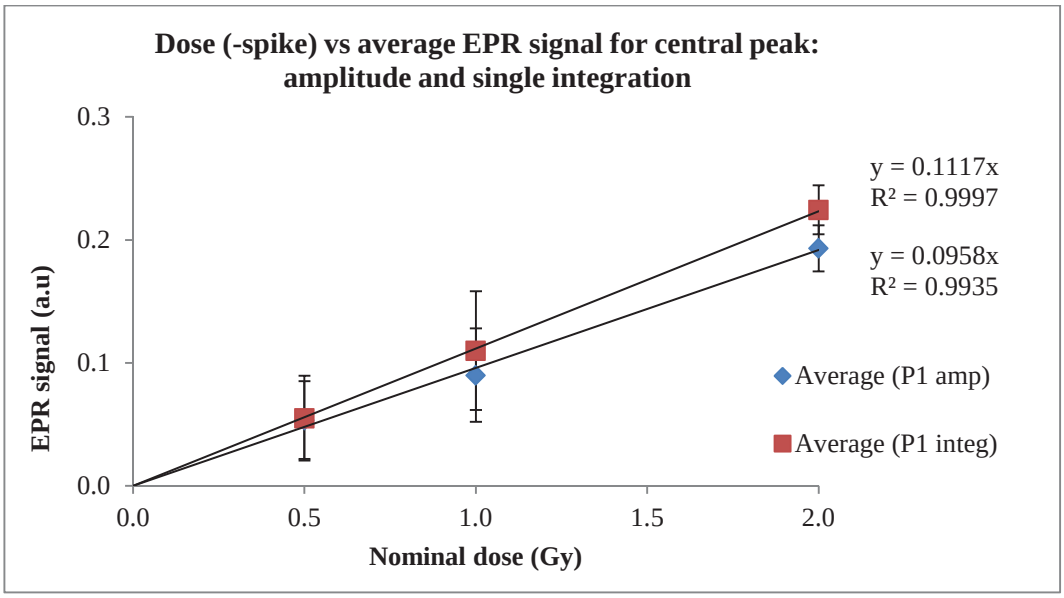

Figure 5-5. Plot of the average EPR signal for the P1 peak amplitude and single integration after subtraction of the spike dose (20 Gy) where the error bars represent the standard deviation between measurements.

5.3.1.2 The calibration pellet

The need for a calibration pellet is shown by removal of the calibration pellets results; 1a, 2a and 3a from **Tables 5-2** and **5-3**. **Figure 5-6** shows the effect on the

averages and standard deviation for the P1 peak's amplitude and single integration (**Table 5-5**), and that quantification of doses below 2 Gy is no longer possible.

Table 5-5. The averages and standard deviations of the EPR signals for each sample set (n=5) using the peak amplitude and single integration of the P1 peak, without the use of a calibration pellet.

		Amplitude P1		Single integ. P1	
Set	2nd dose (Gy) -spike	$<I_{sample}-I_{reference}>$	σ $(I_{sample}-I_{reference})$	$<I_{sample}-I_{reference}>$	σ $(I_{sample}-I_{reference})$
1	2.0	0.467	0.021	0.471	0.091
2	1.0	0.364	0.069	0.401	0.054
3	0.5	0.476	0.035	0.513	0.038

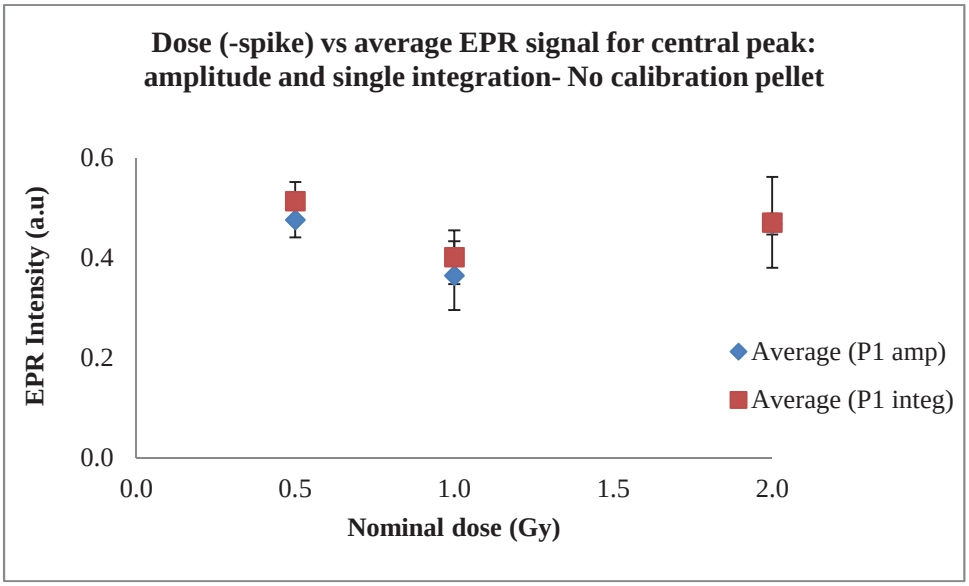

Figure 5-6. Plot of the average EPR signal for the P1 peak amplitude and single integration after subtraction of the spike dose (20 Gy), without a calibration pellet.

5.3.1.3 30 Gy dose spike

A similar method was employed using a 30 Gy spike (one reference pellet and three repeat measurements) with doses of 0.5, 1.0, 1.5, 2.0, 5.0 and 10 Gy. EPR

measurements were completed using 10 accumulated scans (**Tables 5-6** and **5-7**), and the averages of the signal are summarized in **Table 5-8**. **Figure 5-7a** shows the average EPR signal for the amplitude and single integration of P1 versus dose (over the dose range 0.5 to 10 Gy). Both plots have good R^2 values (0.9895 for amplitude and 0.9890 for single integration), and doses of 2.0 Gy and below are distinguishable. From **Figure 5-7a** the limit of detection was determined as; 1.56 Gy for the amplitude method and 0.711 Gy for the single integration method.

Figure 5-7b shows the expansion of the region 0.5 to 2.0 Gy doses with the alanine EPR signal strength as estimated using the maximum and minimum values of dAbs/dH in the P1 region (R^2 = 0.7610) or the maximum and minimum values of the absorbance plot obtained from integration of dAbs/dHslopes (R^2 = 0.9772). Calculations for the limit of detection are; 1.74 Gy for the amplitude method and 1.03 Gy for the single integration method.

Table 5-6. EPR measurements for P1 amplitude, red values indicate the calibration dosimeters 'a' from each set, which only received the 30 Gy spike.

Amplitude of P1 (central peak)				
Pellet #	**Spike (30 Gy)**	**2nd dose (Gy)**	**Spike + 2nd dose**	**-Spike**
1a	5.960		5.381	0.579
b	6.440	**10**	8.375	2.514
c	6.486		8.394	2.487
d	6.569		8.460	2.470
2a	6.326		5.419	0.907
b	6.163	**5**	6.500	1.244
c	6.506		6.891	1.292
d	6.486		6.819	1.240
3a	6.332		5.918	0.414
b	6.545	**2**	6.716	0.585
c	6.633		6.762	0.543
d	6.360		6.534	0.588
4a	6.238		5.952	0.286
b	6.673	**1.5**	6.604	0.217
c	6.563		6.640	0.363
d	6.686		6.654	0.254
5a	7.503		7.077	0.426
b	7.907	**1.0**	7.571	0.090
c	7.820		7.495	0.101
d	7.870		7.532	0.088
6a	7.847		7.247	0.600
b	7.857	**0.5**	7.114	-0.143
c	7.795		7.406	0.211
d*	7.533		5.515	-1.418

*Not used

Table 5-7. EPR measurements for the single integration of P1, showing the spike and low dose readings.

	Single integ. of P1 (central peak)			
Pellet #	**Spike (30 Gy)**	**2nd dose (Gy)**	**Spike + 2nd dose**	**-Spike**
1a	6.1401		5.3361	0.8040
b	6.6624	**10**	8.5817	2.7233
c	6.6493		8.6110	2.7657
d	6.7757		8.6928	2.7211
2a	6.4568		5.5621	0.8947
b	6.3210	**5**	6.8833	1.4570
c	6.7164		7.2638	1.4421
d	6.6725		7.1867	1.4089
3a	6.4003		6.0890	0.3113
b	6.8373	**2**	7.0151	0.4891
c	6.7848		6.8246	0.3511
d	6.9009		6.8879	0.2983
4a	6.5088		6.1317	0.3771
b	6.8056	**1.5**	6.7291	0.3006
c	6.9535		6.8993	0.3229
d	7.0044		6.8802	0.2530
5a	7.6857		7.0704	0.6153
b	8.0645	**1.0**	7.6204	0.1712
c	7.9820		7.6331	0.2664
d	8.1642		7.6481	0.0992
6a	8.1181		7.4591	0.6590
b	8.1045	**0.5**	7.2902	0.0847
c	8.0376		7.5775	0.0989
d	8.3187		7.6580	-0.0017

Table 5-8. The averages and standard deviations for P1 (amplitude and single integration) following calibration adjustment and subtraction of the 30 Gy spike.

		Amplitude P1		Single integ. P1	
Set	**2nd dose (Gy) -spike**	**$\langle I_{sample} - I_{reference} \rangle$**	**σ $(I_{sample} - I_{reference})$**	**$\langle I_{sample} - I_{reference} \rangle$**	**σ $(I_{sample} - I_{reference})$**
1	0.5	0.034	0.177	0.061	0.044
2	1.0	0.093	0.093	0.179	0.068
3	1.5	0.278	0.062	0.292	0.029
4	2.0	0.572	0.021	0.511	0.017
5	5.0	1.259	0.024	1.436	0.020
6	10.0	2.490	0.016	2.737	0.021

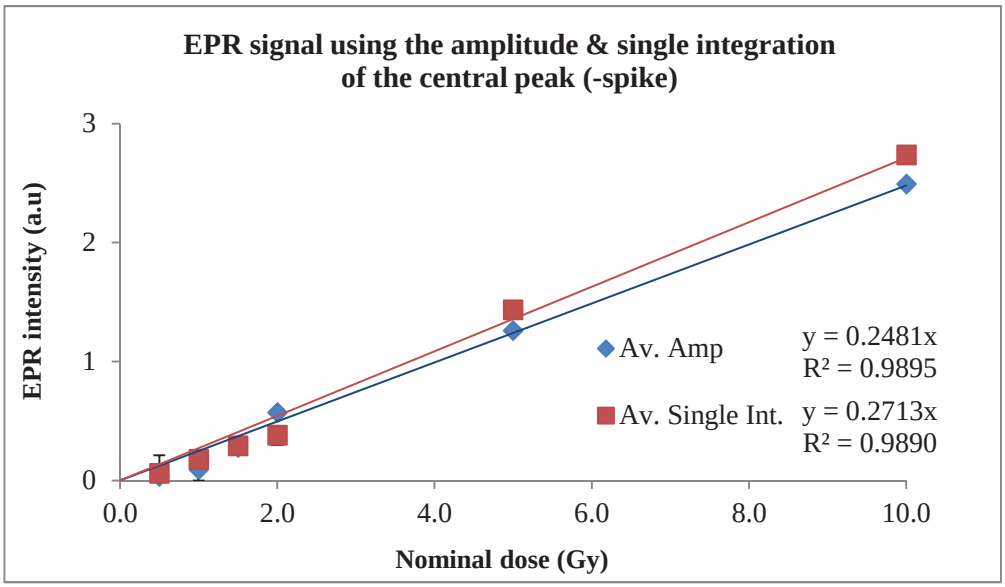

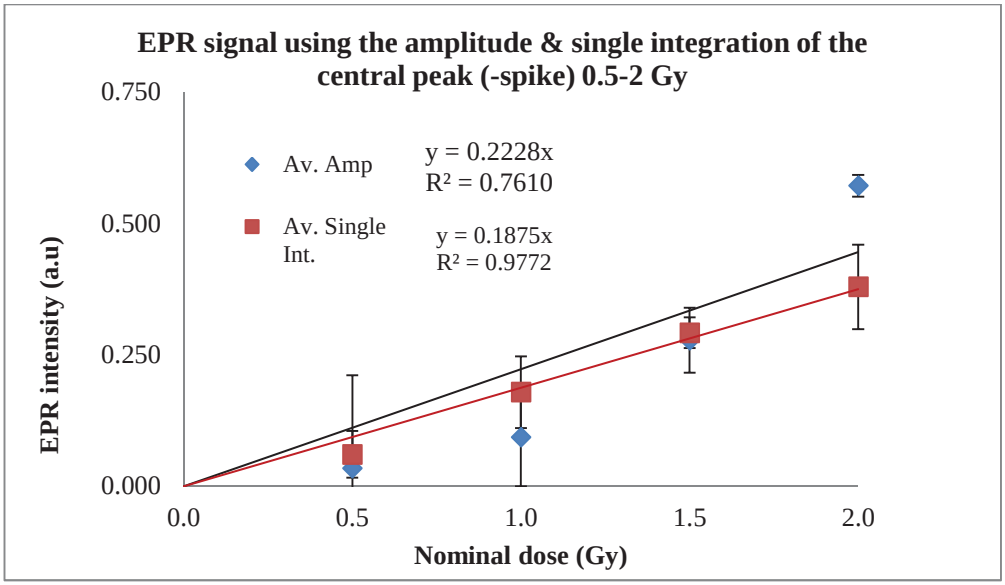

Figure 5-7. Averages of the EPR signal for the low doses received, after subtraction of the initial spike (30 Gy); (a) shows the dose range 0.5 to 10 Gy and (b) scale expansion to highlight the region 0.5 to 2 Gy.

5.3.2 EPR measurements of the alanine peaks P2 and P3

Using the EPR spectra obtained above (10 accumulative scans and a 30 Gy spike dose) the amplitude and single integration of the P2 and P3 peaks of alanine were also examined (**Tables 5-9** and **5-10**). **Tables 5-11** and **5-12** summarize the average measurements for EPR signals obtained for P2 and P3 after calibration and spike subtraction, and **Figures 5-8** and **5-9** show the average EPR signal plotted against dose respectively.

Table 5-9. EPR amplitude measurements for P2 and P3, the red values indicate the calibration dosimeter 'a' from each set.

		Amplitude of P2 peak			Amplitude of P3 peak		
Pellet #	**2nd dose (Gy)**	**Spike (30 Gy)**	**Spike + 2nd dose**	**-Spike**	**Spike (30 Gy)**	**Spike + 2nd dose**	**-Spike**
1a	**10**	3.525	3.190	0.335	4.477	4.015	0.462
b		3.812	4.923	1.446	4.763	6.142	1.841
c		3.850	4.947	1.432	4.772	6.215	1.905
d		3.965	4.967	1.337	4.902	6.215	1.775
2a	**5**	3.689	3.159	0.530	4.608	3.985	0.623
b		3.649	4.132	1.013	4.608	5.226	1.241
c		3.884	4.220	0.866	4.851	5.292	1.064
d		3.869	4.285	0.946	4.769	5.310	1.164
3a	**2**	3.772	3.583	0.189	4.675	4.405	0.270
b		3.945	3.910	0.154	4.879	4.879	0.270
c		4.019	3.909	0.079	5.014	4.845	0.101
d		3.990	3.915	0.114	4.948	4.865	0.187
4a	**1.5**	3.694	3.468	0.226	4.573	4.357	0.216
b		3.907	4.058	0.377	4.879	5.034	0.321
c		3.949	3.922	0.199	4.924	4.857	0.099
d		3.963	3.753	0.016	4.956	4.722	-0.068
5a	**1.0**	4.448	4.204	0.244	5.568	5.301	0.267
b		4.693	4.405	-0.044	5.889	5.523	-0.099
c		4.618	4.406	0.032	5.880	5.523	-0.090
d		4.710	4.454	-0.012	5.972	5.439	-0.266
6a	**0.5**	4.683	4.243	0.440	5.820	5.339	0.481
b		4.660	4.204	-0.016	5.853	5.259	-0.113
c		4.588	4.368	0.220	5.780	5.478	0.179
d		4.969	4.412	-0.117	5.949	5.482	0.014

Table 5-10. EPR measurements for the single integration of P2 and P3, with red values indicating the calibration dosimeters marked 'a'.

		Single integ. of P2 peak			Single integ. of P3 peak		
Pellet #	**2nd dose (Gy)**	**Spike (30 Gy)**	**Spike + 2nd dose**	**-Spike**	**Spike (30 Gy)**	**Spike + 2nd dose**	**-Spike**
1a	**10**	3.5179	3.2357	0.2822	5.3879	5.0379	0.3500
b		3.6994	4.9420	1.5248	5.4479	7.5392	2.4413
c		3.7832	5.0127	1.5117	5.9286	7.8764	2.2978
d		4.0362	5.0580	1.3040	6.1072	7.8817	2.1245
2a	**5**	3.7471	3.1685	0.5786	5.7932	5.0486	0.7446
b		3.6632	4.2223	1.1377	5.6985	6.5128	1.5589
c		3.9030	4.2956	0.9712	5.9614	6.5459	1.3291
d		3.8924	4.2636	0.9498	5.9816	6.6495	1.4125
3a	**2**	3.8424	3.5337	0.3087	5.8341	5.1564	0.6777
b		3.9240	4.0436	0.4283	6.1749	6.1226	0.6254
c		4.0036	4.0120	0.3171	6.1282	6.0804	0.6299
d		3.7764	3.9937	0.5260	6.1671	6.1621	0.6727
4a	**1.5**	3.7184	3.5379	0.1805	5.8598	5.5317	0.3281
b		3.9263	4.1313	0.3855	6.1264	6.0973	0.2990
c		3.9778	3.9930	0.1957	6.2461	6.1249	0.2069
d		4.0201	3.9947	0.1551	6.3316	5.8145	-0.1890
5a	**1.0**	4.3979	4.2638	0.1341	6.9436	6.6582	0.2854
b		4.7544	4.4283	-0.1920	7.3789	6.9497	-0.1438
c		4.7267	4.4588	-0.1338	7.3251	6.8903	-0.1494
d		4.7538	4.5491	-0.0706	7.3677	6.8564	-0.2259
6a	**0.5**	4.7863	4.3107	0.4756	7.3294	6.7825	0.5469
b		4.6382	4.2593	0.0967	7.3699	6.6413	-0.1817
c		4.6390	4.3704	0.2070	7.3327	6.8849	0.2112
d		5.4325	4.4811	-0.4758	6.8434	6.9447	0.7603

Table 5-11. Summary of the averages and standard deviations for and amplitude and single integration of the P2 peak after spike subtraction.

		Amplitude of P2 peak		Single integ. of P2 peak	
Set	**2nd Dose received (Gy)**	**$\langle I_{sample} - I_{reference} \rangle$**	**σ $(I_{sample} - I_{reference})$**	**$\langle I_{sample} - I_{reference} \rangle$**	**σ $(I_{sample} - I_{reference})$**
1	0.5	0.0290	0.1412	-0.0574	0.2993
2	1.0	-0.0080	0.0312	-0.1321	0.0496
3	1.5	0.1973	0.1474	0.2454	0.1004
4	2.0	0.1157	0.0306	0.4238	0.0853
5	5.0	0.9417	0.0601	1.0196	0.0840
6	10.0	1.4050	0.0484	1.4468	0.1011

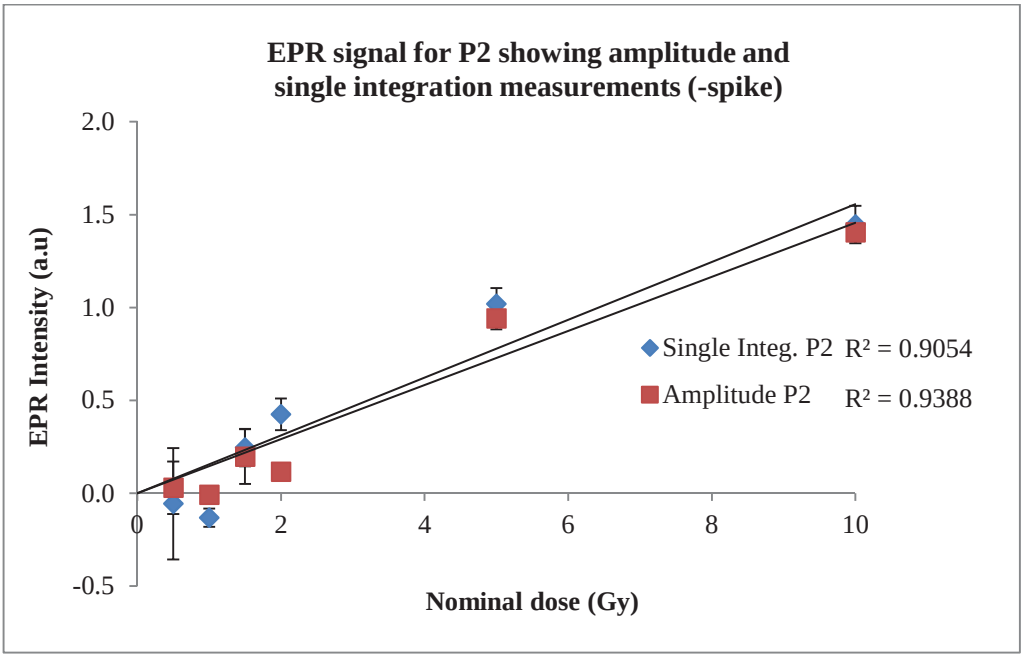

Figure 5-8. Averages of the EPR amplitude measurements for P2 amplitude and single integration after subtraction of the initial spike (30 Gy).

Both the P2 and P3 plots (**Figures 5-8** and **5-9**) show non-linearity and reduced R^2 values; P2: 0.9388 (amplitude) and 0.9054 (single integration) and P3: 0.9259 (amplitude) and 0.9198 (single integration), which strongly suggests that neither peak could be used for determining doses of $\leq$ 10 Gy.

Table 5-12. Summary of the EPR averages for the amplitude and single integration of the P3 peak after spike subtraction.

		Amplitude of P3 peak		Single integ. of P3 peak	
Set	**2nd Dose received (Gy)**	**$\langle I_{sample} - I_{reference} \rangle$**	**σ $(I_{sample} - I_{reference})$**	**$\langle I_{sample} - I_{reference} \rangle$**	**σ $(I_{sample} - I_{reference})$**
1	0.5	0.0267	0.1195	0.2633	0.3863
2	1.0	-0.1517	0.0809	-0.1730	0.0375
3	1.5	0.1173	0.1593	0.1056	0.2117
4	2.0	0.1860	0.0690	0.6427	0.0213
5	5.0	1.1563	0.0725	1.4335	0.0950
6	10.0	1.8403	0.0531	2.2879	0.1295

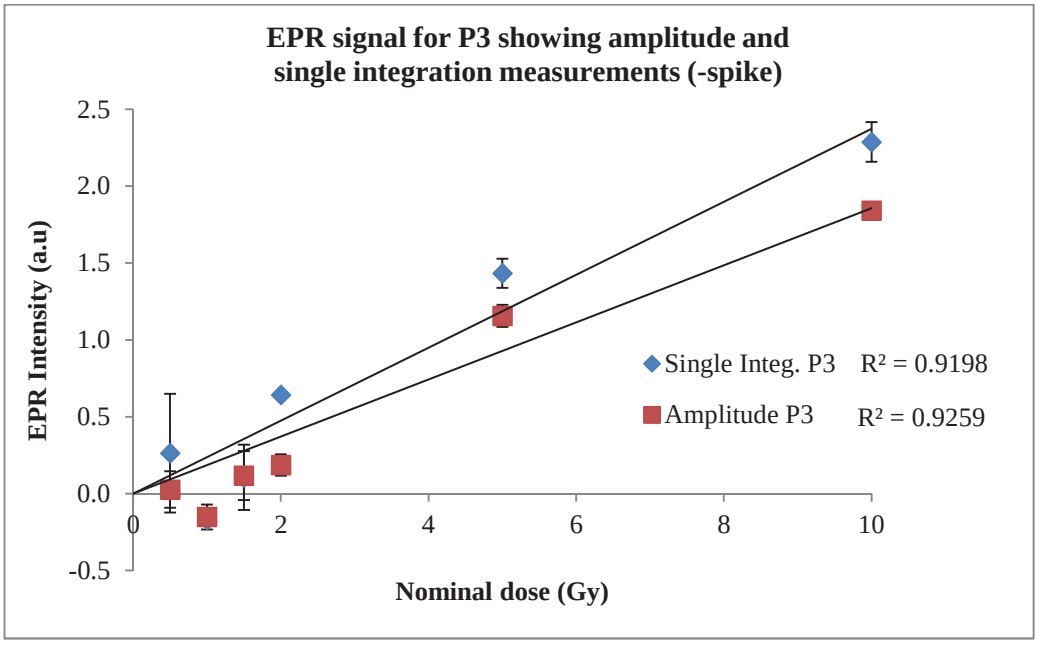

Figure 5-9. Average measurements for the P3 peak's amplitude and single integration after subtraction of the initial spike.

5.4 Discussion

Previous attempts to improve the sensitivity of alanine dosimeters have focused on the use of chemical additives to the dosimeter itself and modifications to the EPR spectrometer; however both methods are limited in their potential. Using the novel

method of spiking; whereby the alanine dosimeter receives a large dose of radiation prior to a second low dose, measurements of 2 Gy and below were determined. The results are discussed in the sections below, including the importance of the calibration pellet used, the effects of varying the spike dose given and changes to some of the EPR conditions. As well, the detection limits over the dose ranges used are presented.

5.4.1 EPR signal analysis and the reference pellet

Quantification of the EPR signal by single and double integration of the entire alanine EPR spectrum was found to give variable results owing to the errors associated with background subtraction and for this reason methods based on use of a more restricted region of the spectrum were investigated. The central peak (P1) is well-defined and the intensity of this signal was quantified by single and double integration (**Figure 5-4**), where the more restricted range of field makes the measurement comparatively insensitive to small baseline distortions.

Critical to the success of the spiking method is the reliable correction for the effect of the spike dose and is evident in **Figures 5-5** (using a calibration pellet) and **Figure 5-6** (no calibration pellet). In the current investigation a single reference pellet was used to quantify this effect. As is evident from **Figure 5-7** there can be excellent agreement between measurements but systematic deviation from a linear relation between the EPR intensity and the nominal dose, as would result from an error in the reference signal. These measurements highlight the need to collect sufficient measurements of the reference signal to give the statistical basis for reliable measurements for nominal doses below 2 Gy.

The variation in the calibration pellets EPR signal is clearly seen for the amplitude and single integration measurements for P1, P2 and P3 (**Tables 5-2**, **5-3**, **5-6**, **5-7**, **5-9** and **5-10**). For example, the variation in the P1amplitude measurements for the calibration pellet, after a spike dose of 30 Gy (**Table 5-6**) varies between 0.286 (pellet 4a) to 0.907 (pellet 2a). This variation in response raises several issues that are the subject of continuing investigation; firstly if there is a time dependence issue between irradiation and read-out. Samples were stored for at least 24 hours post-irradiation to allow signal stabilization of the alanine radical before measurement of the EPR spectrum [135]. Logistical reasons associated with the location and access to the EPR spectrometer contributed to a variation of the measurement time between 24 to 96 hours. While examination of the current sets of measurements does not show a clear relationship between the measurement time and attenuation of the signal, this element of the measurement protocol for EPR measurements requires more systematic investigation.

In this context it is important to note that the storage conditions of the pellets requires careful control due to the possible effects of air moisture and water content on the pellets EPR signal [53]. Finally, revised protocols require the measurement of multiple calibration pellets (≥ 3) both to allow identification of outlier measurements and improve the statistical accuracy of the method. Our current investigations explore the impact of these refinements to the protocols on the accuracy and precision of the measurements.

5.4.2 Measurements using a 20 Gy spike

The results presented in **Table 5-4** and **Figure 5-5** were completed using a 20 Gy spike dose and yielded good regression values (0.9935 and 0.9997). While the 2.0

Gy doses were clearly defined the 1.0 and 0.5 Gy doses had large standard deviations (approximately 0.032 to 0.048), which limited the usefulness of the measurements. The calculated limit of detection for both methods were; 2.23 Gy (amplitude) and 2.01 Gy (single integration) and suggests that doses of approximately 2 Gy can be reliably detected. Whilst, this is an improvement on the current sensitivity of alanine dosimeters further means to extend the low-dose detection limit were examined and are discussed below.

5.4.3 Measurements using a 30 Gy spike

To validate and optimise the accuracy of the spiking method, a larger spike dose was applied in conjunction with an increased number of EPR scans and a change in the measurement statistics (**Table 5-1**). While a decrease in the number of repeat measurements from five to three will reduce the statistical precision of the result, the improved accuracy of the measured spectrum provides an overall improvement in terms of reliability of the measurements (**Figure 5-7**). For the 30 Gy spike and measurement protocols there is a clearer distinction between measurements of doses below 2 Gy. A decrease in the limit of detection was evident for both methods over the dose range 0.5 to 10 Gy (**Figure 5-7a**); 1.56 Gy (amplitude) and 0.711 Gy (single integration) when compared the 20 Gy spike samples (amplitude: 2.23 Gy and single integration 2.01 Gy), which suggests the increase in accumulative EPR scans is of benefit. However, analysis of the dose range 0.5 to 2.0 Gy (**Figure 5-7b**) shows a decrease in the R^2 value for the amplitude measurements; 0.9895 (**Figure 5-7a**) to 0.7610 (**Figure 5-7b**), which did not occur for the single integration results; 0.9890 (**Figure 5-7a**) to 0.9772 (**Figure 5-7b**). Potentially the reduction in sample number (n= 2 for the 2 Gy dose) may have contributed and suggests that a balance between sample number and the number of EPR

scans performed is important. The detection limits over the 0.5 to 2.0 Gy dose range were determined to be 1.74 Gy (amplitude) and 1.03 Gy (single integration), which is lower than those obtained for the 20 Gy spike doses; 2.23 Gy (amplitude) and 2.01 Gy (single integration), suggesting that an increase in EPR scans is advantageous.

Overall, this investigation suggests that half-Gray doses can be achieved by optimisation of the spiking method.

5.4.4 Measurements of P2 and P3 signals

Lastly the amplitude and single integration of the P2 and P3 (**Figure 5-1**) alanine peaks was examined and summarized in **Tables 5-11** and **5-12**. Overall the measurements for P2 and P3 (both amplitude and single integration) had higher standard deviations and reduced linearity when plotted (**Figures 5-8** and **5-9**), which is reflected in the lower regression values for all plots. As well, negative values for all 1.0 Gy measurements for P2 and P3 amplitude and single integration were found.

These results are consistent with earlier work by Heydari *et. al.* [46], who found that the P2 and P3 peaks were altered over time due to changes in the alanine radical composition. P1 is less susceptible to these effects as it is solely composed of the main-deaminated radical species.

5.5 Conclusion

The spiking method can allow doses ≤ 1 Gy to be reliably detected by alanine dosimeters, and overcomes the current limitations which hinder its applications in radiation fields such as in radiotherapy. The addition of a spike dose increases the alanine dosimeters EPR signal making it easily detectable to an X-band EPR

instrument. After the addition of a second low dose, the spike signal can be subtracted from the total signal (spike + low dose) and reliably determined. Both the amplitude or single integration of the central alanine peak P1 can be used, and both are capable of quantifying doses of 0.5 Gy. The advantages of the spiking method are that no foreign materials are added to the alanine dosimeters, thus tissue equivalence is maintained, the EPR signal to noise ratio is improved, and baseline distortions typical at low doses are removed due to the large spike dose given. Furthermore no complex post-analysis is required and can be performed on any standard X-band EPR spectrometer. This work allows for alanine dosimeters to be used in a far wide range of applications in radiation dosimetry, particularly for the low doses often relevant for clinical applications.

Chapter 6: The formation of bimetallic-nanoparticles by neutron capture

Thermal neutron irradiations were undertaken at the Australian Nuclear Science and Technology Organisation (ANSTO) at the LE2-2 facility, and funded by the Australian Institute of Nuclear Science and Engineering (AINSE) Research Award, ID number 11437, 2015. We acknowledge this grant and kindly thank AINSE and ANSTO.

6.1 Introduction

MetNPs possess unique physical and chemical properties, which are not evident in their larger bulk-metal particles, as was discussed in **Section 1.4.1**. It is well known that NPs have larger surface areas to volume, which increases with decreasing particle size [62] so that more surface atoms are available to partake in interactions. In particular, MetNPs with high atomic numbers (Z) are of interest for use in radiotherapy due to the increased probability of photoelectric interactions occurring for kV energy X-rays, and to a lesser extent MV x-rays, which increases dose deposition at a tumour site [24, 39, 63-67, 89].

As the current understandings of mono-metallic-nanoparticles has increased, particularly for AuNPs as possible radiosensitizers (see **Section 1.4.1**) so too has the interest in producing BiMetNPs, (comprising of two different metal nanoparticles), with reasons for this described in **Section 1.4.2**. Current means to produce BiMetNPs focuses largely on wet-chemistry methods, which are limited in the combinations of producible bi-metals, and usually involve the formation of a single NP containing a metal core layered with a secondary metal [73, 136, 137] (**Figure 6-1a**). This type of BiMetNP is synthetically favoured over the alloy type MetNPs (**Figure 6-1b**) mainly because of separation difficulties encounter when isolating the product from reaction waste by-products [85] (**Section 1.4.2**).

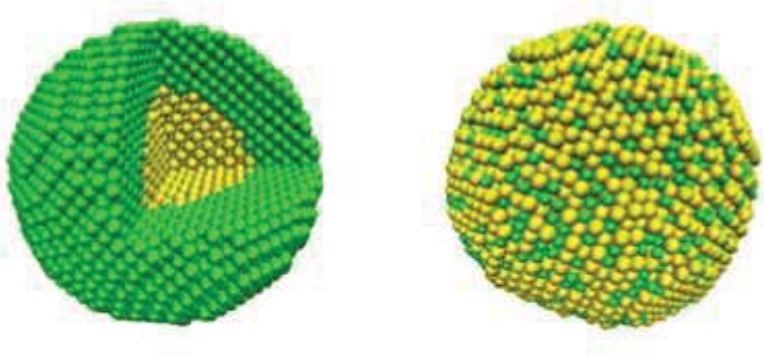

a) Core & layer BiMetNP b) Alloy BiMetNP

Figure 6-1. The different types of BiMetNPs formed: type (a) consists of a core and second metal layer, type (b) is an alloy of the two metals within a single NP (adapted from [136]).

Because of these drawbacks the search for alternative synthetic methods continues, which ultimately provides both a more effective means to produce the alloy-type BiMetNPs, and increases the metallic combinations currently available. In this chapter nuclear reactions are investigated as one such alternative method, whereby

AuNPs undergo neutron activation to form a second metal; mercury, and yield the alloy-type BiMetNP product; AuHgNPs.

6.1.1 Neutron activation of AuNPs and formation of radioactive ^{198}Au

Neutron activation of a target MetNP is the process whereby a target metal atomic nuclei absorbs neutrons, and becomes excited i.e. is in an excited energy state. To return to the ground state it emits gamma rays, protons or alpha particles to form a stable BiMetNP product. AuNPs are a highly suitable target as their interactions with neutrons are well known and the unstable gold radioisotope ^{198}Au is well studied and employed in recent brachytherapy techniques [68, 69]. The decay scheme of ^{198}Au, via gamma and beta emissions is shown in **Figure 6-2** and the subsequent formation of the stable ^{198}Hg product.

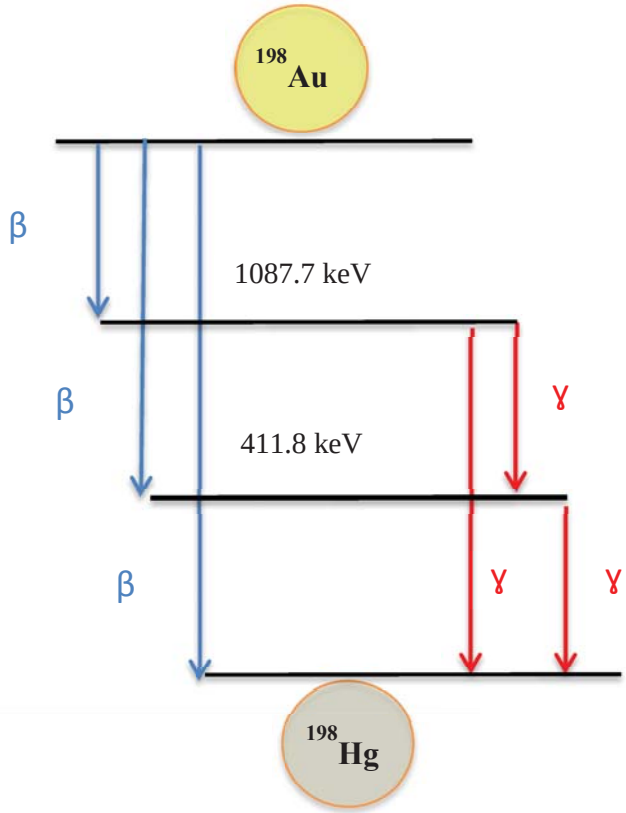

Figure 6-2. The gamma and beta decay process of the radioactive unstable ^{198}Au isotope to the stable ^{198}Hg isotope.

Following neutron bombardment the stable mercury atom ^{198}Hg formed (**Figure 6-2**) would alter the atom packing at the surface of the solid; Au atoms favour the face-centred-cubic (FCC) packing (**Figure 6-3a**), whilst Hg atoms favour the rhombohedral packing arrangement (**Figure 6-3b**). The mean coordination number of the Au atoms present would also be altered, thus causing changes to the properties of the newly synthesized AuHgNPs, and increasing the surface-to-volume ratio, meaning more surface atoms are available to partake in a given interaction.

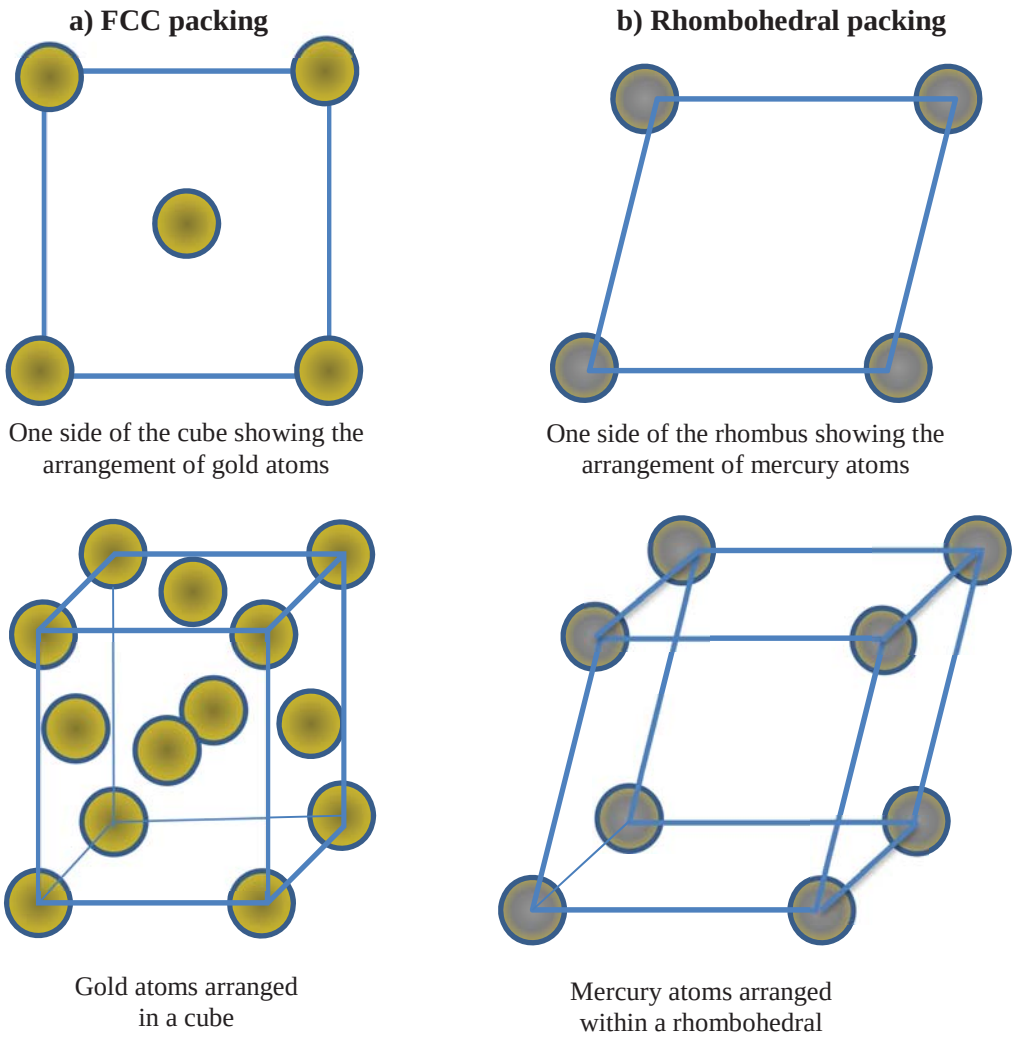

Figure 6-3 a & b. Au atoms arrange in a FCC packing within a solid (a) whilst Hg atoms favour rhombohedral packing (b).

The radioactive isotope ^{198}Au formed after neutron absorption has a half-life of 2.7 days (**Figure 6-2**) and was extensively investigated in the 1950's and 1960's for the treatment of ovarian and prostate cancers. Work by Keettel et al. [138-140] improved the five-year survival rate of Stage I and II ovarian cancer patients from 52 % (surgery alone) to 86 % when using surgery and ^{198}Au-colloid brachytherapy conjointly. Similarly, pioneering work by Flocks et al. [141-143] examined the viability of post-prostate surgery injections of colloidal ^{198}Au administered to patients over a twenty-five year period, which provided a more localised treatment, whilst minimising damage to healthy surrounding tissue. A recent review of Flocks' work [144] found the treatment of locally advanced prostate cancer with ^{198}Au yielded statistically significant improvements to long and short term patient survival rates compared to the work of Flock's contemporaries at that time.

More recently, Khan et al. [69] irradiated aqueous solutions of ^{197}Au-dendrimer salts and ^{197}Au-nanocomposites in a nuclear reactor to produce positively charged poly($^{198}Au^{0}$) radioactive gold-dendrimer composite nanodevices ranging in size from 10 to 29 nm. Single dose injections of the ^{198}Au-nanodevices (74 μCi) directly into tumour-bearing mice produced a > 45 % reduction in tumour size, whilst the non-radioactive analogue yielded no therapeutic benefit. Similarly, Chanda et al. [68] produced spherical functionalized ^{198}Au with Gum Arabic glycoprotein (GA) nanoparticles (GA-^{198}AuNPs) ranging in size from 12 to 18 nm. A single dose (408 μCi) injected into severely compromised immuno-deficient (SCID) prostate tumour-bearing mice, yielded an 82 % reduction in tumour size (harvested 31 days post-treatment), with no measurable uptake of radioactive materials in non-target organs.

Furthermore, Black et al [145] used various ^{198}Au-doped nanostructures (cubic cages, spheres, disks and rods) to measure the biodistribution, tumour uptake and intra-tumoural distribution of the structures within a murine EMT6 breast cancer model, and successfully imaged the distributions *in vivo* using the gamma and beta emissions as the unstable isotope decayed. This work successfully demonstrated the ability to use the unstable ^{198}Au isotope as a theranostic agent; for targeted brachytherapy and imaging, which allowed for real time analysis. Black et al [145] also reported that significantly more tumour uptake occurred for nanospheres and disks but was limited to the tumour surface, whilst nanorods and cubic cages showed less overall uptake but were more dispersed throughout the entire tumour.

6.1.2 Gold-mercury nanoparticles (AuHgNPs)

Whilst mercury is highly toxic, the number of mercury atoms generated by gold undergoing neutron capture and decaying to mercury is small due to the low cross-section (reaction probability) and is estimated to be approximately 500 ng per 50 mg of AuNP sample used. Williams et al. [146] demonstrated by administering mercuric acetate to human KB cells that mercury acts to decrease cell viability by inducing oxidative stress (via a series of enzyme activations and inhibitions) to promote DNA damage. Other studies have also shown that even low concentrations (10 to 500 μM) of mercury ions (Hg^{2+}) produce a high percentage of cell deaths by both necrosis and apoptosis [147]. Therefore, it is conceivable that if AuHgNPs were administered to a tumour site the small amount of mercury atoms present would still induce negative chemical and biological affects on the tumour cells.

The AuHgNPs may also provide a suitable target for radiotherapy, whereby the high Z number metals would yield additional DE due to secondary electron emissions.

Similarly, if the unstable product containing ^{198}Au was administered to a tumour (after neutron capture), the decay process (via gamma and beta emissions) to ^{198}Hg may also provide an additional localised dose to the tumour site. These effects and how they could impact on the tumour are illustrated in **Figure 6-4**.

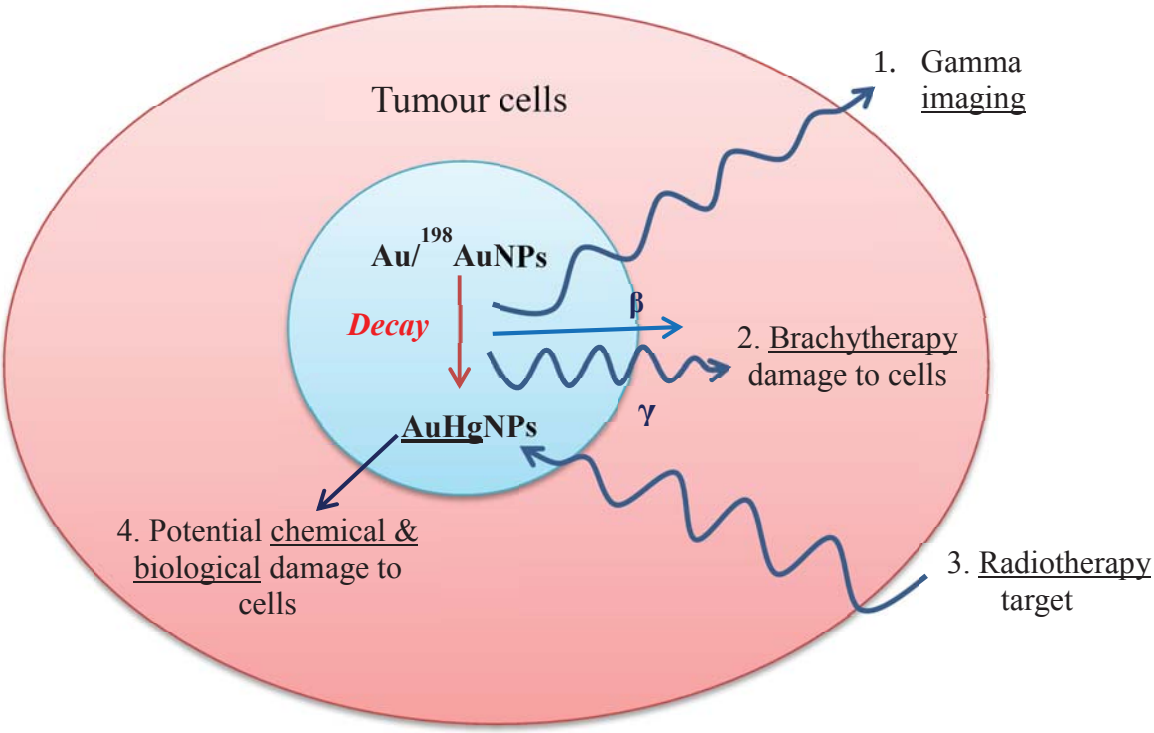

Figure 6-4. The decay of radioactive unstable ^{198}Au isotope to the stable ^{198}Hg isotope within target tumour cells and the four possible uses of the decay process and stable product.

6.2 Methods

This section describes the materials and thermal neutron irradiation conditions to generate BiMetNPs, including sample preparation for ICP-MS analysis and detection methods used to measure the emitted radiation during the decay process.

6.2.1 Neutron irradiation of AuNPs to form AuHgNPs

Neutron irradiations were conducted at the Open Pool Australian Lightwater (OPAL) reactor (20 Megawatt) at the Australian Nuclear Science and Technology Organisation (ANSTO) using the LE2-2 facility, position A (**Figure 6-5**).

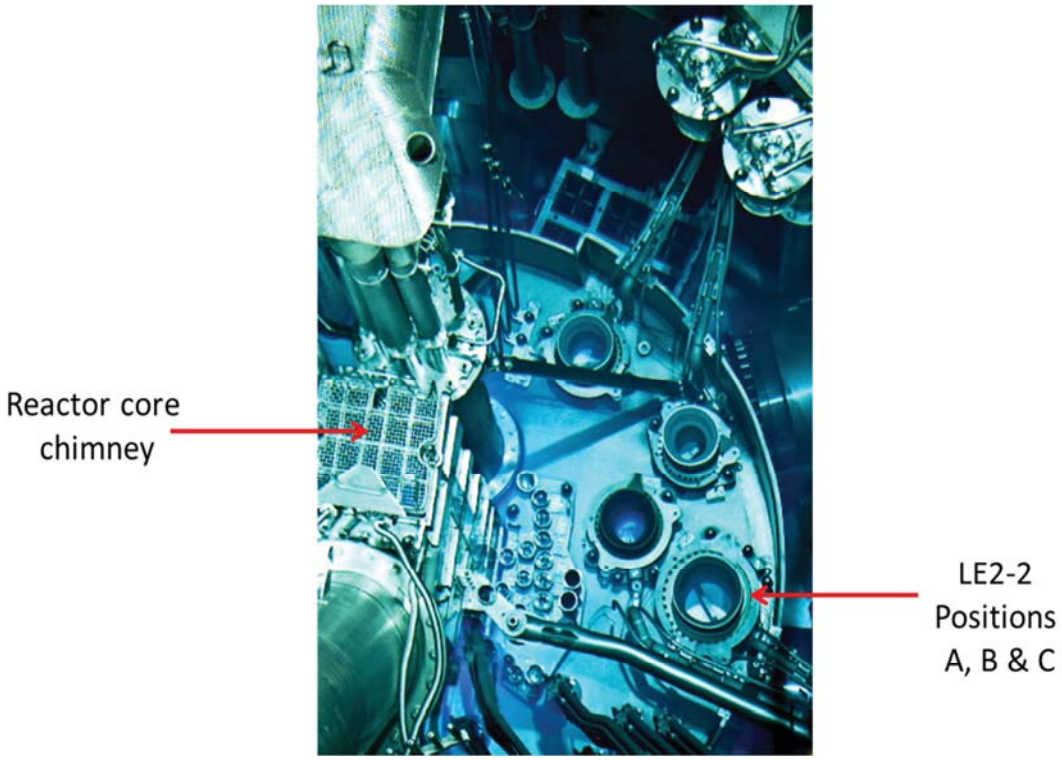

Figure 6-5. Inside the OPAL pool showing the reactor core and placement of samples for neutron bombardment.

AuNP samples were weighed into polyethylene capsules, wrapped in aluminium foil and placed within an irradiation canister (**Figure 6-6**) with a spacer to prevent sample movement. For the long irradiation (used to determine the presence of mercury by ICP-MS) a single capsule containing 51 mg of sample was irradiated for four hours with a neutron flux of approximately 8×10^{12} $cm^{-2}s^{-1}$. For the short irradiation (used only to measure the gamma-decay from ^{198}Au to ^{198}Hg) five capsules containing

approximately 10 mg of sample were irradiated for ten minutes with a neutron flux of approximately 2.8×10^{12} $cm^{-2}s^{-1}$.

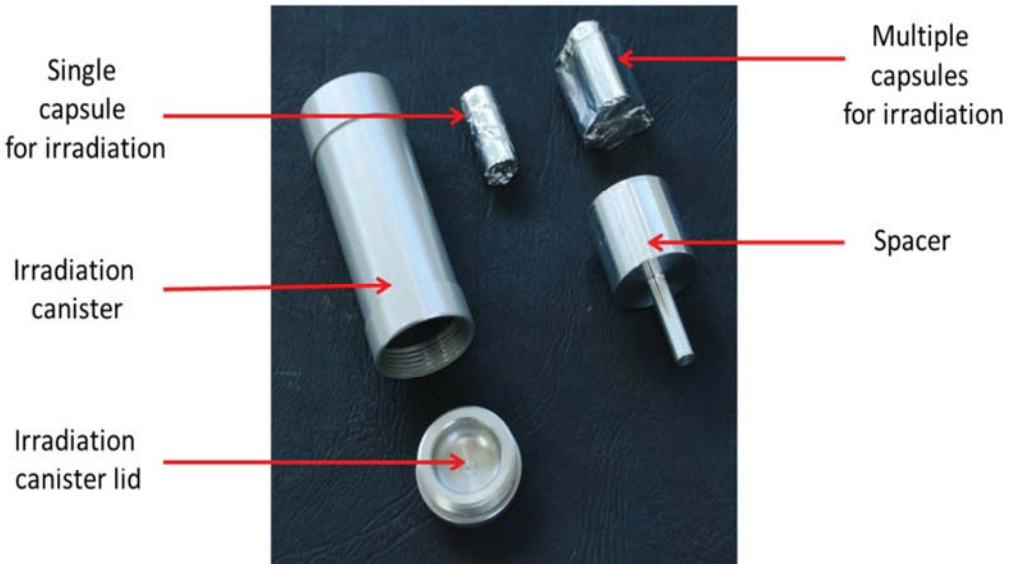

Figure 6-6. The irradiation setup used for neutron bombardment of the AuNPs.

6.2.2 Materials and detectors

All chemicals used in the irradiation process and analysis by ICP-MS were purchased from Sigma Aldrich, of analytical grade, and used without further purification; Gold nanopowder (AuNP), <100 nm particle size (99.9 % trace metals basis), Mercury standard for AAS and ICP (TraceCERT®, 1000 mg/L Hg in nitric acid), Hydrochloric acid (fuming, 37 % for trace analysis) and Nitric acid (redistilled, 70 %, ≥99.999 % for trace metal basis).

The gamma-detectors used for the analysis of the AuNPs following short neutron irradiation were; two types of Gafchromic films of different sensitivities, TLD detectors and OSL nanoDots®. The Gafchromic films self-develop in real time, are near tissue equivalent and do not require processing:

i. RTQA2-1010 (GAFCHROMIC®), dose range 0.02 to 8 Gy, consists of three layers; one active layer (17 microns) between two polyester layers (97 microns).

ii. EBT3 (GAFCHROMIC®), dose range 1 cGy to > 40 Gy EBT3, consists of three layers; one active layer (30 microns) between two polyester layers (50 and 175 microns).

Both films were scanned using an EPSOM Perfection V700 scanner in transmission mode, and analysis was completed using ImageJ software.

TLDs (TLD100) were purchased from Thermo Scientific Harshaw. Each TLD had the following specifications: dimensions; 3.2 x 3.2 x 0.89 mm, containing; lithium fluoride (Li natural) LiF:Mg, dose range; 10 pGy to 10 Gy, and dose accuracy; ±15 (±2 sigma) %. Approximately 24 hours prior to use all TLDs were annealed at 400 °C for one hour and then 100 °C for 4 hours. Measurements were completed using a Harshaw QS 5500 TLD reader at the Alfred Hospital, Department of Radiotherapy, Melbourne, Australia.

Single point OSL nanoDots® were purchased from Landauer. Each dosimeter had the following specifications: dimensions; 10 mm x 10 mm, thickness 2 mm within a plastic covering of 45 mm x 40 mm, containing; aluminium oxide doped with carbon (Al_2O_3:C), dose range for beta (150 keV to 10 MeV); 0.05 mGy to 10 Gy and for photons (gamma and X- rays from 5 keV to 40 MeV); 0.05 mGy to 10 Gy, dose accuracy; ± 5 % for photons and electrons (5 MeV to 20 MeV), total uncertainty per single measurement; +/- 10 %. Approximately 24 hours prior to use all dosimeters were annealed by exposure to fluorescent light tubes (for approximately 12 hours), then pre-scanned using the commercially available microStar® dosimetry reader (Landauer), at RMIT University, Melbourne, Australia.

6.2.3 Preparation of samples for ICP-MS

To identify the presence of mercury in the samples following neutron irradiation a method called acid digestion was employed. Acid digestion is a well-known means of dissolving a solid sample to release the analytes from the product matrix without loss or contamination. The resultant solution is then able to be analysed by ICP-MS [148-152]. Acid digestion of the samples was completed in a fume hood and all glassware was pre-washed with hydrochloric acid to remove organic contaminants. The AuHgNP sample (approximately 26 mg, following long irradiation) was added to a glass conical flask (50 mL), and 10 mL of aqua regia (2 mL HCl: 8 mL HNO_3) was slowly added at room temperature with gentle stirring. A glass stopper was placed in the top of the flask, so that excess gases could escape, whilst preventing contaminants from entering (**Figure 6-7**). The mixture was left at room temperature overnight (approximately 16 hours) so that complete digestion of the sample occurred, and yielded a dark orange solution (**Figure 6-7**).

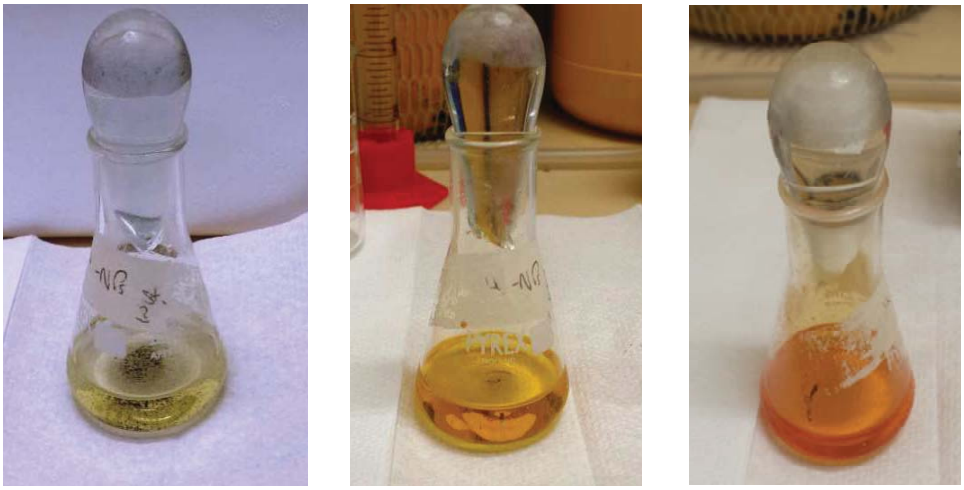

0 hours ~3 hours – ~16 hours

Figure 6-7. The acid digestion of the irradiated AuNPs over time, showing the solid sample digestion (the colour darkens with time). The mercury atoms were released from the product matrix and the solution was then analysed by ICP-MS.

Three ICP-MS samples were prepared containing 1 mL, 2 mL and 3 mL of the digested sample in solution. All solutions were filtered (Millex®, syringe filter 0.45 µm pore size) into 15 mL centrifuge screw top tubes (Corning®, PET, sterile) and the volume total made up to 10 mL with Milli Q water. Measurements were completed using the Agilent Technologies ICP-MS with laser ablation capability, and ASX-500 Series Autosampler.

The ICP-MS detects the ions of interest by the process shown in **Figure 6-8 a & b**. The samples are diluted prior to introduction into the ICP-MS, and then nebulized to form an aerosol. A carrier gas takes the aerosol to the high temperature argon plasma torch (approximately 6000 to 10000 K) where it is vaporized, atomized, and ionized (mainly into singly charged positive ions). The ions are extracted and focused using a series of ion lenses, then separated by the quadrupole mass analyser by their mass/charge ratio, and detected by an electron multiplier (**Figure 6-8b**).

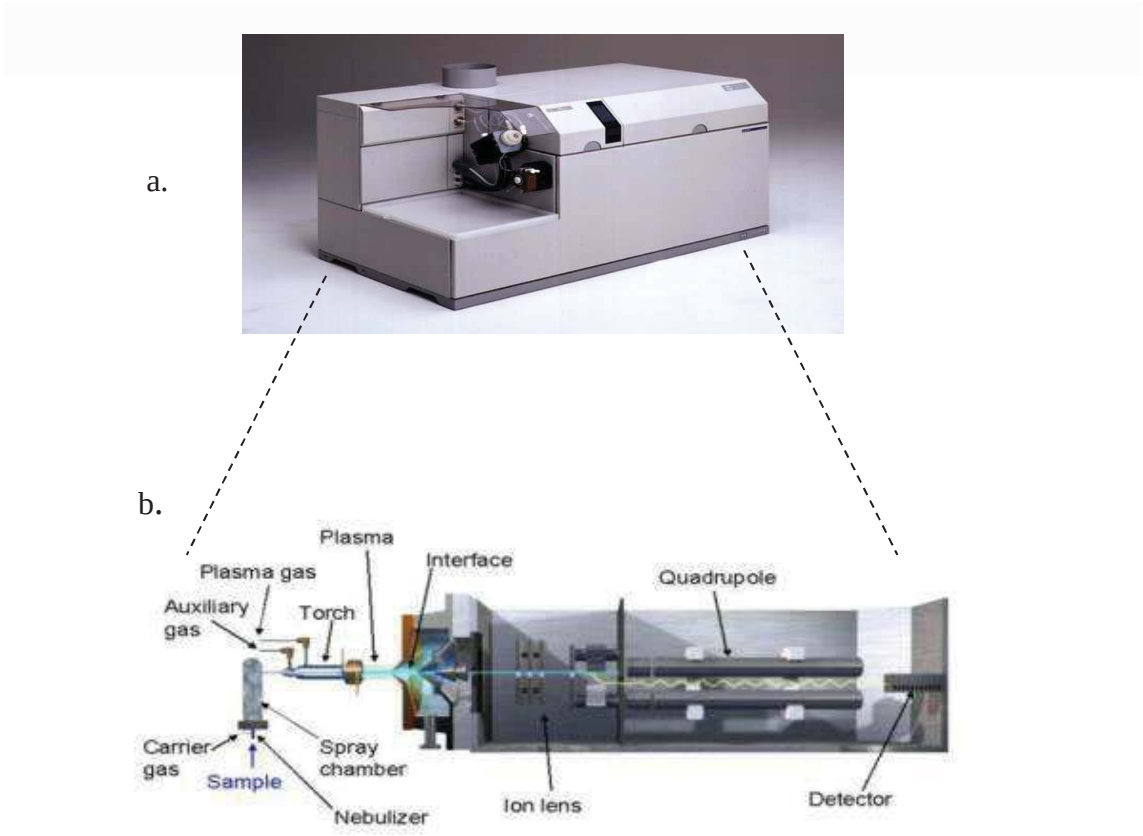

Figure 6-8 a & b. The Agilent Technologies ICP-MS (a) showing the inner workings (b) from the induction of the liquid sample through to its detection

6.2.4 Gamma detection for short-irradiated samples

Five vials containing approximately 10 mg of neutron irradiated AuNP (short irradiation) were placed on top of two sheets of Gafchromic film; RTQA2-1010 (top layer) and EBT3 (bottom layer) (**Figure 6-9**). This was done as the EBT3 film is more sensitive to low-doses (**Section 6.2.2**), and capable of detecting gamma-emissions through the RTQA2-1010 film, thus providing an additional set of measurements for the decay process. Two TLDs were placed on either side of the vial and an OSL nanoDot® on top (**Figure 6-9**).

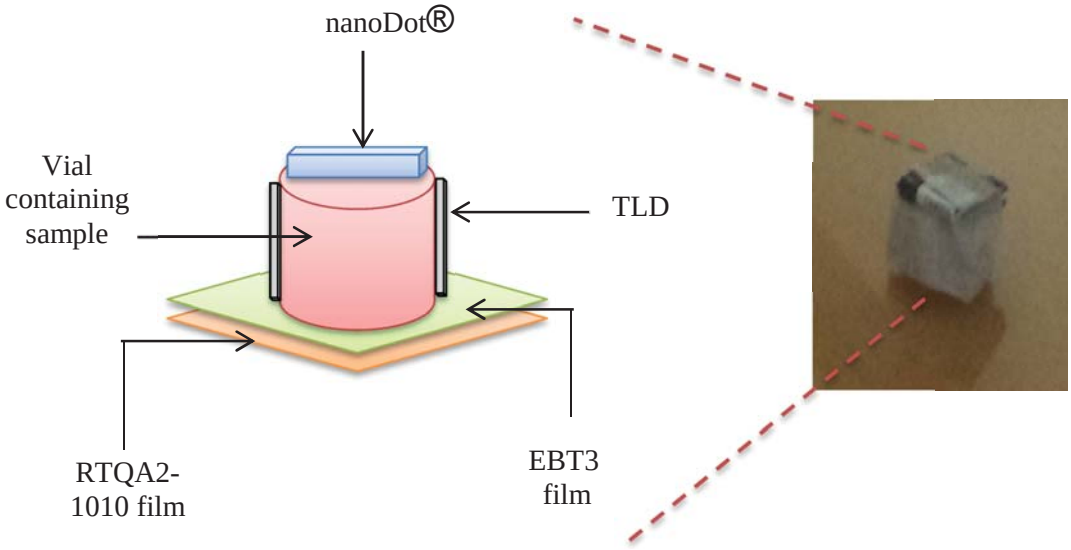

Figure 6-9. The sample vial showing the positioning of the OSL nanoDot® (top of vial) and two TLDs (sides of vial) and two Gafchromic films (under the vial).

The TLDs, OSL nanoDot® and films were removed from the sample vials at different time points as presented in **Table 6-1**.

Table 6-1. Time points that the TLDs, OSL nanoDot® and films were removed from sample vials 1 to 5.

	Time removed (exposure time) in hours			
Sample number	**TLD (x2)**	**OSL nanoDot®**	**RTQA2 film**	**EBT3 film**
1	2.5	2.5	2.5	2.5
2	4	4	4	4
3	6	6	6	6
4	8	8	8	8
5	10	10	10	10

6.3 Results

The results for the formation of the AuHgNPs after long irradiation with thermal neutrons (≃ 0.025 eV) are presented below. The gamma spectrum was taken after

sufficient decay time for the sample to be handled (approximately 96 hours, because of the high activity following removal from the reactor) and confirms the presence of the main ^{198}Au peak at 412 keV due to gamma-decay, and the minor peaks at 676 keV and approximately 1088 keV as indicated in **Figure 6-10**. Additional peaks in the spectrum indicate the presence of contaminant isotopes, mainly silver and iridium, which are lower in intensity, and concentration, and have shorter half-lives than the Au peaks of interest.

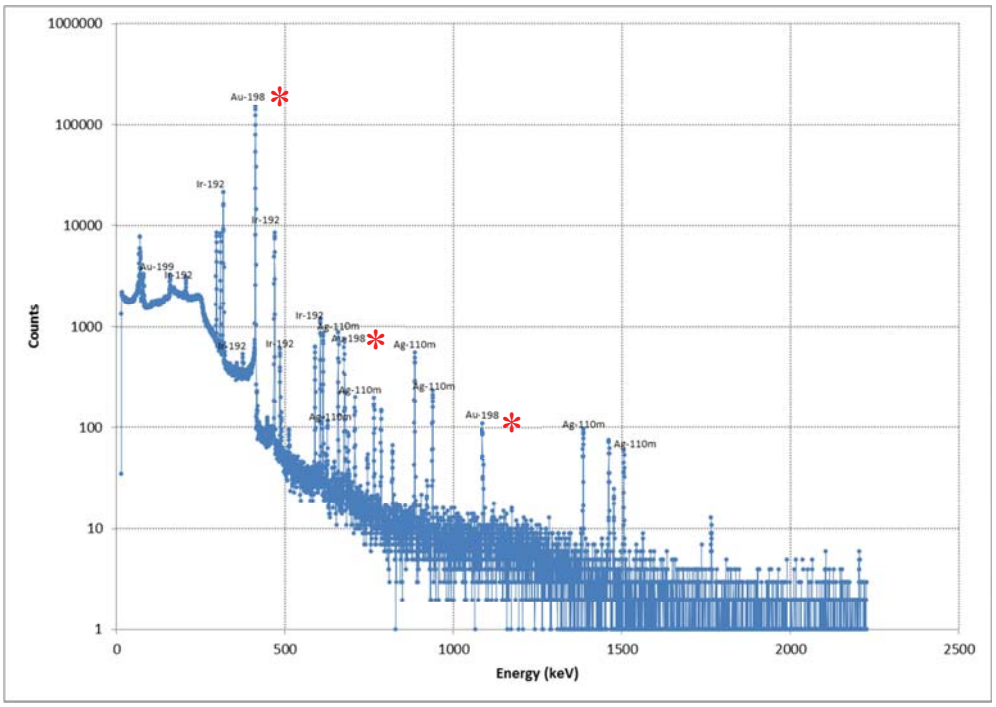

Figure 6-10. The sample after long irradiation showing the presence of ^{198}Au (indicated) which decays via gamma and beta emissions to ^{198}Hg.

6.3.1 ICP-MS and formation of AuHgNPs (long irradiation)

After thermal neutron bombardment the samples were digested in strong acid to release the mercury isotopes from the sample matrix (**Section 6.2.3**), for detection by ICP-MS. Three samples containing 1, 2 and 3 mL of the digested product were

analysed, and the amount of ^{198}Hg isotope present in each sample determined. The detection of the naturally more abundant mercury isotope ^{202}Hg was also examined and the results are presented in **Table 6-2**.

Table 6-2. The results for the three samples of AuHgNP product formed after long neutron irradiation of the AuNP starting material, showing the detection of the two isotopes ^{198}Hg and ^{202}Hg by ICP-MS.

	^{198}Hg (prod)		^{202}Hg (prod)	
	Conc. (ppb)	Ratio (CPS)	Conc. (ppb)	Ratio (CPS)
Hg Std 1	0	0	0	0
Hg Std 2	50	0.044	50	0.132
Sample 1	19.443	0.017	1.191	0.003
Sample 2	74.384	0.066	1.274	0.004
Sample 3	142.519	0.125	0.989	0.003

The ratio of the ^{198}Hg isotope and the ICP-MS internal standard (^{209}Bi) in counts per second (CPS) are plotted against the concentration (ppb) and shown in **Figure 6-11**.

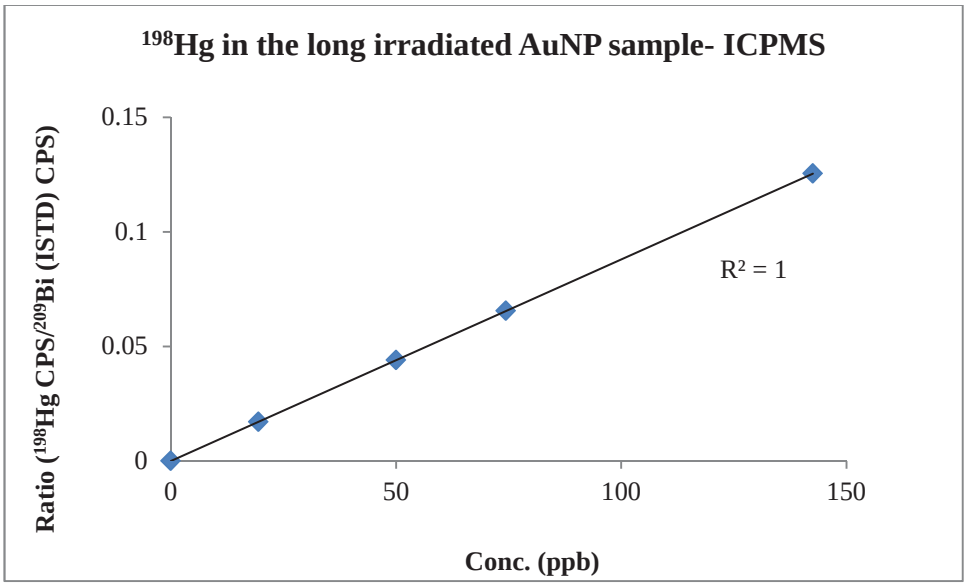

Figure 6-11. Plot showing the increasing concentrations of ^{198}Hg in samples 1 to 3 (after long thermal neutron irradiation and acid digestion) as detected by ICP-MS (mercury standards are at 0 and 50 ppb).

The non-irradiated AuNP starting material was also analysed for the presence of the ^{198}Hg and ^{202}Hg isotopes. From a stock sample solution containing 70 mg of AuNPs in 10 mL HNO_3, three samples of 1, 2 and 3 mL were removed and made up to 10 mL with Milli Q water and analysed, the results are shown in **Table 6-3**.

Table 6-3. The results for the starting material AuNP (non-irradiated) samples analysed by ICP-MS for the presence of the two isotopes ^{198}Hg and ^{202}Hg.

	^{198}Hg Conc. (ppb)	^{202}Hg Conc. (ppb)
Std 1	0	0
Std 2	50	50
Sample 1	0.379	0.389
Sample 2	0.359	0.342
Sample 3	0.265	0.259

6.3.2 Gamma decay of ^{198}Au to ^{198}Hg (short irradiation)

The gamma decay of ^{198}Au to ^{198} Hg was measured using three different dosimetry methods (**Figures 6-9**); Gafchromic films (RTQA2-1010 and EBT3), TLDs and OSL nanoDots®, and the results are presented below.

6.3.2.1 Gafchromic film γ-decay response

Films were collected after 2.5, 4, 6, 8 and 10 hours exposure time to the activated samples and scanned in transmission mode, and the results are shown in **Figure 6-12**.

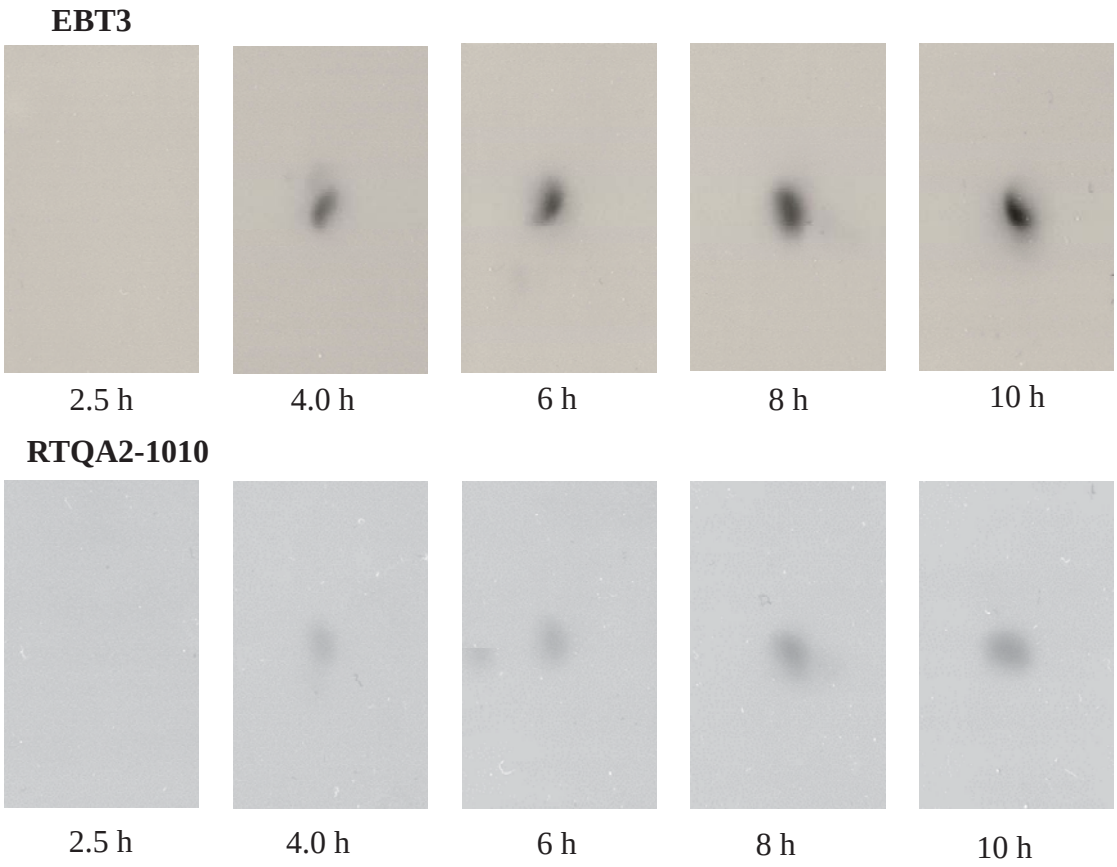

Figure 6-12. EBT3 (top) and RTQA2-1010 (bottom) Gafchromic film after exposure to the irradiated ^{198}Au samples decaying to ^{198}Hg over time (Note: the RTQA2-1010 film was positioned under the EBT3 film and has a fainter response).

The films were analysed using ImageJ software and a plot profile taken over a known distance (where darkening of the film had occurred) for each exposure time. Using the plot profiles (**Figures 6-13** and **6-15**), the maximum possible gray-scale value (200) was assigned a '0 % dose response' and the minimum gray-scale value (0) a '100 % dose response. A dose-response percentage (%) was then determined for each plot-profile using the gray-scale value at each peak minima (**Figures 6-13**) and plotted against the exposure time (**Figures 6-14** and **6-17**).

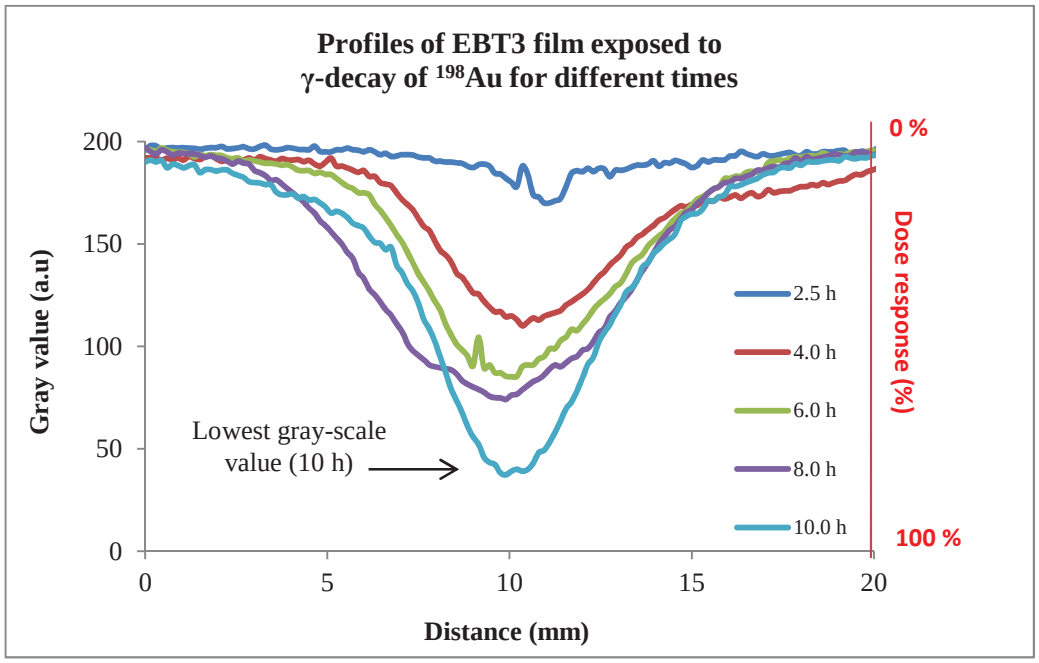

Figure 6-13. Analysis of the EBT3 films after exposure to ^{198}Au, showing an increase in the dose response value (%) with increasing exposure time to the γ-decay of ^{198}Au.

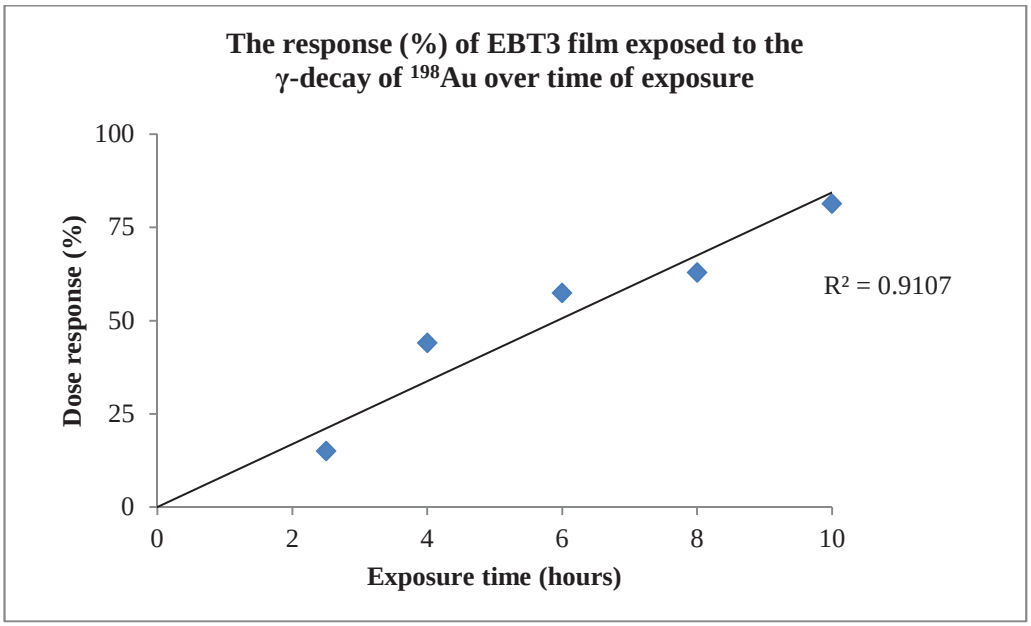

Figure 6-14. The dose response (%) determined for EBT3 films versus the length of time of exposure to the γ-decay of ^{198}Au.

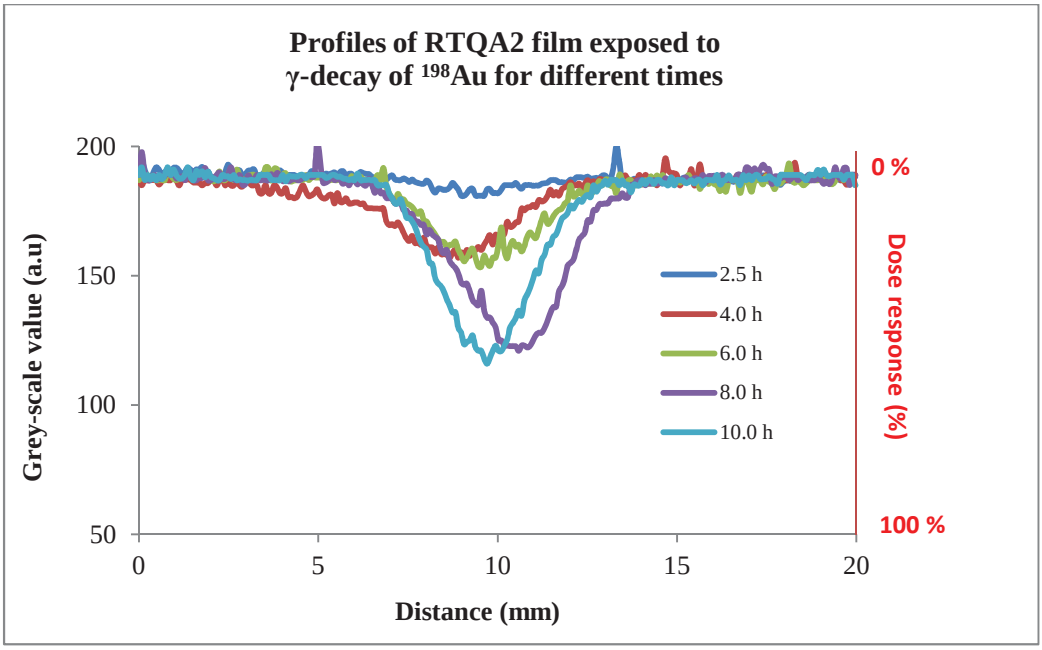

Figure 6-15. Analysis of the RTQA2 films after exposure to ^{198}Au, showing an increase in the dose response value (%) with increasing exposure time to the γ-decay of ^{198}Au.

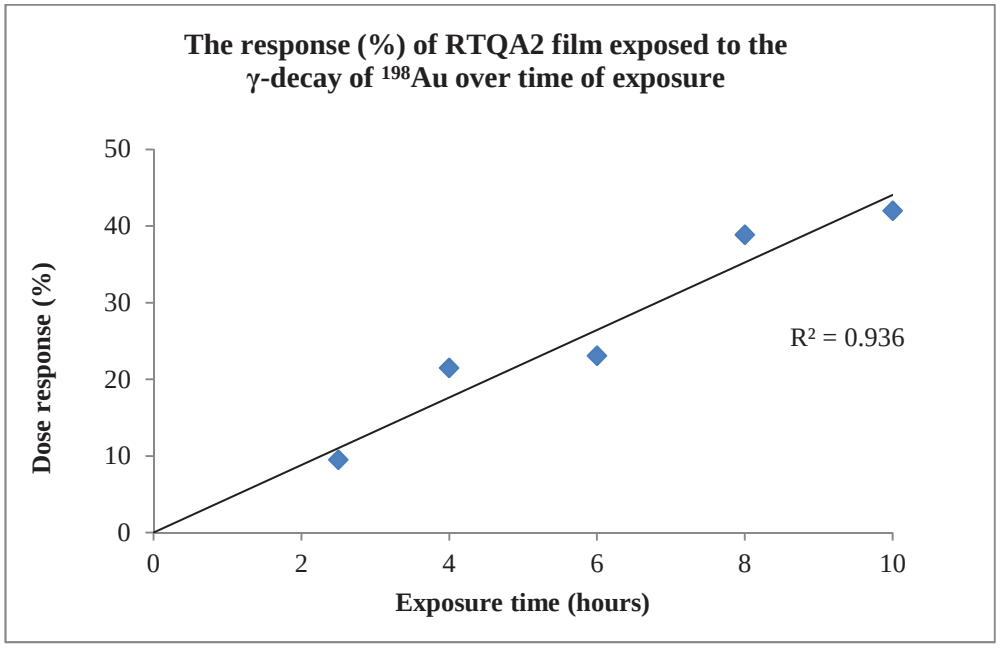

Figure 6-16. The dose response (%) determined for RTQA2 films versus the length of time of exposure to the γ-decay of ^{198}Au.

6.3.2.2 OSL nanoDot® gamma decay response

Results for the OSL nanoDots® were obtained by placing one on each lid of the sample vials (**Figure 6-9**), which were removed after 2.5, 4, 6, 8 and 10 hours exposure time, and plotted against the determined dose (mGy) received (**Figure 6-17**).

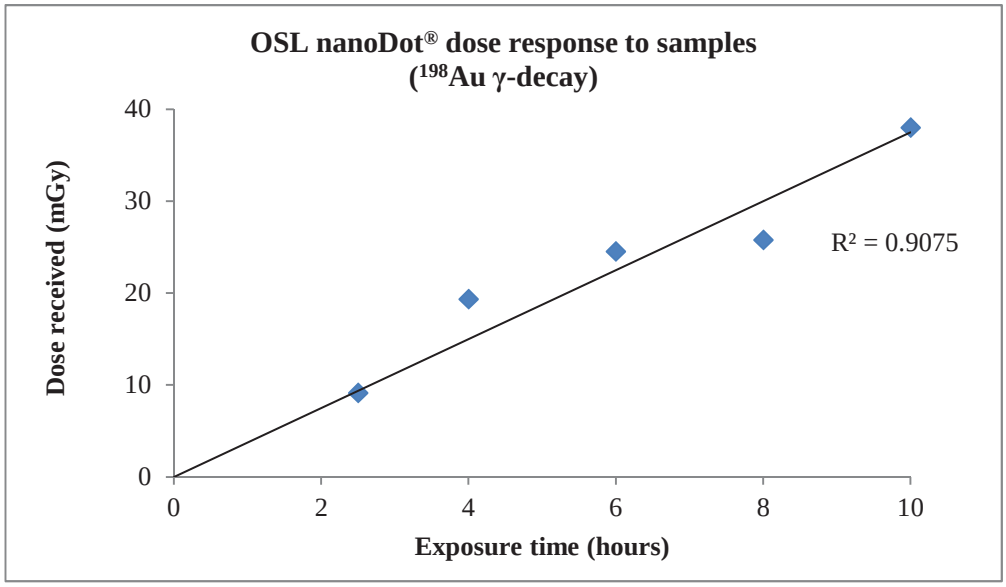

Figure 6-17. Plot of the OSL nanoDot® response to the γ-decay of the samples from ^{198}Au to ^{198}Hg over time.

6.3.2.3 TLD gamma decay response

The TLDs were positioned on either side of each sample vial, and the dose received determined for each TLD, which was averaged and plotted against the exposure time (**Figure 6-18**).

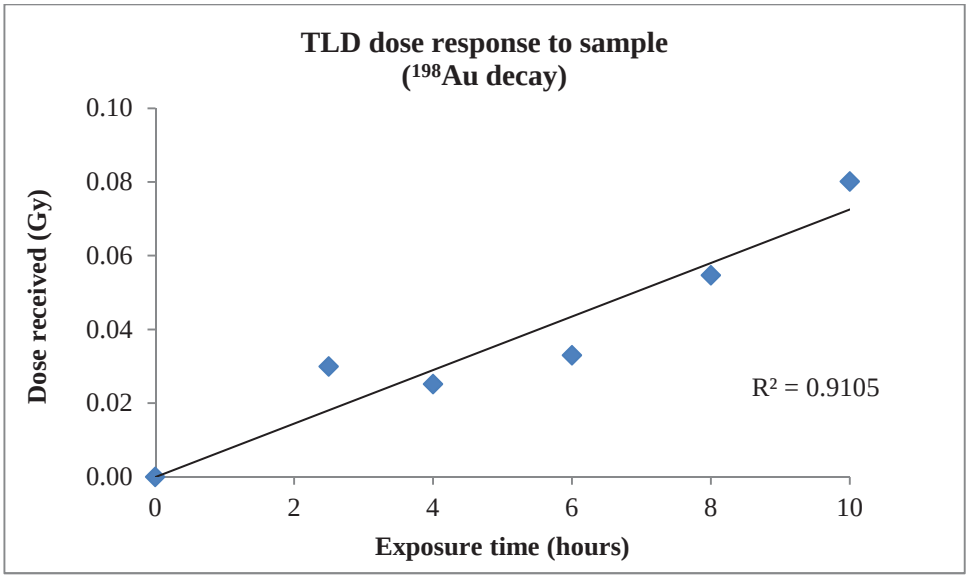

Figure 6-18. Plot of the TLD response to the γ-decay of the samples from ^{198}Au to ^{198}Hg over time.

6.4 Discussion

In this section, the analysis of both the BiMetNP product and AuNP starting material by ICP-MS is examined, and the results for the detection of the gamma-decay of the unstable ^{198}Au isotope following neutron capture.

6.4.1 ICP-MS analysis of AuHgNPs

The ICP-MS confirmed the presence of the ^{198}Hg isotope (**Table 6-2** and **Figure 6-11**) following neutron bombardment. The high R^2 value; 1.000 is reflective of the good linearity between the ratio of CPS for the ^{198}Hg atoms present versus the ICP-MS internal standard (^{209}Bi) and the concentration (ppb) of the isotope present in each sample. Clearly evident is the increase in ^{198}Hg concentration as the sample volume also increases; 19.443 ppb (sample 1, 1 mL) to 142.519 ppb (sample 3, 3 mL) and the CPS ratio of ^{198}Hg to standard ^{209}Bi; 0.017 (sample 1) to 0.125 (sample 3).

No such increase in the concentration of the naturally more abundant ^{202}Hg isotope was evident, with levels remaining consistent (approximately 1 ppb) for all three samples (**Table 6-2**). These results confirm that the higher ^{198}Hg concentrations in the product material (AuHgNPs) can only be due to successful neutron capture occurring, and not natural occurrences.

To further confirm that neutron capture had occurred, the un-irradiated AuNP starting material was also analysed and the initial amount of ^{198}Hg isotope present in the sample determined. The AuNP starting material (70 mg) was dissolved in HNO_3 (10 mL), and three samples of 1, 2 and 3 mL volumes removed and made up to 10 mL with Milli-Q water. Despite using a larger mass of the AuNP starting material (70 mg compared to 26 mg of the irradiated product) the ICP-MS analysis (**Table 6-3**) confirmed that all three samples contained much lower levels of the ^{198}Hg isotope (approximately 0.3 ppb), compared to that detected for the BiMetNP samples (approximately 19 to 143 ppb) (**Table 6-2**).

Overall the ICP-MS results confirmed the formation of the ^{198}Hg stable atom resulting from the decay of ^{198}Au, and that thermal neutron capture had occurred. Furthermore, these results support the use of this method as a viable alternative for the synthesis of BiMetNPs.

6.4.2 Gamma decay

The gamma energy spectrum of the activated AuNPs was measured by a germanium/lithium Ge(Li) detector, with a calibrated multi-channel analyser, and a typical spectrum is displayed in **Figure 6-10**. From the spectrum the dominant gamma-emissions come from the activated ^{198}AuNPs, with some additional smaller contaminant

peaks present; mainly silver and iridium. However, these products are of lower intensity and concentration, and have shorter half-lives, meaning that their contribution to this analysis is low. The gamma decay of ^{198}Au to ^{198} Hg was measured over time using three different dosimetry methods and is discussed below.

6.4.2.1 Gafchromic film response

Both films (**Figures 6-12**) showed a clear darkening over time when exposed to the activated samples, indicating gamma-emission detection. Analysis of the films yielded plot profiles (**Figures 6-13** and **6-15**), which gave a dose response (%) for each time point investigated, which was plotted against the exposure time (**Figures 6-14** and **6-16**). Both films yielded high regression values (R^2), with a higher dose response (%) evident for the EBT3 film (and more visual darkening) (**Figure 6-13**) compared to the RTQA2-1010 film (**Figure 6-15**). Interestingly, the RTQA2 film had a slightly higher R^2 value (0.936) compared to the EBT3 film (0.911) despite emissions having to pass through the sample vial container and the EBT3 film above it, and may be indicative of its higher sensitivity to low-doses.

Overall the good agreement between the films highlights that low-level gamma emissions are detectable and deliver dose from the decaying ^{198}Au sample. This is advantageous for any potential future use of the decay process for either gamma-imaging or as a brachytherapy type source for additional dose deposition within a tumour (numbers 1 and 2 in **Figure 6-4**). It should be noted that the films used in this study are designed for dosimetry and radiotherapy usage, and not imaging, meaning that the gamma-emission levels detected were relatively high. Given that the films are not energy dependent, other gamma-emitters have also contributed to the measured dose determined (**Figure 6-11**), however their contributions are low.

6.4.2.2 OSL nanoDot® response

Using OSL nanoDots® positioned on the sample lid (**Figure 6-9**) measurements were taken after 2.5, 4, 6, 8 and 10 hours exposure time. A linear response was obtained for the dose received (mGy) versus the exposure time, with a R^2 value of 0.908 (**Figure 6-17**), which is comparable to the EBT3 Gafchromic film (0.911), suggesting that this method is also a reliable means of detecting gamma emissions from the decaying ^{198}Au sample.

6.4.2.3 TLD response

The response of the TLDs (two per sample) (**Figure 6-18**) showed good agreement between the readings for dose received (Gy) versus the exposure time, with a high R^2 value; 0.911, which is comparable to the film and OSL values. Therefore, TLDs are also an adequate means for detecting gamma emissions, with all three methods confirming a linear dose response over time.

6.5 Conclusions

An alternative method for the production of BiMetNPs was successfully completed by thermal neutron bombardment of the starting monometallic-nanoparticles (AuNPs) to produce the stable AuHgNPs. This method is advantageous as current wet-chemistry methods are limited in their ability to produce BiMetNPs consisting of two different metals present as an alloy, and therefore, expands on the current means available. The presence of the ^{198}Hg isotope in the product material was confirmed by ICP-MS, and the decay process of the unstable isotope ^{198}Au to the stable ^{198}Hg (via gamma emissions) was successfully measured using three different detection systems; Gafchromic films (EBT3 and RTQA2), OSL nanoDots®, and TLDs. All three methods

showed good linear responses with high regression values, and highlights the potential future use of the decay process of the unstable ^{198}Au isotope as a theranostic agent; providing both gamma-emission imaging and brachytherapy dose deposition (i.e. therapeutic benefit). As well, the BiMetNP (AuHgNP) product offers an additional target for external radiotherapy, and may also act chemically and biologically to damage tumour cells.

Chapter 7: Conclusions and future directions

7.1 Conclusions

The work undertaken in this thesis and the results generated are both novel and innovative, and provide greater insight into key areas of radiotherapy research. This thesis has focused on five main areas with the aims and findings summarised below:

7.1.1 Chapter 2- Dose enhancement due to AuNP size, concentration and beam quality

This chapter focused on the effects of smaller sized AuNP sizes, mainly due to the limited amount of current research examining this size range, and the AuNP sizes that were available for use and their cost. The effects of AuNP size and concentration when irradiated with different beam types (X-ray, protons and electrons) and the DE levels achieved were investigated, with a strong emphasis on proton irradiations. The use of proton therapy beams has increased worldwide over the last decade and been the focus of much research due to the unique energy deposition profile. However, conflicting reports on the DE levels obtained when irradiating AuNPs between animal/cell studies and computer simulations was of interest, and was the main focus of this work. Using an experimental approach, whereby; AuNPs were embedded within

the dosimeter alanine, the DE levels were directly related to the amount of alanine radicals formed, which was analysed by EPR analysis.

The main findings of this work were:

- Low energy X-rays (80 kV) yielded the highest overall DE levels, which were linearly dependent on AuNP concentration (3, 2 and 1 %), with the highest AuNP concentrations (3 %) yielding the highest DE levels. As well, the smallest AuNP size (1.9 nm) yielded the highest DE levels (which is consistent with having a larger surface area). All findings were in agreement with recent Monte Carlo simulations [89, 99, 101]. However, as only a few sizes were examined, and the 15 nm AuNP size gave larger DE levels than the 5 nm AuNP, further investigations using more sizes are needed to determine the causes of this result.

- For MV X-ray irradiations of AuNPs DE levels also showed a clear dependence on AuNP concentration, although this was not as high as those observed for kV X-rays due to the increased dominance of Compton interactions at this energy range, and was in agreement with literature reports. Similar to the kV X-ray irradiations, the smallest AuNPs (1.9 nm) yielded the highest DE levels, followed by the 15 nm and 5 nm AuNPs, however, the responses were not as clear as the effects of AuNP concentration, and was in agreement with recent computer simulations [92, 98].

- The DE results for electron and proton irradiations of AuNPs showed no dependence on AuNP concentration or size, and agreed well with published cell studies using electron beams, and proton simulation data [24, 79, 81, 102]. These results suggest that the much larger DE results observed for proton irradiation of AuNP loaded tumours in cell and animal studies was not mainly due to an increase

in the yield of radical species. Therefore, it is likely that other biological and chemical processes are occurring, such as, AuNP catalysis and the formation of reactive species (including ROS), which are not accounted for in computer simulations or the experimental design used in this work. More recently, there has been an increase in studies reporting these types of interactions as possible causes for the greater radiosensitization observed in cell/animal studies when irradiating AuNPs with high LET beams [90, 108, 109]. Therefore, for high-energy proton beams the recent Monte Carlo simulations provide a good estimate of the enhanced radical yield following addition of AuNPs to alanine.

- Finally, it can be concluded that alanine dispersed in wax can be used effectively as a phantom/dosimeter for all radiation types used in radiotherapy including protons. This work also presented a novel means to experimentally determine the DE caused by secondary electron emissions from AuNPs by impregnating them within the 'reporter' dosimeter alanine.

7.1.2 Chapter 3- Examination of the novel dosimeter IRGANOX®1076

The work undertaken in this chapter helped to improve the current knowledge about the novel EPR-dosimeter IRGANOX®1076 and highlighted some of its advantages for potential use in radiotherapy. The manufactured IWSS pellets yielded a single EPR peak due to the formation of the phenoxyl radical, and were of sufficient sensitivity for dose quantification over the range of 2 Gy to 20 Gy for all radiation beams investigated (kV & MV X-rays, electron and protons). Furthermore, the use of IRGANOX®1076 is advantageous due to its simple EPR spectrum, good long term

post-irradiation signal stability, tissue equivalence, low toxicity, low cost, and high wax solubility, meaning it can be moulded to any shape and size dosimeter required.

The major findings were:

- The IWSS pellets gave a linear dose response for all types of radiation examined, which was LET independent in the MV energy range and for electron and proton beams, and energy-dependent in the kV X-ray ranges.

- Irradiations of the IWSS pellets yielded the highly stable phenoxyl radical as an EPR singlet, due to complete hydrogen abstraction. Previous work by other groups [120] had incorrectly identified the EPR-doublet signal as the phenoxyl radical, however, this work conclusively showed that the doublet signal is in fact due to the formation of the phenol cation radical, obtained by electron loss following irradiation of the crystalline solid.

- Post-irradiation EPR measurements of the proton irradiated samples, stored in the dark and at room temperature, showed good signal stability with minimal signal fading (between 1.6 to 3.8 %) up to 77 days post-irradiation. However, after 466 days post-irradiation, signal fading was apparent, and highlighted the need for controlled storage conditions (temperature and humidity) to reduce the effects of signal fading for long-term measurements.

- The wax used to manufacture the IWSS pellets was found to be an ideal supporting medium in which IRGANOX®1076 completely dissolved. Under these

circumstances a single EPR singlet was observed which, unlike alanine, has an intensity independent on the orientation of the sample within the EPR cavity.

- The EPR signal intensity of the IWSS pellets was comparable to alanine-wax pellets containing the same amount of dosimeter material (w/w), whilst the shortcomings associated with the use of alanine in dosimeters (sensitivity at low dose, reproducibility of EPR spectra, multiple radical species, hydrophilicity, angular dependence of the EPR spectra) are either substantially or completely eliminated in the case of IRGANOX®1076.

7.1.3 Chapter 4- A Comparison of the EPR angular response of alanine and IRGANOX®1076

As alanine is highly hygroscopic, air moisture can promote post-irradiation radical transformations, and consequently alter the resonance within the EPR cavity. Both these effects can cause changes in the amplitude of the EPR central peak, and influence measurement reliability. Therefore, this work examined the angular response of alanine encased within wax as a means to reduce these effects. The alanine-wax samples were compared with alanine powder samples (in capsules), commercially available alanine pellets and IRGANOX®1076 powder samples also encased within wax. All samples were measured over the same time intervals post-irradiation (3 and 30 days) and multiple measurements at different angles within the EPR cavity taken.
The major findings of this work were:

- Dispersing alanine powder within wax, so that the wax is the bulk component of the pellet helped to physically protect the alanine from external water and reduce its

EPR angular response.

- At 3 days post-irradiation deviation ranges for the alanine-wax pellets were low, and comparable to the values obtained for commercially manufactured alanine pellets (where alanine is the bulk component).

- After 30 days post-irradiation the protection provided by the wax pellets to alanine was more evident, with the deviation ranges remaining largely unchanged to that at 3 days post-irradiation. Conversely, deviation ranges for the commercial pellets had nearly doubled, despite being stored in controlled conditions (at reduced temperature and humidity).

- Investigations of the wax pellets containing alanine that were manufactured more than eight months prior showed a high angular dependence at 3 days post-irradiation, suggesting environmental water contamination had occurred. This result highlighted the importance of using the samples within a reasonable time frame after manufacture and storing the samples in a controlled environment (with humidity and temperature controlled).

- IRGANOX®1076 encased within wax (containing w/w the same amount of dosimetric material) yielded the lowest angular responses overall. This low response was attributed to the hydrophobic structure and the formation of a single radical species when irradiated.

7.1.4 Chapter 5- Investigation of the novel method 'spiking' to determine low doses (< 2 Gy) using alanine dosimeters

The spiking method detailed in this chapter allows for doses ≤ 1 Gy to be reliably detected by alanine dosimeters, and overcomes the current limitations that hinder its use in radiotherapy. This work allows for alanine dosimeters to be used in a far wider range of applications in radiation dosimetry, particularly for the low doses often relevant for clinical applications.

The major findings of this work are:

- The addition of a spike dose increases the alanine dosimeters EPR signal making it easily detectable to an X-band EPR instrument.

- After the addition of a second low dose, the spike signal can be subtracted from the total signal (spike + low dose) and the low-dose reliably determined. Either the amplitude or single integration of the central alanine peak P1 can be used for quantification, with both capable of quantifying doses of 0.5 Gy.

- The advantages of the spiking method are that no foreign materials are added to the alanine dosimeters, thus tissue equivalence is maintained, the EPR signal to noise ratio is improved, and baseline distortions typical at low doses are removed due to the large spike dose given.

- Furthermore no complex EPR post-analysis is required and this method can be performed on any standard X-band EPR spectrometer.

7.1.5 Chapter 6- The formation of bimetallic-nanoparticles by neutron capture

An alternative nuclear method for the production of alloy-type BiMetNPs was successful, whereby, the target product (AuHgNPs) was formed by neutron activation of the starting metallic-nanoparticles (AuNPs). The decay of the unstable ^{198}Au isotope was successfully monitored over time.

The major findings of this work were:

- Thermal neutron activation resulted in the formation of the unstable ^{198}Au isotope.

- Decay of the unstable ^{198}Au isotope yielded the stable AuHgNP product containing the mercury isotope ^{198}Hg, which was confirmed by ICP-MS.

- An increase in the concentration of the ^{198}Hg isotope was consistent with an increase in the sample size analysed by ICP-MS. However, this was not so for the naturally more abundant ^{202}Hg isotope, which can only occur due to neutron capture during the irradiation process.

- The gamma decay of ^{198}Au to ^{198}Hg was successfully measured using Gafchromic films (EBT3 and RTQA2), OSL nanoDots® and TLDs which yielded linear responses over time.

7.1.6 Summary

Overall the work undertaken in this thesis adds to the current knowledge of the interactions between AuNPs and commonly used radiotherapy beams, and the levels of

DE due to the production of secondary electrons. The novel method of neutron activation of AuNPs has been shown to occur and the target BiMetNP alloy product formed. This provides a viable alternative to the wet-chemistry techniques currently used for BiMetNP production. Furthermore, a novel technique (spiking) to improve the sensitivity of alanine dosimeters for possible use in radiotherapy (for doses of less than 5 Gy) was investigated and shows potential to develop the current application of alanine dosimeters, as well as, the use of wax-encasement to reduce the EPR angular response for alanine samples. Also, the novel dosimeter IRGANOX®1076 shows much promise for use in radiotherapy, with good signal stability and response to different quality beams within radiotherapy dose ranges. Though limitations in this work due to funding, material availability and access to irradiation facilities have prevented more extensive studies being carried out, many key findings have been explored, offering an array of areas for future investigations, which are discussed below.

7.2 Future directions

Based on the results determined in the five key areas of research undertaken, possible future directions and areas of extended research are presented below.

7.2.1 Chapter 2- Dose enhancement due to AuNP size, concentration and beam quality

The use of alanine as a dosimeter embedded with AuNPs in wax provided a reliable means to determining the DE levels with varied AuNP size and concentration, as well as the irradiation beam type used. However, the AuNP size results for kV and MV x-ray irradiations showed a DE level preference for 1.9 nm followed by 15 nm and

finally 5 nm. It is not clear why the 15 nm AuNPs gave a higher DE response than the 5 nm, warranting further investigation.

Therefore, two studies are proposed for future work to elucidate this anomaly:

- To extend the AuNP size analysis by examining a larger size range, ideally between 1- 80 nm, which may help to further the understanding between AuNP size and DE levels for kV and MV X-ray irradiations.

- Using the same experimental approach (AuNP embedded in alanine) to determine the effects of the AuNPs polymeric capping, which may reabsorb ejected electrons and subsequently cause a decrease in the resultant alanine EPR signal obtained.

Another area for potential examination is in proton irradiations, where the DE levels obtained showed no clear dependence on AuNP concentration or size. These findings strongly suggest that the higher DE levels reported in animal and cell studies (using AuNP loaded tumours irradiated with protons) was due to other processes. Currently it is thought that AuNPs present in biological systems act to promote/catalyse other chemical processes (mainly the formation of ROS), which are responsible for the higher efficacy reported.

Therefore future areas of study could include:

- To examine the effects on ROS concentrations using various cell types when AuNPs of different sizes and concentrations are present, with a focus on irradiations with high LET beams.

- Also, the effects of the AuNP polymeric capping could be investigated, with a focus on how the presence of cationic or anionic groups at the NP surface, impacts on ROS production, and cell viability.

7.2.2 Chapter 3- Examination of the novel dosimeter IRGANOX®1076

The IWSS pellets manufactured were of sufficient sensitivity for dose quantification over the range 2 Gy to 20 Gy for all radiation beams investigated (kV & MV X-rays, electron and protons), and were comparable in their response to alanine.

Therefore, other possible future directions for investigation are:

- Irradiation measurements using other beam types, particularly high LET beams, such as neutrons and carbon ions, would be of interest as these are growth areas for future radiotherapy treatments.

- Further optimization of the EPR settings is needed, as this may further extend the dose range below 1 Gy.

7.2.3 Chapter 4- A Comparison of the EPR angular response of alanine and IRGANOX®1076

Dispersing alanine powder within wax, so that the wax is the bulk component, helped protect the alanine from external water diffusion, which also reduced its EPR angular response. This work indicated that the alanine-wax pellets could be stored for

more than three months post-irradiation in conditions where the humidity and temperature were not controlled, without affecting the EPR angular response.

Further areas of work and investigation include:

- Investigating the possibility of using commercial alanine pellets coated in a layer of wax to see if this helps to reduce the effects of angular response post-irradiation. If successful, it would be a quick and reliable means to reduce the effects in commercially available alanine pellets and remove the need to average several EPR cavity measurements.

- The lower EPR angular response for IRGANOX® 1076 is possibly due to its hydrophobic structure, which reduces its water content, and therefore its effects on the resonance within the EPR cavity. Similarly, IRGANOX® 1076 in wax forms a solid solution, which when irradiated yields a single radical species, therefore radical transformations do not occur. These properties are not shared by alanine, which is highly hygroscopic and forms three radical species, which can undergo transformations post-irradiation. Therefore, future work could examine the importance of these properties further by analysing the water content of IRGANOX® 1076 and alanine samples and how it affects the angular response over time. Repeating this work with more samples and measurements may yield a statistically significant result in favour of IRGANOX® 1076 over alanine.

- IRGANOX®1076 showed the same decrease in radical yield for kV X-ray irradiations as does alanine, which may be reflective of another process

occurring that is not evident in the other irradiations completed. It was thought that bond-dissociation energy differences needed to form the dosimeter's radical species; -O-H for IRGANOX®1076 compared to -C-H for alanine may be a factor. As there is no literature information regarding this further investigation is warranted.

7.2.4 Chapter 5- Investigation of the novel method 'spiking' to determine low doses (< 2 Gy) using alanine dosimeters

The spiking method allowed doses of ≤ 2 Gy to be reliably detected using alanine dosimeters; the method is advantageous as it is easy to perform, does not modify the chemical composition of alanine or require changes to the EPR spectrometer.

Future work to be completed would be:

- Repeat studies of the method to further validate its use as a reliable protocol.

- To determine the effects of the spike dose size upon sensitivity. Doses of 20 Gy and 30 Gy were employed as baseline distortions at less than 10 Gy are known to affect measurements of the central alanine peak's amplitude, therefore, the spike size may be of importance and an optimum spike dose could be determined.

- Optimisation of the EPR spectrometer conditions needs investigation, as this too could increase the sensitivity and reliability of the method, and help

further reduce the lower limits of detection.

- To further validate the method, the use of more calibration pellets (from which an average is used) would improve the statistical strength of the method and may also improve the lower limits of detection.

7.2.5 Chapter 6- The formation of bimetallic-nanoparticles by neutron capture

Using neutron capture the BiMetNP product; AuHgNP was successfully produced from the AuNP starting material, and the gamma decay of the unstable ^{198}Au isotope to the stable ^{198}Hg successfully measured.

Future work in this area could focus on the following:

- To examine and measure the biological effects of AuHgNPs on cells; such as cell viability and toxicity measurements. This would be beneficial, particularly, as mercury is known to induce oxidative stress on cells.

- Following neutron capture, the beta and gamma-decay of the ^{198}Au isotope to the ^{198}Hg could be used as an imaging agent; therefore further assessment is needed. Furthermore, as the decay process also has a therapeutic benefit, cell studies to determine the extent of this dose deposition is of interest.

- Irradiations of AuHgNPs using therapeutic beams and the DE levels obtained would also be of interest as the product could provide an additional target in treatment.

References

1. R. Baskar, K.A. Lee, R. Yeo, K.W. Yeoh, "Cancer and radiation therapy: current advances and future directions," Int J Med Sci **9**, 193- 199 (2012).
2. C.G.B.o.D. Cancer, "Global, regional, and national cancer incidence, mortality, years of life lost, years lived with disability, and disability-adjusted life-years for 32 cancer groups, 1990 to 2015: A systematic analysis for the global burden of disease study," JAMA Oncol **3**, 524- 548 (2017).
3. K. Cheung, "Intensity modulated radiotherapy: advantages, limitations and future developments," Biomed Imaging Interv J **2**, e19 (2006).
4. J.F. Hainfeld, F.A. Dilmanian, D.N. Slatkin, H.M. Smilowitz, "Radiotherapy enhancement with gold nanoparticles," J Pharm Pharmacol **60**, 977- 985 (2008).
5. E.J. Hall, A.J. Giaccia, *Radiobiology for the Radiologist*. (Lippincott Williams & Wilkins, 2006).
6. D. Eriksson, T. Stigbrand, "Radiation-induced cell death mechanisms," Tumor Biology **31**, 363- 372 (2010).
7. D. Gautam, "Radiation Effects on Cells," in *Technology, Health & Medicine* (Slideshare.net, 2013).
8. P. Symonds, C. Deehan, J.A. Mills, C. Meredith, *Water and Miller's Textbook of Radiotherapy, Radiation Physics, Therapy and Oncology*. (Elsevier Ltd., China, 2012).
9. C. Leroy, P.G. Rancoita, *Principles of Radiation Interaction in Matter and Detection*. (World Scientific Publishing Company, 2015).
10. P. Cherry, A.M. Duxbury, *Practical Radiotherapy, Physics and Equipment*, Second ed. (Blackwell Publishing Ltd, Singapore, 2009).
11. T.C. Zhu, K.K.H. Wang, "Linear Accelerators (LINAC)," in *Encyclopedia of Radiation Oncology,* edited by L.W. Brady, T.E. Yaeger (Springer Berlin Heidelberg, Berlin, Heidelberg, 2013), pp. 437- 450.
12. F. Khan, *Physics of Radiation Therapy*, 4th ed. (Lippincott Williams & Wilkins, Baltimore, MD, 2010).
13. W. Roa, X. Zhang, L. Guo, A. Shaw, X. Hu, Y. Xiong, S. Gulavita, S. Patel, X. Sun, J. Chen, R. Moore, J.Z. Xing, "Gold nanoparticle sensitize radiotherapy of prostate cancer cells by regulation of the cell cycle," Nanotechnology **20**, 375101 (2009).
14. J.C. Breneman, "Electron Beam Therapy," in *Radiation Treatment and Radiation Reactions in Dermatology,* edited by R.G. Panizzon, J.S. Cooper (Springer Berlin Heidelberg, Berlin, Heidelberg, 2004), pp. 89- 96.
15. M. Chalmers, "How particles can be therapeutic," Physics World **16**, v (2003).

16. J.G. Douglas, S. Lee, G.E. Laramore, M. Austin-Seymour, W. Koh, T.W. Griffin, "Neutron radiotherapy for the treatment of locally advanced major salivary gland tumors," Head Neck **21**, 255- 263 (1999).
17. M. Marrale, M. Brai, G. Gennaro, A. Triolo, A. Bartolotta, M.C. D'Oca, G. Rosi, "Alanine blends for ESR measurements of thermal neutron fluence in a mixed radiation field," Radiat Prot Dosimetry **126**, 631- 635 (2007).
18. F.M. Wagner, B. Loeper-Kabasakal, H. Breitkreutz, "Neutron medical treatment of tumours — a survey of facilities," J Instrum **7**, 45- 47 (2012).
19. D. Hamilton, presented at the Radioactivity-Radionuclides-Radiation 8th Multi-Media Training Course with Nuclides, Institute Joszef Stefan, Ljuljana, Slovenia, 2006 (unpublished).
20. J. Lilley, *Nuclear Physics: Principles and Applications*. (John Wiley and Sons Ltd. , 2001).
21. K. Sorensen, "Welcome to the Energy from Thorium Foundation!," (2006).
22. W.D. Newhauser, R. Zhang, "The physics of proton therapy," Phys Med Biol **60**, R155- 209 (2015).
23. S. Tavernier, "Interactions of Particles in Matter," in *Experimental Techniques in Nuclear and Particle Physics* (Springer Berlin Heidelberg, Berlin, Heidelberg, 2010), pp. 23- 53.
24. W.N. Rahman, N. Bishara, T. Ackerly, C.F. He, P. Jackson, C. Wong, R. Davidson, M. Geso, "Enhancement of radiation effects by gold nanoparticles for superficial radiation therapy," Nanomed **5**, 136- 142 (2009).
25. J. Seco, B. Clasie, M. Partridge, "Review on the characteristics of radiation detectors for dosimetry and imaging," Phys Med Biol **59**, R303- 347 (2014).
26. F.C. Abrego, C.S. Calcina, A. de Almeida, C.E. de Almeida, O. Baffa, "Relative output factor and beam profile measurements of small radiation fields with an L-alanine/K-band EPR minidosimeter," Med Phys **34**, 1573- 1582 (2007).
27. M. Marrale, S. Galloa, A. Longo, S. Panzeca, A. Parlato, A. Buttafava, D. Dondi, A. Zeffiro, "Study of the response of phenol compounds exposed to thermal neutrons beams for Electron Paramagnetic Resonance dosimetry," Radiat Meas **75**, 15- 20 (2015).
28. G.F. Knoll, *Radiation detection and measurement*, 4th ed. (John Wiley, Hoboken, N.J., 2010).
29. J. Adamovics, M.J. Maryanski, "Characterisation of PRESAGE: A new 3-D radiochromic solid polymer dosemeter for ionising radiation," Radiat Prot Dosimetry **120**, 107- 112 (2006).

30. J. Izewska, G. Rajan, "Radiation Dosimeters," in *Radiation Oncology Physics: A Handbook for Teachers and Students,* edited by E.B. Podgorsak, Ed. (International Atomic Energy Agency-IAEA, Vienna, 2005).
31. P.R. Almond, P.J. Biggs, B.M. Coursey, W.F. Hanson, M. Saiful Huq, R. Nath, D.W. Rogers, "AAPM's TG-51 protocol for clinical reference dosimetry of high-energy photon and electron beams," Med. Phys. **26**, 1847- 1870 (1999).
32. M.J. Butson, P.K.N. Yu, T. Cheung, P. Metcalfe, "Radiochromic film for medical radiation dosimetry," Mater Sci Eng R Rep **41**, 61- 120 (2003).
33. M. Williams, P. Metcalfe, "Radiochromic film dosimetry and its applications in radiotherapy," AIP Conference Proceedings **1345**, 75- 99 (2011).
34. G.R. Eaton, S.S. Eaton, K.M. Salikhov, *Foundations of Modern EPR*. (World Scientific, Singapore, 1998).
35. J.E. Wertz, J.R. Bolton, *Electron Spin Resonance: Elementary Theory and Practical Applications*. (McGraw-Hill, New York, 1972).
36. D.A. Schauer, A. Iwasaki, A.A. Romanyukha, H.M. Swartz, S. Onori, "Electron paramagnetic resonance (EPR) in medical dosimetry," Radiat Meas **41**, 117- 123 (2007).
37. Y.E. Nesmelov, A. Gopinath, D.D. Thomas, "Aqueous sample in an EPR cavity: sensitivity considerations," J Magn Reson **167**, 138-146 (2004).
38. E.J. Guidelli, A.P. Ramos, M.E. Zaniquelli, P. Nicolucci, O. Baffa, "Synthesis and characterization of gold/alanine nanocomposites with potential properties for medical application as radiation sensors," ACS Appl Mater Interfaces **4**, 5844- 5851 (2012).
39. E.J. Guidelli, A.P. Ramos, M.E. Zaniquelli, P. Nicolucci, O. Baffa, "Synthesis and characterization of silver/alanine nanocomposites for radiation detection in medical applications: the influence of particle size on the detection properties," Nanoscale **4**, 2884- 2893 (2012).
40. B. Ciesielski, K. Schultka, A. Kobierska, R. Nowak, Z. Peimel-Stuglik, "In vivo alanine/EPR dosimetry in daily clinical practice: a feasibility study," Int J Radiat Oncol Biol Phys **56**, 899- 905 (2003).
41. O. Baffa, A. Kinoshita, "Clinical applications of alanine/electron spin resonance dosimetry," Radiat Environ Biophys **53**, 233- 240 (2014).
42. B. Michalec, G. Mierzwińska, U. Sowa, M. Ptaszkiewicz, T. Nowak, J. Swakoń, "Alanine dosimetry of 60 MeV proton beam - preliminary results " Nukleonika **57**, 503- 506 (2012).
43. R. Herrmann, O. Jakel, H. Palmans, P. Sharpe, N. Bassler, "Dose response of alanine detectors irradiated with carbon ion beams," Med Phys **38**, 1859- 1866 (2011).
44. E. Lund, E. Adolfsson, N. Kolbun, H. Gustafsson, "EPR imaging of dose distributions aiming at applications in radiation therapy," Radiat Prot Dosimetry **159**, 130- 136 (2014).

45. S. Onori, F. d'Errico, C. De Angelis, E. Egger, P. Fattibene, I. Janovsky, "Alanine dosimetry of proton therapy beams," Med Phys **24**, 447- 453 (1997).
46. M.Z. Heydari, E. Malinen, E.O. Hole, E. Sagstuen, "Alanine Radicals. 2. The composite polycrystalline alanine EPR spectrum studied by ENDOR, thermal annealing, and spectrum simulations," J Phys Chem A **106**, 8971–8977 (2002).
47. E.J. Guidelli, O. Baffa, "Influence of photon beam energy on the dose enhancement factor caused by gold and silver nanoparticles: An experimental approach," Med Phys **41**, 032101 (2014).
48. R.B. Hayes, E.H. Haskell, A. Wieser, A.R. Romanyukha, B.L. Hardy, J.K. Barrus, "Assessment of an alanine EPR dosimetry technique with enhanced precision and accuracy," Nucl Instrum Meth A **440**, 453- 461 (2000).
49. J.M. Dolo, V. Feaugas, "Analysis of parameters that influence the amplitude of the ESR/alanine signal after irradiation," Appl Radiat Isot **62**, 273- 279 (2005).
50. M. Marrale, A. Longo, M. Spano, A. Bartolotta, M.C. D'Oca, M. Brai, "Sensitivity of alanine dosimeters with gadolinium exposed to 6 MV photons at clinical doses," Radiat Res **176**, 821- 826 (2011).
51. F. Chen, P. Nicolucci, O. Baffa, "Enhanced sensitivity of alanine dosimeters to low-energy X-rays:Preliminary results," Radiat Meas **43**, 467- 470 (2008).
52. E.H. Haskell, R.B. Hayes, G.H. Kenner, "A high sensitivity EPR technique for alanine dosimetry," Radiat Prot Dosim **77**, 43- 49 (1998).
53. V.V. Nagy, "Accuracy considerations in EPR dosimetry," Appl Radiat Isot **52**, 1039- 1050 (2000).
54. F. Chen, C.F. Graeff, O. Baffa, "K-band EPR dosimetry: small-field beam profile determination with miniature alanine dosimeter," Appl Radiat Isot **62**, 267- 271 (2005).
55. F. Chen, C.F.O. Graeff, O. Baffa, "Response of L-alanine and 2-methylalanine minidosimeters for K-Band (24 GHz) EPR dosimetry," Nucl Instrum Meth B **264**, 277- 281 (2007).
56. S. Jain, D.G. Hirst, J.M. O'Sullivan, "Gold nanoparticles as novel agents for cancer therapy," Br J Radiol **85**, 101- 113 (2012).
57. J.C. Tarafdar, T. Adhikari, *Soil Science: An Introduction*. (Indian Society of Soil Science, India, 2015).
58. S. Bhattacharyya, R.A. Kudgus, R. Bhattacharya, P. Mukherjee, "Inorganic nanoparticles in cancer therapy," Pharm Res **28**, 237- 259 (2011).
59. K.T. Butterworth, S.J. McMahon, F.J. Currell, K.M. Prise, "Physical basis and biological mechanisms of gold nanoparticle radiosensitization," Nanoscale **4**, 4830- 4838 (2012).

60. U.K. Parida, S.K. Biswal, P.L. Nayak, P.K. Bindhani, "Gold nanoparticles for biomedical applications," WJNSE **2**, 47- 57 (2013).
61. P.K. Jain, I.H. El-Sayed, M.A. El-Sayed, "Au nanoparticles target cancer," Nano Today **2**, 18- 29 (2007).
62. R. Kannan, V. Rahing, C. Cutler, R. Pandrapragada, K.K. Katti, V. Kattumuri, J.D. Robertson, S.J. Casteel, S. Jurisson, C. Smith, E. Boote, K.V. Katti, "Nanocompatible chemistry toward fabrication of target-specific gold nanoparticles," J Am Chem Soc **128**, 11342- 11343 (2006).
63. G. Schmid, B. Corain, "Nanoparticulated gold: syntheses, structures, electronics, and reactivities," Eur J Inorg Chem **17**, 3081- 3098 (2003).
64. S. Eustis, M.A. El-Sayed, "Why gold nanoparticles are more precious than pretty gold: Noble metal surface plasmon resonance and its enhancement of the radiative and nonradiative properties of nanocrystals of different shapes.," Chem Soc Rev **35**, 209- 217 (2006).
65. H. Zhang, T. Watanabe, M. Okumura, M. Haruta, N. Toshima, "Catalytically highly active top gold atom on palladium nanocluster," Nat Mater **11**, 49- 52 (2012).
66. M. Meena Kumari, S.A. Aromal, D. Philip, "Synthesis of monodispersed palladium nanoparticles using tannic acid and its optical non-linearity," Spectrochim Acta A Mol Biomol Spectrosc **103**, 130- 133 (2013).
67. Y. Dai, X. Kang, D. Yang, X. Li, X. Zhang, C. Li, Z. Hou, Z. Cheng, P. Ma, J. Lin, "Platinum (IV) pro-drug conjugated NaYF4 :Yb(3+) /Er(3+) nanoparticles for targeted drug delivery and up-conversion cell imaging," Adv Healthc Mater **2**, 562- 567 (2013).
68. N. Chanda, P. Kan, L.D. Watkinson, R. Shukla, A. Zambre, T.L. Carmack, H. Engelbrecht, J.R. Lever, K. Katti, G.M. Fent, S.W. Casteel, C.J. Smith, W.H. Miller, S. Jurisson, E. Boote, J.D. Robertson, C. Cutler, M. Dobrovolskaia, R. Kannan, K.V. Katti, "Radioactive gold nanoparticles in cancer therapy: therapeutic efficacy studies of GA-198AuNP nanoconstruct in prostate tumor-bearing mice," Nanomedicine **6**, 201- 209 (2010).
69. M.K. Khan, L.D. Minc, S.S. Nigavekar, M.S. Kariapper, B.M. Nair, M. Schipper, A.C. Cook, W.G. Lesniak, L.P. Balogh, "Fabrication of {198Au0} radioactive composite nanodevices and their use for nanobrachytherapy," Nanomedicine **4**, 57- 69 (2008).
70. C.C. You, A. Chompoosor, V.M. Rotello, "The biomacromolecule-nanoparticle interface," Nano Today **2**, 34- 43 (2007).
71. A.K. Iyer, G. Khaled, J. Fang, H. Maeda, "Exploiting the enhanced permeability and retention effect for tumor targeting," Drug Discov Today **11**, 812- 818 (2006).
72. H. Kobayashi, R. Watanabe, P.L. Choyke, "Improving conventional enhanced permeability and retention (EPR) effects; What is the appropriate target?," Theranostics **4**, 81- 89 (2014).

73. H. Zhang, J. Okuni, N. Toshima, "One-pot synthesis of Ag-Au bimetallic nanoparticles with Au shell and their high catalytic activity for aerobic glucose oxidation," J Colloid Interface Sci **354**, 131- 138 (2011).
74. S. Valetti, S. Mura, B. Stella, P. Couvreur, "Rational design for multifunctional non-liposomal lipid-based nanocarriers for cancer management: theory to practice," J Nanobiotechnology **11 Suppl 1**, S6 (2013).
75. L. Smith, Z. Kuncic, K. Ostrikov, S. Kumar, "Nanoparticles in cancer imaging and therapy," J Nanomater **2012**, 1- 7 (2012).
76. J.F. Hainfeld, D.N. Slatkin, H.M. Smilowitz, "The use of gold nanoparticles to enhance radiotherapy in mice," Phys Med Biol **49**, N309- 315 (2004).
77. S.J. McMahon, M.H. Mendenhall, S. Jain, F. Currell, "Radiotherapy in the presence of contrast agents: a general figure of merit and its application to gold nanoparticles," Phys Med Biol **53**, 5635- 5651 (2008).
78. S.H. Cho, "Estimation of tumour dose enhancement due to gold nanoparticles during typical radiation treatments: a preliminary Monte Carlo study," Phys Med Biol **50**, N163- 173 (2005).
79. C. Walzlein, E. Scifoni, M. Kramer, M. Durante, "Simulations of dose enhancement for heavy atom nanoparticles irradiated by protons," Phys Med Biol **59**, 1441- 1458 (2014).
80. J.K. Kim, S.J. Seo, H.T. Kim, K.H. Kim, M.H. Chung, K.R. Kim, S.J. Ye, "Enhanced proton treatment in mouse tumors through proton irradiated nanoradiator effects on metallic nanoparticles," Phys Med Biol **57**, 8309- 8323 (2012).
81. J.C. Jeynes, M.J. Merchant, A. Spindler, A.C. Wera, K.J. Kirkby, "Investigation of gold nanoparticle radiosensitization mechanisms using a free radical scavenger and protons of different energies," Phys Med Biol **59**, 6431- 6443 (2014).
82. H. Zhang, M. Haba, M. Okumura, T. Akita, S. Hashimoto, N. Toshima, "Novel formation of Ag/Au bimetallic nanoparticles by physical mixture of monometallic nanoparticles in dispersions and their application to catalysts for aerobic glucose oxidation," Langmuir **29**, 10330- 10339 (2013).
83. S. Tokonami, S. Morita, K. Takasaki, N. Toshima, "Novel synthesis, structure, and oxidation catalysis of Ag/Au bimetallic nanoparticles," J Phys Chem A **114**, 10336- 10341 (2010).
84. R.W. Scott, A.K. Datye, R.M. Crooks, "Bimetallic palladium-platinum dendrimer-encapsulated catalysts," J Am Chem Soc **125**, 3708- 3709 (2003).
85. S. Devarajan, P. Bera, S. Sampath, "Bimetallic nanoparticles: a single step synthesis, stabilization, and characterization of Au-Ag, Au-Pd, and Au-Pt in sol-gel derived silicates," J Colloid Interface Sci **290**, 117- 129 (2005).

86. Y. Wu, P. Jiang, M. Jiang, T.W. Wang, C.F. Guo, S.S. Xie, Z.L. Wang, "The shape evolution of gold seeds and gold@silver core-shell nanostructures," Nanotechnology **20**, 305602 (2009).
87. J.L.H. Chau, C. Chen, M. Yang, K. Lin, S. Sato, T. Nakamura, C. Yang, C. Cheng, "Femtosecond laser synthesis of bimetallic Pt–Au nanoparticles," Mater Lett **65**, 804- 807 (2011).
88. H. Zhang, J. Okuni, N. Toshima, "Size-controlled synthesis of gold nanoparticles by thermolysis of a

gold(I)-sulfide complex in the presence of alkylamines," J Colloid Interface Sci **354**, 131- 138 (2010).
89. X.Y. Su, P.D. Liu, H. Wu, N. Gu, "Enhancement of radiosensitization by metal-based nanoparticles in cancer radiation therapy," Cancer Biol Med **11**, 86- 91 (2014).
90. M. Misawa, J. Takahashi, "Generation of reactive oxygen species induced by gold nanoparticles under x-ray and UV Irradiations," Nanomed Nanotech Biol Med **7**, 604- 614 (2011).
91. K.B. Lee, J.S. Lee, J.W. Park, T.L. Huh, Y.M. Lee, "Low energy proton beam induces tumor cell apoptosis through reactive oxygen species and activation of caspases," Exp Mol Med **40**, 118- 129 (2008).
92. A. Mesbahi, F. Jamali, N. Garehaghaji, "Effect of photon beam energy, gold nanoparticle size and concentration on the dose enhancement in radiation therapy," Bioimpacts **3**, 29- 35 (2013).
93. S. Das, N. Debnath, S. Mitra, A. Datta, A. Goswami, "Comparative analysis of stability and toxicity profile of three differently capped gold nanoparticles for biomedical usage," Biometals **25**, 1009- 1022 (2012).
94. C.M. Goodman, C.D. McCusker, T. Yilmaz, V.M. Rotello, "Toxicity of gold nanoparticles functionalized with cationic and anionic side chains," Bioconjug Chem **15**, 897- 900 (2004).
95. J.F. Hainfeld, H.M. Smilowitz, M.J. O'Connor, F.A. Dilmanian, D.N. Slatkin, "Gold nanoparticle imaging and radiotherapy of brain tumors in mice," Nanomedicine (Lond) **8**, 1601- 1609 (2013).
96. X.D. Zhang, D. Wu, X. Shen, J. Chen, Y.M. Sun, P.X. Liu, X.J. Liang, "Size-dependent radiosensitization of PEG-coated gold nanoparticles for cancer radiation therapy," Biomaterials **33**, 6408- 6419 (2012).
97. D.R. Cooper, D. Bekah, J.L. Nadeau, "Gold nanoparticles and their alternatives for radiation therapy enhancement," Front Chem **2**, 86 (2014).
98. C. Hwang, J.M. Kim, J.H. Kim, "Influence of concentration, nanoparticle size, beam energy, and material on dose enhancement in radiation therapy," J Radiat Res, 1– 7 (2017).
99. E. Lechtman, N. Chattopadhyay, Z. Cai, S. Mashouf, R. Reilly, J.P. Pignol, "Implications on clinical scenario of gold nanoparticle radiosensitization

in regards to photon energy, nanoparticle size, concentration and location," Phys Med Biol **56**, 4631- 4647 (2011).
100. M. Khadem Abolfazli, S.R. Mahdavi, G. Ataei, "Studying effects of gold nanoparticle on dose enhancement in megavoltage radiation," J Biomed Phys Eng **5**, 185- 190 (2015).
101. M. Hossain, M. Su, "Nanoparticle location and material dependent dose enhancement in X-ray radiation therapy," J Phys Chem C Nanomater Interfaces **116**, 23047- 23052 (2012).
102. M.Y. Chang, A.L. Shiau, Y.H. Chen, C.J. Chang, H.H. Chen, C.L. Wu, "Increased apoptotic potential and dose-enhancing effect of gold nanoparticles in combination with single-dose clinical electron beams on tumor-bearing mice," Cancer sci **99**, 1479- 1484 (2008).
103. J.C. Polf, L.F. Bronk, W.H. Driessen, W. Arap, R. Pasqualini, M. Gillin, "Enhanced relative biological effectiveness of proton radiotherapy in tumor cells with internalized gold nanoparticles," Appl Phys Lett **98**, 193702 (2011).
104. I. Martinez-Rovira, Y. Prezado, "Evaluation of the local dose enhancement in the combination of proton therapy and nanoparticles," Med Phys **42**, 6703- 6710 (2015).
105. Y. Liu, X. Liu, X. Jin, P. He, X. Zheng, Z. Dai, F. Ye, T. Zhao, W. Chen, Q. Li, "The dependence of radiation enhancement effect on the concentration of gold nanoparticles exposed to low- and high-LET radiations," Phys Med **31**, 210- 218 (2015).
106. P. Ionita, M. Conte, B.C. Gilbert, V. Chechik, "Gold nanoparticle-initiated free radical oxidations and halogen abstractions," Org Biomol Chem **5**, 3504- 3509 (2007).
107. C. Sicard-Roselli, E. Brun, M. Gilles, G. Baldacchino, C. Kelsey, H. McQuaid, C. Polin, N. Wardlow, F. Currell, "A new mechanism for hydroxyl radical production in irradiated nanoparticle solutions," Small **10**, 3338- 3346 (2014).
108. R.A. Davidson, T. Guo, "Average physical enhancement by nanomaterials under X-ray irradiation," J Phys Chem C **118**, 30221- 30228 (2014).
109. X. Yao, C. Huang, X. Chen, Z. Yi, L. Sanche, "Chemical radiosensitivity of DNA induced by gold nanoparticles," J Biomed Nanotechnol **11**, 478- 485 (2015).
110. J.M. Dolo, T. Garcia, "Angular response of alanine samples: From powder to pellet," Radiation Measurements **42**, 1201- 1206 (2007).
111. B. Adu, L. Otten, "Effect of polarization on the heat of desorption of water in dielectrics.," J Microwave Power EE **31**, 43- 49 (1996).
112. C. De Angelis, V. De Coste, P. Fattibene, S. Onori, E. Petetti, "Use of alanine for dosimetry intercomparisons among Italian radiotherapy centers," Appl Radiat Isot **62**, 261- 265 (2005).

113. M. Anton, "Development of a secondary standard for the absorbed dose to water based on the alanine EPR dosimetry system," Appl Radiat Isot **62**, 779- 795 (2005).
114. R.J.J. Fehir, J.K. McCusker, "Differential polarization of spin and charge density in substituted phenoxy radicals," J Phys Chem A **113**, 9249- 9260 (2009).
115. C. McCrory-Joy, J.M. Rosamilia, "Electrochemical oxidation and determination of high-molecular-weight sterically hindered phenols," Anal Chim Acta **141**, 371- 376 (1982).
116. J.A. Richards, P.E. Whitson, D.E. Evans, "Electrochemical oxidation of 2,4,6-tri-tert-butylphenol," J Electroanal Chem **63**, 311- 327 (1975).
117. J.P. Collman, R.A. Decreau, C.J. Sunderland, "Single-turnover intermolecular reaction between a Fe(III)-superoxide-Cu(I) cytochrome c oxidase model and exogeneous Tyr244 mimics," Chem Commun (Camb), 3894- 3896 (2006).
118. B. Heyne, V. Maurel, J.C. Scaiano, "Mechanism of action of sensors for reactive oxygen species based on fluorescein-phenol coupling: the case of 2-[6-(4'-hydroxy)phenoxy-3H-xanthen-3-on-9-yl]benzoic acid," Org Biomol Chem **4**, 802- 807 (2006).
119. A.P. Neal-Kluever, A.B. Bailey, K.R. Hatwell, "Safety assessment for octadecyl 3-(3,5-di-tert-butyl-4-hydroxyphenyl)-propionate (CAS Reg. No. 2082-79-3) from use in food contact applications," Food Chem Toxicol **86**, 176- 190 (2015).
120. M. Marrale, A. Longoa, S. Panzecaa, S. Galloa, F. Principatoa, E. Tomarchioc, A. Parlatoc, A. Buttafavad, D. Dondid, A. Zeffirod, "ESR response of phenol compounds for dosimetry of gamma photon beams," Nucl Instrum Meth B **339**, 15- 19 (2014).
121. T.A. Gadosy, D. Shukla, L.J. Johnston, "Generation, characterization, and deprotonation of phenol radical cations," J Phys Chem A **103**, 8834- 8839 (1999).
122. I. Miyagawa, W. Gordy, "Electron spin resonance of an irradiated single crystal of alanine: Second-order effects in free radical resonances. ," J Chem Phys **32**, 255- 263 (1960).
123. J.M. Dolo, F. Moignau, "Use of the entire spectrum of irradiated alanine for dosimetry," Appl Radiat Isot **62**, 281- 285 (2005).
124. T. Kron, J. Lehmann, P.B. Greer, "Dosimetry of ionising radiation in modern radiation oncology," Phys Med Biol **61**, R167- 205 (2016).
125. F.J. Ahlers, C.C.J. Schneider, "Alanine ESR dosimetry: an assessment of peak-to-peak evaluation," Radiat Prot Dosimetry **37**, 117- 122 (1991).
126. P.H. Sharpe, K. Rajendran, J.P. Sephton, "Progress towards an alanine/ESR therapy level reference dosimetry service at NPL," Appl Radiat Isot **47**, 1171- 1175 (1996).
127. D. Harvey, *Modern Analytical Chemistry*. (Mc Graw Hill, New York, 2000).

128. V. Chumak, J. Pavlenko, S. Sholom, "An approach to the assessment of overall uncertainty of determination of dose using an ESR technique," Appl Radiat Isot **47**, 1287- 1291 (1996).
129. V.A. Kirillov, J.I. Kuchuro, "Exposure dose reconstruction from EPR spectra of tooth enamel exposed to the combined effect of X-rays and gamma radiation," J Appl Spectrosc **81**, 649- 653 (2014).
130. A.A. Romanyukha, D.A. Schauer, J.A. Thomas, D.F. Regulla, "Parameters affecting EPR dose reconstruction in teeth," Appl Radiat Isot **62**, 147- 154 (2005).
131. A. Wieser, "Review of reconstruction of radiation incident air kerma by measurement of absorbed dose in tooth enamel with EPR," Radiat Prot Dosimetry **149**, 71- 78 (2012).
132. G.A. Yordanov, V. Gancheva, *EPR of Free Radicals in Solids*. (Kluwer Academic Publishers, Dordrecht, 2003).
133. F. Trompier, J. Sadlo, J. Michalik, W. Stachowicz, A. Mazal, I. Clairand, J. Rostkowska, W. Bulski, A. Kulakowski, J. Sluszniak, S. Gozdz, A. Wojcik, "EPR dosimetry for actual and suspected overexposures during radiotherapy treatments in Poland," Radiat Meas **42**, 1025- 1028 (2007).
134. D.B. Hibbert, J.J. Gooding, "Calibration," in *Data Analysis for Chemistry* (Oxford University Press, New York, 2006), pp. 162- 165.
135. J. Seco, B. Clasie, M. Partridge, "Review on the characteristics of radiation detectors for dosimetry and imaging," Phys Med Biol **59**, R303-347 (2014).
136. S. Duan, R. Wang, "Bimetallic nanostructures with magnetic and noble metals and their physicochemical applications " Prog Nat Sci **23**, 113- 126 (2013).
137. Z. Swiatkowska-Warkocka, A. Pyatenko, F. Krok, B.R. Jany, M. Marszalek, "Synthesis of new metastable nanoalloys of immiscible metals with a pulse laser technique," Sci Rep **5**, 9849 (2015).
138. H.B. Elkins, W.C. Keettel, "Radioactive gold in the treatment of ovarian carcinoma," Am J Roentgenol Radium Ther Nucl Med **75**, 1117- 1123 (1956).
139. W.C. Keettel, M.R. Fox, D.S. Longnecker, H.B. Latourette, "Prophylactic use of radioactive gold in the treatment of primary ovarian cancer," Am J Obstet Gynecol **94**, 766- 779 (1966).
140. H.J. Buchsbaum, W.C. Keettel, "Radioisotopes in treatment of stage Ia ovarian cancer," Natl Cancer Inst Monogr **42**, 127- 128 (1975).
141. R.H. Flocks, H.B. Elkins, D. Culp, "Treatment of cancer of prostate by interstitial injection of Au 198: studies in problem of distribution," J Urol **77**, 505- 520 (1957).
142. R.H. Flocks, H.D. Kerr, H.B. Elkins, D.A. Culp, "The treatment of carcinoma of the prostate by interstitial radiation with radioactive gold (Au198); a follow-up report," J Urol **71**, 628- 633 (1954).

143. H.D. Kerr, R.H. Flocks, H.B. Elkins, D. Culp, "The treatment of moderately advanced carcinoma of the prostate with radioactive gold," Am J Roentgenol Radium Ther Nucl Med **69**, 969- 677 (1953).
144. H.M. Rosevear, A.J. Lightfoot, M.A. O'Donnell, C.E. Platz, S.A. Loening, C.E. Hawtrey, "Rubin H. Flocks and colloidal gold treatments for prostate cancer," Sci World J **11**, 1560- 1567 (2011).
145. K.C. Black, Y. Wang, H.P. Luehmann, X. Cai, W. Xing, B. Pang, Y. Zhao, C.S. Cutler, L.V. Wang, Y. Liu, Y. Xia, "Radioactive 198Au-doped nanostructures with different shapes for in vivo analyses of their biodistribution, tumor uptake, and intratumoral distribution," ACS Nano **8**, 4385- 4394 (2014).
146. M.V. Williams, T. Winters, K.S. Waddell, "In vivo effects of mercury (II) on deoxyuridine triphosphate nucleotidohydrolase, DNA polymerase (alpha, beta), and uraciI-DNA glycosylase activities in cultured human cells: Relationship to DNA damage, DNA repair, and cytotoxicity.," Mol Pharmacol **31**, 200- 207 (1987).
147. E.A. Belyaeva, D. Dymkowska, M.R. Wieckowski, L. Wojtczak, "Mitochondria as an important target in heavy metal toxicity in rat hepatoma AS-30D cells," Toxicol Appl Pharmacol **231**, 34- 42 (2008).
148. "Appendix to Method 1631: Total Mercury in Tissue, Sludge, Sediment, and Soil by Acid Digestion and BrCl Oxidation," edited by U.S.E.P.A. (EPA) (National Service Centre for Environmental Publications (NSCEP), USA, 2001), pp. 13.
149. C.A. Shand, M. Balsam, S.J. Hillier, G. Hudson, G. Newman, J.R. Arthur, F. Nicol, "Aqua regia extractable selenium concentrations of some Scottish topsoils measured by ICP-MS and the relationship with mineral and organic soil components," J Sci Food Agric **90**, 972- 980 (2010).
150. Y. Sun, M. Chen, Y. Wang, "Microwave acid-digestion ICP-MS method for the determination of sixteen elements in marine products," Guang Pu Xue Yu Guang Pu Fen Xi **19**, 601- 603 (1999).
151. V. Korunova, J. Dedina, "Determination of trace concentrations of mercury in biological materials after digestion under pressure in nitric acid catalysed by vanadium pentoxide," Analyst **105**, 48-51 (1980).
152. V.F. Taylor, A. Toms, H.P. Longerich, "Acid digestion of geological and environmental samples using open-vessel focused microwave digestion," Anal Bioanal Chem **372**, 360- 365 (2002).

Appendices

Appendix i: Permission to reproduce published materials in Chapter 2

ELSEVIER LICENSE
TERMS AND CONDITIONS

Sep 07, 2017

This Agreement between Ms. Clare Smith ("You") and Elsevier ("Elsevier") consists of your license details and the terms and conditions provided by Elsevier and Copyright Clearance Center.

License Number	4182340559028
License date	Sep 05, 2017
Licensed Content Publisher	Elsevier
Licensed Content Publication	Radiation Measurements
Licensed Content Title	Determination of dose enhancement caused by gold-nanoparticles irradiated with proton, X-rays (kV and MV) and electron beams, using alanine/EPR dosimeters
Licensed Content Author	Clare L. Smith,Trevor Ackerly,Stephen P. Best,Frank Gagliardi,Katahira Kie,Peter J. Little,Giulia McCorkell,Charlotte A. Sale,Yusuke Tsunei,Takahiro Tominaga,Sioe See Volaric,Moshi Geso
Licensed Content Date	Nov 1, 2015
Licensed Content Volume	82
Licensed Content Issue	n/a
Licensed Content Pages	7
Start Page	122
End Page	128
Type of Use	reuse in a thesis/dissertation
Intended publisher of new work	other
Portion	full article
Format	both print and electronic
Are you the author of this Elsevier article?	Yes
Will you be translating?	No
Title of your	The examination of alanine/EPR dosimetry for low-dose

Appendix ii: Permission to reproduce published materials in Chapter 2

ELSEVIER ORDER DETAILS

Sep 07, 2017

Order Number	501304816
Order date	Sep 05, 2017
Licensed Content Publisher	Elsevier
Licensed Content Publication	Radiation Measurements
Licensed Content Title	The effects of gold nanoparticles concentrations and beam quality/LET on dose enhancement when irradiated with X-rays and protons using alanine/EPR dosimetry
Licensed Content Author	Clare L. Smith,Stephen P. Best,Frank Gagliardi,Takahiro Tominaga,Moshi Geso
Licensed Content Date	Available online 3 February 2017
Licensed Content Volume	n/a
Licensed Content Issue	n/a
Licensed Content Pages	1
Start Page	
End Page	
Type of Use	reuse in a thesis/dissertation
Portion	full article
Format	both print and electronic
Are you the author of this Elsevier article?	Yes
Will you be translating?	No
Title of your thesis/dissertation	The examination of alanine/EPR dosimetry for low-dose determination, dose enhancement caused by AuNPs, and the novel synthesis of bimetallic-nanoparticles via neutron capture.
Expected completion date	Sep 2017
Estimated size (number of pages)	250

Appendix iii: Permission to reproduce published materials in Chapter 3 & 4

ELSEVIER LICENSE
TERMS AND CONDITIONS

Sep 07, 2017

This Agreement between Ms. Clare Smith ("You") and Elsevier ("Elsevier") consists of your license details and the terms and conditions provided by Elsevier and Copyright Clearance Center.

License Number	4182340464121
License date	Sep 05, 2017
Licensed Content Publisher	Elsevier
Licensed Content Publication	Radiation Physics and Chemistry
Licensed Content Title	Investigation of IRGANOX®1076 as a dosimeter for clinical X-ray, electron and proton beams and its EPR angular response
Licensed Content Author	Clare L. Smith,Elizabeth Ankers,Stephen P. Best,Frank Gagliardi,Kai Katahira,Yseu Tsunei,Takahiro Tominaga,Moshi Geso
Licensed Content Date	Dec 1, 2017
Licensed Content Volume	141
Licensed Content Issue	n/a
Licensed Content Pages	8
Start Page	284
End Page	291
Type of Use	reuse in a thesis/dissertation
Intended publisher of new work	other
Portion	full article
Format	both print and electronic
Are you the author of this Elsevier article?	Yes
Will you be translating?	No
Title of your thesis/dissertation	The examination of alanine/EPR dosimetry for low-dose determination, dose enhancement caused by AuNPs, and the novel synthesis of bimetallic-nanoparticles via neutron capture.

Filename:	Thesis CLS Feb 2018.docx
Directory:	\\ntapprdfs01n02.rmit.internal\eh9\e15459
Template:	C:\Users\e15459\AppData\Roaming\Microsoft\Templates\Normal.dotm
Title:	
Subject:	
Author:	Clare Smith
Keywords:	
Comments:	
Creation Date:	10/06/2017 12:01:00 AM
Change Number:	146
Last Saved On:	12/02/2018 7:19:00 PM
Last Saved By:	Clare Smith
Total Editing Time:	58,550 Minutes
Last Printed On:	12/02/2018 7:19:00 PM

As of Last Complete Printing

Number of Pages:	264
Number of Words:	91,011 (approx.)
Number of Characters:	518,764 (approx.)